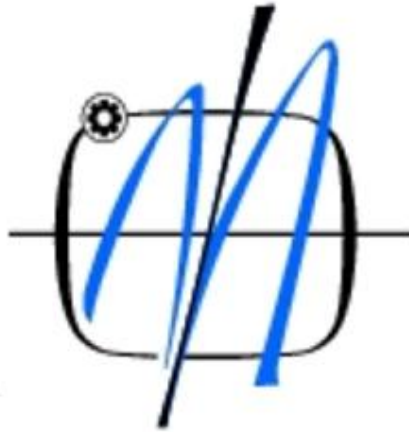


UNIVERSITY OF BELGRADE
FACULTY OF MECHANICAL ENGINEERING



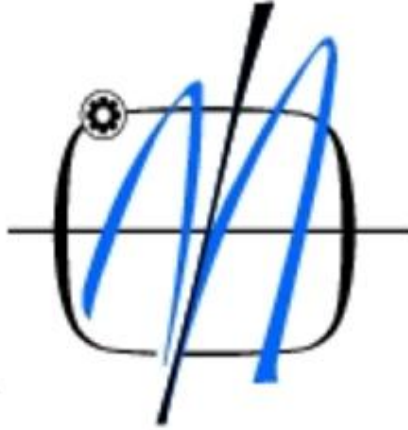
MOSTAFA ABOBAKER

LOW REYNOLDS NUMBER AIRFOILS

DOCTORAL DISSERTATION

BELGRADE 2017

УНИВЕРЗИТЕТ У БЕОГРАДУ
МАШИНСКИ ФАКУЛТЕТ



Мостафа Абобакер

АЕРОПРОФИЛИ ЗА МАЛЕ
РЕЈНОЛДСОВЕ БРОЈЕВЕ

Докторска дисертација

БЕОГРАД, 2017

TO MY FAMILY

ACKNOWLEDGEMENTS

I would like to express my sincere thanks and gratitude to my advisor professor Zlatko Petrović for his valuable and continuous advice, thoughtfulness and assistance throughout the duration of this work.

I would like to express my sincere thanks and gratitude to all PhD program staff members of Faculty of Mechanical Engineering, University of Belgrade and to the Innovation Center at the Faculty of Mechanical Engineering, University of Belgrade.

I would like to express my gratitude to Libyan Ministry of High Education and Science Research and to Libyan Scholarship Administration for their financial support. This research would not have been accomplished without their support.

I also would like to take this opportunity to thank my family who are surely proud of me on this day.

Special thanks to the staffs, students and friends that I have met during my research study especially those working on doctoral theses at the Faculty of Mechanical Engineering, University of Belgrade.

Above all, I am very much grateful to almighty Allah for giving me courage and good health for completing this research.

Mostafa Abobaker

BELGRADE 2017

Abstract

In this thesis, the flow around airfoils at low Reynolds numbers has been modeled. The model utilizes inviscid-viscous interaction method. The inviscid-viscous interaction method supplemented by an adequate laminar separation bubble modeling has been proven to be efficient design tool when numerical optimization, by systematic shape modification, is anticipated.

The inviscid solution of the potential flow equation is based on conformal mapping. The viscous formulation employs the solution of integral momentum and energy boundary layer equations. Eppler transition prediction model is followed when no laminar separations occur. In case of laminar flow separation, however, Drela modified transition is applied inside a laminar separation bubble model. The laminar separation bubble is divided into three parts, laminar part, turbulent part and reattachment region. After reattachment the boundary layer dissipation coefficient equation is solved with the standard two boundary layer equations. This formulation allows the method to account for drag effects from laminar separation bubble, as well as tracking boundary layer features.

The calculation method is also applicable to higher range of Reynolds numbers since it is based on methods that were successfully used to design many nowadays working airfoils. It is, on the other hand, limited by low range Reynolds number by the violation of basic assumptions of boundary layer theory and laminar separation bubble model.

The above mentioned procedure is coded in a Matlab, and the results of the calculation is validated over an important range of Reynolds numbers (from 2×10^5 to 5×10^5) using recent published experimental data for benchmark airfoils.

Airfoil design in this Reynolds number range is important for many widely used applications. These applications include UAV's , wind turbines, and propellers as well as sport cars.

Surface pressure distributions together with drag polar and boundary layer features are calculated and compared with experimental data. The comparisons show acceptable agreement with experimental data.

After validation, this code is used for airfoil optimization examples by systematic shape modification. In this context airfoil shape parameterization and objective function formulations are discussed and sample calculations are shown. Airfoil optimization studies at the mentioned Reynolds number range is successfully accomplished using the proposed code and methodology. Airfoil shape design is efficiently achieved by systematic shape modification and direct aerodynamic calculation.

Key words: Airfoils, low Reynolds number, conformal mapping, airfoil aerodynamics, airfoil shape parameterization, aerodynamic optimization.

Scientific discipline: Aeronautical Engineering

Scientific sub-discipline: Computational Aerodynamics

UDC: 533.6.011.12:629.7.015(043.3)

АПСТРАКТ

У овој тези је моделирано струјање око аеропрофила са ниским Рејнолдсовим бројем. Вискозно невискозна интеракција комбинована са моделирањем ламинарног мехура је ефикасан метод за конструисање нових аеропрофила систематским модификовањем облика аеропрофила. Невискозно решење је засновано на конформном пресликавању. Вискозна формулација је заснована на решавању интегралних једначина за количину кретања и енергије. Када нема одцепљења струјања примењен је Еплеров модел за предвиђање транзиције из ламинарног у турбулентно струјање. Ламинарни мехур, који узрокује отцепљење је моделиран из три сегмента: ламинарни део, турбулентни део и област прилепљења струјања. Овиме је омогућено одређивање доприноса укупном отпору аеропрофила, такође је омогућено и праћење карактеристика граничног слоја.

Прорачунски метод је применљив и за конструисање аеропрофила за лет при вишим Рејнолдсовим бројевима јер је базиран на методима који су превиђени за такво конструисање. Метод је програмиран помоћу MATLAB-а за област Рејнолдсових бројева (од 2×10^5 до 5×10^5) решења су поређена са експерименталним резултатима. Одабрана област Рејнолдсових бројева има веома велики праткчни значај. Конструисани аеропрофили су примењиви код беспилотних летелица, лопатица ветротурбина, лопатица пропелера, као и код узгонских аеропрофила на аутомобилима.

Прорачунате су расподеле притисака, поларе, и карактеристике граничног слоја и упоређене са расположивим експерименталним подацима. Поређење показује задовољавајуће слагање између прорачуна и експерименталних података.

Након верификације прорачуном је одређено више оптималних аеропрофила за различите услове. Аеропрофил је параметризован на неколико опционих начина, а функција циља за оптимизацију је дефинисана такође на више начина. Продискутовани су различити оптимизациони критеријуми и за њих је одређен

оптимални облик аеропрофила. Развијени софтвер омогућује ефикасно пројектовање нових облика аеропрофила са систематском модификацијом облика аеропрофила.

Key words: Аеропрофили, мали Рејнолдсов број, комформно пресликавање, аеродинамика аеропрофила, параметризација облика аеропрофила, аеродинамичка оптимизација

Scientific discipline: Ваздухопловство

Scientific sub-discipline: Прорачунска Аеродинамика

UDC: 533.6.011.12:629.7.015(043.3)

Table of Contents

Table of Contents

ABSTRACT	I
NOMENCLATURE	XVII
1 INTRODUCTION	1
1.1 LOW REYNOLDS NUMBER AIRFOILS	3
1.2 EFFICIENCY IN AIRFOIL DESIGN.....	5
1.3 THESIS OUTLINE.....	6
2 TWO DIMENSIONAL IDEAL FLUID FLOW	8
2.1 ASSUMPTION OF AN IDEAL FLUID [12].....	9
2.2 FUNDAMENTAL PRINCIPLES	10
2.2.1 Irrotational flow	10
2.2.2 Velocity Potential and stream function.....	11
2.2.3 The complex Velocity.....	12
2.2.4 The Complex Potential	13
2.2.5 Circular Cylinder with Circulation	16
2.3 APPLICATION TO AIRFOILS AND CONFORMAL TRANSFORMATIONS.....	18
2.4 KARMA-TREFFTZ TRANSFORMATION.....	22
2.5 FLOW ANALYSIS OVER AN AIRFOIL USING CONFORMAL MAPPING.....	22
2.5.1 Airfoil shape.....	24
2.5.2 Apply Karman-Trefftz Transformation	25
2.5.3 Translation of the near circle to the origin.....	26
2.5.4 Mapping of near circle in (z^2 plane) to true circle (z plane).	27
2.5.5 Calculation of modulus of transformation	30
2.5.6 Finding velocities in the true circle plane	32
3 BOUNDARY LAYER MODELING	37
3.1 BOUNDARY LAYER CONCEPT	37
3.2 BOUNDARY LAYER SEPARATION	39
3.3 SHEAR STRESS AND FRICTION DRAG	41
3.4 BOUNDARY LAYER MOMENTUM AND ENERGY INTEGRAL EQUATIONS.....	42
3.4.1 Boundary layer integral approach.....	44
3.4.2 Laminar boundary layer	45
3.4.3 Turbulent boundary layer.....	47
3.5 BOUNDARY LAYER TRANSITION.....	48
3.6 LAMINAR SEPARATION BUBBLE	50
3.7 EPPLER'S BUBBLE PREDICTION METHOD	52
3.8 LIFT, DRAG AND MOMENT.....	52
3.8.1 Integration of pressure and shear stress distributions	54
3.8.2 Lift Drag Moment corrections	55

3.9	COMPARISON OF TURBULENT CLOSURE RELATIONS	56
3.9.1	Eppler turbulent model:	57
3.9.2	Drela Turbulent closure	57
3.9.3	Modified Drela model used by LUTZ and Wagner [38]	59
3.9.4	Lutz and Wagner model	59
3.10	VERIFICATION OF BOUNDARY LAYER CALCULATIONS	63
3.10.1	Comparison with Eppler code	63
3.10.2	Comparisons with XFOIL code	69
4	LAMINAR SEPARATION BUBBLE MODELING	72
4.1	REYNOLDS NUMBER AND ANGLE OF ATTACK VARIATION	76
4.2	LAMINAR SEPARATION BUBBLE MODEL	78
4.2.1	Laminar part of the bubble [36]	80
4.2.2	Transition	82
4.2.3	Turbulent part of the bubble	84
4.2.4	Intersection with inviscid distribution	88
4.2.5	Attached turbulent boundary layer	88
4.3	VALIDATION OF AERODYNAMIC CALCULATIONS	91
4.3.2	Variation of aerodynamic coefficients with Reynolds number	102
4.3.3	Variation of boundary layer features with Reynolds number	105
5	AIRFOIL PARAMETRIC REPRESENTATION	109
5.1	GENERAL REQUIREMENT	109
5.2	NACA AIRFOIL SERIES	110
5.3	4-DIGIT SERIES AIRFOILS	110
5.4	PARSEC METHOD	113
5.5	BEZIER PARAMETERIZATION	117
5.6	CST METHOD	121
5.7	MATCHING OF NACA 4412 AIRFOIL SHAPE	127
5.8	MATCHING OF TARGET PRESSURE DISTRIBUTION	132
5.8.1	CST with n=2 parameters	133
5.8.2	CST with n=4 parameters	135
6	AERODYNAMIC DESIGN AND SHAPE OPTIMIZATION	138
6.1	INVERSE DESIGN APPROACH	139
6.2	DIRECT DESIGN APPROACH	140
6.3	NUMERICAL OPTIMIZATION	141
6.3.1	Formulation of the mathematical problem	142
6.3.2	Genetic Search algorithms	142
6.3.3	Choice of constraints	144
6.3.4	Formulation of objective function	144
6.3.5	Single objective versus multi objective optimization	145
6.4	DIRECT AERODYNAMIC OPTIMIZATION BY SHAPE PERTURBATION	146
7	AIRFOIL OPTIMIZATION CASE STUDIES	149
7.1	PROBLEM FORMULATION	152
7.2	GEOMETRIC CONSTRAINTS:	153

7.3	AIRFOIL PARAMETERIZATION	153
7.4	FORMULATION OF THE OBJECTIVE FUNCTION	154
7.4.1	Equality and Inequality Constrained Optimization and Penalty Function.....	154
7.5	DESIGN FOR GIVEN PRESSURE DISTRIBUTION (INVERSE DESIGN)	157
7.5.1	NACA 0012	157
7.5.2	LIEBECK LNV109A high lift airfoil	162
7.6	SINGLE POINT SINGLE OBJECTIVE.....	165
7.6.1	Aerodynamic constraints	165
7.6.2	Optimization Results.....	165
7.6.3	Airfoil shape and pressure distributions.....	167
7.6.4	Aerodynamic coefficients	169
7.7	SINGLE POINT MULTI OBJECTIVE	170
7.7.1	Optimization Results.....	171
7.7.2	Airfoil shape and pressure distributions.....	173
7.7.3	Aerodynamic coefficients	174
7.8	MULTI POINT SINGLE OBJECTIVE.....	176
7.8.1	Aerodynamic constraints	176
7.8.2	Optimization Results.....	176
7.8.3	Airfoil shape and pressure distributions.....	177
7.8.4	Lift and drag polar	179
7.9	MULTI POINT MULTI OBJECTIVE	180
7.9.1	Drag minimization at a range of operating lift coefficients	180
7.9.2	Objective function formulation.....	180
7.9.3	Optimization Results.....	181
7.9.4	Airfoil shape and pressure distributions.....	182
7.9.5	Lift and drag polar	184
7.10	DESIGN AT DIFFERENT REYNOLDS NUMBERS.....	186
7.10.1	Optimization at different Reynolds numbers	189
	8 CONCLUSION.....	194
8.1	AERODYNAMIC ANALYSIS	194
8.2	AIRFOIL PARAMETERIZATION	196
8.3	OBJECTIVE FUNCTION AND CONSTRAINTS.....	196
8.4	AIRFOIL DESIGN AND OPTIMIZATION.....	197
8.5	FUTURE WORK.....	200
	9 REFERENCES.....	201

Table of Figures

FIGURE 1.1 THE CODE FLOW CHART	2
FIGURE 1.2 CHORD REYNOLDS NUMBER VS. FLIGHT SPEED FOR DIFFERENT NATURAL AND MANMADE OBJECTS	4
FIGURE 1.3 REYNOLDS NUMBER EFFECT ON REPRESENTATIVE AIRFOILS PERFORMANCE.....	5
FIGURE 2.1 HIERARCHY OF THE DIFFERENT LEVELS OF APPROXIMATION [12].....	9
FIGURE 2.2 CIRCULATION AROUND CLOSED PATH [13].....	11
FIGURE 2.3 VARIABLES DEFINING COMPLEX VELOCITY	13
FIGURE 2.4 A TYPICAL STREAM LINES OF FLOW AROUND CIRCULAR CYLINDER WITH MODERATE CIRCULATION Γ	16
FIGURE 2.5 (A) A UNIT CIRCLE IN Z PLANE CENTERED AT ORIGIN WITH UNIT RADIUS. (B) JOUKOWSKY TRANSFORM OF Z PLANE UNIT CIRCLE TO A STRAIGHT LINE SEGMENT FROM -2 TO 2 IN ζ PLANE.	20
FIGURE 2.6 (A) A CIRCLE CENTERED AT ORIGIN WITH RADIUS DIFFERENT THAN 1 IN Z PLANE TRANSFORMED INTO ELLIPSE IN ζ PLANE.....	20
FIGURE 2.7 CLOSE UP OF TRAILING EDGE REGIONS SHOWING ZERO TRAILING EDGE ANGLE.	20
FIGURE 2.8 (A) A CIRCLE CENTERED OFF THE ORIGIN AND HAS TOUCHES THE UNIT CIRCLE AT ONE POINT . (B) TRANSFORMED INTO AN ELLIPSE WHICH TOUCHES MID-REAL AXIS IN ζ PLANE AT ONE POINT.....	21
FIGURE 2.9 (A) A UNIT CIRCLE WITH CENTER OFFSET ON REAL X AXIS IN z PLANE (B) A NON CAMBERED AIRFOIL IN ζ PLANE.....	21
FIGURE 2.10 (A) CIRCLE WITH CENTER OFF THE ORIGIN IN BOTH $\mu_x = 0.2$ AND $\mu_y = 0.2$. WITH PART OF THE CONTOUR OUTSIDE THE UNIT CIRCLE (B) CAMBERED AIRFOIL IN ζ PLANE WITH PART OF ITS CONTOUR ABOVE REAL AXIS.	21
FIGURE 2.11 KARMAN-TREFFTZ TRANSFORM OF AN OFF CENTERED UNIT CIRCLE WITH $\mu_x = -0.05$ AND $\mu_y = 0.05$ AND RADIUS OF 1.0512 IN z PLANE INTO AN AIRFOIL, WITH FINITE TRAILING EDGE ANGLE OF 2 DEG IN ζ PLANE.....	22

FIGURE 2.12 STEPS INVOLVED IN TRANSFORMATIONS OF AIRFOIL TO TRUE CIRCLE.....	24
FIGURE 2.13 AIRFOIL GENERATED FOR CONFORMAL MAPPING	25
FIGURE 2.14 AIRFOIL TRANSFORMED TO NEAR CIRCLE.....	26
FIGURE 2.15 SHIFTED NEAR CIRCLE	27
FIGURE 2.16 NACA4412 AIRFOIL TRANSFORMED TO NEAR CIRCLE THEN SHIFTED TO ORIGIN.....	27
FIGURE 2.17 POTENTIAL FLOW VELOCITY AROUND CIRCULAR CYLINDER DW/DZ	34
FIGURE 2.18 DERIVATIVE OF TRANSFORMATION (DZ_2/DZ) FOR E387 AIRFOIL.....	34
FIGURE 2.19 DERIVATIVE OF TRANSFORMATION DZ_1/Σ FOR E387 AIRFOIL ...	35
FIGURE 2.20 INVISCID PRESSURE DISTRIBUTIONS AT 2^0 AND REYNOLDS NUMBER OF 300,000 FOR E387 AIRFOIL.	35
FIGURE 2.21 FLOW CHART FOR THE METHOD OF CALCULATION.....	36
FIGURE 3.1 BOUNDARY LAYER CONCEPT	38
FIGURE 3.2 SEPARATION OF BOUNDARY LAYER, DEFINED WHEN THE SLOPE OF THE VELOCITY GRADIENT AT THE WALL IN THE NORMAL DIRECTION EQUALS ZERO.	39
FIGURE 3.3 VELOCITY DISTRIBUTION IN BOUNDARY LAYER AT DIFFERENT PRESSURE SITUATIONS.....	40
FIGURE 3.4 BOUNDARY LAYER EFFECTS	41
FIGURE 3.5 VISCOUS DRAG COMPUTATION FROM SHEAR STRESS	42
FIGURE 3.6 EPPLER TRANSITION CRITERIA FOR DIFFERENT ROUGHNESS FACTOR VALUES	49
FIGURE 3.7 SKETCH OF LAMINAR SEPARATION BUBBLE.....	50
FIGURE 3.8 EFFECT OF SEPARATION BUBBLE ON VELOCITY DISTRIBUTION.....	51
FIGURE 3.9 EPPLER'S BUBBLE ANALOGY	52
FIGURE 3.10 SIGN CONVENTIONS FOR PRESSURE AND SHEAR STRESS	53
FIGURE 3.11 BODY AND WIND AXIS SYSTEMS	53
FIGURE 3.12 LIFT AND MOMENT CORRECTIONS DUE TO BOUNDARY LAYER SEPARATION	56
FIGURE 3.13 COMPARISONS OF DIFFERENT SHAPE FACTOR RELATIONS FOR INCOMPRESSIBLE TURBULENT BOUNDARY LAYER AT $Re\delta_2 = 5000$	59
FIGURE 3.14 COMPARISONS OF DIFFERENT SHAPE FACTOR RELATIONS FOR INCOMPRESSIBLE TURBULENT BOUNDARY LAYER AT $Re\delta_2 = 400$	60

FIGURE 3.15 COMPARISONS OF DIFFERENT SHAPE FACTOR RELATIONS FOR INCOMPRESSIBLE TURBULENT BOUNDARY LAYER AT $Re\delta_2 = 275$	60
FIGURE 3.16 COMPARISONS OF DIFFERENT SHAPE FACTOR RELATIONS FOR INCOMPRESSIBLE TURBULENT BOUNDARY LAYER AT $Re\delta_2 = 200$	61
FIGURE 3.17 COMPARISONS OF DIFFERENT SHAPE FACTOR RELATIONS FOR INCOMPRESSIBLE TURBULENT BOUNDARY LAYER AT $Re\delta_2 = 100$	61
FIGURE 3.18 COMPARISONS OF DIFFERENT SHAPE FACTOR RELATIONS FOR INCOMPRESSIBLE TURBULENT BOUNDARY LAYER, FROM REFERENCE [38].....	62
FIGURE 3.19 EPPLER AIRFOIL E1098 AND VELOCITY DISTRIBUTION AT $RE = 1E06$ AND $\alpha = 0$	63
FIGURE 3.20 COMPARISON OF DRAG COEFFICIENT FOR E1098 AT 1×1006 BETWEEN CURRENT CALCULATION AND EPPLER CODE.	64
FIGURE 3.21 COMPARISON OF LOCATION OF UPPER SURFACE TRANSITION POINT FOR E1098 AT 1×1006 BETWEEN CURRENT CALCULATION AND EPPLER CODE.	65
FIGURE 3.22 H_{32} COMPARISONS OVER E1098 AIRFOIL UPPER SURFACE AT $RE = 1E06$, $\alpha = 0$	65
FIGURE 3.23 H_{32} COMPARISONS OVER E1098 AIRFOIL LOWER SURFACE AT $RE = 1E06$, $\alpha = 0$	66
FIGURE 3.24 δ_2 COMPARISONS OVER E1098 AIRFOIL UPPER SURFACE AT $RE = 1E06$, $\alpha = 0$	66
FIGURE 3.25 δ_2 COMPARISONS OVER E1098 AIRFOIL LOWER SURFACE AT $RE = 1E06$, $\alpha = 0$	67
FIGURE 3.26 SHAPE FACTOR H_{12} DEVELOPMENT OVER E1098 AIRFOIL SURFACES AS CALCULATED	67
FIGURE 3.27 REYNOLDS NUMBER BASED ON δ_2 OVER THE AIRFOIL SURFACE.....	68
FIGURE 3.28 REYNOLDS NUMBER BASED ON C_f OVER THE AIRFOIL SURFACE.....	68
FIGURE 3.29 NACA 4412 AIRFOIL SHAPE AND VELOCITY DISTRIBUTION USING CURRENT CALCULATION	69
FIGURE 3.30 COMPARISONS OF SHAPE FACTOR H_{12} ,	70
FIGURE 3.31 COMPARISONS OF BOUNDARY LAYER THICKNESS δ_2	70

FIGURE 3.32 COMPARISONS OF SKIN FRICTION COEFFICIENT ON UPPER SURFACE C_f	71
FIGURE 4.1 CHORD REYNOLDS NUMBER VS. FLIGHT SPEED FOR DIFFERENT NATURAL AND MANMADE OBJECTS	73
FIGURE 4.2 A SCHEMATIC SHAPE OF SHORT LAMINAR SEPARATION BUBBLE.[52].....	74
FIGURE 4.3 EFFECT OF LONG AND SHORT BUBBLE AT HIGH REYNOLDS NUMBER[51].....	75
FIGURE 4.4 HIGH REYNOLDS NUMBER FLOW OVER A LARGE WING.....	77
FIGURE 4.5 LOW REYNOLDS NUMBER FLOW AT LOW ANGLE OF ATTACK ...	77
FIGURE 4.6 LOW REYNOLDS NUMBER FLOW OVER AIRFOIL AT HIGHER ANGLE OF ATTACK, A CASE WHEN HIGHER ANGLE OF ATTACK IS ENCOUNTERED WHERE BUBBLE IS SHORTER AND CLOSER TO THE LEADING EDGE.....	78
FIGURE 4.7 LOW REYNOLDS NUMBER FLOW AT STALL, WHEN THE BUBBLE BURSTS, AIRFOIL STALLS AND AIRFOIL CHARACTERISTICS ARE AFFECTED BY STALL TYPE AND BUBBLE LENGTH.....	78
FIGURE 4.8 SCHEMATIC OF BUBBLE AND ITS EFFECTS ON PRESSURE DISTRIBUTION [DINI]	79
FIGURE 4.9 PRESSURE RECOVERY IN THE LAMINAR PART OF THE BUBBLE AS FUNCTION OF GASTER'S PRESSURE GRADIENT PARAMETER	81
FIGURE 4.10 BUBBLE GEOMETRY AND SCALING PARAMETERS	82
FIGURE 4.11 NORMALIZED SHAPE FACTOR TURBULENT RECOVERY FUNCTION	85
FIGURE 4.12 SCHEMATICS OF POSSIBLE FLOW ON AIRFOIL WITH AND WITHOUT BUBBLE	89
FIGURE 4.13 FLOW CHART FOR LAMINAR SEPARATION BUBBLE MODEL	90
FIGURE 4.14 C_l VERSUS α FOR FOR E387 AIRFOIL AT RE 300000, EXP FROM [SUMMARY OF LOW-SPEED AIRFOIL DATA-2012].	92
FIGURE 4.15 C_d VERSUS C_l FOR FOR E387 AIRFOIL AT RE 300000, EXP FROM [SUMMARY OF LOW-SPEED AIRFOIL DATA-2012]......	92
FIGURE 4.16 COMPARISONS OF UPPER SURFACE BOUNDARY LAYER FEATURES FOR E387 AIRFOIL AT RE 300,000.....	93
FIGURE 4.17 COMPARISON OF EXPERIMENTAL AND CALCULATED PRESSURE DISTRIBUTION.....	94

FIGURE 4.18 COMPARISON OF PRESSURE DISTRIBUTION WITH XFOIL CODE FOR E387 AIRFOIL AT RE 300000 AND ANGLE OF ATTACK 2 DEG.	94
FIGURE 4.19 UPPER SURFACE BOUNDARY LAYER PARAMETERS AT RE 300000 AND $\alpha=2$ DEG. (CONTINUED).....	96
FIGURE 4.20 UPPER SURFACE BOUNDARY LAYER DEVELOPMENT CHART FOR E387 AT RE 300000 AND $\alpha = 2$ DEG.	97
FIGURE 4.21 COMPARISON OF UPPER SURFACE BOUNDARY LAYER SHAPE FACTOR H_{12} FOR E387 AT RE 300000 AND $\alpha = 2$ DEG.	97
FIGURE 4.22 COMPARISON OF UPPER SURFACE BOUNDARY LAYER MOMENTUM THICKNESS FOR E387 AT RE 300000 AND $\alpha = 2$ DEG.	98
FIGURE 4.23 LOWER SURFACE VELOCITY DISTRIBUTION FOR E387 AT RE 300000 AND $\alpha=2$ DEG.....	98
FIGURE 4.24 VARIATION OF MOMENTUM THICKNESS FOR THE LOWER SURFACE OF E387 AT RE 300000 AND $\alpha =2$ DEG.....	99
FIGURE 4.25 LOWER SURFACE BOUNDARY LAYER DEVELOPMENT PARAMETERS AT RE 300000 AND $\alpha=2$ DEG.....	100
FIGURE 4.26 LOWER SURFACE BOUNDARY LAYER DEVELOPMENT CHART FOR E387 AT RE 300000 AND $\alpha = 2$ DEG.....	101
FIGURE 4.27 COMPARISONS BETWEEN CALCULATED AND EXPERIMENTAL DRAG POLAR FOR E387 AT RE=200,000.	102
FIGURE 4.28 COMPARISONS BETWEEN CALCULATED AND EXPERIMENTAL DRAG POLAR FOR E387 AT RE=350,000.	102
FIGURE 4.29 COMPARISONS BETWEEN CALCULATED AND EXPERIMENTAL DRAG POLAR FOR E387 AT RE=500,000.	103
FIGURE 4.30 COMPARISONS BETWEEN CALCULATED AND EXPERIMENTAL DRAG POLAR FOR S8036 AT RE=200,000.....	103
FIGURE 4.31 COMPARISONS BETWEEN CALCULATED AND EXPERIMENTAL DRAG POLAR FOR S8036 AT RE=350,000.....	104
FIGURE 4.32 COMPARISONS BETWEEN CALCULATED AND EXPERIMENTAL DRAG POLAR FOR S8036 AT RE=500,000.....	104
FIGURE 4.33 PRESSURE DISTRIBUTION FOR E387 AT RE 300 000 AND $\alpha =4^\circ$.	106
FIGURE 4.34 PRESSURE DISTRIBUTION FOR E387 AT RE 300 000 AND $\alpha = 6^\circ$	107
FIGURE 4.35 COMPARISONS OF LOCATIONS OF UPPER SURFACE FLOW FEATURES FOR E387 AND S8036 AT RE 200,000, 350,000, AND 500,000. (SOLID LINES REPRESENT EXPERIMENTAL DATA, DASHED LINES IS XFOIL, AND FILLED SYMBOLS ARE CURRENT CALCULATIONS).....	108

FIGURE 5.1 NACA AIRFOIL GEOMETRICAL PARAMETERS	111
FIGURE 5.2 NACA 4- DIGIT AIRFOIL REPRESENTATION PARAMETERS	112
FIGURE 5.3 PARSEC METHOD FOR AIRFOIL PARAMETERS	113
FIGURE 5.4 PARSEC REPRESENTATION (DOTTED LINE) OF NACA 4412 AIRFOIL (SOLID LINE)	117
FIGURE 5.5 TWO BEZIER CURVES OF ORDER 5 REPRESENTING UPPER SURFACE OF AN AIRFOIL.....	118
FIGURE 5.6 NACA 2424 AIRFOIL REPRESENTED BY BEZIER CURVE USING THE ABOVE METHOD.....	120
FIGURE 5.7 CST REPRESENTATION OF AIRFOIL UPPER SURFACE USING 3 TERMS (N=2). UPPER PART: SHOWS 3 TERMS OF BERNSTEIN POLYNOMIAL OF EQUATION (5.37) (DOTTED CURVE), AND ITS SUMMATION IS EQUAL TO 1 . LOWER PART: SHOWS AIRFOIL UPPER SURFACE SHAPE (SOLID) AND TERMS OF EQUATIONS (5.38) (DOTTED), THE SUMMATION OF THESE THREE CURVES AT EACH POINT RESULTS IN A POINT ON AIRFOIL SURFACE.....	123
FIGURE 5.8 CST REPRESENTATION OF AIRFOIL UPPER SURFACE USING 4 TERMS (N=3). UPPER PART: SHOWS 4 TERMS OF BERNSTEIN POLYNOMIAL OF EQUATION (5.37) (DOTTED CURVE), AND ITS SUMMATION IS EQUAL TO 1 . LOWER PART: SHOWS AIRFOIL UPPER SURFACE SHAPE (SOLID) AND TERMS OF EQUATIONS (5.38) (DOTTED), THE SUMMATION OF THESE FOUR CURVES AT EACH POINT RESULTS IN A POINT ON AIRFOIL SURFACE.....	124
FIGURE 5.9 CST REPRESENTATION OF AIRFOIL UPPER SURFACE USING 5 TERMS (N=4)	125
FIGURE 5.10 CONSTRUCTION OF AN AIRFOIL UPPER SURFACE SHAPE USING N=5	126
FIGURE 5.11 NACA 2412 REPRESENTED WITH TWO COEFFICIENTS FOR EACH SURFACE AND DIFFERENCE Y IN COORDINATES. $A_{UP}=[$ $0.1995 \ 0.2103]$ AND $A_{LO}=[-0.1350 \ -0.0584]$	128
FIGURE 5.12 CONVERGENCE HISTORY AND COEFFICIENTS WITH BEST VALUES WHEN TWO CST COEFFICIENTS FOR EACH SURFACE ARE USED.	129
FIGURE 5.13 NACA 2412 REPRESENTED WITH FOUR COEFFICIENTS FOR EACH SURFACE AND DIFFERENCE IN Y COORDINATES. $A_{up}=[$ $0.1899 \ 0.2254 \ 0.1847 \ 0.2193]$ AND $ALO = [-0.1518 \ -0.0788 \ -$ $0.0990 \ -0.0677]$	130

FIGURE 5.14 CONVERGENCE HISTORY AND COEFFICIENTS WITH BEST VALUES WHEN FOUR CST COEFFICIENTS FOR EACH SURFACE.....	131
FIGURE 5.15 NACA 2412 USED AS TEST AIRFOIL	132
FIGURE 5.16 TARGET PRESSURE DISTRIBUTION	133
FIGURE 5.17 NACA 2412 AIRFOIL AND OBTAINED CST SHAPE WHEN NUMBER OF CST PARAMETERS $N=2$	133
FIGURE 5.18 FITNESS VALUE VERSUS NUMBER OF GENERATIONS FOR TARGET PRESSURE DISTRIBUTION AT $A=2$ DEGREES AND NUMBER OF CST COEFFICIENTS $N=2$	134
FIGURE 5.19 COMPARISON OF TARGET AND CST PRESSURE DISTRIBUTIONS WHEN NUMBER OF CST PARAMETERS $N=2$	135
FIGURE 5.20 COMPARISON OF TARGET AND CST PRESSURE DISTRIBUTIONS WHEN NUMBER OF CST PARAMETERS $N=4$	136
FIGURE 5.21 FITNESS VALUE VERSUS NUMBER OF GENERATIONS FOR TARGET PRESSURE DISTRIBUTION AT $A=2$ DEGREES AND NUMBER OF CST COEFFICIENTS $N=4$	137
FIGURE 6.1 INVERSE AND DIRECT AERODYNAMIC PROBLEMS.....	138
FIGURE 6.2 FLOWCHART ILLUSTRATING DESIGN SEARCH AND OPTIMIZATION PROCESS.....	141
FIGURE 6.3 FLOWCHART ILLUSTRATING DIRECT AERODYNAMIC OPTIMIZATION BY SHAPE PERTURBATION	148
FIGURE 7.1 RELATIONS BETWEEN PRESSURE DISTRIBUTION SHAPE, AND DRAG POLAR, AND AIRFOIL SHAPE [11]	151
FIGURE 7.2 SPSO GEOMETRIC CONSTRAINTS	153
FIGURE 7.3 PENALTY FUNCTION $\Phi(x)$	155
FIGURE 7.4 A PENALTY FUNCTION $\Phi(x) = x$ ADDED TO THE OBJECTIVE FUNCTION IF $x < 1$ and 3 RESPECTIVELY	155
FIGURE 7.5 NACA 0012 GEOMETRY	158
FIGURE 7.6 TARGET AIRFOIL SHAPE AND TARGET PRESSURE DISTRIBUTION AT REYNOLDS NUMBER OF 3×10^5 AND AT ANGLE OF ATTACK OF 4 DEGREES.....	158
FIGURE 7.7 INITIAL AND TARGET AIRFOILS AND CORRESPONDING PRESSURE DISTRIBUTIONS.....	159
FIGURE 7.8 AIRFOIL SHAPE AND PRESSURE DISTRIBUTION AFTER 5 GENERATIONS.....	160
FIGURE 7.9 AIRFOIL SHAPE AND PRESSURE DISTRIBUTION AFTER 15 GENERATIONS.....	161
FIGURE 7.10 CONVERGENCE HISTORY FOR CASE OF NACA 0012 AIRFOIL ..	161

FIGURE 7.11 LIEBECK LNV109A AIRFOIL GEOMETRY	162
FIGURE 7.12 TARGET PRESSURE DISTRIBUTION FOR LIEBECK AIRFOIL LNV109A AT REYNOLDS NUMBER OF 0.5×10^6 AND $\alpha = 5^\circ$	163
FIGURE 7.13 TARGET AIRFOIL (LNV109A) AND INITIAL AIRFOIL (NACA 2412) AND PRESSURE DISTRIBUTIONS AT REYNOLDS NUMBER OF 0.5×10^6 AND $\alpha = 5^\circ$	164
FIGURE 7.14 AIRFOIL SHAPE AND PRESSURE DISTRIBUTION AFTER 15 GENERATIONS.....	164
FIGURE 7.15 CONVERGENCE HISTORY FOR LIEBECK LNV109A AIRFOIL	165
FIGURE 7.16 RESULTS OF GENETIC SEARCH METHOD, (A) BEST AIRFOIL FITNESS AND MEAN FOR EACH GENERATION.....	166
FIGURE 7.17 COMPARISON IN AIRFOIL SHAPE.....	167
FIGURE 7.18 AIRFOIL SHAPE AND PRESSURE DISTRIBUTION FOR SPSO AT RE 3×10^5 AND AT $\alpha = 0^\circ$	168
FIGURE 7.19 DRAG POLAR PLOT OF THE INITIAL AND OPTIMIZED AIRFOIL AT SINGLE ANGLE OF ATTACK OF ZERO DEGREE.....	170
FIGURE 7.20 RESULTS OF GENETIC SEARCH METHOD, (A) BEST AIRFOIL FITNESS AND MEAN FOR EACH GENERATION. (B) THE PARAMETERS OF THE BEST AIRFOIL SHAPE AT LAST GENERATION. (C) THE FITNESS OF EACH AIRFOIL SHAPE IN THE CURRENT GENERATION.	172
FIGURE 7.21 COMPARISON IN AIRFOIL SHAPE FOR SPMO	173
FIGURE 7.22 AIRFOIL SHAPE AND PRESSURE DISTRIBUTION.....	173
FIGURE 7.23 DRAG POLAR FOR SPMO DRAG MINIMIZATION AT GIVEN LIFT FOR ZERO ANGLE OF ATTACK.....	174
FIGURE 7.24 XFOIL RESULTS FOR OPTIMIZED AND INITIAL AIRFOILS	175
FIGURE 7.25 RESULTS OF GENETIC SEARCH METHOD, BEST AIRFOIL SHAPE AND MEAN FOR EACH GENERATION (A), THE BEST AIRFOIL SHAPE AT THE FINAL GENERATION (B), THE FITNESS OF EACH AIRFOIL SHAPE IN THE FINAL GENERATION (C).	177
FIGURE 7.26 OPTIMIZED AIRFOIL FOR MPSO FOR MINIMUM DRAG AT RANGE OF ANGLES OF ATTACK.....	178
FIGURE 7.27 AERODYNAMIC PERFORMANCE SHOWING COMPARISON WITH EXPERIMENTAL LIFT AND DRAG COEFFICIENTS FOR INITIAL AIRFOIL.....	179
FIGURE 7.28 GENETIC OPTIMIZATION RESULTS.....	182
FIGURE 7.29 AIRFOIL SHAPE	183

FIGURE 7.30 BEST AIRFOIL SHAPE FOR MULTIPOINT MULTI OBJECTIVE OPTIMIZATION	183
FIGURE 7.31 COMPARISON OF PRESSURE DISTRIBUTIONS FOR INITIAL AND OPTIMIZED AIRFOILS AT $\alpha = 4 \text{ deg}$ $Re = 300,000$ FOR MPMO	184
FIGURE 7.32 DRAG POLAR SHOWING AN IMPROVEMENT IN DRAG AT DESIGN LIFT COEFFICIENTS.....	185
FIGURE 7.33 EFFECT OF REYNOLDS NUMBER ON E387 AIRFOIL CHARACTERISTICS [61].	187
FIGURE 7.34 EFFECT OF REYNOLDS NUMBER ON S8064 AIRFOIL AERODYNAMIC CHARACTERISTICS [61].	187
FIGURE 7.35 COMPARISON BETWEEN EXPERIMENTAL [61] AND COMPUTED FOR E387 AIRFOIL AT 200,000	188
FIGURE 7.36 COMPARISON BETWEEN EXPERIMENTAL [61] AND COMPUTED FOR E387 AIRFOIL AT 3×10^5	188
FIGURE 7.37 COMPARISON BETWEEN EXPERIMENTAL [61] AND COMPUTED FOR E387 AIRFOIL AT 500,000	189
FIGURE 7.38 COMPARISON BETWEEN OPTIMIZED AIRFOIL SHAPES AT DIFFRENT REYNOLDS NUMBERS.....	190
FIGURE 7.39 MINIMIZATION OF DRAG COEFFICIENT AT REYNOLDS NUMBERS 2×10^5 . OPEN CIRCLES ARE EXPERIMENTAL DATA FOR INITIAL AIRFOIL [61].....	191
FIGURE 7.40 MINIMIZATION OF DRAG COEFFICIENT AT REYNOLDS NUMBERS 3×10^5 . OPEN CIRCLES ARE EXPERIMENTAL DATA FOR INITIAL AIRFOIL [61].....	192
FIGURE 7.41 MINIMIZATION OF DRAG COEFFICIENT AT REYNOLDS NUMBERS 5×10^5 . OPEN CIRCLES ARE EXPERIMENTAL DATA FOR INITIAL AIRFOIL [61].....	193

Nomenclature

V_∞	Free stream velocity
$Re = \frac{V_\infty c \rho}{\mu}$	Chord Reynolds number where μ is dynamic viscosity
C	Airfoil chord length
x	x coordinates along airfoil chord
y	y coordinates normal to airfoil chord
u	Component of velocity along x direction
v	Component of velocity along y direction
P	Pressure acting at a point
s	Airfoil surface distance from stagnation point
z	Complex variable $z = x + i y = r e^{i\theta}$
$w(z)$	Complex velocity $w(z) = u(z) - i. v(z)$
$\theta(z)$	Phase angle $\theta(z) = -\arg(w)$
r	Radius of the complex number
C_p	Pressure coefficient
C_p^T, C_p^K	Target and computed pressure coefficient at k th iteration.
ζ plane, z_1 plane , z_2 plane , z plane	Planes used in conformal transformation: Airfoil plane, near circle plane, centered near circle plane and true circle plane respectively.
R	True circle radius = e^{ψ_0}
Re_{δ_2}	Reynolds number based on boundary layer momentum thickness ($U\delta_2 R_e$)
L	Lift force
D	Drag force
A	Axial force
N	Normal force
M	Pitching moment
$c_l, c_d, \text{ and } c_m$	Lift, drag and pitching moment coefficients

L/D	Lift to drag ratio
U	Boundary layer edge velocity
U_s, U_R, U_M , and U_{TE}	Potential flow velocities at laminar separation, reattachment merge, and at trailing edge points, respectively.
ΔU_B	Variation in potential flow velocity across the bubble
P	Gaster parameter
δ	Distance from the wall to boundary layer edge
τ_0	Shear stress at the wall defined as $\mu \left(\frac{\partial u}{\partial y} \right)_{y=0}$
δ_1	Boundary layer displacement thickness
δ_2	Boundary layer momentum thickness
δ_{2s}	Boundary layer momentum thickness at separation point
δ_3	Boundary layer energy thickness
c_f	Skin friction coefficient
C_D	Dissipation coefficient
H_{12}	Boundary layer shape factor δ_1/δ_2
H_{32}	Boundary layer shape factor δ_3/δ_2
L_B	Bubble length
h_τ	Bubble height
l_1	Laminar bubble length, from separation S to transition T
l_2	Turbulent bubble length, from transition T to reattachment M
$n(s)$	Disturbance amplification factor used by Drela
N_{cr}	Critical value of disturbance amplification.
A_{up}, A_{LO}	CST method coefficients for upper and lower airfoil sides, respectively.
UB, and LB	Upper and lower bounds in the GA optimization
n	Number of parameters used by CST method
w_i, w_j	weighing coefficients in the objective function formulation

Greek Symbols

α	Angle of attack
π	$\cong 22/7$
π	$\cong 22/7$
ρ	Air density
Γ	Circulation around closed path
ξ	Vorticity defined as $\frac{\partial v}{\partial x} - \frac{\partial u}{\partial y}$
$\phi(x, y)$	Velocity potential field
$\psi(x, y)$	Stream function field
m	Source strength
μ	Doublet strength
Γ	Vortex strength
φ	Penalty function

Abbreviations

LSB	Laminar separation bubble
RANS	Reynolds averaged Navier Stocks equations
CFD	Computational fluid dynamics
DNS	Direct Numerical Simulation
LES	Large eddy simulation
LTPT	NASA Langley Low Turbulence Tunnel
UIUC	University of Illinois at Urbana-Champaign
GAs	Genetic search Algorithms
SPSO	Single point single objective optimization
SPMO	Single point multi objective optimization
MPSO	Multi point single objective optimization
MPMO	Multi point multi objective optimization
CST	geometric Class function, Shape function Transformation technique

CHAPTER 1

1 Introduction

In this work, direct potential flow solution procedure over airfoils using conformal mapping is implemented. The obtained pressure distribution is then used to derive an uncoupled boundary layer formulation over the airfoil upper and lower surfaces in which, a boundary layer displacement thickness calculation is included. Within this boundary layer development a laminar separation bubble model has been incorporated.

The transition criterion is hybrid between that of Eppler and XFOIL codes. When laminar separation does not occur Eppler criterion is utilized. If laminar separation appears on either airfoil surfaces Drela e^n formula is used within the laminar separation bubble model. This approach allows the calculation of lift, drag and pitching moment including laminar separation bubble effects. A computer code to perform the aerodynamic calculations is developed and validated for Reynolds number range from 2×10^5 to 5×10^5 .

The efficiency of the airfoil design and optimization procedures is demonstrated using several case studies. In doing this airfoil parameterization methods are reviewed and CST method is chosen for the demonstration. Representative objective function formulations are illustrated.

A computer code is developed that utilizes genetic search algorithms (GAs) to call the above mentioned, airfoil parametric representation function, the aerodynamic function, and the objective function. The code flow chart is shown in Figure 1.1. The flow chart starts with input section where the design flight conditions, the initial airfoil and the desired airfoil aerodynamic objectives are specified. The next section is an outer GAs function that calls airfoil parameterization function, aerodynamic calculation function, and the objective function. Within the aerodynamic function three sub-functions are shown, namely inviscid flow solution (conformal mapping), boundary layer development and laminar separation bubble model.

When the optimization process converges drag polar for the selected best airfoil is computed to check airfoil off design conditions.

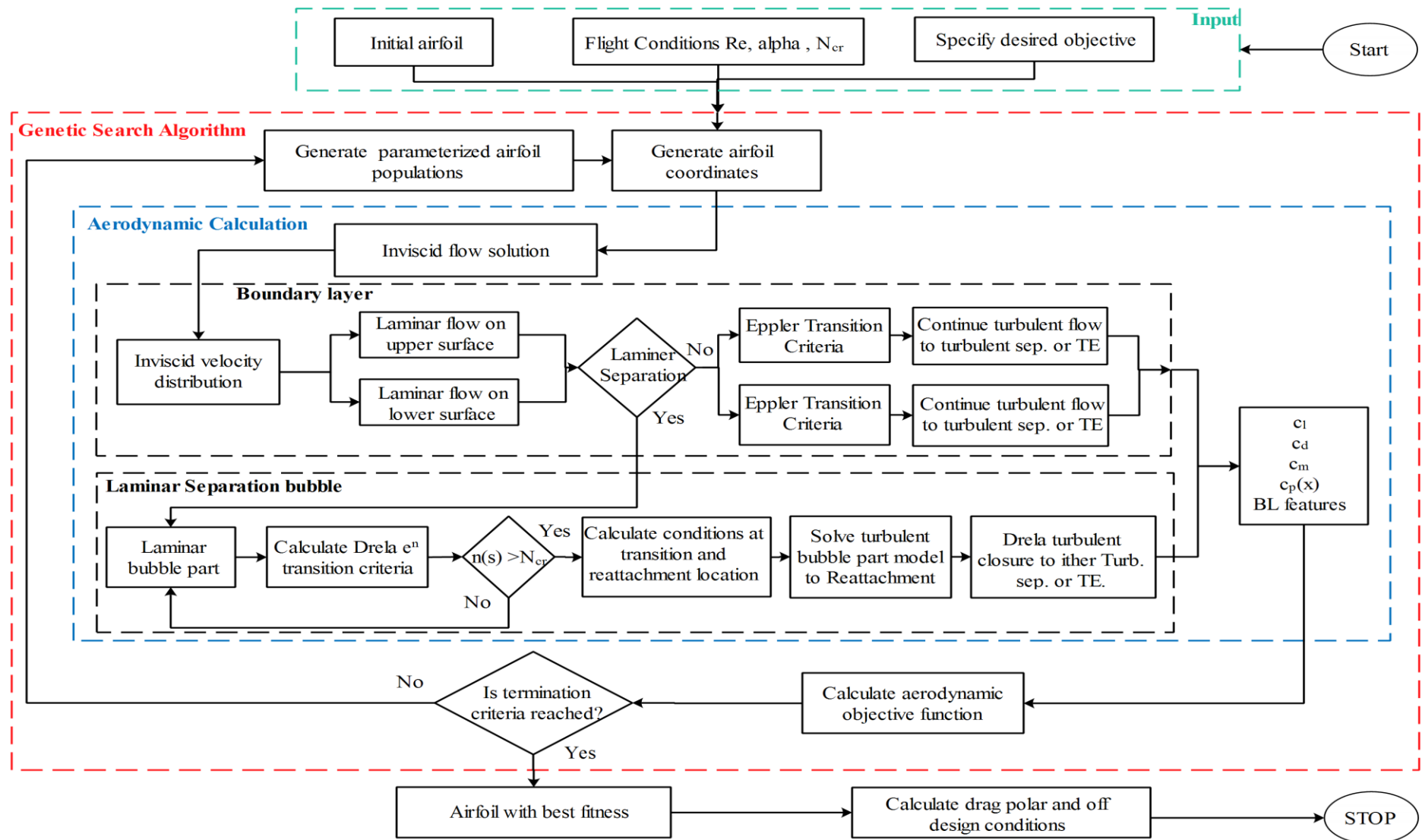


Figure 1.1 The code flow chart

1.1 Low Reynolds number airfoils

Airfoils operating at low Reynolds number range are characterized by presence of laminar flow over most of the airfoil surface. They are called laminar flow airfoils. Their applications cover civil, military and hobby model sectors. UAV's operating at low speeds or high altitudes are usually flying at this range. Wind turbines form important and growing field of interest to low Reynolds number airfoils. Figure 1.2 shows chord Reynolds number versus flight speed for some important applications. It can be said that, whenever airfoils operate at relatively low speeds or high altitudes, they most likely to operate at low Reynolds number regime.

Carmichael [1] has presented a classification of flow over low Reynolds number airfoils. He pointed out that, the main difficulty in low Reynolds number flow is laminar flow separations. In high Reynolds number, typically exceeding 10^6 , laminar flow extends for short percent of chord length, soon after that flow transition to turbulent occur mostly during favorable pressure gradient, before theoretical laminar separation point. Turbulent flows are known to be more resistant to flow separations, therefore, flow remains attached over most chord length for large range of angles of attack.

In case of low Reynolds numbers, as flow starts laminar, it continue for relatively longer percent of chord length than higher Reynolds numbers. Laminar flow, which is less resistant to separation, can separate before transition to turbulent flow takes place. This laminar flow separation complicates the flow and modifies the effective airfoil shape causing degradation of airfoils performance. That is way, airfoils designed for high Reynolds numbers does not work as efficient at low Reynolds number conditions. It is now more a common practice to design airfoils for specific application and not to select airfoil from ready catalogue.

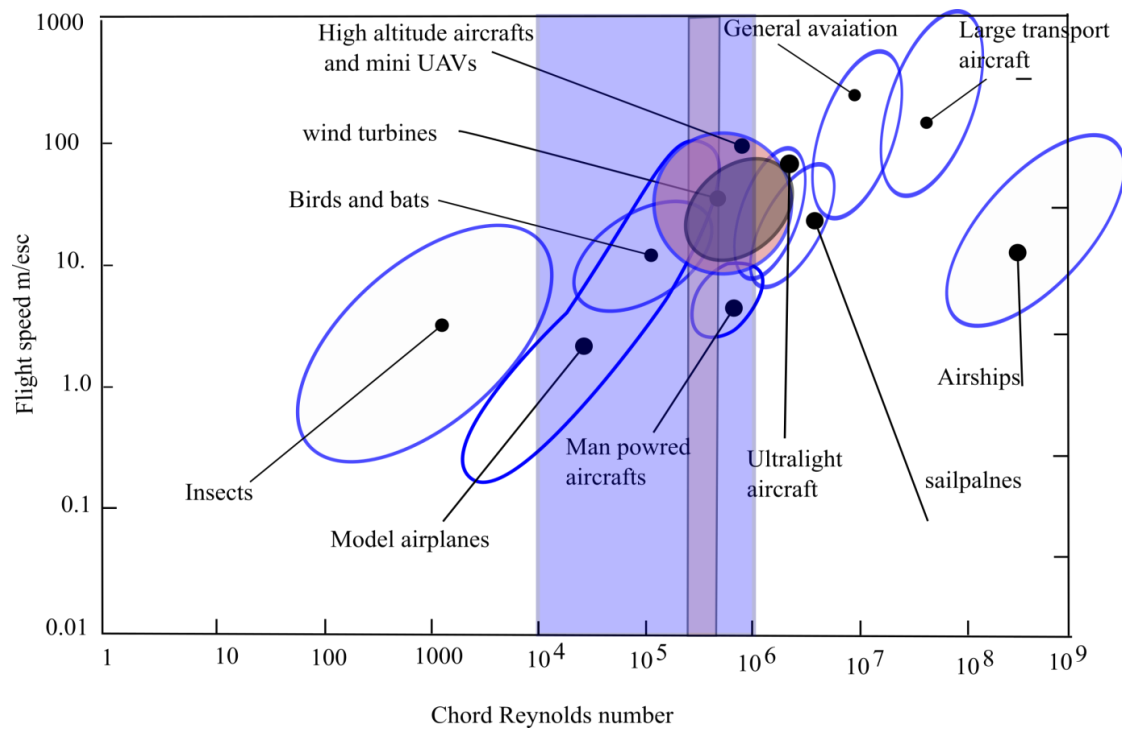


Figure 1.2 Flight speed versus chord Reynolds number for different natural and manmade objects

Tani [5] presented a review of published results of flows involving separation. He pointed out that one condition for laminar flow separation at low Reynolds number flows is existence of severe pressure gradients. He also pointed out that there exists a range of Reynolds numbers for which separated flow may reattach again forming Laminar Separation Bubble (LSB). If Reynolds number is further lowered flow may not attach and will stay separated. According to Carmichael rough rule, the Reynolds number necessary for reattachment based on free stream velocity and distance from separation to reattachment is 5×10^4 . It means that for airfoil with chord Reynolds number lower than 5×10^4 separation bubble will not form because flow will not reattach. Airfoils with chord Reynolds number higher than this number will have a separation bubble with different lengths, as noted by Gad-EL-HAK [4].

Therefore, LSB formation is possible only for limited range of Reynolds numbers and its formation also depends on local Reynolds number, pressure distribution, airfoil surface curvature, airfoil surface roughness and free stream turbulence.

Shyy [2] has illustrated based on Lissaman [3] the effect of lowering Reynolds number using several representative airfoils as shown in Figure 1.3. As Reynolds number is decreased the

lift to drag ratio is substantially reduced. The reason is related back to the transition from laminar flow to turbulent.

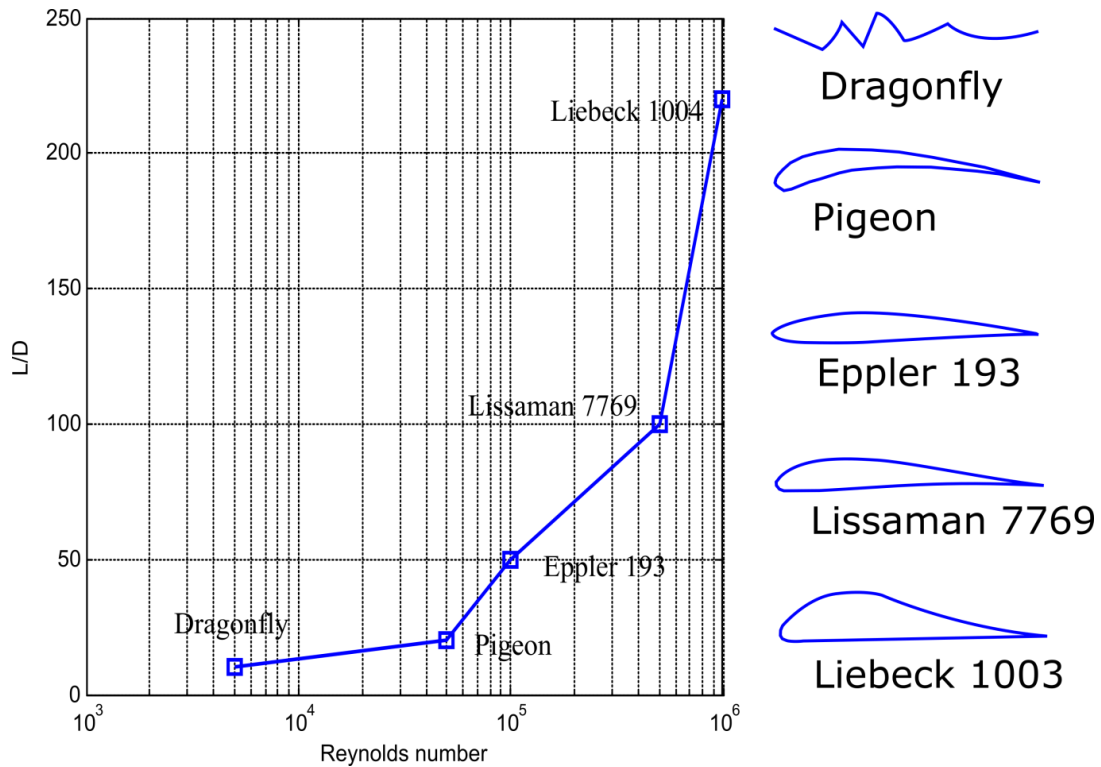


Figure 1.3 Reynolds number effect on representative airfoils performance

1.2 Efficiency in airfoil design

In predicting aerodynamic characteristics at high Reynolds numbers there exists a sophisticated Computational Fluid Dynamics (CFD) based flow solvers that uses Direct Numerical simulation (DNS), Large Eddy Simulation (LES), and Reynolds's Averaged Navier Stocks equations (RANS). At low Reynolds number airfoil design however, these codes are not preferable due to two reasons. Firstly, the domination of separation and transition phenomena at low Reynolds number flows which is not suitably solved by classical turbulence models. Secondly, CFD based codes which can capture these physical phenomena requires high computational cost (memory and time).

The inviscid viscous interaction solvers are most suitable for airfoil design and trade off studies and optimization [6], [7], and [8]. In practice, two programs are in use. Eppler code [9]

and XFOIL [10]. The two codes use for analysis and design of airfoils potential flow solvers and a boundary layer solution method.

In Eppler code conformal mapping is used as inverse design tool, in which a velocity distribution is specified. Uncoupled boundary layer calculations are then followed. The transition criterion is empirically based which is function of boundary layer momentum thickness, boundary layer shape factor H_{32} , and local condition in the boundary layer. This code does not contain LSB formulation but it issues a warning when LSB exists.

XFOIL code uses panel method for solving potential flow coupled with integral boundary layer formulations. The transition prediction criterion is also empirically derived from e^n method formulation [11]. It is capable of moderate LSB but only mild separations. The maximum lift which is usually close to complete stall with large separations is still over estimated by both codes. In fact, it is hard to estimate by most CFD solvers as well. This means that experimental work is still required to verify the airfoil performance.

These codes can carry out calculations extremely fast and also can perform efficient airfoil shape analysis. Therefore, they are more suitable for airfoil optimization studies.

1.3 Thesis Outline

The purpose of this thesis is twofold. The first, is to model the aerodynamic flow around airfoils at low Reynolds numbers (from 2×10^5 to 1×10^6). The second is to demonstrate the airfoil aerodynamic design approach by systematic shape modification. Therefore, in order to accomplish these two tasks, a computer MATLAB code is developed as explained in the thesis outline below.

In chapters 2, 3 and 4 the modeling and calculation of airfoil aerodynamic characteristics, boundary layer features and separation bubble effects are explained. The calculation of inviscid pressure distribution is based on conformal mapping method (chapter 2). The boundary layer development method is explained in chapter 3. The laminar separation bubble model is explained in chapter 4. Validation of the aerodynamic characteristics and locations of boundary layer features for two airfoils are also presented

In Chapter 5, most common airfoil parametric representation methods are reviewed, a Matlab code is prepared for each method and sample calculations are performed. Those methods are NACA, and PARSEC, Bezier curves and CST method. Airfoil shape parameterization with each method is examined, and finally as an illustration of method robustness a matching of pressure distribution is performed.

In chapter 6, some aerodynamic airfoil design methods are described from point of view of optimization algorithms usage. This includes formulation of design problem and specification of objective function and constraints to genetic search algorithms. Finally, the direct aerodynamic optimization based on shape perturbation is discussed.

In Chapter 7, aerodynamic design case studies are performed using the established code. They include design for given point and objective. The cases covered include inverse design, or design for given pressure distribution. The design can be for single point or multipoint, and the objective can vary from single to multi objective optimization. Design for varying Reynolds numbers is also accomplished. In chapter 8, concluding remarks and few suggested future research points are given.

CHAPTER 2

2 Two dimensional Ideal Fluid Flow

There are many levels of fluid flow approximations starting from Navier–Stokes equations (N-S) equations where most complex flow equations are considered, to the most simplified equations of potential flow models. Navier–Stokes equations are five highly nonlinear coupled partial differential equations, with six unknowns. When the equation of state for perfect gas is added these equations are still hard to solve. It is normally simplified by making appropriate assumptions about flow [12]. Figure 2.1 illustrates a hierarchy of the different levels of approximation. This figure illustrates how appropriate assumption can lead to simplified solutions and faster computations.

One main assumption is if viscosity effects are neglected or taken into account. In many engineering problems neglecting viscosity leads to solutions of acceptable accuracy. These solutions are either in close form or require low computational power. This makes inviscid approximation very interesting for analysis and design methods utilizing large number of repeated calculations. Aerodynamic drag is an essential aerodynamic physical quantity which requires viscous effects to be taken into consideration. The use of these models depend on application requirement, time available and computational cost.

According to this classification this chapter discusses the part where viscosity effects are neglected, and the next two chapters deal with solution of flow inside boundary layer. It is known that the solution of inviscid flow is much faster than that of boundary layer even with many other assumptions.

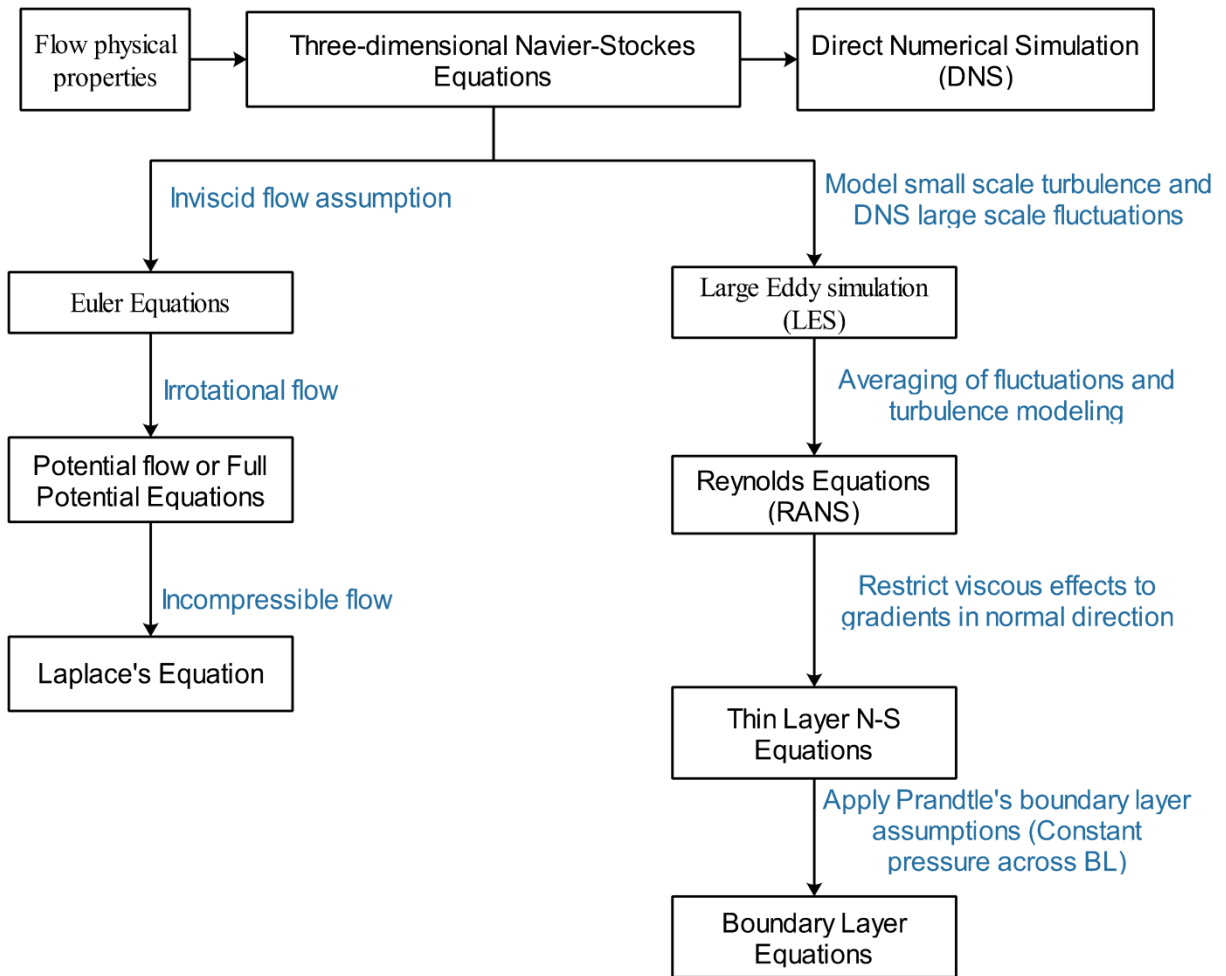


Figure 2.1 Hierarchy of the different levels of approximation [12]

2.1 Assumption of an Ideal Fluid [12]

The perfect fluid concept is significant simplification in fluid mechanics. In this concept ideal or perfect fluid is assumed to be a continuous and homogeneous medium, so that no effect of shearing stresses is considered. For ideal fluid the compressibility is neglected, and fluid is assumed incompressible. Not considering shearing stresses has the consequence of inability to know information about airfoil drag or about flow separations from airfoil surfaces. But this assumption simplifies the equations of motion and enables many close form solutions to wide range of problems to be found with reasonable accuracy. In many cases, the viscous forces are small compared to the inertia forces. The exception is in the layer of fluid adjacent to the surface, known as boundary layer, where viscosity must be considered.

The incompressibility assumption is acceptable when dealing with low speeds, since relative change in air density is small provided that the speed is well below the speed of sound.

2.2 Fundamental principles

The fundamental physical principles that should be satisfied are:

Principle of conservation of mass.

Principle of conservation momentum.

The first principle is enforced by applying the continuity equation. If a fixed area is filled with a perfect gas then the mass must remain constant. This means that the net rate of outflow must be zero. Mathematically the continuity equation is given by Eq.(2.1)

$$\frac{\partial u}{\partial x} + \frac{\partial v}{\partial y} = 0 \quad (2.1)$$

The second principle is satisfied by applying Newton's second law of motion to fluid particles which states that the rate of change of momentum of a particle is equal to the resultant of the forces acting on it. The resulting equations are Euler equations and are given by Eq.(2.2)

$$\rho \left(\frac{\partial \mathbf{u}}{\partial t} + \mathbf{u} \frac{\partial \mathbf{u}}{\partial x} + \mathbf{v} \frac{\partial \mathbf{u}}{\partial y} \right) = - \frac{\partial p}{\partial x} \quad (2.2)$$

$$\rho \left(\frac{\partial \mathbf{v}}{\partial t} + \mathbf{u} \frac{\partial \mathbf{v}}{\partial x} + \mathbf{v} \frac{\partial \mathbf{v}}{\partial y} \right) = - \frac{\partial p}{\partial y}$$

These two equations can be simplified further, if the steady flow is assumed, the resulting equation is Bernoulli's equation which is given by Eq.(2.3)

$$p + \frac{\rho V^2}{2} = \mathbf{const.} \quad (2.3)$$

This equation is valid for perfect gas, steady flows along stream line.

2.2.1 Irrotational flow

The circulation around closed curve \mathbf{s} is defined as the negative integral in anticlockwise direction of the tangential velocity around that curve expressed as in Eq.(2.4) and illustrated in Figure 2.2 .

$$\Gamma = - \oint \mathbf{V}_t ds == - \oint u dx - \oint v dy \quad (2.4)$$

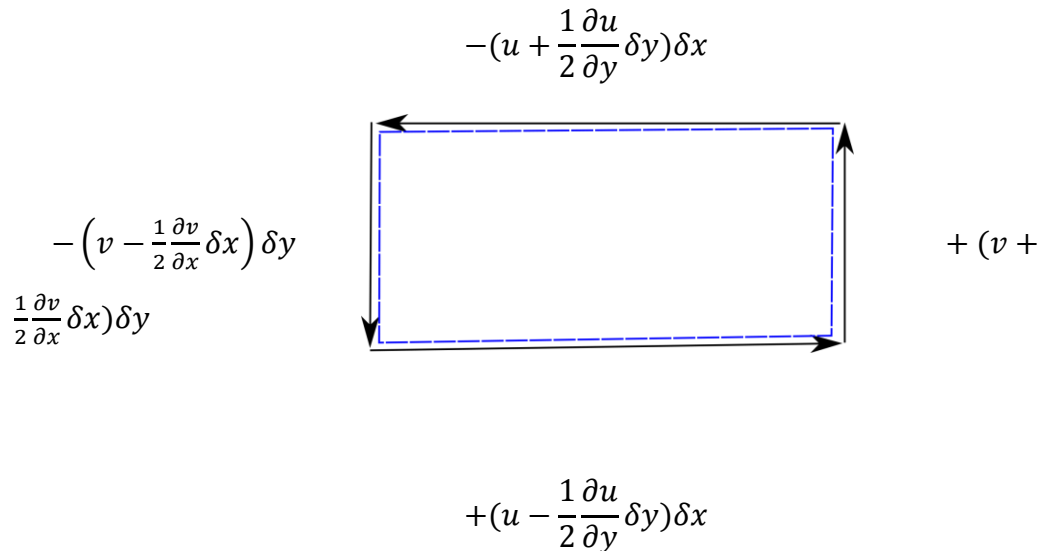


Figure 2.2 Circulation around closed path [13]

The circulation for an area R enclosed by boundary C can be expressed as Γ_C and is given by:

$$\Gamma_C = - \iint_R \left(\frac{\partial v}{\partial x} - \frac{\partial u}{\partial y} \right) dx dy \quad (2.5)$$

Where the term $\left(\frac{\partial v}{\partial x} - \frac{\partial u}{\partial y} \right)$ is called the vorticity ξ . Thus the vorticity is given by Eq.(2.6)

$$\xi = \left(\frac{\partial v}{\partial x} - \frac{\partial u}{\partial y} \right) \quad (2.6)$$

If the vorticity is zero the flow is termed irrotational flow. Flows around airfoils can be assumed irrotational except in very small region close to the boundary layer where the fluid particles experience rotational motion. Irrationality condition ($\xi = 0$) which implies:

$$\frac{\partial v}{\partial x} = \frac{\partial u}{\partial y} \quad (2.7)$$

2.2.2 Velocity Potential and stream function

For irrotational flow, which is an appropriate approximation of inviscid flow outside the boundary layer, a velocity potential function $\phi(x, y)$ exists which defines the velocity components of flow at each point. In two dimensional Cartesian coordinate system the velocity components (u, v) at coordinates (x, y) are given in terms of the velocity potential ϕ by the following equations respectively:

$$u = \frac{\partial \phi(x, y)}{\partial x} \quad (2.8)$$

$$v = \frac{\partial \phi(x, y)}{\partial y} \quad (2.9)$$

Substitution these two equations back into the continuity equation Eq.(2.1) results in the Laplace equation Eq.(2.10).

$$\nabla^2 \phi = 0 \quad (2.10)$$

Laplace equation describes the continuity equation of incompressible irrotational fluid. It has an important property being linear differential equation, so that solutions may be superimposed and the resulting function is also a solution to the Laplace equation. If the Laplace equation in terms of the velocity potential is known the velocity components can be readily obtained.

The stream function $\psi(x, y)$ is also defined so that it is constant along specific lines called a stream lines. The flow is always parallel to these lines and never cross them. The velocity components (u, v) are defined in terms of stream function as

$$u = \frac{\partial \psi(x, y)}{\partial y} \quad (2.11)$$

$$v = -\frac{\partial \psi(x, y)}{\partial x} \quad (2.12)$$

This function satisfies Laplace equation which is given in terms of the stream function as

$$\nabla^2 \psi = 0 \quad (2.13)$$

The stream function ψ and velocity potential ϕ lines are perpendicular to each other through any point in the flow field. They are commonly used in complex form.

2.2.3 The complex Velocity

Conformal mapping, which is used in the calculation of wing section characteristics depends on the use of complex variables. If z defined as $z = x + iy = re^{i\theta}$ is a complex number, where both x and y are real numbers, then the function $w(z) = u(z) - i.v(z)$ is called the *complex velocity*, if it satisfies the Cauchy-Riemann equation given by Eq. (2.14) [18]. It is clear that the complex velocity function $w(z)$ satisfies also the Euler and continuity equations.

$$\begin{aligned}\frac{\partial u}{\partial x} &= -\frac{\partial v}{\partial y} \\ \frac{\partial v}{\partial x} &= \frac{\partial u}{\partial y}\end{aligned}\tag{2.14}$$

The speed is given by $V = |w(z)| = \sqrt{u^2 + v^2}$ and the direction is given by the slope of the velocity at the point $\frac{v}{u} = \tan(-\arg w)$. In polar form the complex velocity is expressed alternatively in exponential form $w(z) = u - iv = Ve^{-iarctan\frac{v}{u}} = Ve^{i\theta}$. Where $\theta(z) = -\arg(w)$ is the angle of the velocity at point $z = x + iy$ to the positive real axis, as shown in Figure 2.3.

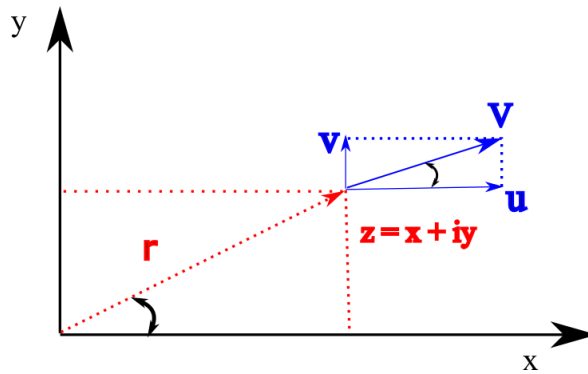


Figure 2.3 Variables defining complex velocity

2.2.4 The Complex Potential

The function $W(z)$ is called complex potential if,

$$w = u - iv = \frac{dW}{dz}$$

In words it means that the derivation of the complex potential with respect to z will result in the velocity potential.

The complex potential is given by

$$w = \phi + i\psi$$

If the velocity components are expressed in terms of ϕ or ψ as given by Eq.(2.15)

$$\begin{aligned}u &= \frac{\partial \phi}{\partial x} = \frac{\partial \psi}{\partial y} \\ v &= \frac{\partial \phi}{\partial y} = -\frac{\partial \psi}{\partial x}\end{aligned}\tag{2.15}$$

If we let $w = f(z)$ i.e.

$$w = \phi + i\psi = f(x + iy)$$

Then

$$\frac{\partial^2 \phi}{\partial x^2} + i \frac{\partial^2 \psi}{\partial x^2} = f_{xx}(x + iy) = f''(z)$$

and

$$\frac{\partial^2 \phi}{\partial y^2} + i \frac{\partial^2 \psi}{\partial y^2} = f_{yy}(x + iy) = -f''(z)$$

adding the two last equations, we get

$$\begin{aligned} & \frac{\partial^2 \phi}{\partial x^2} + i \frac{\partial^2 \psi}{\partial x^2} + \frac{\partial^2 \phi}{\partial y^2} + i \frac{\partial^2 \psi}{\partial y^2} \\ & \frac{\partial^2 \phi}{\partial x^2} + \frac{\partial^2 \phi}{\partial y^2} + i \left(\frac{\partial^2 \psi}{\partial x^2} + \frac{\partial^2 \psi}{\partial y^2} \right) = 0 \end{aligned}$$

In any equation involving complex variables, the real and imaginary parts must be equal to each other independently. Therefore

$$\begin{aligned} \frac{\partial^2 \phi}{\partial x^2} + \frac{\partial^2 \phi}{\partial y^2} &= 0 \\ \frac{\partial^2 \psi}{\partial x^2} + \frac{\partial^2 \psi}{\partial y^2} &= 0 \end{aligned} \tag{2.16}$$

These equations are the same as Laplace equation in two dimensional flow and thus any differentiable function $w = f(z)$ where $w = \phi + i\psi$ and $z = x + iy$ may be interpreted as a possible case of irrotational fluid motion by giving ϕ and ψ the meaning of velocity potential and stream function, respectively.

The derivative dw/dz has a simple meaning in terms of the velocities in the flow field, and can be illustrated as follows

$$\begin{aligned} dw &= d\phi + i d\psi \\ dz &= dx + i dy \end{aligned}$$

and

$$\begin{aligned} d\phi &= \frac{\partial \phi}{\partial x} dx + \frac{\partial \phi}{\partial y} dy \\ d\psi &= \frac{\partial \psi}{\partial x} dx + \frac{\partial \psi}{\partial y} dy \end{aligned}$$

Therefore

$$\frac{dw}{dz} = \frac{\left[\frac{\partial \phi}{\partial x} dx + \frac{\partial \phi}{\partial y} dy \right] + i \left[\frac{\partial \psi}{\partial x} dx + \frac{\partial \psi}{\partial y} dy \right]}{dx + i dy}$$

In order for dw/dz to have a definite meaning, it is necessary that the value of dw/dz be independent of the manner with which dz approaches zero. If dy is assumed to be zero, the value of the differential quotient dw/dz is

$$\frac{\partial \phi}{\partial x} + i \frac{\partial \psi}{\partial x} = u - iv = \frac{dw}{dz} \quad (2.17)$$

Similarly, if dx is assumed to be zero, the value of the differential quotient dw/dz is

$$\frac{1}{i} \frac{\partial \phi}{\partial y} + \frac{\partial \psi}{\partial y} = -iv + u$$

The expressions for simple two-dimensional elementary flows may be expressed conveniently in terms of complex variables [13] as illustrated in the following section.

Uniform stream parallel to x axis $w = V z$ **(2.18)**

Source at origin $w = \frac{m}{2\pi} \ln z$ **(2.19)**

Doublet at origin with axis along x axis $w = \frac{\mu}{2\pi z}$ **(2.20)**

Vortex at origin $w = \frac{i\Gamma}{2\pi} \ln z$ **(2.21)**

The superposition principle plays an important role to the general solution of incompressible potential flow problems. The solution to the governing equation (Laplace equation) can be obtained by defining elementary solutions that satisfy the infinity boundary condition of undisturbed flow and have singular solutions at the coordinate origin. Therefore, these elementary flows sometimes called singular solutions. The linear nature of the Laplace equation allows the solution of individual elementary flow and adding the resulting solution either numerically or analytically. The most widely used combined flows are given below

Circular cylinder of radius a in a uniform stream

$$w = V \left(z + \frac{a^2}{z} \right) \quad (2.22)$$

Circular cylinder with circulation

$$w = V \left(z + \frac{a^2}{z} \right) + \frac{i\Gamma}{2\pi} \ln \frac{z}{a} \quad (2.23)$$

Where :

V is uniform stream velocity

m source strength

μ Doublet strength

a Circular cylinder radius

Γ Circulation.

More about this flow is given in the next section.

2.2.5 Circular Cylinder with Circulation

A few simple flows upon which the theory of airfoils is based, can be used to calculate the flow around circular cylinder see references [13] and [15] among many others. The lift force can be calculated but drag force cannot be found because boundary layer viscous effects are not included. The flow pattern represented by a circular cylinder with circulation is the basic flow pattern from which the flow about wing sections of arbitrary shape at various angles of attack is calculated. Such a flow pattern is obtained by superposing the flow produced by a point vortex upon the flow about a circular cylinder. The stream function is given as

$$\psi = V r \left(1 - \frac{a^2}{r^2} \right) \sin\theta + \frac{\Gamma}{2\pi} \ln \frac{r}{a} \quad (2.24)$$

Where

a is circle radius

r is radial distance from origin to any point.

V is free stream velocity of uniform flow.

θ is angular position calculated anti-clock wise from x axis.

Γ is the value of circulation.

A typical flow pattern for a moderate value of the circulation Γ is given in Figure 2.4.

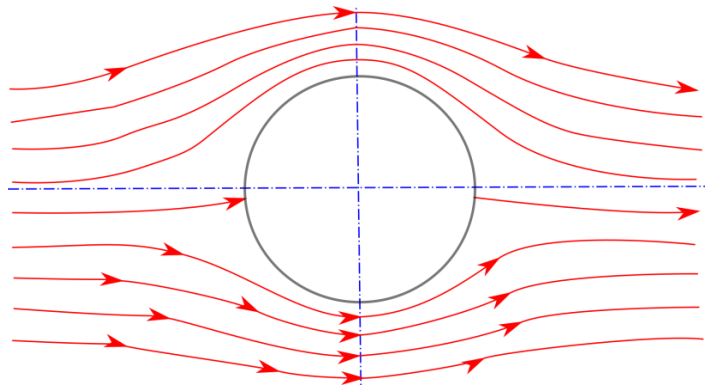


Figure 2.4 A typical stream lines of flow around circular cylinder with moderate circulation Γ
 The velocity distribution about the cylinder is found by differentiating the expression for the stream function Eq. (2.24) as follows:

$$\frac{\partial\psi}{\partial r} = V \left(1 + \frac{a^2}{r^2} \right) \sin\theta + \frac{\Gamma}{2\pi r} \quad (2.25)$$

The tangential component of velocity v' (positive counterclockwise) at the surface of the cylinder is obtained from the relation $v' = -\frac{\partial\psi}{\partial r}$ and the substitution of $r = a$.

$$v' = -2V \sin\theta + \frac{\Gamma}{2\pi a} \quad (2.26)$$

It is seen that the addition of the circulation Γ moves the points of zero velocity (stagnation points) from the positions $\theta = 0$ and $\theta = \pi$ to the positions

$$\theta = \sin^{-1} \frac{\Gamma}{4\pi aV} \quad (2.27)$$

The pressure distribution about the cylinder may be found by applying Bernoulli's equation along the streamline $\psi = 0$.

$$p + \frac{1}{2}\rho \left(4V^2 \sin^2 \theta - \frac{2V\Gamma \sin \theta}{\pi a} + \frac{\Gamma^2}{4\pi^2 a^2} \right) \quad (2.28)$$

The pressure coefficient C_p is given thus by

$$C_p = 4 \sin^2 \theta - 4K \sin \theta + K^2 \quad (2.29)$$

where $\frac{\Gamma}{2\pi aV} = K$. Eqn. (2.29) is symmetric about the line $\theta = \frac{\pi}{2}$ which means that there can be no drag force. The lift on the cylinder can be obtained by integration, over the surface, of the components of pressure normal to the cylinder.

$$Lift = \frac{1}{2}\rho V^2 \int_0^{2\pi} c_p a \sin \theta d\theta \quad (2.30)$$

$$= \frac{1}{2}\rho V^2 \int_0^{2\pi} (4a \sin^3 \theta - 4a K \sin^2 \theta + aK^2 \sin \theta) d\theta \quad (2.31)$$

$$= 1/2\rho V^2 aK [2\theta - \sin 2\theta]_0^{2\pi} \quad (2.32)$$

$$L = 2\rho V^2 aK\pi = \rho V\Gamma \quad (2.33)$$

This formula is valid for any shape. It states that the lift is function of air density, air velocity, and the magnitude of circulation Γ . The correct value of circulation is fixed by applying Kutta condition at the trailing edge.

2.3 Application to airfoils and conformal transformations

Superposition principle can be used to find the flow field about circular cylinder with circulation in a uniform stream. It is possible to relate this field of flow to that about an arbitrary wing section by means of conformal mapping. In relating these fields of flow, the circulation is selected to satisfy the Kutta condition that the velocity at the trailing edge of the section must be finite. Airfoil characteristics such as the lift and pressure distribution may then be determined from the known flow about the circular cylinder. The resulting theory permits the approximate calculation of the angle of zero lift, the moment coefficient, the pressure distribution, and the field of flow about the airfoil section under the condition that the flow stick to the surface.

A conformal transformation consists in mapping a region of one plane on another plane in such a manner that the angles are preserved. For instance, equipotential lines and streamlines intersect at right angles, thus create a large number of small rectangles in the flow field.

If the equation $w = f(z)$ represents a possible flow pattern, and also the equation $w = g(\zeta)$ represents another possible flow pattern where ζ is a complex variable $\zeta = \xi + i\eta$. The coordinate in z plane are considered to be x and y , and those in the ζ plane are ξ and η . If the equipotential lines and streamlines are plotted in either of the planes, they will divide the plane into a large number of small rectangles. These rectangles will be similar at corresponding points in both planes. The corresponding points are found from the relation $f(z) = g(\zeta)$. This equation represents a conformal transformation from z plane to the ζ plane, and it is necessary to solve this relation for ζ and to obtain the relation in the form $\zeta = h(z)$.

The velocities in z plane are given by differentiating the complex velocity w with respect to z .

$$\frac{dw}{dz} = u - i v \quad (2.34)$$

The corresponding velocities in ζ plane are given by the relation

$$\frac{dw}{d\zeta} = \frac{dw}{dz} \frac{dz}{d\zeta} \quad (2.35)$$

As a an example of a conformal transformation, consider the relations

$$w = V \left(z + \frac{a^2}{z} \right) = V\zeta$$

circular cylinder in z plane = uniform flow in
 ζ plane

(2.36)

These relations transform the flow about a circular cylinder on the z plane to uniform flow parallel to the ξ axis on the ζ plane. Corresponding points of both planes are obtained by the Joukowski transformation given by Eq.(2.37).

$$\zeta = z + \frac{a^2}{z}$$
(2.37)

This transformation transforms circle placed at coordinate origin with radius a in the z plane to a straight line segment of length $4a$ overlapping real axis symmetrically with respect to coordinate origin in ζ plane , as shown in Figure 2.5. If this transformation is applied to any circle in z plane which encloses circle with radius a then closed curve is obtained in plane ζ which encloses straight line segment, as shown in Figure 2.6. (note curves from Figure 2.5).

If the larger circle is moved off the center in z plane such that it touches the unit circle in one point as in Figure 2.8 a , then the resulting shape is an ellipse which touches mid-real axis in ζ plane at one point as in Figure 2.8 b. A symmetric airfoil shape appears in ζ plane if the unit circle is off centered on real x axis in z plane as in Figure 2.9. The camber is added to the airfoil shape if the center of the unit circle is off the origin in both x and y . in z plane, see Figure 2.10. The airfoil shapes obtained by Joukowski transform in Eq.(2.37) are cusped at the trailing edge, as can be seen in Figure 2.7 which makes them impractical. Karman-Trefftz transform can be used to form airfoils with non zero trailing edge is reviewed in the next section.

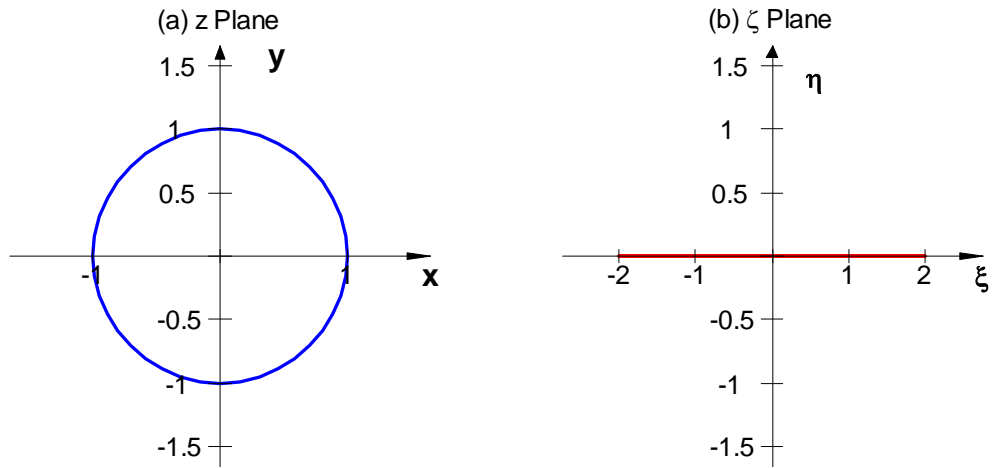


Figure 2.5 (a) a unit circle in z plane centered at origin with unit radius. (b) Joukowski transform of z plane unit circle to a straight line segment from -2 to 2 in ζ plane.

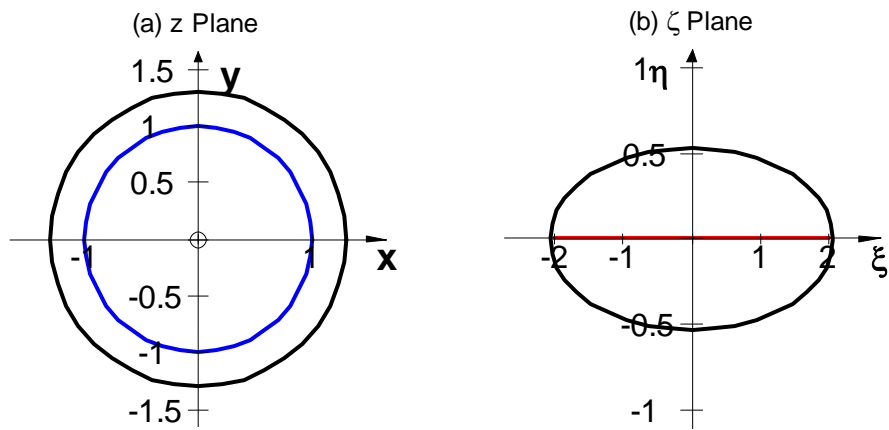


Figure 2.6 (a) A circle centered at origin with radius different than 1 in z plane transformed into ellipse in ζ plane.

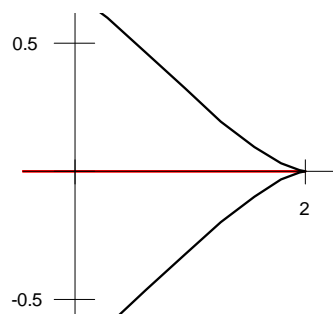


Figure 2.7 Close up view of trailing edge regions showing zero trailing edge angle.

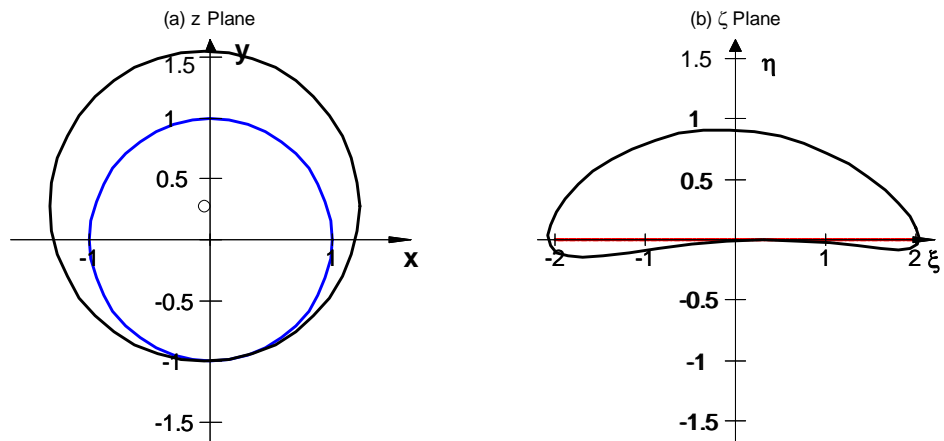


Figure 2.8 (a) a circle centered off the origin and has touches the unit circle at one point . (b) Transformed into an ellipse which touches mid-real axis in ζ plane at one point.

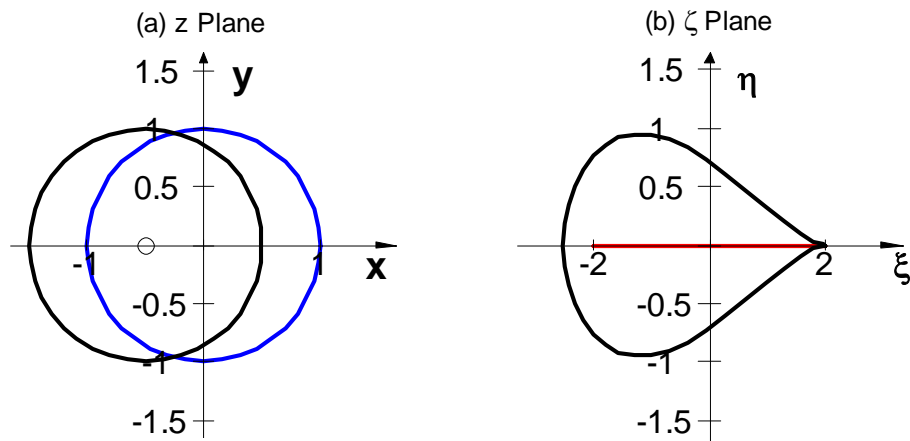


Figure 2.9 (a) a unit circle with center offset on real x axis in z plane (b) A non cambered airfoil in ζ plane.

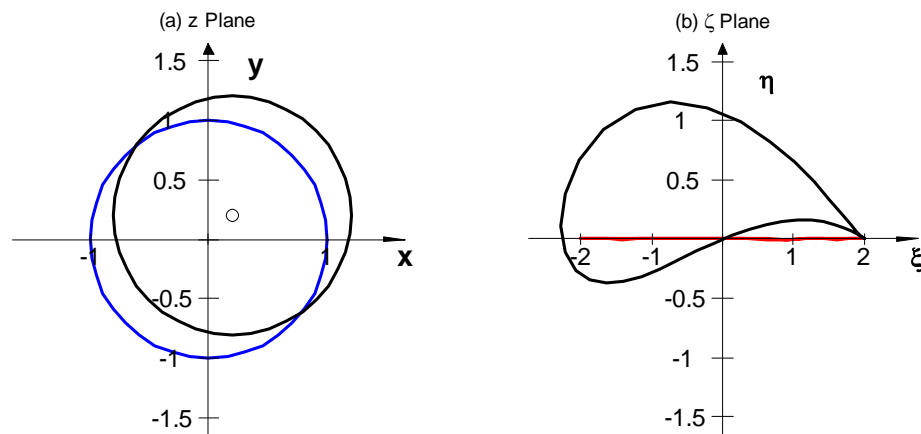


Figure 2.10 (a) circle with center off the origin in both $\mu_x = 0.2$ and $\mu_y = 0.2$. with part of the contour outside the unit circle (b) Cambered airfoil in ζ plane with part of its contour above real axis.

2.4 Karma-Trefftz transformation

This transformation can be used to transform a circle in z plane into an airfoil shape in ζ plane or vice versa. It is given by Eq.(2.38). The coordinates of singular points $s_0 = -1/\beta$ and $s_1 = 1/\beta$ are chosen to simplify this figure generation, and $\beta = 2 - \frac{\tau}{\pi}$ is slightly less than 2, and τ is airfoil trailing edge angle. Figure 2.11 is generated by this transformation from a circle in z plane with a center at $(-0.05, 0.05)$ and a radius of 1.0512.

$$\frac{\zeta - s_0}{\zeta - s_1} = \left(\frac{z - \beta s_0}{z - \beta s_1} \right)^{1/\beta} \quad (2.38)$$

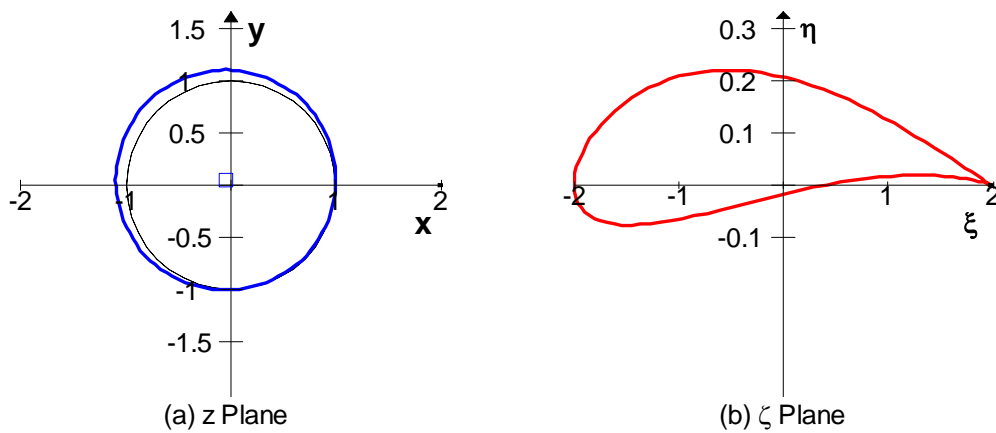


Figure 2.11 Karman-Trefftz transform of an off centered unit circle with $\mu_x = -0.05$ and $\mu_y = 0.05$ and radius of 1.0512 in z plane into an airfoil, with finite trailing edge angle of 2 deg in ζ plane.

2.5 Flow Analysis over an Airfoil Using Conformal Mapping

The Joukowski and Karman-Trefftz conformal transformations are used to transform a circle in z plane into a curve resembling an airfoil in the ζ plane as shown in the above sections. Theodorsen showed that if inverse transformation is applied to an airfoil in ζ plane, the resulting curve in z plane will therefore be a near circle. He also showed that the flow about near circle, and hence the airfoil can be calculated from the flow about the true circle through an iterative procedure. The basic method is presented in references [12]to [17].

The procedure starts with given (ξ, η) airfoil coordinates in ζ plane, flow angle of attack α and free stream velocity V . Airfoil coordinates are used to calculate near circle coordinates using Karman-Trefftz transformation, i.e. from Figure 2.12a to, Figure 2.12b. Every point on airfoil is conformly mapped to corresponding point on the near circle. There are two singular points s_0 and s_1 which are specified midway between airfoil leading edge and center of

curvature, and at airfoil trailing edge, respectively. The near circle shape is transformed to the origin of the coordinate system after finding its centroid, see Figure 2.12c. Fast Fourier Transform (FFT) is then used to find relations between the flow in the centered near circle (z_2 plane) and in the plane of the true circle (z_3 plane). The final step, is combining the foregoing relations to obtain the final expression for the velocity distribution in the airfoil plane in terms of airfoil coordinates.

The calculation of the velocity distribution about an airfoil is done mainly in few steps. Figure 2.12 shows schematically these steps:

- Generation of airfoil shape.
- Analytical mapping of airfoil to near circle shape by using Karmen-Traffitz transformation.
- Translation of the near circle to the origin of the coordinate system.
- Representing near circle couture as function of true circle this is done iteratively utilizing Fast Fourier Transform.
- Obtaining velocity distribution on true circle and calculate modulus of transformations.

And finally, calculate pressure distributions over the airfoil surface at given flow angle of attack and velocity.

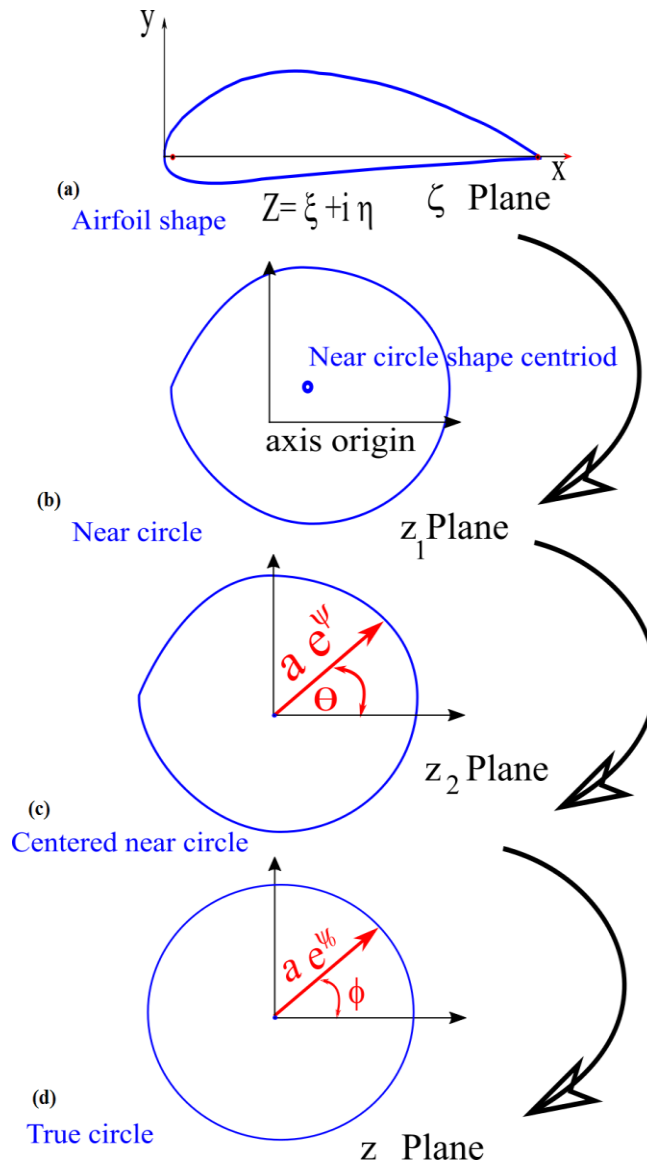


Figure 2.12 Steps involved in transformations of airfoil to true circle

2.5.1 Airfoil shape

The airfoil (ξ, η) coordinates are generated using one of the geometric representation methods discussed in chapter (5). The points start from the trailing edge through the upper surface to the leading edge, and then back through the lower surface to the trailing edge. Thus the first point is same as last point, as illustrated in Figure 2.13. These coordinates are changed to complex variables in ζ plane and their radius and phase angles are computed $\zeta = \xi + i\eta = re^{i\theta}$.

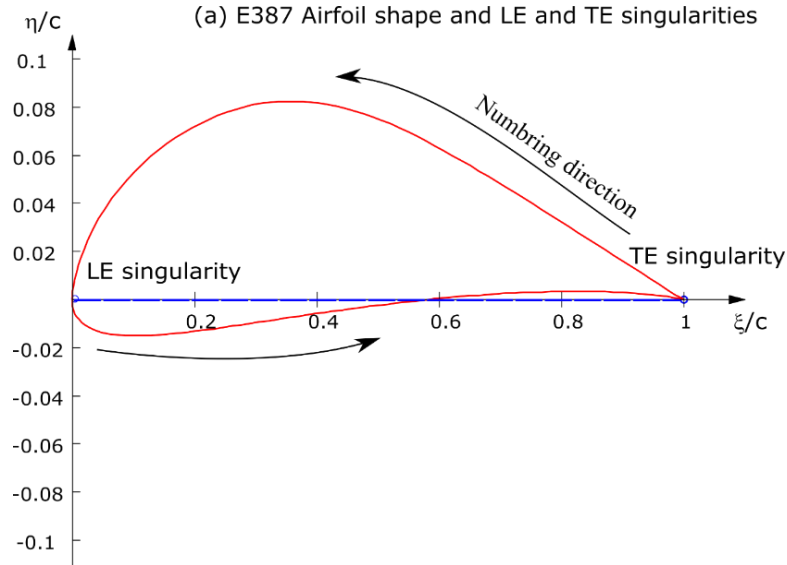


Figure 2.13 Airfoil generated for conformal mapping

2.5.2 Apply Karman-Trefftz Transformation

The basic relation between the near circle plane (z_1 plane) and the airfoil plane (ζ plane) is performed through the Karman-Trefftz transformation (2.39) by which corners are removed from airfoil where $\beta = 2 - \frac{\tau}{\pi}$ and τ is airfoil trailing edge angle. Points s_0 and s_1 are locations of the singular points. The location of s_0 is set med way between leading edge and nose center of curvature, while s_1 is set at the trailing edge. The coordinate of the resulting nearly circular shape Figure 2.14 is given by z_1 . The airfoil coordinates are defined by ζ with the relation

$$\zeta = \xi + i \eta$$

$$\frac{\zeta - s_0}{\zeta - s_1} = \left(\frac{z_1 - \beta s_0}{z_1 - \beta s_1} \right)^{1/\beta} \quad (2.39)$$

From which z_1 can be expressed explicitly as follows

$$z_1 = \beta \frac{s_0(\zeta - s_1)^\beta - s_1(\zeta - s_0)^\beta}{(\zeta - s_1)^\beta - (\zeta - s_0)^\beta} \quad (2.40) \text{ A}$$

$$z_1 = \beta \frac{(s_1 - s_0)}{e^{\beta 2\pi i} \left(\frac{\zeta - s_0}{\zeta - s_1} \right)^\beta - 1} - \beta s_0 \quad \text{B}$$

Equation (2.40) is valid when near the trailing edge upper surface is above real axis and lower surface is below it. For the points of the lower surface which are above real axis Eq.(2.40) is used.

The coordinates of z_1 are defined by the relation

$$z_1 = a e^{\psi+i\theta} = a e^{\psi} \cdot e^{i\theta} = r(\theta) e^{i\theta} \quad (2.41)$$

Where $r(\theta) = a e^{\psi}$ is the radius at any point, and θ is the angle at that point, as shown in the Figure 2.12.

Knowing that $e^{i\theta} = \cos \theta + i \sin \theta$ the above relation can be split into real and imaginary parts.

$$\text{Where } z_1 = \begin{array}{l} r(\theta) \cos \theta \\ \text{Real part} \end{array} + \begin{array}{l} i r(\theta) \sin \theta \\ \text{Imaginary part} \end{array} \quad (2.42)$$

The factor relating velocities in the z_1 plane to those in the ζ plane is $dz_1/d\zeta$ is called modulus of transformation and is calculated in later step.

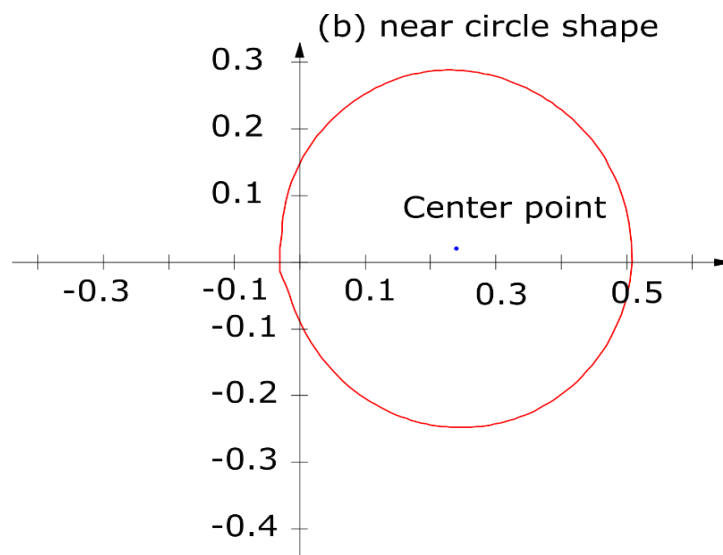


Figure 2.14 Airfoil transformed to near circle

2.5.3 Translation of the near circle to the origin

The center of gravity of the near circular shape is calculated by Eq.(2.43)

$$z_{1cg} = \frac{\sum_{i=1}^{n-1} (z_{1(i+1)} + z_{1(i)}) / (z_{1(i+1)} - z_{1(i)})}{2 \cdot \sum_{i=1}^{n-1} (z_{1(i+1)} - z_{1(i)})} \quad (2.43)$$

After calculating the center of gravity, the translated near circle coordinates z_2 are obtained by subtracting z_{1cg} from each point.

$$z_2 = z_1 + z_{1cg} \quad (2.44)$$

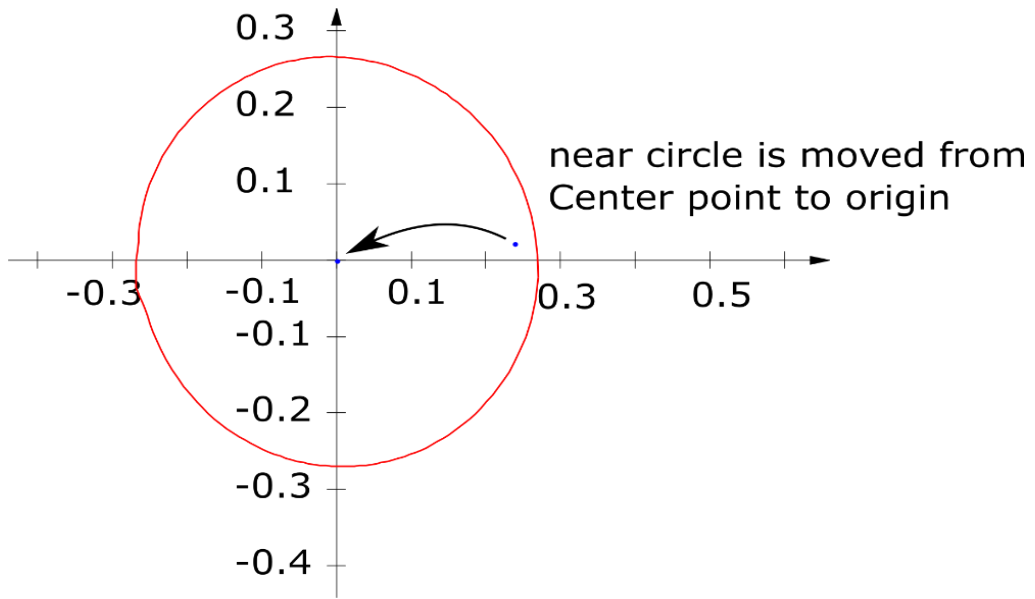


Figure 2.15 Shifted near circle

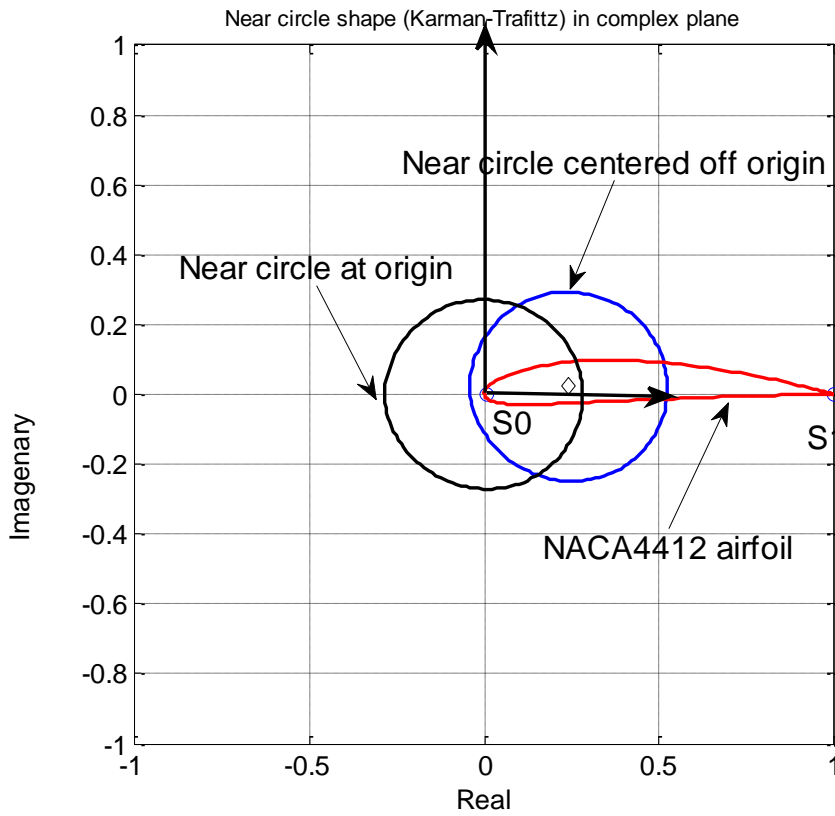


Figure 2.16 NACA4412 airfoil transformed to near circle then shifted to origin

2.5.4 Mapping of near circle in (z_2 plane) to true circle (z plane).

The coordinates of z are defined by the relation

$$z = a e^{\psi_0 + i\varphi} = R \cdot e^{i\varphi} \tag{2.45}$$

The transformation relating the z_2 plane to the z plane is the general transformation

$$z_2 = z e^{\sum_{n=1}^{\infty} (A_n + i B_n)(1/z^n)} \quad (2.46)$$

But by definition this transformation should result in near circle

$$z_2 = z e^{\psi - \psi_0 + i(\theta - \varphi)} \quad (2.47)$$

Consequently

$$\psi - \psi_0 + i(\theta - \varphi) = \sum_{n=1}^{\infty} (A_n + i B_n)(1/\zeta^n) \quad (2.48)$$

Knowing that

$$\frac{1}{\zeta^n} = \frac{1}{r^n} e^{-i n \varphi} = \frac{1}{r^n} (\cos n \varphi - i \sin n \varphi) \quad (2.49)$$

Substituting $\frac{1}{\zeta^n}$ into (2.48) we get

$$\begin{aligned} \psi - \psi_0 + i(\theta - \varphi) &= \sum_{n=1}^{\infty} (A_n + i B_n) \frac{1}{r^n} (\cos n \varphi - i \sin n \varphi) \end{aligned} \quad (2.50)$$

$$\begin{aligned} \psi - \psi_0 + i(\theta - \varphi) &= \sum_{n=1}^{\infty} \left(\frac{A_n}{r^n} \cos n \varphi + \frac{B_n}{r^n} \sin n \varphi \right) \\ &+ i \sum_{n=1}^{\infty} \left(\frac{B_n}{r^n} \cos n \varphi - \frac{A_n}{r^n} \sin n \varphi \right) \end{aligned} \quad (2.51)$$

Equating real and imaginary parts from both sides we obtain

$$\psi - \psi_0 = \sum_{n=1}^{\infty} \left(\frac{A_n}{r^n} \cos n \varphi + \frac{B_n}{r^n} \sin n \varphi \right) \quad (2.52)$$

$$(\theta - \varphi) = \sum_{n=1}^{\infty} \left(\frac{B_n}{r^n} \cos n \varphi - \frac{A_n}{r^n} \sin n \varphi \right) \quad (2.53)$$

These relations show that $\psi - \lambda$ and $(\theta - \varphi)$ are conjugate functions. The true circle radius is chosen such that there is minimum deviation between points radii on the near circle ψ and the radius of the true circle which is found from the relation $R = e^{\psi_0}$.

$$\lambda = \psi_0 = \frac{1}{2\pi} \int_0^{2\pi} \psi d\varphi \quad (2.54)$$

It can be written as

$$\psi = \psi_0 + \sum_{n=1}^{\infty} (a_n \cos n \varphi + b_n \sin n \varphi) \quad (2.55)$$

$$\theta = \varphi + \sum_{n=1}^{\infty} (b_n \cos n\varphi - a_n \sin n\varphi) \quad (2.56)$$

Where $a_n = \frac{A_n}{r^n}$ and $b_n = \frac{B_n}{r^n}$

Equations (2.55) and (2.56) constitute $2N$ equations, and $2N + 2$ unknowns. These unknowns are A_n and B_n , where $n=1$ to N . Other two unknowns are ψ_0 which is related to the true circle radius R as $R = e^{\psi_0}$. In order to place the trailing edge at the real axis ($\varphi = 0$) Equation (2.56) will be

$$\theta_{TE} = b_0 + \sum_{n=1}^N (b_n) \quad (2.57)$$

The unknowns can be obtained by applying Fast Fourier transform (FFT) iteratively [20]. Theodorsen originally solved those equations based on interpolation which requires $O(N^2)$ multiplications, but Fast Fourier Transform simplifies a lot this step with only $O(N \log N)$ multiplications. this approach is used by many authors and found to be efficient [21] [22] [23][24]. The main steps involved in the numerical procedure are listed below:

1. Divide the true circle z into 2^M equally spaced points φ which is not changed during the rest of calculation procedure.
2. Find the corresponding points in the centered near circle z_2 plane i.e $\theta(\varphi)$ by iteration.
3. As first step assume that coefficients a_n and b_n are zero i.e coefficients $a_n = 0$ and $b_n = 0$, Eq.(2.56) will reduce to $\theta = \varphi$ at every point.
4. Since ψ is a known function of θ at every point in near circle plane i.e. $\psi(\theta)$, and θ is known from previous step, the left side of Eq. (2.56) is now known. The right side of this equation is easily computed by using FFT algorithm by which the coefficients a_n and b_n are obtained, as an estimate.
5. Having obtained coefficients a_n and b_n a new estimate of angle θ as function of φ is possible through Eq.(2.56). This is done by applying Inverse Fourier Transform IFFT. In this step new values of θ are obtained.
6. The value of b_0 is obtained by letting $\varphi = 0$ at trailing edge. And thus the angle at trailing edge in near circle plane is $\theta_{TE} = b_0 + \sum_{n=1}^{\infty} b_n$. The value of a_0 is obtained directly from FFT algorithm.

Steps 4 through 6 should be repeated until convergence is reached.

2.5.5 Calculation of modulus of transformation

The total modulus of transformation is obtained by multiplying modulus of all transformations.

$$\frac{dw}{dz} = \frac{dw}{dz} \cdot \frac{dz}{dz_2} \cdot \frac{dz_2}{dz_1} \cdot \frac{dz_1}{dz} \quad (2.58)$$

1-Airfoil shape is transformed by using analytic Karman-Trefftz transformation Eqn.(2.40) A which is function of ζ . Differentiating this equation with respect to ζ we get $\frac{dz_1}{d\zeta}$ as follows

$$\frac{dz_1}{d\zeta} = \beta z_1 \left\{ \frac{s_0(\zeta - s_1)^{\beta-1} - s_1(\zeta - s_0)^{\beta-1}}{s_0(\zeta - s_1)^\beta - s_1(\zeta - s_0)^\beta} - \frac{(\zeta - s_1)^{\beta-1} - (\zeta - s_0)^{\beta-1}}{(\zeta - s_1)^\beta - (\zeta - s_0)^\beta} \right\} \quad (2.59)$$

2- Shifting the near circle plane to origin has a modulus of 1, thus

$$\frac{dz_2}{dz_1} = 1 \quad (2.60)$$

3- The third transformation is transformation of near circle z_2 to true circle z which modulus of transformation is given by $\frac{dz}{dz_2}$. Mapping from near circle to circle is performed by the relation

$$z_2 = z e^{\sum_{n=1}^{\infty} (A_n + i B_n)(1/z^n)} \quad (2.61)$$

But

$$z_2 = a e^{\psi + i \theta} \quad (2.62)$$

and

$$z = a e^{\psi_0 + i \varphi} = r e^{i \varphi} \quad \text{where} \quad r = a e^{\psi_0} \quad (2.63)$$

Substituting Eqs(2.63) and (2.62) into Eqs (2.61) and substituting for z . The expression $\frac{dz}{dz_2}$ can be written in the form

$$\frac{dz}{dz_2} = \frac{\frac{dz}{d\varphi}}{\frac{dz_2}{d\varphi}} \quad (2.64)$$

since ψ and θ are functions of φ and ψ_0 is constant. Thus

$$\frac{dz}{d\varphi} = i. a e^{\psi_0 + i \varphi} = i. z$$

and

$$\frac{dz_2}{d\varphi} = \frac{d(\psi + i\theta)}{d\varphi} a e^{\psi+i\theta} = z_2 \frac{d(\psi + i\theta)}{d\varphi}$$

Substituting back into equation (2.64) we get

$$\frac{dz}{dz_2} = \frac{i \cdot z}{z_2 \frac{d(\psi + i\theta)}{d\varphi}} \quad (2.65)$$

Where $\frac{d(\psi+i\theta)}{d\varphi} = \frac{d\psi}{d\varphi} + i \frac{d\theta}{d\varphi}$, to find this derivative we proceed as follows:

Knowing that

$$\sum_{n=1}^{\infty} \frac{A_n + i B_n}{1/z^n} = \sum_{n=1}^{\infty} \left(\frac{A_n}{r^n} \cos n\varphi + \frac{B_n}{r^n} \sin n\varphi \right) + i \sum_{n=1}^{\infty} \left(\frac{B_n}{r^n} \cos n\varphi - \frac{A_n}{r^n} \sin n\varphi \right)$$

Substituting in Eq.(2.61) we get

$$a e^{\psi+i\theta} = a e^{\psi_0+i\varphi} e^{\sum_{n=1}^{\infty} \left(\frac{A_n}{r^n} \cos n\varphi + \frac{B_n}{r^n} \sin n\varphi \right) + i \sum_{n=1}^{\infty} \left(\frac{B_n}{r^n} \cos n\varphi - \frac{A_n}{r^n} \sin n\varphi \right)}$$

Dropping out a and taking the log of both sides we get

$$\psi + i\theta = \psi_0 + i\varphi + \sum_{n=1}^{\infty} \left(\frac{A_n}{r^n} \cos n\varphi + \frac{B_n}{r^n} \sin n\varphi \right) + i \sum_{n=1}^{\infty} \left(\frac{B_n}{r^n} \cos n\varphi - \frac{A_n}{r^n} \sin n\varphi \right)$$

Separating real and imaginary part we get

$$\psi = \psi_0 + \sum_{n=1}^{\infty} \left(\frac{A_n}{r^n} \cos n\varphi + \frac{B_n}{r^n} \sin n\varphi \right)$$

$$\theta = \varphi + \sum_{n=1}^{\infty} \left(\frac{B_n}{r^n} \cos n\varphi - \frac{A_n}{r^n} \sin n\varphi \right)$$

It is worth to note that $\psi = \ln(r(\theta))$ and $\psi_0 = \ln(R)$

Differentiating w.r.t φ both equations we get $\frac{d\psi}{d\varphi}$ and $\frac{d\theta}{d\varphi}$

$$\frac{d\psi}{d\varphi} = \sum_{n=1}^{\infty} \left(-\frac{A_n}{r^n} \cdot n \cdot \sin n\varphi + \frac{B_n}{r^n} \cdot n \cdot \cos n\varphi \right)$$

$$\frac{d\theta}{d\varphi} = 1 + \sum_{n=1}^{\infty} \left(-\frac{B_n}{r^n} \cdot n \cdot \sin n\varphi - \frac{A_n}{r^n} \cdot n \cdot \cos n\varphi \right)$$

$$\frac{d\psi}{d\varphi} = \sum_{n=1}^{\infty} \left(\frac{B_n}{r^n} \cdot n \cdot \cos n\varphi - \frac{A_n}{r^n} \cdot n \cdot \sin n\varphi \right)$$

$$\frac{d\theta}{d\varphi} = 1 - \sum_{n=1}^{\infty} \left(\frac{B_n}{r^n} \cdot n \cdot \sin n\varphi + \frac{A_n}{r^n} \cdot n \cdot \cos n\varphi \right)$$

$$\frac{d\psi}{d\varphi} + i \frac{d\theta}{d\varphi} = \sum_{n=1}^{\infty} \left(\frac{B_n}{r^n} \cdot n \cdot \cos n\varphi - \frac{A_n}{r^n} \cdot n \cdot \sin n\varphi \right) + i \left[1 - \sum_{n=1}^{\infty} \left(\frac{B_n}{r^n} \cdot n \cdot \sin n\varphi + \frac{A_n}{r^n} \cdot n \cdot \cos n\varphi \right) \right]$$

If we proceed

$$\begin{aligned} \frac{d\psi}{d\varphi} + i \frac{d\theta}{d\varphi} &= \frac{1}{i} \left\{ i \sum_{n=1}^{\infty} \left(\frac{B_n}{r^n} \cdot n \cdot \cos n\varphi - \frac{A_n}{r^n} \cdot n \cdot \sin n\varphi \right) \right. \\ &\quad \left. + \left[-1 + \sum_{n=1}^{\infty} \left(\frac{B_n}{r^n} \cdot n \cdot \sin n\varphi + \frac{A_n}{r^n} \cdot n \cdot \cos n\varphi \right) \right] \right\} \\ \frac{d\psi}{d\varphi} + i \frac{d\theta}{d\varphi} &= \frac{1}{i} \left\{ i \sum_{n=1}^{\infty} \left(\frac{B_n}{r^n} \cdot n \cdot \cos n\varphi - \frac{A_n}{r^n} \cdot n \cdot \sin n\varphi \right) \right. \\ &\quad \left. + \sum_{n=1}^{\infty} \left(\frac{B_n}{r^n} \cdot n \cdot \sin n\varphi + \frac{A_n}{r^n} \cdot n \cdot \cos n\varphi \right) - 1 \right\} \\ \frac{d\psi}{d\varphi} + i \frac{d\theta}{d\varphi} &= \frac{1}{i} \left\{ \sum_{n=1}^{\infty} n \cdot (A_n + i B_n) (1/z^n) - 1 \right\} \end{aligned}$$

Now we can substitute back into Eq.(2.65)

$$\frac{dz}{dz_2} = \frac{i \cdot z}{z_2 \cdot \frac{1}{i} \left\{ \sum_{n=1}^{\infty} n \cdot (A_n + i B_n) (1/z^n) - 1 \right\}} \quad (2.66)$$

$$\frac{dz}{dz_2} = \frac{z}{z_2 \cdot \left\{ 1 - \sum_{n=1}^{\infty} n \cdot (A_n + i B_n) (1/z^n) \right\}} \quad (2.67)$$

If we further substitute the equations for z_2 and z we will get the following relation

$$\frac{dz}{dz_2} = \frac{e^{-\sum_{n=1}^{\infty} (A_n + i B_n) (1/z^n)}}{1 - \sum_{n=1}^{\infty} n \cdot (A_n + i B_n) (1/z^n)} \quad (2.68)$$

Equation (2.68) represents the modulus of transformation from the near circle plane to the true circle plane.

2.5.6 Finding velocities in the true circle plane

Flow around true circle with radius of $R = ae^{\psi_0}$ is obtained by the equation

$$w = V_{\infty} e^{-i\alpha} (z - z_0) + \frac{R^2 V_{\infty} e^{i\alpha}}{(z - z_0)} + \frac{i \Gamma}{2\pi} \ln (z - z_0) \quad (2.69)$$

Conjugate complex velocity on the true circle are obtained with

$$\frac{dw}{dz} = V_{\infty} e^{-i\alpha} - \frac{R^2 V_{\infty} e^{i\alpha}}{(z - z_0)^2} + \frac{i \Gamma}{2\pi} \frac{1}{(z - z_0)} \quad (2.70)$$

Since $z - z_0 = r e^{i\phi}$

$$\frac{dw}{dz} = V_{\infty} e^{-i\alpha} - \frac{R^2 V_{\infty} e^{i\alpha}}{r^2 e^{i2\phi}} + \frac{i \Gamma}{2\pi r} e^{-i\phi} \quad (2.71)$$

$$\frac{dw}{dz} = V_{\infty} e^{-i\alpha} - \frac{R^2 V_{\infty} e^{i\alpha} e^{-i2\phi}}{r^2} + \frac{i \Gamma}{2\pi r} e^{-i\phi} \quad (2.72)$$

But at the circle surface $r = R$ and at the trailing edge where $\phi = \mu$, Kutta condition must be satisfied by letting the total velocity to zero and obtaining the required circulation Γ to satisfy this condition.

Thus

$$0 = V_{\infty} e^{-i\alpha} - V_{\infty} e^{-i\alpha} e^{-i2\mu} + \frac{i\Gamma}{2\pi R} e^{-i\mu} \quad (2.73)$$

At trailing edge there is a rotation by an angle of μ and thus the angle of attack will be modified by this amount. The equation of circulation finally will be

$$\Gamma = 4\pi R V_{\infty} \sin(\alpha - \mu) \quad (2.74)$$

Circulation Γ necessary to satisfy Kutta condition thus, depends on angle of attack α and position of trailing edge image in circle plane μ . Having obtained the value of circulation, the modulus of transformation is calculated by substitution. The last step is to calculate the velocities in airfoil plane by

$$\frac{dw}{d\zeta} = \frac{dw}{dz} \cdot \frac{dz}{dz_2} \cdot \frac{dz_2}{dz_1} \cdot \frac{dz_1}{d\zeta} \quad (2.75)$$

Once velocity distribution is obtained by the above method, pressure distribution is obtained via the relation

$$C_p = 1 - \left| \frac{dw}{d\zeta} \right| \frac{1}{V_{\infty}} \quad (2.76)$$

Sample calculations for Low Reynolds number airfoil E387 are shown in Figure 2.17, Figure 2.18, and Figure 2.19. The pressure distribution calculated by this approach at angle of attack of 2 degrees and Reynolds number of 300,000 is compared with XFOIL code. Figure 2.20

show that the pressure distribution agrees well with XFOIL results. The flow chart for the above method is summarized in the flow chart shown on Figure 2.21.

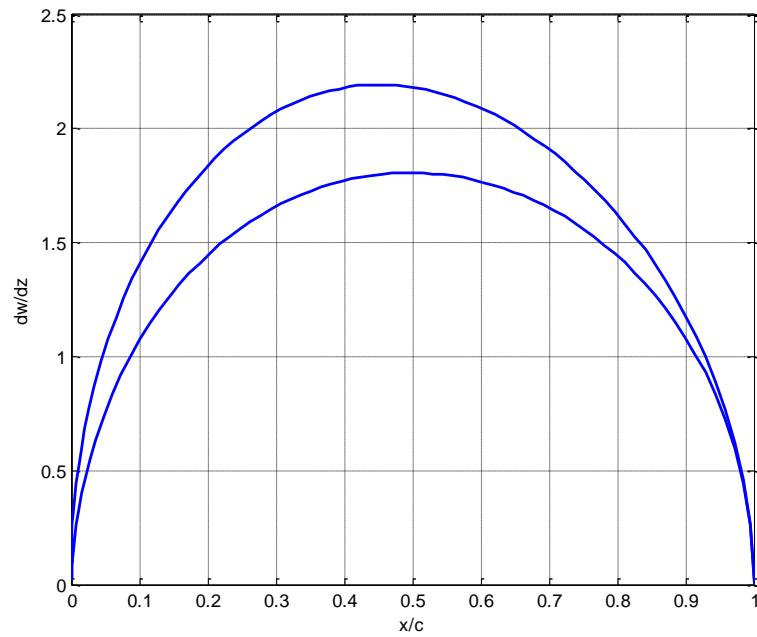


Figure 2.17 Potential flow velocity around circular cylinder dw/dz

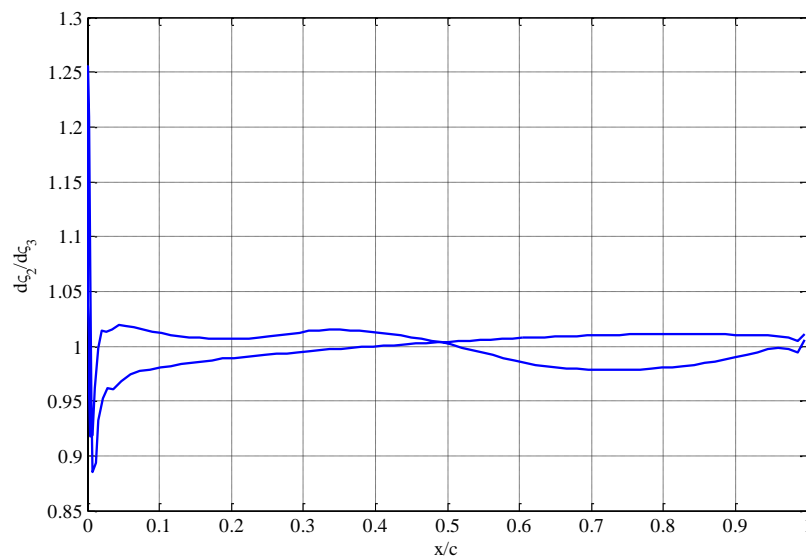


Figure 2.18 Derivative of transformation ($d\zeta_2/dz$) for E387 airfoil.

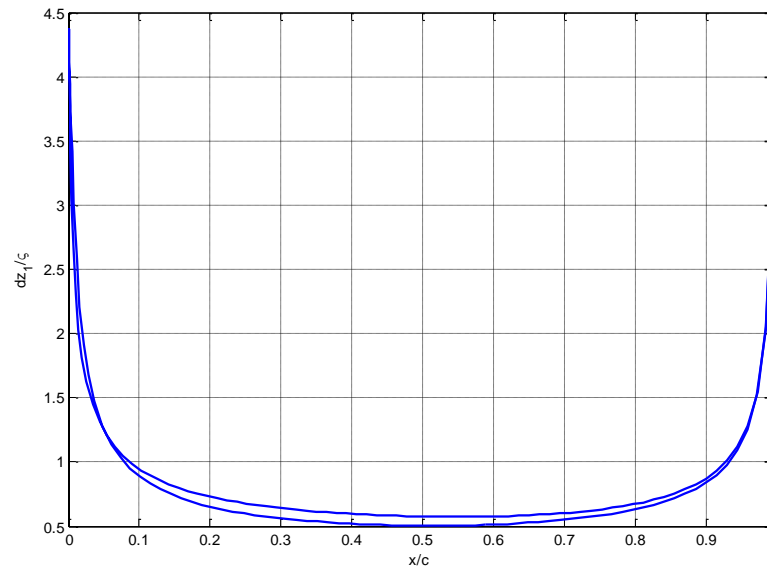


Figure 2.19 Derivative of transformation dz_1/ζ for E387 airfoil

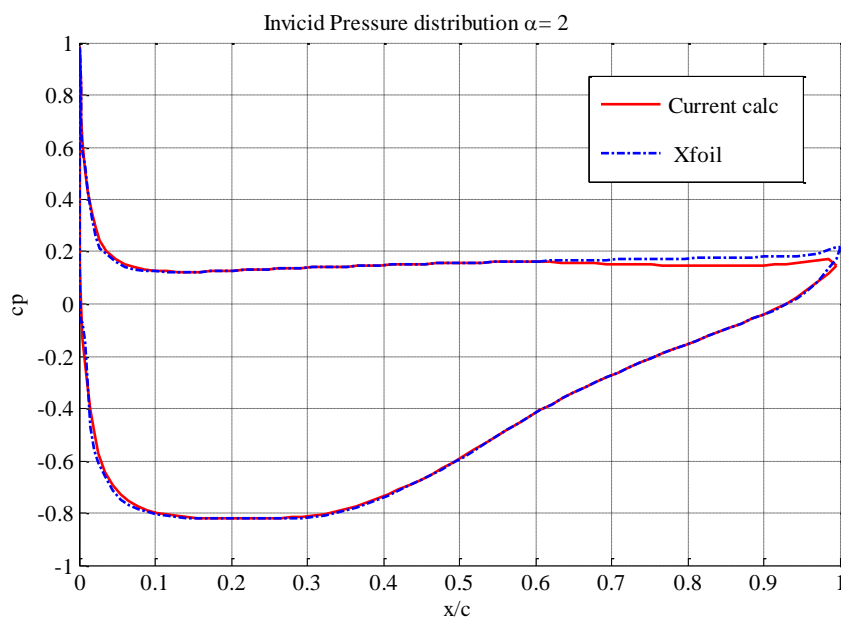


Figure 2.20 Inviscid pressure distributions at 2° and Reynolds number of 300,000 for E387 airfoil.

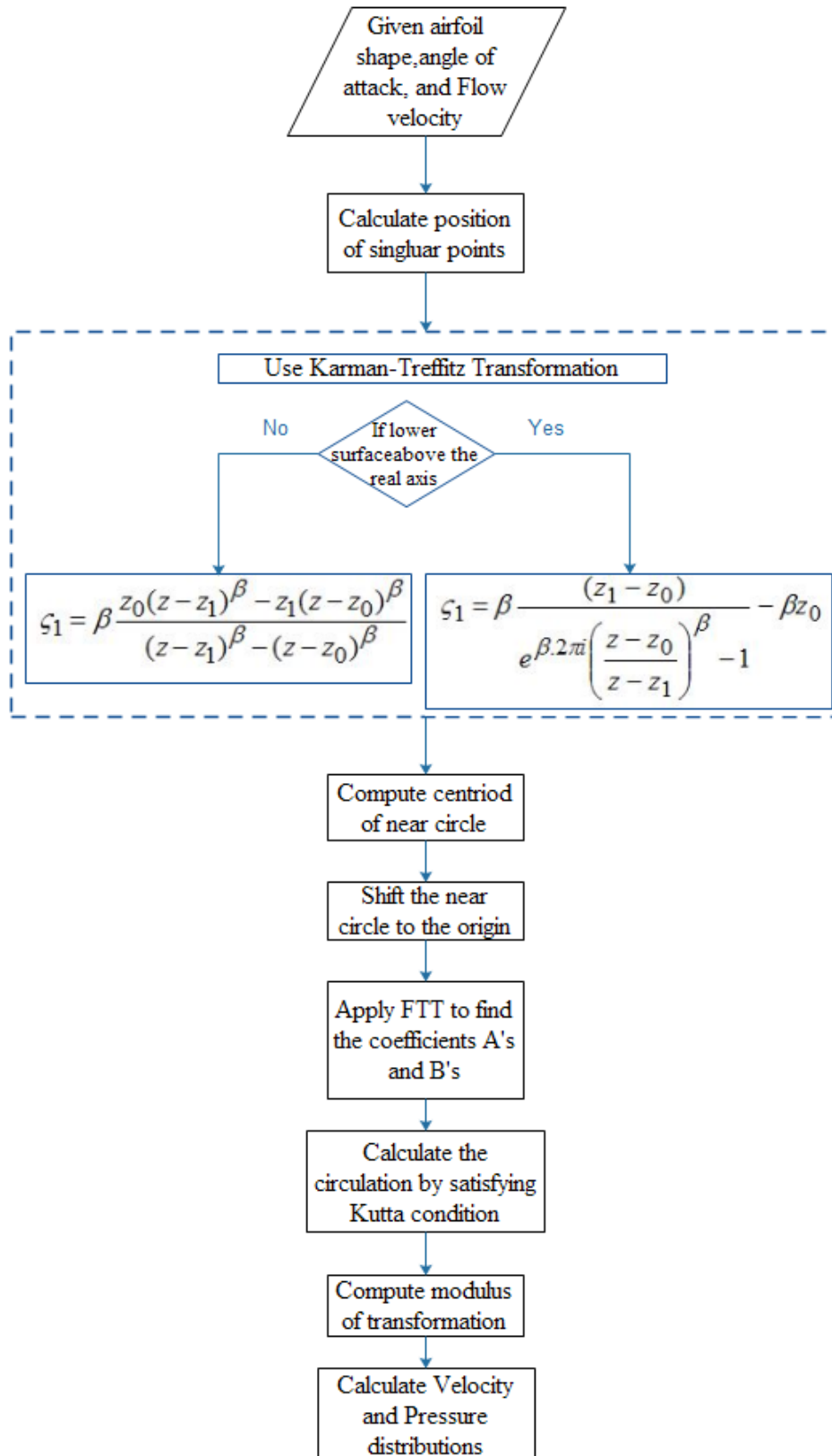


Figure 2.21 Flow chart for the method of calculation

CHAPTER 3

3 Boundary Layer Modeling

As already stated in chapter 2, the assumption of neglecting viscosity leads to two main flow equations with different levels of complexity. Neglecting viscosity results in calculation of pressure distribution and lift for airfoils with acceptable accuracy at low angles of attack, when flow is mostly staying stick to the wall. When angle of attack increases flow separates and inviscid assumption become less accurate. The other important point is the calculation of airfoil total drag which is not possible without considering boundary layer flow. Therefore, this chapter deals with flow inside boundary layer, The first part introduces main concept of boundary layer, and fundamental integral boundary layer equations. Important boundary layer phenomena of laminar, turbulent flow transitions, separations are discussed and the method of solution is also explained. Finally, verification of obtained results are presented.

The separation bubble which constitutes an important part of the boundary layer effort is left to next chapter.

3.1 Boundary Layer Concept

The boundary layer concept is related back to Ludwig Prandtl in 1904, who noted based on experimental work that a thin region exists close to the wall when a fluid passes over it. He divided the flow to two regions, one very close to the wall called boundary layer where all viscous effects occur. The second layer is inviscid where viscosity effects are negligible, as seen in Figure 3.1. The boundary layer is the thin region in which, a fluid velocity changes from zero at the wall $y = 0$ to potential flow value at boundary layer edge $y = \delta$. In this region the viscous force are comparably to inertia forces and thus the viscosity effects can't be neglected. Outside this region, $y > \delta$, the viscous effects can be assumed unimportant, and the flow can be analyzed as potential flow. The ratio of inertia forces to the viscous forces is called Reynolds number, defined as

$$Re = \frac{UL\rho}{\mu} \quad (3.1)$$

Prandtl derived the boundary layer equations, by simplifying the Navier-Stokes equations. The simplification is based on two main assumptions

- The boundary layer is thin compared to characteristic stream wise dimension of the body. $\frac{\delta}{L} \ll 1$ where L is the characteristic length of the body and δ is the distance from wall where the velocity equals the inviscid stream velocity.
- The highest viscous term must have same order of magnitude when compared with inertia term.

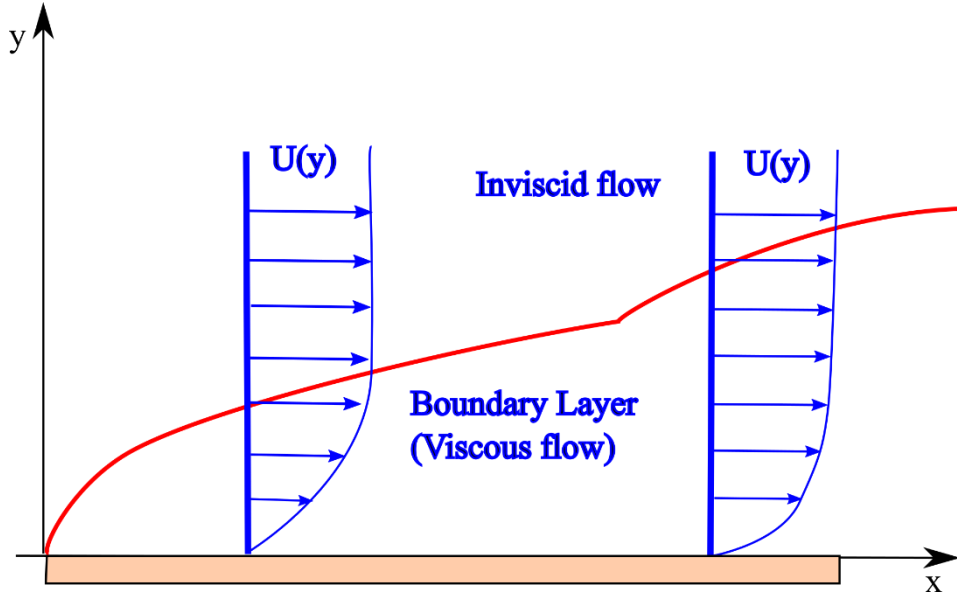


Figure 3.1 Boundary layer concept

It is also further assumed that the pressure change across the boundary layer is small and can be neglected. Thus the pressure on the wall (inside boundary layer) is assumed equal to that outside the boundary layer. Hence, the pressure is calculated using potential flow region laws as depending on stream wise distance x.

$$\frac{\partial U}{\partial t} + U \frac{\partial U}{\partial x} = -\frac{1}{\rho} \frac{\partial p}{\partial x} \quad (3.2)$$

If steady flow is assumed then the pressure is function of x only and the equation reduces to

$$U \frac{dU}{dx} = -\frac{1}{\rho} \frac{dp}{dx} \quad (3.3)$$

Prandtl's boundary layer equations for steady, two dimensional flow is given by the Eq.s (3.4) together with boundary conditions stated beneath. The first equation is continuity equation, and the second is momentum equation. The pressure term can be replaced with velocity from Eq.(3.3).

$$\frac{\partial u}{\partial x} + \frac{\partial v}{\partial y} = 0 \quad (3.4)$$

$$u \frac{\partial u}{\partial x} + v \frac{\partial u}{\partial y} = -\frac{1}{\rho} \frac{dp}{dx} + \nu \frac{\partial^2 u}{\partial y^2}$$

Acceleration Pressure Viscous
 Forces. Forces. Forces.

B.C. $u(x, 0) = 0, v(x, 0) = 0$ and $u(x, \delta) = U(x)$

Where ν is the viscosity of the fluid. u and v are components of velocity inside boundary layer in x, y directions, respectively, and p is the pressure at distance x , as calculated from potential flow.

3.2 Boundary layer separation

When a region of adverse pressure gradient exists along the flow, the fluid particles decelerate and cannot continue moving in forward direction. Thus a region of separated flow appears near the surface and the boundary layer deflects away from the wall into the main stream. Generally, fluid particles start to move in direction opposite to the external flow [25].

The separation point is defined by the condition when shear stress vanishes or mathematically when the slope of the velocity gradient at the wall in the normal direction equals zero. This is shown in Figure 3.2 . a region of reversed flow downstream of separation point.

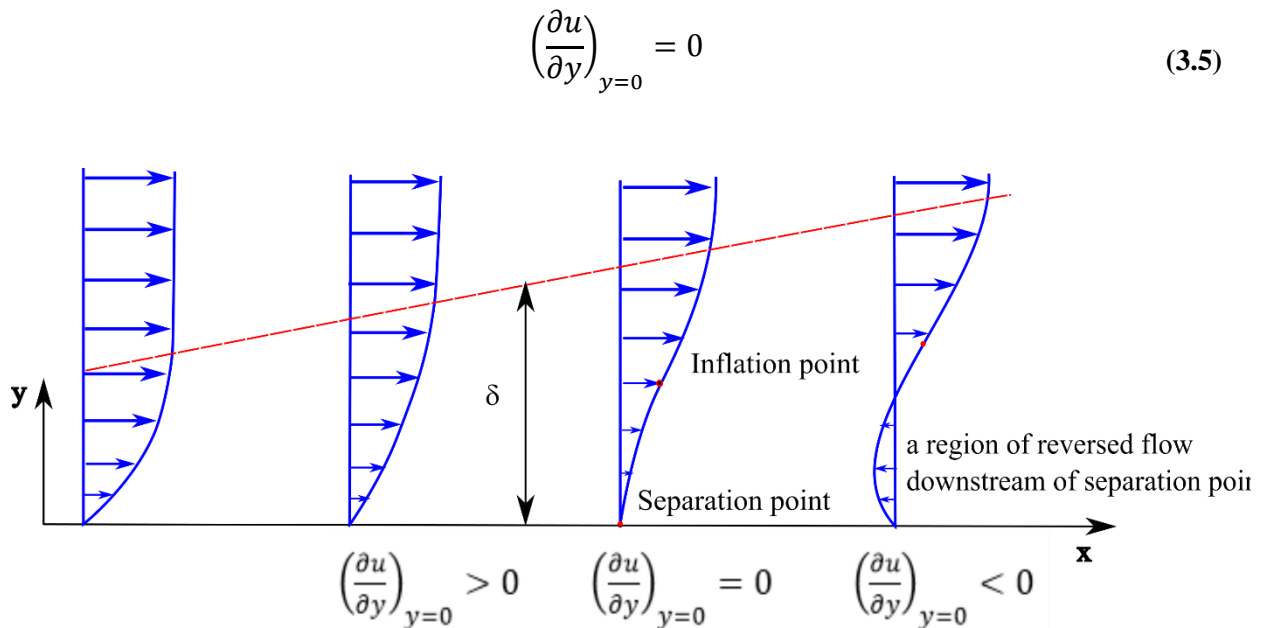


Figure 3.2 Separation of boundary layer, defined when the slope of the velocity gradient at the wall in the normal direction equals zero.

From Prandtl’s boundary layer equations Eq.(3.4), the left hand side of the second equation represents the acceleration of fluid particles in the flow. The pressure term will be negative if

$\frac{dp}{dx}$ is positive, i.e. if pressure increases with increasing x , thus the acceleration will be negative, which means that fluid particles will decelerate, and will have low momentum leading to separation as illustrated in Figure 3.3a.

For steady flows, the flow may separate only when the pressure increases with increasing x , i.e. only when $\frac{dp}{dx} > 0$ the flow separation is possible. If the pressure term is negative fluid particles will accelerate, hence no separation danger exists, Figure 3.3 b.

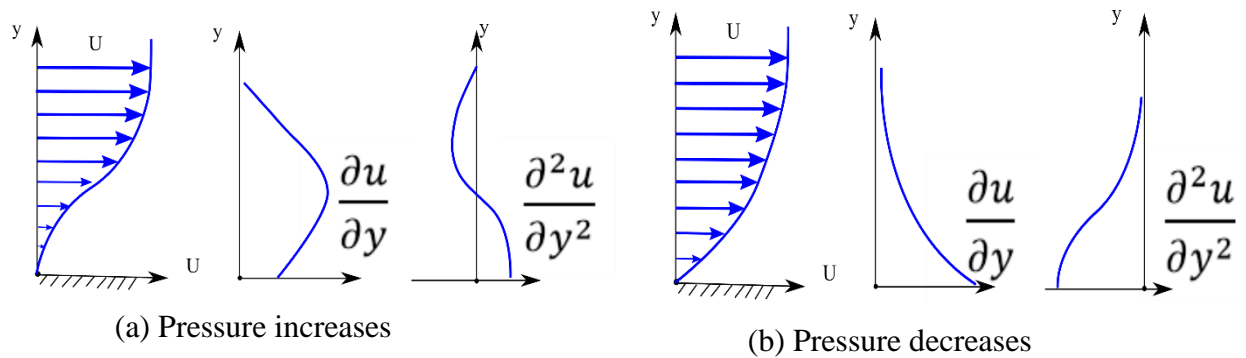


Figure 3.3 Velocity distribution in boundary layer at different pressure situations

Laminar boundary layer separations can occur, resulting in turbulent boundary layer. Turbulence adds shear stresses to the original viscous shear stress due to viscosity; the additional shear stresses are called Reynolds stresses. First consequence is that similar solutions in boundary layer are no longer true. Secondly, turbulence may start inside the separated laminar boundary layer. In this case, the separated shear layer may reach the airfoil surface and the turbulent flow may reattach again. The region formed after this process is called a laminar separation bubble (LSB). Laminar separation bubble is known to decrease lift and increase drag of airfoils, with higher degree as Reynolds number is decreased. Transition from laminar to turbulent may also occur without bubble formation. Figure 3.4, illustrates this possibility where airflows on upper and lower surfaces starting from stagnation point. Laminar boundary layer prolongs for some distance on both surfaces also. On upper surface the laminar boundary layer separates and flow moves away from the wall forming a circulatory region before it reattaches again as turbulent boundary layer. Attached turbulent flow continues until it separates totally from the airfoil surface. Turbulent separation eliminates the contribution of that portion of the surface from producing lift and produces more drag due to wake formation.

The lower surface experiences a different scenario. The laminar boundary layer become turbulent before it separates. This is called natural boundary layer transition. Turbulent flow continues until trailing edge without separation.

The locations on airfoil surface where boundary layer laminar separation, bubble transition, bubble reattachment, natural transition, and turbulent separation occur are very important airfoil flow features. They are sometimes called boundary layer features normally measured in wind tunnels and predicted by computational procedures. For instance, as turbulent separation point moves toward the airfoil's leading edge the lift decreases and the drag increases, airfoils may be designed based on this fact to maximize lift with smooth stall characteristics by optimizing turbulent separation point movement with angle of attack, or using other boundary layer feature. One example is given in reference [26].

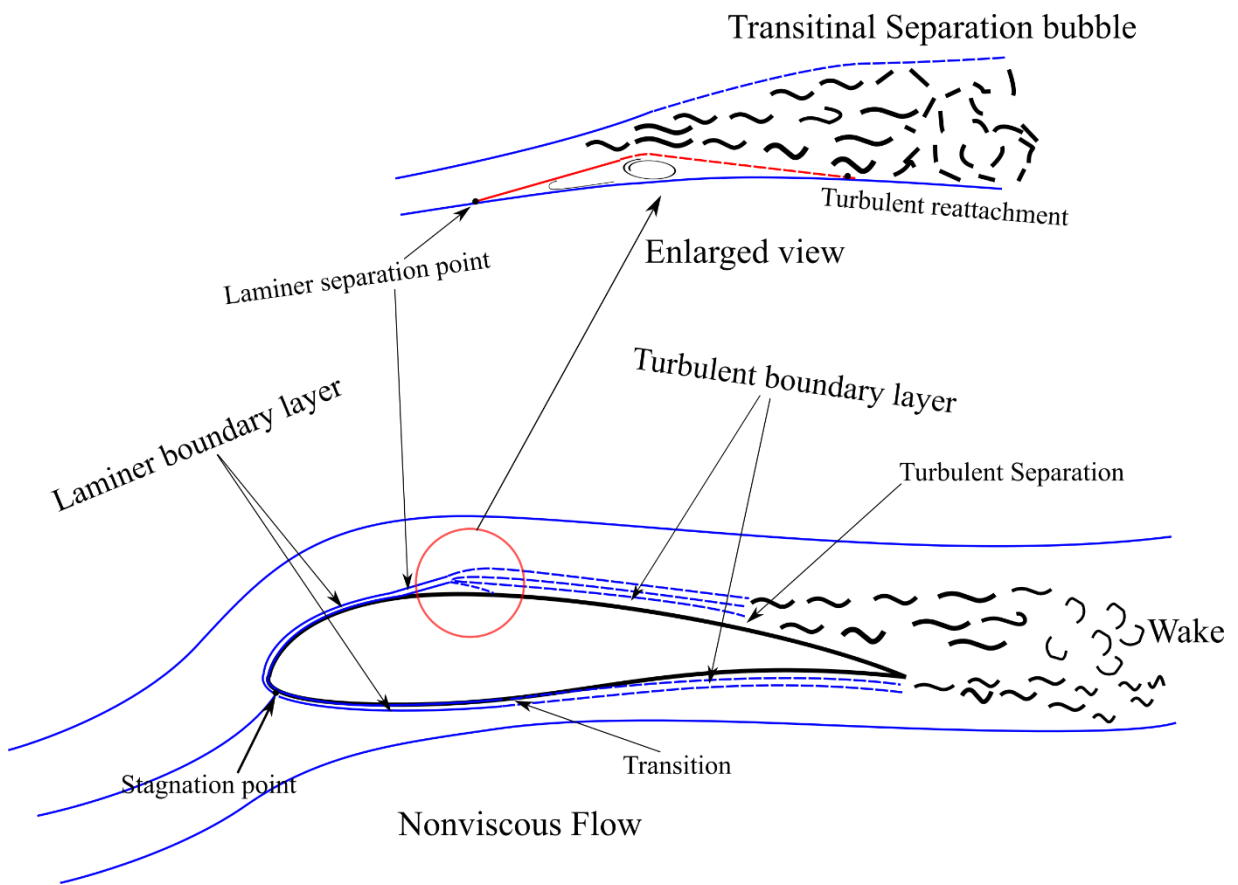


Figure 3.4 Boundary layer effects

3.3 Shear stress and friction drag

The shearing stress at the wall is defined as

$$\tau_0 = \mu \left(\frac{\partial u}{\partial y} \right)_{y=0} \quad (3.6)$$

The viscous drag is obtained from integrating shear stress over the body surface , as given by Eq. (3.7) and shown in Figure 3.5. Taking $dx = \cos\phi ds$ we get:

$$D_f = b \int_{x=0}^l \tau_0 \cos\phi ds = b \mu \int_{x=0}^l \left(\frac{\partial u}{\partial y} \right)_{y=0} dx \quad (3.7)$$

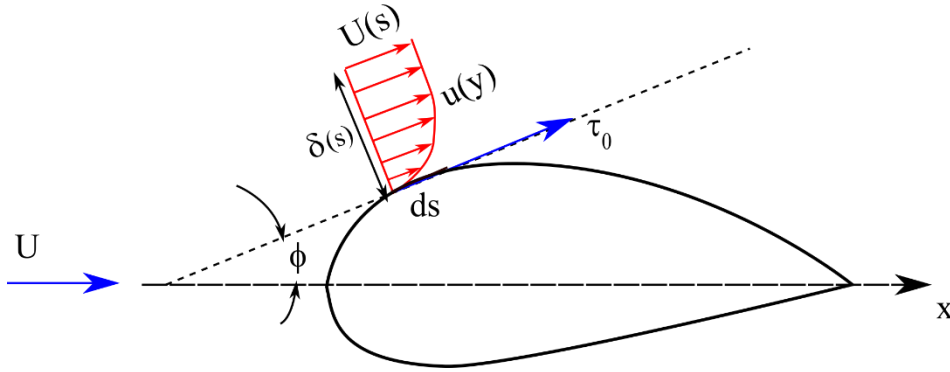


Figure 3.5 Viscous drag computation from shear stress

3.4 Boundary layer momentum and energy integral equations

For steady two dimensional incompressible flows, boundary layer momentum equations can be integrated with respect to y from the wall to some height h then, after substituting the wall shear stress from Eqn.(3.6) , one obtains:

$$\int_{y=0}^h \left(u \frac{\partial u}{\partial x} + v \frac{\partial u}{\partial y} - U \frac{dU}{dx} \right) dy = - \frac{\tau_0}{\rho} \quad (3.8)$$

From the continuity equation the velocity component $v = - \int_0^y \left(\frac{\partial u}{\partial x} \right) dy$, which upon substitution becomes

$$\int_{y=0}^h \left(u \frac{\partial u}{\partial x} - \frac{\partial u}{\partial y} \int_0^y \left(\frac{\partial u}{\partial x} \right) dy - U \frac{dU}{dx} \right) dy = - \frac{\tau_0}{\rho} \quad (3.9)$$

Integration by parts gives

$$\int_{y=0}^h \left(\frac{\partial u}{\partial y} \int_0^y \left(\frac{\partial u}{\partial x} \right) dy \right) dy = U \int_0^h \left(\frac{\partial u}{\partial x} \right) dy - \int_0^h u \left(\frac{\partial u}{\partial x} \right) dy \quad (3.10)$$

Substituting we get

$$\int_{y=0}^h \left(2u \frac{\partial u}{\partial x} - U \left(\frac{\partial u}{\partial x} \right) - U \frac{dU}{dx} \right) dy = -\frac{\tau_0}{\rho} \quad (3.11)$$

Rearranging

$$\int_{y=0}^h \frac{\partial}{\partial x} u(U - u) dy + \frac{dU}{dx} \int_0^h (U - u) dy = \frac{\tau_0}{\rho} \quad (3.12)$$

Introducing the definitions

Displacement thickness
$$\int_0^{\infty} (U - u) dy = \delta_1 U \quad (3.13)$$

Momentum thickness
$$\int_0^{\infty} u(U - u) dy = \delta_2 U^2 \quad (3.14)$$

The substitution of these two definitions results in Von Karman integral equations given by

$$\frac{\partial}{\partial x} (\delta_2 U^2) + \delta_1 U \frac{dU}{dx} = \frac{\tau_0}{\rho} \quad (3.15)$$

The energy integral equation is deduced by K. Wieghadt [100] for laminar boundary layer flow. It is obtained by multiplying the equations by u and integrating with respect to y , similarly to the above procedure;

$$\rho \int_{y=0}^{y=h} \left[u^2 \frac{\partial u}{\partial x} - u \frac{\partial u}{\partial y} \left(\int_0^y \frac{\partial u}{\partial x} dy \right) - u U \frac{dU}{dx} \right] dy = \mu \int_{y=0}^{y=h} \frac{\partial^2 u}{\partial y^2} dy \quad (3.16)$$

The second term is treated by integration by parts as

$$\rho \int_{y=0}^{y=h} \left[u \frac{\partial u}{\partial y} \left(\int_0^y \frac{\partial u}{\partial x} dy \right) \right] dy = \frac{1}{2} \int_{y=0}^{y=h} (U^2 - u^2) \frac{\partial u}{\partial x} dy \quad (3.17)$$

The first and third parts can be combined

$$\rho \int_{y=0}^{y=h} \left[u^2 \frac{\partial u}{\partial y} - uU \frac{dU}{dx} \right] dy = \frac{1}{2} \int_{y=0}^{y=h} u \frac{\partial}{\partial x} (u^2 - U^2) dy \quad (3.18)$$

After integration

$$\frac{\rho}{2} \frac{d}{dx} \int_{y=0}^{y=\infty} u(U^2 - u^2) dy = \mu \int_{y=0}^{y=\infty} \left(\frac{\partial u}{\partial y} \right)^2 dy \quad (3.19)$$

The term on the right side represents energy per unit volume and time, dissipated into heat. Introducing again the dissipation energy thickness δ_3 defined as

$$\text{Energy thickness} \quad \int_0^{\infty} u(U^2 - u^2) dy = \delta_3 U^3 \quad (3.20)$$

The energy integral equation can be written in the following form

$$\frac{d}{dx} (\delta_3 U^3) = 2\nu \int_0^{\infty} \left(\frac{\partial u}{\partial y} \right)^2 dy \quad (3.21)$$

Which is the energy integral equation for two dimensional laminar incompressible flow in the boundary layer. For turbulent flow this equation takes the form

$$\frac{d}{dx} (\delta_3 U^3) = 2 \int_0^{\infty} \frac{\tau}{\rho} \left(\frac{\partial u}{\partial y} \right) dy \quad (3.22)$$

3.4.1 Boundary layer integral approach

The boundary layer integral parameters are

$$\begin{aligned} \delta_1(x) &= \int_0^{\infty} \left(1 - \frac{u(x,y)}{U(x)} \right) dy \\ \delta_2(x) &= \int_0^{\infty} \frac{u(x,y)}{U(x)} \left(1 - \frac{u(x,y)}{U(x)} \right) dy \\ \delta_3(x) &= \int_0^{\infty} \frac{u(x,y)}{U(x)} \left[1 - \left(\frac{u(x,y)}{U(x)} \right)^2 \right] dy \end{aligned} \quad (3.23)$$

The displacement thickness $\delta_1(x)$ represents the displacement of boundary layer, and the momentum thickness $\delta_2(x)$ is related to the friction drag from stagnation point up to the position x . The energy thickness $\delta_3(x)$ is connected to the energy dissipation in the boundary layer. The boundary layer separates if velocity near the surface reverses direction. Using these parameters the integral equations are written as:

$$\frac{d\delta_2}{dx} + (\delta_1 + 2\delta_2) \frac{1}{U} \frac{dU}{dx} = c_f \quad (3.24)$$

Where U is potential flow velocity at location x , and c_f is skin friction coefficient and is given by

$$c_f = \frac{\tau_0}{\rho U^2} \quad (3.25)$$

The energy equation is also written as

$$\frac{d\delta_3}{dx} + 3\delta_3 \frac{1}{U} \frac{dU}{dx} = c_D \quad (3.26)$$

Where c_D is the dissipation coefficient given by

$$c_D = \frac{2}{\rho U^3} \int_0^\infty \tau \frac{\partial u}{\partial y} dy \quad (3.27)$$

If the ratios of the local parameters are also defined as

$$H_{12} = \frac{\delta_1}{\delta_2} \quad \text{and} \quad H_{32} = \frac{\delta_3}{\delta_2} \quad (3.28)$$

3.4.2 Laminar boundary layer

The solution method for laminar boundary layer is based on the statement that H_{12} and H_{32} are only function of one parameter. Thus H_{12} , ϵ , and D can be expressed as function of the shape parameter H_{32} . The following relations hold for skin friction coefficient and dissipation coefficient, respectively.

$$c_f = \frac{\epsilon^*(H_{32})}{Re U \delta_2'} \quad (3.29)$$

$$c_D = \frac{2D^*(H_{32})}{Re U \delta_2'} \quad (3.30)$$

Where $\epsilon^*(H_{32})$ and $D^*(H_{32})$ are given functions of the shape parameter H_{32} . The Reynolds number based on boundary layer momentum thickness is defined as

$$\text{Re}_{\delta_2} = \frac{U \delta_2}{\nu} = U \delta_2 \text{Re} \quad (3.31)$$

Noting that in dimensionless form of chord based Reynolds number $\text{Re} = \frac{1}{\mu}$. Where the reference velocity is V_∞ the reference length is the chord c , and the reference density is ρ_∞ . [27].

The relation for H_{12} , ϵ^* , and D^* are given by the following equations as described by Eppler works in references [9], and [27] through [30],

$$\begin{aligned} H_{12} = & 4.02922 - (583.60182 - 724.5591H_{32} \\ & + 227.18220H_{32}^2)\sqrt{H_{32} - 1.51509} \\ & \text{If } H_{32} < 1.57258 \end{aligned} \quad (3.32)$$

$$H_{12} = 79.80845 - 89.58214 H_{32} + 25.715786 H_{32}^2) \quad \text{If } H_{32} > 1.57258$$

$$\begin{aligned} \epsilon^* = & 2.512589 - 1.686096 H_{12} + 0.391541 H_{12}^2 + 0.031729 H_{12}^3 \\ & \text{If } H_{32} < 1.57258 \\ \epsilon^* = & 1.372391 - 4.226253 H_{32} + 2.221687 H_{32}^2) \quad \text{If } H_{32} > 1.57258 \end{aligned} \quad (3.33)$$

$$D^* = 7.853976 - 10.260551 H_{32} + 3.418898 H_{32}^2 \quad (3.34)$$

Equations (3.24) and (3.26) are coupled ordinary differential equations, which is solved by numerical integration for δ_2 and δ_3 from which the shape factors H_{32} and H_{12} are also calculated. Skin friction coefficient c_f and dissipation coefficient c_D can be obtained from the calculation using the above equations. The velocity U and it's derivative U' are imposed by the potential flow.

$$\delta_2' + (H_{12} + 2) \frac{\delta_2 U'}{U} = c_f \quad (3.35)$$

$$\delta_3' + 3 \delta_3 \frac{U'}{U} = c_D \quad (3.36)$$

The shape factor $H_{32} = 1.51509$ specifies laminar separation. If the velocity U is constant the value of the shape factor H_{32} is greater than 1.57258 .

The initial values of solution is given by the Eq. (3.37) [27], which corresponds to the first step of Δx after the stagnation point , where the value 1.61998 is the value of the parameter H_{32} at stagnation condition.

$$\delta_2(\Delta x) = 0.29004 \sqrt{\frac{\Delta x}{Re U(\Delta x)}} , \quad \delta_3 = 1.61998 \delta_2 \quad (3.37)$$

From which the initial value of the shape parameter in case when boundary layer starts from stagnation point is given by $H_{32} = 1.61998$.

3.4.3 Turbulent boundary layer

The same differential equations can be used for turbulent boundary layer. The relations between the δ_2 and δ_3 and, c_f and c_D are given by [27]:

$$H_{12} = \frac{11 H_{32} + 15}{48 H_{32} - 59} \quad (3.38)$$

$$c_f = 0.045716[(H_{12} - 1) Re U \delta_2]^{-0.232} e^{-1.26 H_{12}} \quad (3.39)$$

$$c_D = 0.0100[(H_{12} - 1) Re U \delta_2]^{-1/6} \quad (3.40)$$

These relations are derived for Reynolds number range from $10^3 < Re U \delta_2 < 10^5$ using empirical and semi-empirical investigations of turbulent boundary layer done by Ludwig-Tillmann. As argued in [27] it is also applicable to outside of upper range but for the lower range it should be investigated.

Turbulent separation, in this approach, is hardly related to a fixed value of the shape factor H_{32} . It is certainly known that for $H_{32} > 1.58$ there will be no turbulent separation and for values of $H_{32} < 1.46$ there will be for sure turbulent separation. In the calculations the turbulent separations is assumed to occur at $H_{32} = 1.46$ because it is more reliable for thick boundary layers, where separations is expected to happen.

It is known that turbulent boundary layer separation depends on Reynolds number, such that separation occurs later if Reynolds number increases. Laminar boundary layers separates in much shallower adverse pressure gradient as compared to turbulent boundary layer.

The friction drag caused by laminar boundary layers is much less than that of turbulent boundary layer. For these reasons transition from laminar to turbulent is important issue.

3.5 Boundary layer transition

Laminar boundary layer separates in mild pressure gradients for which turbulent boundary layers can resist and stay attached. Skin friction drag, on the other hand, is higher for turbulent boundary layer. It is a compromise between laminar boundary layer where skin friction drag is smaller but separation risk is higher and turbulent boundary layer where skin friction drag is higher with higher separation resistance.. Boundary layer starts usually laminar and then disturbances grow until it become either separated (laminar separation) or it become turbulent through either transition (forced or natural transition) or transitional separation bubble. The LSB becomes more important as Reynolds number is lowered.

Boundary layer transition is connected with stability of so called Tollmien-Schlichting waves. This stability is function of local Reynolds number based on boundary layer momentum thickness δ_2 , Re_{δ_2} which is, defined by Eq.(3.31) repeated here for convenience.

$$Re_{\delta_2} = \frac{U \delta_2}{\nu} = U \delta_2 Re$$

There exists a critical value of Re_{δ_2} below which no wave will be amplified. This critical local Reynolds number Re_{δ_2} depends in turn on local velocity profile. Local velocity profiles without inflection points (which occur normally with favorable pressure gradients) have higher values of Re_{δ_2} and thus have later transition. In contrast, velocity profiles with inflection point have lower values of Re_{δ_2} which make transition more likely to happen in flow areas where separation risk is higher. The velocity profile itself is assumed to be function only of the shape parameter H_{32} .

There are two general methods for transition analysis. The first method is based on analysis of amplification of Tollmien-Schlichting waves which assumes transition when one of the waves amplifies to the value of e^N . Where N is a specified critical number usually around 10 and depends on turbulence level in wind tunnels or flight test measurements. Drela [31] developed a method based on amplification envelopes and implemented it in XFOIL code, this criteria will discussed in next section.

The second method is empirically derived transition criteria based on local boundary layer parameters. The transition criterion adopted in this work is the one given in Eppler works. It is used to predict transition when no laminar separation occurs. If laminar separation is detected Drela method is invoked in the code.

Equation (3.41) which depends on local values of shape factor H_{32} , which represent velocity profile shape, local Reynolds number based on δ_2 , and on roughness factor r . The

roughness factor r may vary from 0 for theoretically very smooth surface to 6 which represents a highly turbulent air.

$$\ln Re_{\delta_2} \geq 18.4 H_{32} - 21.74 + 125 (H_{32} - 1.573)^2 - 0.36 r \quad (3.41)$$

This criterion is plotted on Figure 3.6 for different roughness r . Higher values of roughness factor r shifts the curve down which means transition will occur earlier.

Transition is assumed to occur if this criterion is satisfied (area above any red dashed curve). Flow starts from stagnation point at $H_{32} = 1.62$ as shown and as flow develops the shape factor H_{32} decreases and Re_{δ_2} increases toward either transition curve (red dashed) or laminar separation line (blue broken) depending boundary layer development calculations. If the transition criteria is reached first the calculations switches from laminar closure correlations Eq.(3.32) through Eq.(3.34) to turbulent correlations Eq.(3.38) through Eq.(3.40). Furthermore, if the laminar separation line is attained first a laminar separation bubble calculations are required. The next section discusses main laminar bubble features and addresses its effects on airfoil characteristics. Details of adopted LSB molding is discussed in chapter 5.

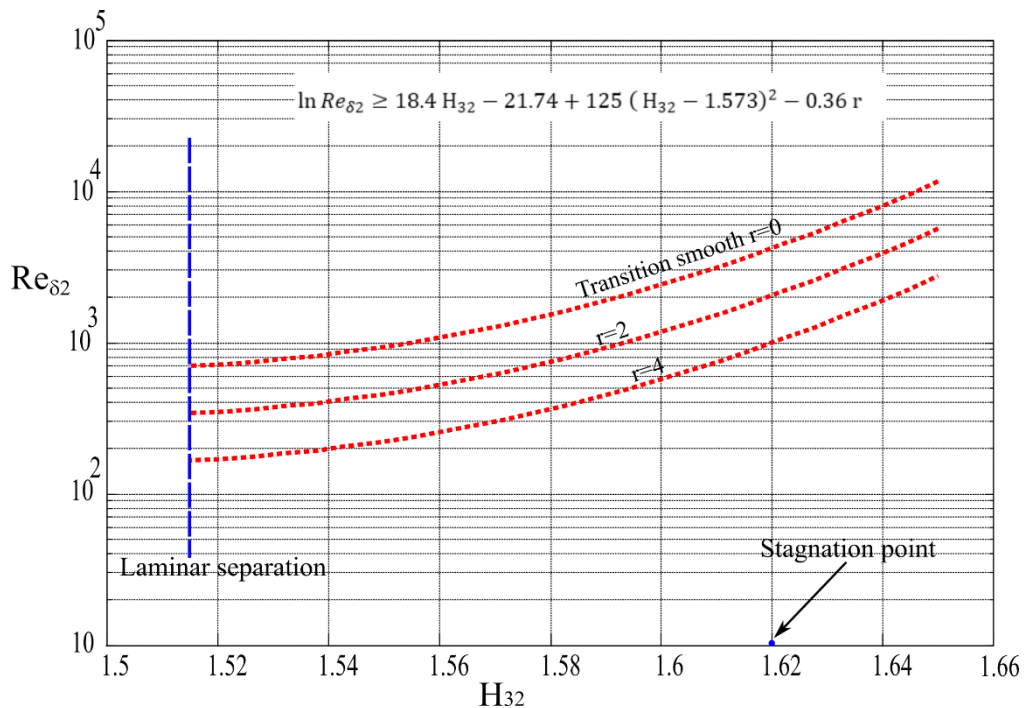


Figure 3.6 Eppler Transition criteria for different roughness factor values

3.6 Laminar separation bubble

As stated previously, transition could occur through laminar separation bubble, called sometimes laminar transitional bubble because it acts as a mechanism for transition from laminar to turbulent flow. Laminar separation bubble happens when laminar flow separates before transition criteria is reached and flow under goes a transition to turbulent in the separated shear layer, as illustrated in Figure 3.7. Now turbulent flow has higher momentum to resist adverse pressure gradients therefore it reattaches again to the surface after some distance along the airfoil chord. The distance from separation point to reattachment is called bubble length L_B and the distance from separation to transition is called transition length L_T where flow is still treated as laminar. Between transition location and reattachment point with length of L_R the flow is turbulent and there is a considerable velocity change in this region. The velocity profile at laminar separation point and at reattachment point is defined for the value of shape factor $H_{32} = 1.51509$ which corresponds to zero shear stress, as shown in Figure 3.7.

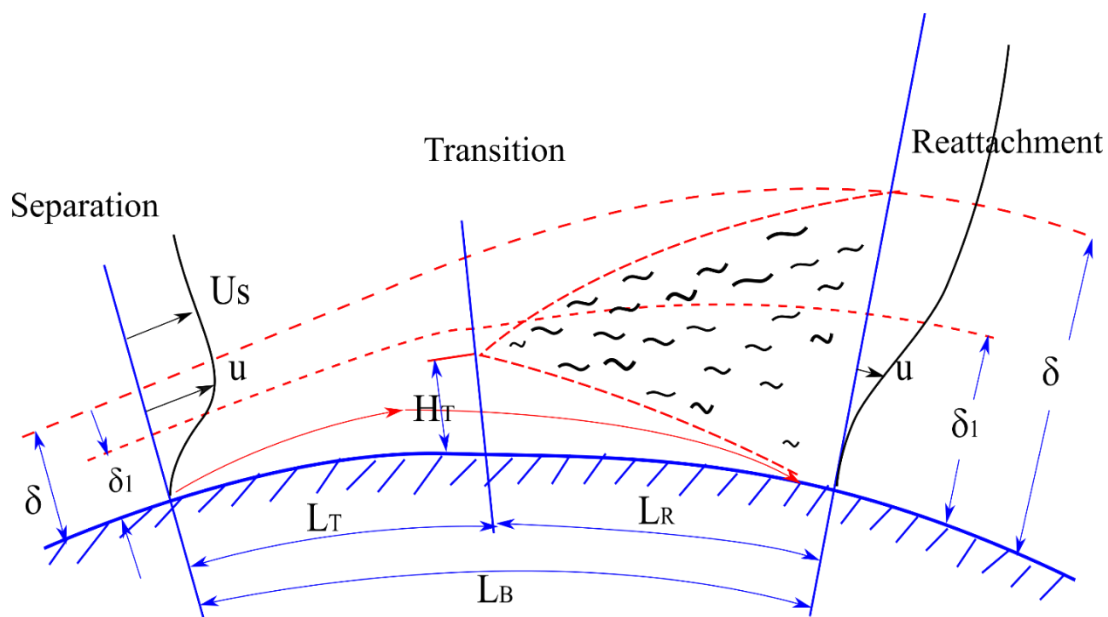


Figure 3.7 Sketch of laminar separation bubble

The main effects of laminar separation bubble are:

(a) Potential flow velocity distribution is modified by the bubble as shown in Figure 3.8 which suggested by Tani [34]. The solid lines represent velocity distribution without bubble, and the dashed lines represent the modified velocity. From the separation point S to transition point T the velocity is nearly constant $U_B(x)$, which drops from this value to the intersection with the solid curve at reattachment. In some cases it was experimentally observed by Dini in

[35] and [36] that the reattachment occur with undershoot until the velocity distribution merges with viscous distribution without bubble. For longer bubbles this velocity distribution is modified along the bubble length and affects the entire airfoil surface. As Reynolds number is decreased the first part of the bubble L_T increases in length.

(b) Thickness of separation bubble H_T is shown in Figure 3.7 and it is an important factor which indicates whether the reattachment will occur or not. It depends on the length L_T . It is also affected by the potential flow pressure gradient in the region of the bubble. This fact was studied by Gaster [37] who suggested a non-dimensional parameter P . This parameter is given by

$$P = \frac{\delta_{2s}^2 \Delta U_B^*}{\nu L_B} \tag{3.42}$$

Where δ_{2s} is the value the boundary layer momentum thickness at separation point. ΔU_B^* which is the velocity drop along the bubble above which no reattachment can occur. This drop in velocity is equivalent to adverse pressure gradient in the region after separation point $\frac{dU}{dx}$, this slope depends on the angle of attack being higher for greater angles of attack α , thus bubble thickness increase with increased angle of attack and decreases as angle of attack decreases. Furthermore, the location of separation point depends on angle of attack being more toward the leading edge for higher angles of attack. Therefore, in order to decrease bubble effects on airfoil performance, it is possible to decrease the operating angle of attack.

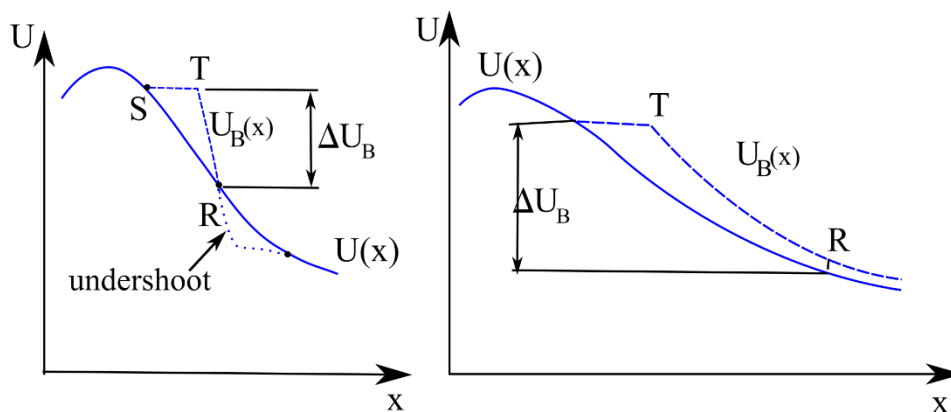


Figure 3.8 Effect of separation bubble on velocity distribution

3.7 Eppler's Bubble prediction method

This method is based on predicting the distance from laminar separation to the point when the shape factor H_{32} increases to a value of about 1.6. At $H_{32} = 1.6$ reattachment is assumed. A warning is issued if a bubble exists and its effect on drag is not included.

When the turbulent boundary layer starts after either laminar separation or transition criteria is reached the turbulent closure relations are directly evoked to solve the same differential equations. When Separation happens at $H_{32} = 1.5151$ the shape factor then increases to higher values following the turbulent closure relations. As shown in Figure 3.9, if the condition given by the equation is satisfied then a bubble warning is issued.

$$1 - \frac{\Delta U_B}{U_s} < 0.958 \quad (3.43)$$

Where U_s the value of potential flow velocity at the laminar separation point, and ΔU_B is the difference between the value of potential flow velocity at separation and reattachment points.

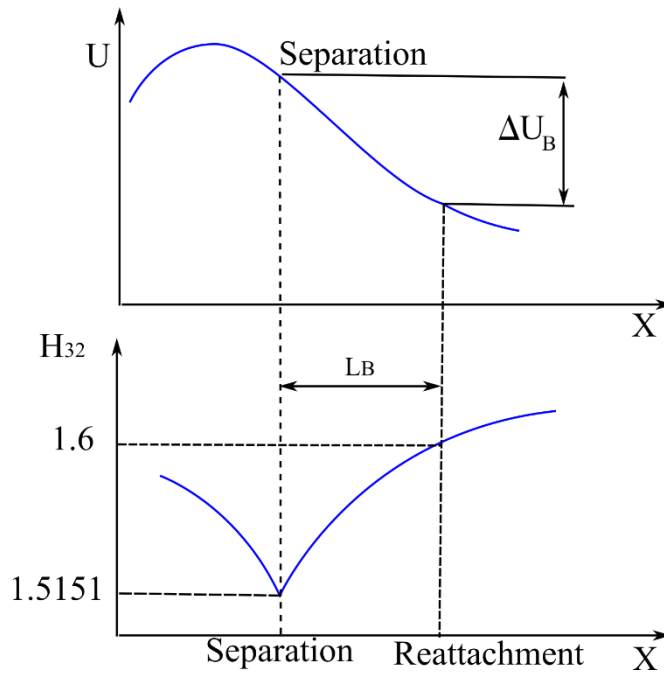


Figure 3.9 Eppler's bubble analogy

3.8 Lift, drag and moment

From the potential flow analysis an inviscid pressure distribution $p(s)$ can be obtained and from the boundary layer calculations shear stress distribution $\tau(s)$ is also obtained. These two distributions constitute the main sources of all forces and moments affecting airfoil at

given flow conditions. Their integration over the surface produces the resultant force \vec{R} and moment \vec{M} which can be resolved into lift and drag. This reference frame is shown in Figure 3.10 where the pressure distribution acts normal to the surface while the shear stress acts in the tangent direction. The starting point is chosen at the leading edge which normally different than stagnation point where boundary layer calculation begins.

The Resultant force is resolved into two coordinate axis systems (1) body axis system as normal N and axial A . (2) wind (aerodynamic) axis system as lift L and drag D . the angle between them is angle of attack α . The relation between these two frames is given by

$$\begin{aligned} L &= N \cos \alpha - A \sin \alpha \\ D &= N \sin \alpha + A \cos \alpha \end{aligned} \tag{3.44}$$

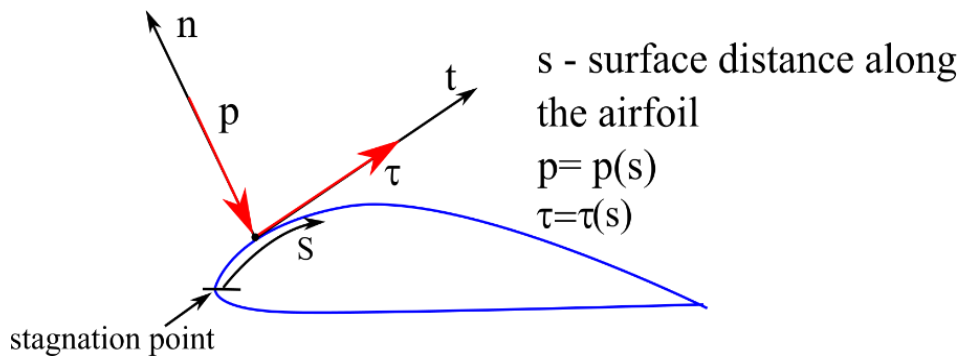


Figure 3.10 Sign conventions for pressure and shear stress

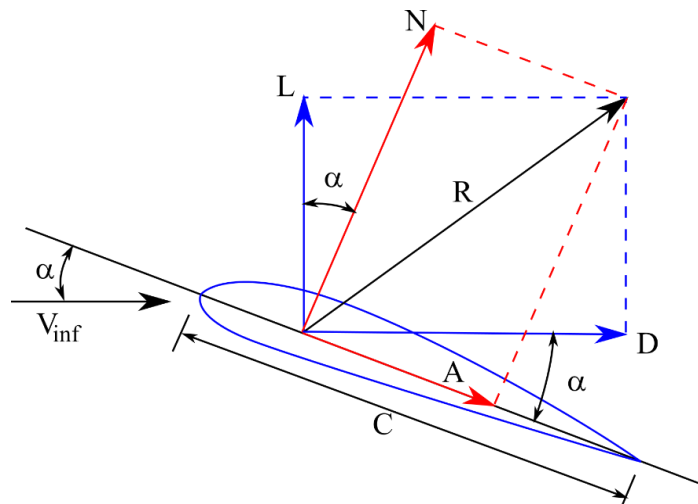


Figure 3.11 Body and wind axis systems

3.8.1 Integration of pressure and shear stress distributions

If an airfoil of unit span [32] as shown in Figure 3.10 is considered. The integration of pressure and shear stress is performed from leading edge to trailing edge as follows:

For small element of surface length ds on the upper surface, there are normal and axial elemental forces dN and dA respectively given as

$$\begin{aligned} dN_u &= -p_u ds_u \cos \theta - \tau_u ds_u \sin \theta \\ dA_u &= -p_u ds_u \sin \theta + \tau_u ds_u \cos \theta \end{aligned} \quad (3.45)$$

For the lower surface

$$\begin{aligned} dN_l &= -p_l ds_l \cos \theta - \tau_l ds_l \sin \theta \\ dA_l &= -p_l ds_l \sin \theta + \tau_l ds_l \cos \theta \end{aligned} \quad (3.46)$$

The normal force N and axial force A can be obtained from

$$N = - \int_{LE}^{TE} [p_u \cos \theta + \tau_u \sin \theta] ds_u + \int_{LE}^{TE} [p_l \cos \theta + \tau_l \sin \theta] ds_l \quad (3.47)$$

$$A = - \int_{LE}^{TE} [-p_u \sin \theta + \tau_u \cos \theta] ds_u + \int_{LE}^{TE} [p_l \sin \theta + \tau_l \cos \theta] ds_l \quad (3.48)$$

The moment can be obtained in similar manner, keeping in mind sign convention when the reference point is the leading edge is positive when increasing angle of attack, and using the non dimensional coefficients the following working form is obtained, $dy = -ds \sin \theta$ and $dx = ds \cos \theta$ and reference area S and c is the airfoil chord.

$$C_N = \frac{1}{c} \left[\int_0^c (C_{pl} - C_{pu}) dx + \int_{LE}^{TE} (C_{fu} - C_{fl}) dy \right] \quad (3.49)$$

$$C_A = \frac{1}{c} \left[\int_{LE}^{TE} (C_{pu} - C_{pl}) dy + \int_0^c (C_{fu} - C_{fl}) dx \right] \quad (3.50)$$

$$\begin{aligned} C_{m@LE} = \frac{1}{c^2} \left[\int_0^c (C_{pu} - C_{pl}) x dx - \int_{LE}^{TE} (C_{fu} - C_{fl}) x dy + \int_{LE}^{TE} (C_{pu} - C_{pl}) y dy + \right. \\ \left. \int_0^c (C_{fu} - C_{fl}) y dx \right] \end{aligned} \quad (3.51)$$

From which the aerodynamic coefficients c_l and c_d are obtained with the equations:

$$\begin{aligned} c_l &= c_N \cos \alpha - c_A \sin \alpha \\ c_d &= c_N \sin \alpha + c_A \cos \alpha \end{aligned} \quad (3.52)$$

3.8.2 Lift Drag Moment corrections

When viscous separations are present these coefficients are corrected by using Eppler method [28], as follows: Total drag coefficient is calculated from boundary layer solution data evaluated at trailing edge using Squire and Young formula [33] which is modified for high values of H_{12} which was found to produce better results. And also corrected when separations exists [27].

$$C_d = \begin{cases} 2 \delta_{2TE} \left(\frac{U_{TE}}{V_\infty} \right)^{\frac{5+H_{12}^*}{2}} & \text{for } U_s < V_\infty \\ 2 \delta_{2sep} \left(\frac{U_s}{V_\infty} \right)^{3.75} \left(\frac{U_s}{U_{TE}} \right)^{0.15} & \text{for separated flow} \end{cases} \quad (3.53)$$

Where

$$H_{12}^* = \begin{cases} H_{12TE} & \text{for } H_{12} \leq 2.5 \\ 2.5 & \text{for } H_{12} > 2.5 \end{cases} \quad (3.54)$$

Equation (3.53) when applied to each surface results in drag due to that surface. The sum of upper and lower surfaces results in total drag on airfoil.

The greatest effect on aerodynamic comes from boundary layer separation than that from boundary layer thickness. Thus when high separations exists on upper surface lift coefficient corrections are applied in which angle of attack is modified. The lift coefficient correction is computed based on the separated distance S_{sep} travelled by air on the surface which is used to find out the angle of attack correction.

$$\Delta\alpha = -\frac{S_{sep}}{2c} (\delta_{us} + \alpha_c) \quad (3.55)$$

Where, δ_{us} is the slope of the upper surface at the area close to trailing edge, and α_c is the angle of attack relative to chord line, as shown in Figure 3.12. Lift coefficient is modified for the upper and lower surfaces using the Eq.(3.56) . The lift correction on upper surface is always negative and always positive for the lower surface, so lift is reduced in both cases.

$$\Delta c_l = 2 \pi \Delta\alpha \quad (3.56)$$

The moment coefficient is also corrected in similar manner using the relation

$$\Delta c_m = -\frac{1}{4} \Delta c_l \left(1 - \frac{S_{sep}}{c} \right)^{1.5} \quad (3.57)$$

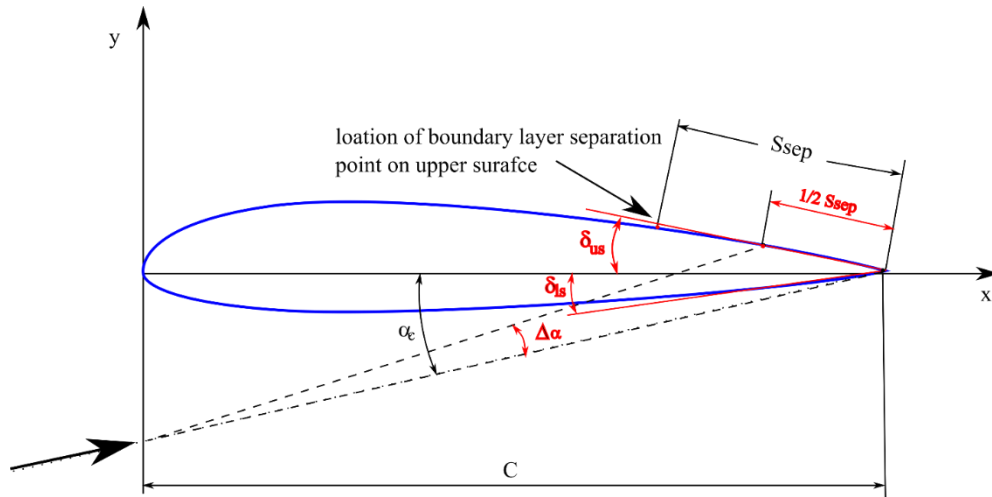


Figure 3.12 Lift and moment corrections due to boundary layer separation

3.9 Comparison of turbulent closure relations

The calculation of turbulent boundary layer using two Von Karman momentum and energy equations, with five unknowns, namely $\delta_1, \delta_2, \delta_3, C_f$, and C_D , additional closure relations are required. For turbulent boundary layer, Drela has developed a shape factor relations [31]. One important parameter is the dissipation coefficient C_D , which depends on the distribution of Reynolds stresses in the boundary layer. The Reynolds stresses in turn depend on the upstream conditions. In order to take into account these effects Drela used Greens lag equation to calculate the maximum shear stress coefficient. $C_{\tau_{max}}$ from which the dissipation coefficient C_D is computed. An additional differential equation is thus, added to the two Von Karman integral boundary layer equations. This equation has the form:

$$\frac{\delta}{C_{\tau_{max}}} \frac{dC_{\tau_{max}}}{ds} = 5.6 * \left(\sqrt{C_{\tau_{max}|eq}} - \sqrt{C_{\tau_{max}}} \right) + 2\delta \left[\frac{4}{3\delta_1} \left(\frac{c_f}{2} - \left(\frac{H_{12} - 1}{6.7H_{12}} \right)^2 \right) - \frac{1}{U_e} \frac{dU_e}{ds} \right] \quad (3.58)$$

It is worth to note that these models are modified from time to time and there exists different forms of the equations and coefficients. For example the above equation only the first term is used by Dini [35] with a coefficient of 4.2 instead of 5.6.

In the rest of this section a comparison is shown between Drela as presented by Dini , modified Drela as presented by Lutz and Wagner [38], and finally Lutz & Wagner model. All these models are derived for incompressible turbulent boundary layer flows. Eppler's model is independent of Re_{δ_2} and presented here for reference. It can be seen that at high local Reynolds number of 5000, Figure 3.13 ,the three models match and produce same results. As the local Reynolds number based on momentum thickness is decreased to about 400 – 275 the

Drela model separates from other models and still produce same results, as shown of Figure 3.14 and Figure 3.15. Further decrease of Re_{δ_2} to about 200 - 100 Drela models produce different results and even deviate from the known limit, as seen on Figure 3.16 and Figure 3.17 and supported by Lutz and Wagner work , Figure 3.18.

As a conclusion the above presented Drela models should not be used in low Re_{δ_2} range below about 400. Lutz and Wagner seem to produce acceptable results at this range of local Reynolds number.

3.9.1 Eppler turbulent model:

The relations between the δ_2 and δ_3 and, c_f and c_D are given by Eppler, These relations does not depend on Re_{δ_2} .

$$H_{12} = \frac{11 H_{32} + 15}{48 H_{32} - 59} \quad (3.59)$$

$$c_f = 0.045716[(H_{12} - 1) \text{Re } U \delta_2]^{-0.232} e^{-1.26 H_{12}} \quad (3.60)$$

$$c_D = 0.0100[(H_{12} - 1) \text{Re } U \delta_2]^{-1/6} \quad (3.61)$$

3.9.2 Drela Turbulent closure

Following Dini because of completeness of expressions and report,

$$\frac{\delta}{C_{\tau max}} \frac{dC_{\tau max}}{ds} = 4.2 * \left(\sqrt{C_{\tau max}|_{eq}} - \sqrt{C_{\tau max}} \right) \quad (3.62)$$

The maximum shear stress is for equilibrium state is obtained using

$$C_{\tau max}|_{eq} = \frac{0.015 H_{32}}{1 - U_{slip}} \left[\frac{H_{12} - 1}{H_{12}} \right]^3 \quad (3.63)$$

The value of δ , is given by the equation

$$\delta = \delta_2 \left(3.15 + \frac{1.72}{H_{12}-1} \right) + \delta_2 \quad (3.64)$$

The closure relation

$$C_D = f \cdot CD_{Drela} \quad (3.65)$$

Where

$$f = \begin{cases} 1 + (CD_{max} - 1) \left(\frac{s-s_\tau}{l_2}\right)^2 & \text{for } 0 \leq \frac{s-s_\tau}{l_2} \leq 1 \\ 1 + (CD_{max} - 1)e^{-r\left(\frac{s-s_\tau}{l_2}-1\right)} & \text{for } \left(\frac{s-s_\tau}{l_2}\right) > 1 \end{cases} \quad (3.66)$$

$$r = 15 - 1000 \frac{h_\tau}{c} \quad (3.67)$$

$$CD_{max} = 1. + \sqrt{200 \frac{h_\tau}{c}} \quad (3.68)$$

$$CD_{Drela} = C_f U_{slip} + 2C_\tau(1 - U_{slip}) \quad (3.69)$$

$$U_{slip} = \frac{H_{32}}{6} \left[\frac{4}{H_{12}} - 1 \right] \quad (3.70)$$

$$H_{12} = \frac{H_{120}}{1 + \left[\frac{H_{32} - H_{320}}{c_1} \right]^{1.27}} \quad \text{for } C_f > 1 \quad (3.71)$$

$$H_{12} = H_{120} + \left[\frac{H_{32} - H_{320}}{c_2} \right]^{1/3} \quad \text{for } C_f < 1$$

Where

$$H_{320} = 1.505 + \frac{4}{Re_{\delta_2}} \quad (3.72)$$

$$H_{120} = 3 + \frac{400}{Re_{\delta_2}} \quad (3.73)$$

$$c_1 = 0.081 (Re_{\delta_2} - 300)^{0.1} \quad (3.74)$$

$$c_2 = 0.0158(Re_{\delta_2} - 300)^{0.08} \quad (3.75)$$

$$c_3 = 1.06 + \frac{3000}{(Re_{\delta_2} + 600)^{1.5}} \quad (3.76)$$

$$C_{fmin} = -\sqrt{.0002 \frac{h_\tau}{c}} \quad (3.77)$$

3.9.3 Modified Drela model used by LUTZ and Wagner [38]

$$H_{32} = 1.505 + \frac{4}{Re_{\delta_2}} + \left(0.165 - \frac{1.6}{\sqrt{Re_{\delta_2}}}\right) \frac{(H_{120} - H_{12})^{1.6}}{H_{12}} \quad \text{for } H < H_0 \quad (3.78)$$

Where

$$H_{120} = 3 + 400/Re_{\delta_2} \quad (3.79)$$

3.9.4 Lutz and Wagner model

This model is published in [38] , and they claimed that it produces good results compared with Drela model at low local Reynolds number, such that H_{12} is always greater than 1.

$$H_{12} = k - \sqrt{k^2 - H_{120}^2} \quad \text{for } H_{12} < H_{120} \quad (3.80)$$

$$k = H_{120} + \frac{H_{32} - H_{320}}{2(2 - H_{320})} (H_{120} - 1)^2 \quad (3.81)$$

$$H_{320} = 1.505 + \frac{4}{Re_{\delta_2}} \quad H_{120} = 3 + 400/Re_{\delta_2} \quad (3.82)$$

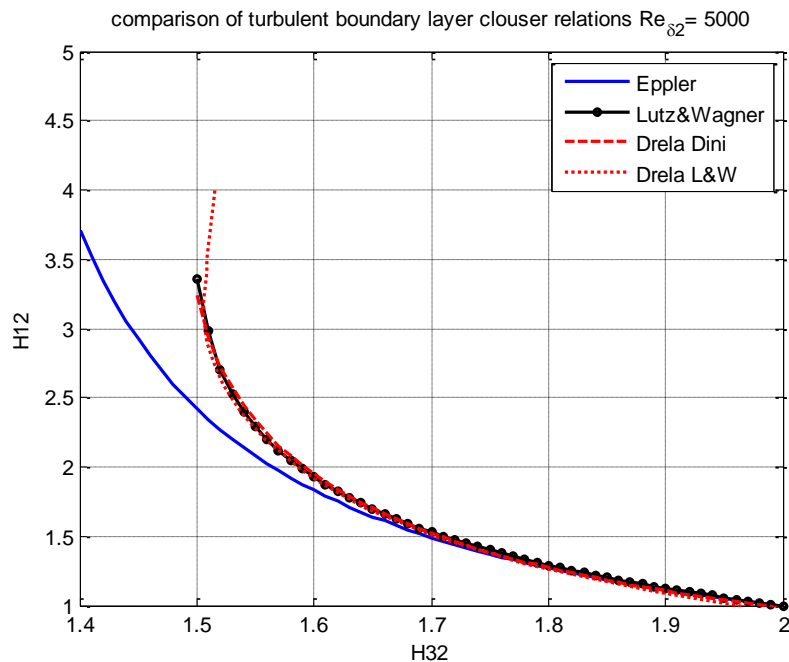


Figure 3.13 Comparisons of different shape factor relations for incompressible turbulent boundary layer at $Re_{\delta_2} = 5000$

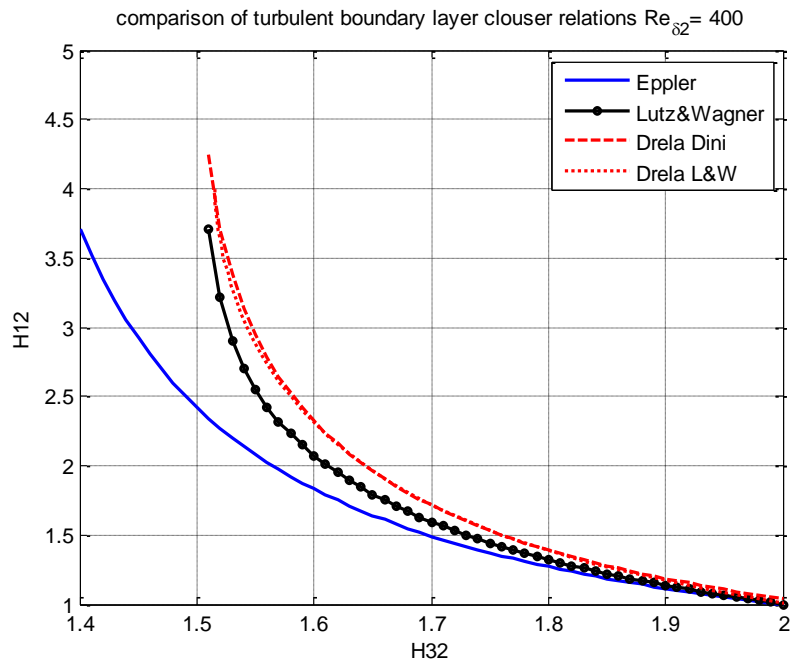


Figure 3.14 Comparisons of different shape factor relations for incompressible turbulent boundary layer at $Re_{\delta_2} = 400$

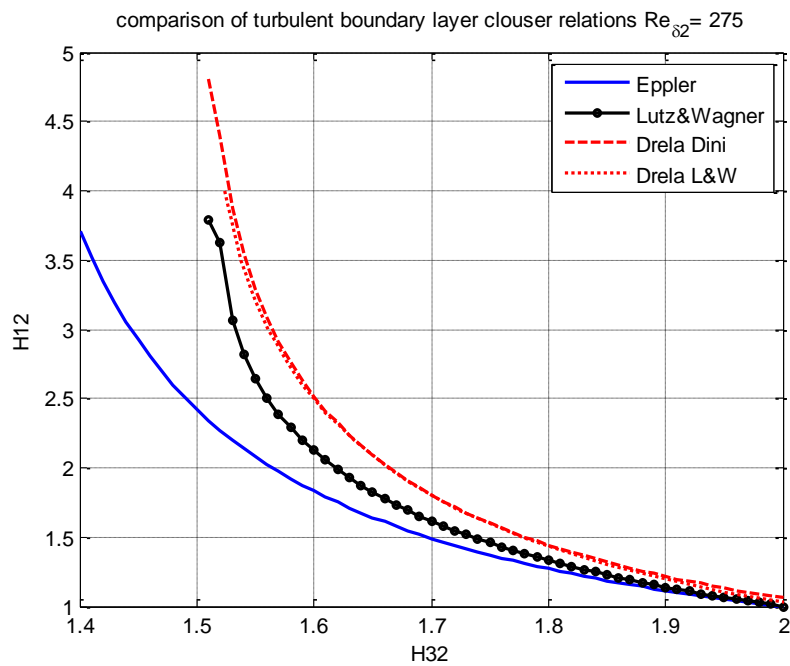


Figure 3.15 Comparisons of different shape factor relations for incompressible turbulent boundary layer at $Re_{\delta_2} = 275$

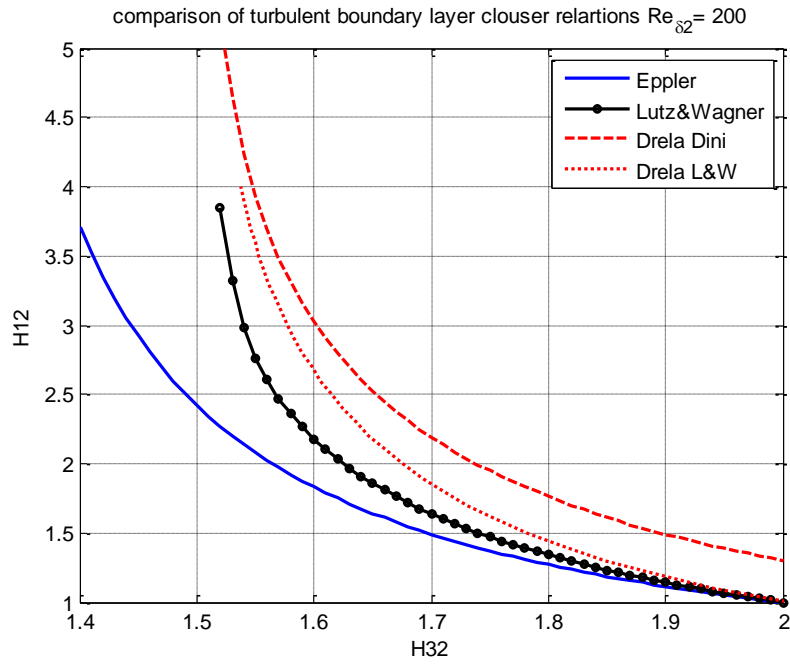


Figure 3.16 Comparisons of different shape factor relations for incompressible turbulent boundary layer at $Re_{\delta_2} = 200$

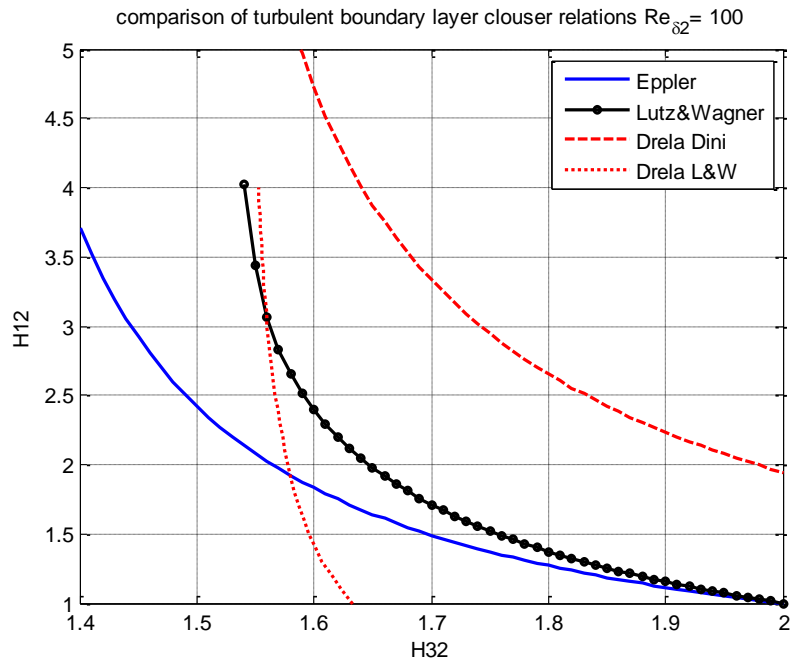


Figure 3.17 Comparisons of different shape factor relations for incompressible turbulent boundary layer at $Re_{\delta_2} = 100$

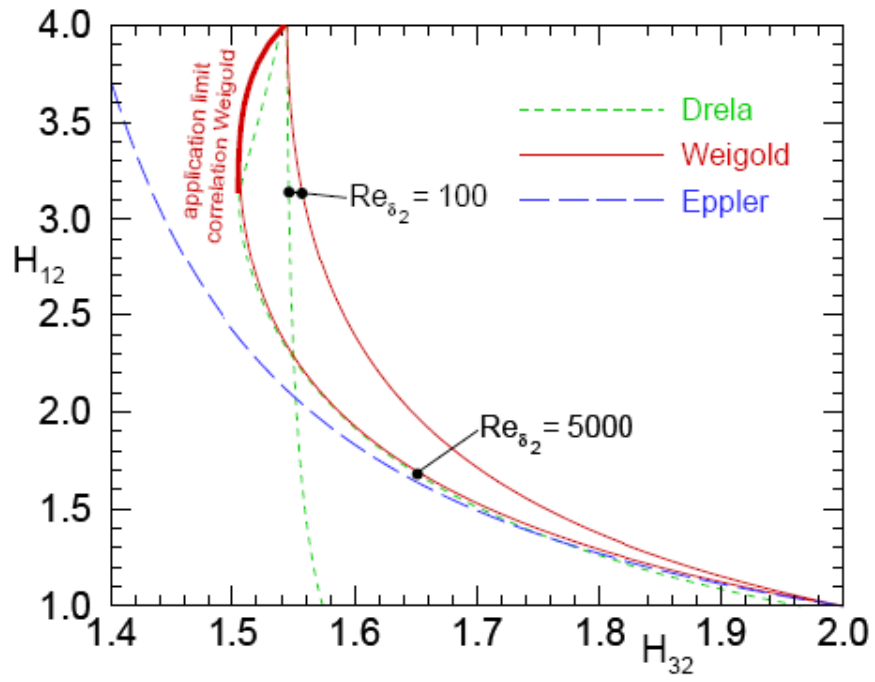


Figure 3.18 Comparisons of different shape factor relations for incompressible turbulent boundary layer, from reference [38]

3.10 Verification of boundary layer calculations

3.10.1 Comparison with Eppler code

Boundary layer calculations are verified by comparison with Eppler code results as for Eppler airfoil E1098 which shown in Figure 3.19. The velocity distribution shown in this figure is that obtained from Eppler code for the propose of boundary layer computations, such that any differences in velocity calculation methods between current calculations and Eppler's calculations will be avoided.

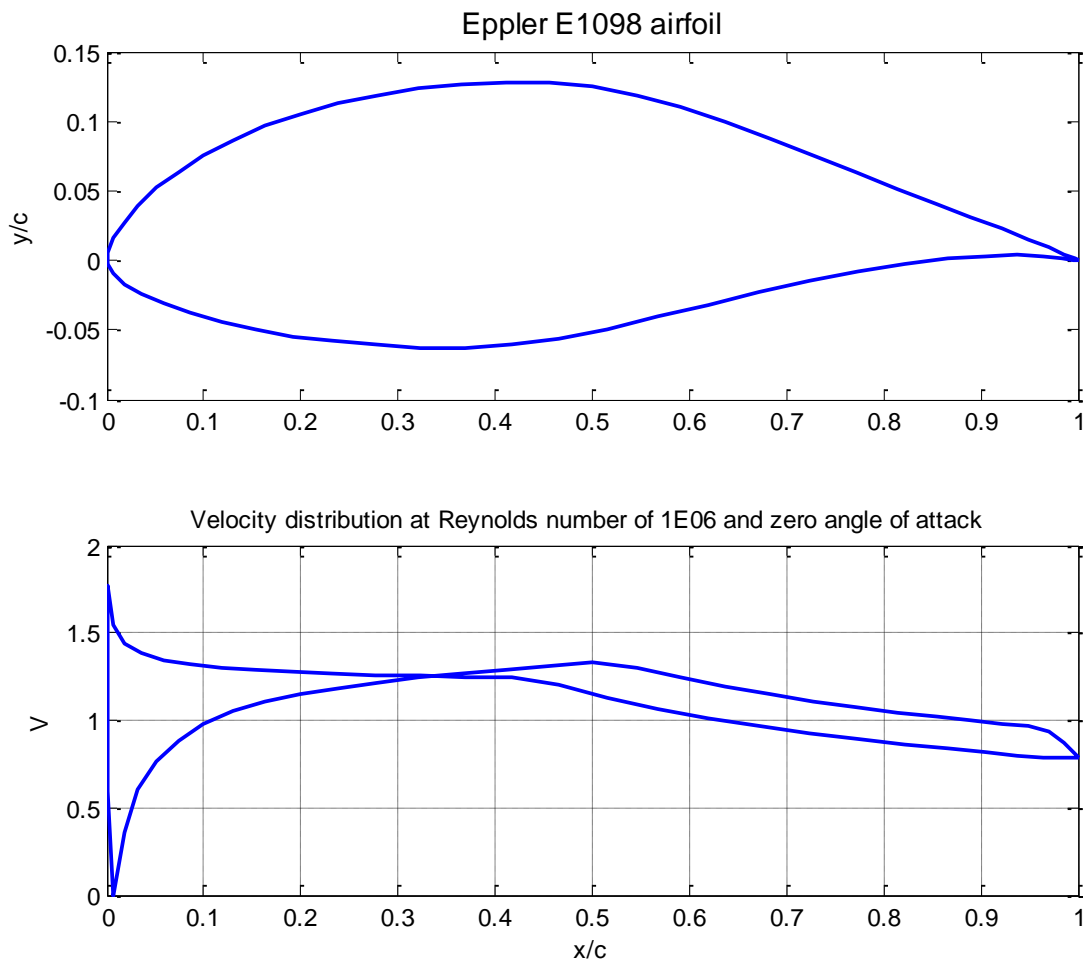


Figure 3.19 Eppler airfoil E1098 and velocity distribution at Re 1E06 and $\alpha = 0$

Boundary layer development is compared in terms of main parameters which is the shape factor H_{32} and the boundary layer momentum thickness δ_2 as function of surface distance for both upper and lower surfaces as shown in Figure 3.22 through Figure 3.25. They comparisons show identical shape and trend of variation of the parameters on both upper and lower surfaces. Since drag is computer using these parameters the comparison of drag is

illustrated for three angle of attack together with transition point location on upper surface on the following table. The results are identical for this airfoil at these conditions. The transition point location values seem to be overestimated, the reason may be related to the very fine integration step used in Eppler code close to separation point. Figure 3.26 through Figure 3.28 show other important boundary layer parameters calculated on lower and upper surface for reference.

Table 3.1 Comparisons of total drag and transition point location on upper surface at $Re=1e06$

ALFA	CD total		Upper Transition point location	
	Current	Eppler	Current	Eppler
0	.0106	.0104	0.57736	0.4549
2	.0072	.0071	0.58	0.4597
8	.0081	.0079	0.5722	0.4794

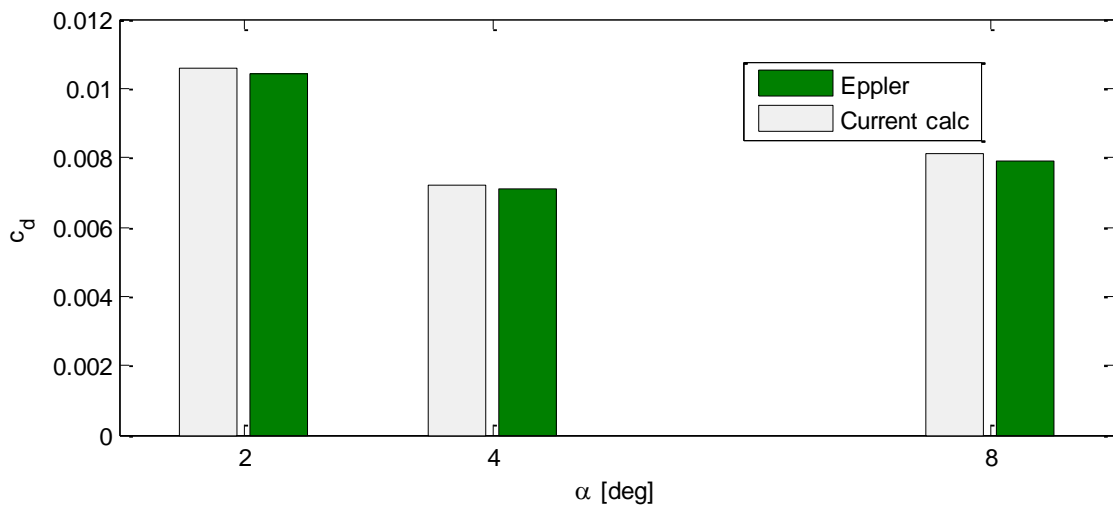


Figure 3.20 Comparison of drag coefficient for E1098 at 1×10^6 between current calculation and Eppler code.

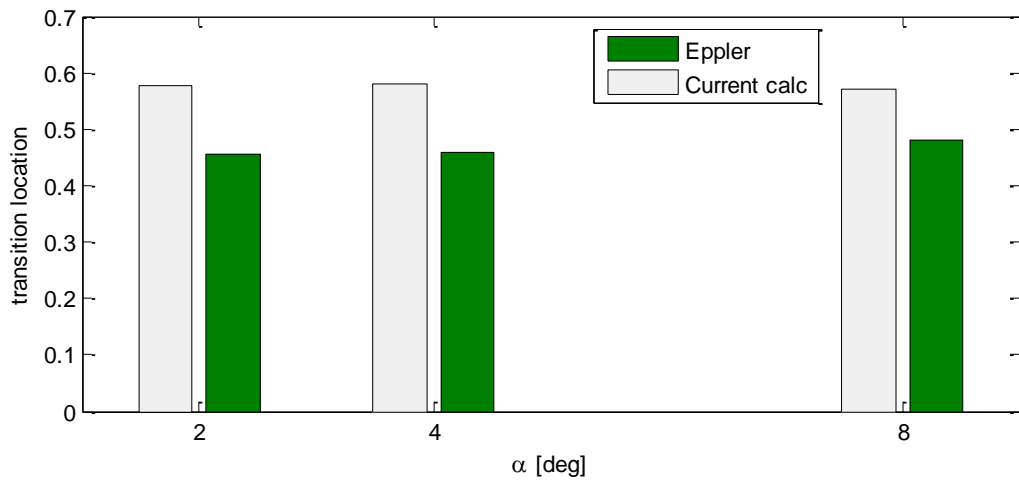


Figure 3.21 Comparison of location of upper surface transition point for E1098 at 1×10^6 between current calculation and Eppler code.

STR = for Eppler E1098 airfoil at Re1M and zero angle of attack used in verification

	S	V	δ_2	H_{12}	H_{32}	Re_{δ_2}
$Lam. sep.$	0	0	0	0	0	0
$Turb. sep.$	1.0324	0.794	0.0045623	2.8032	1.46	3622.4
$Reattachment$	0	0	0	0	0	0
$Transition$	0.57736	1.285	0.0004	3.6034	1.5186	505.02

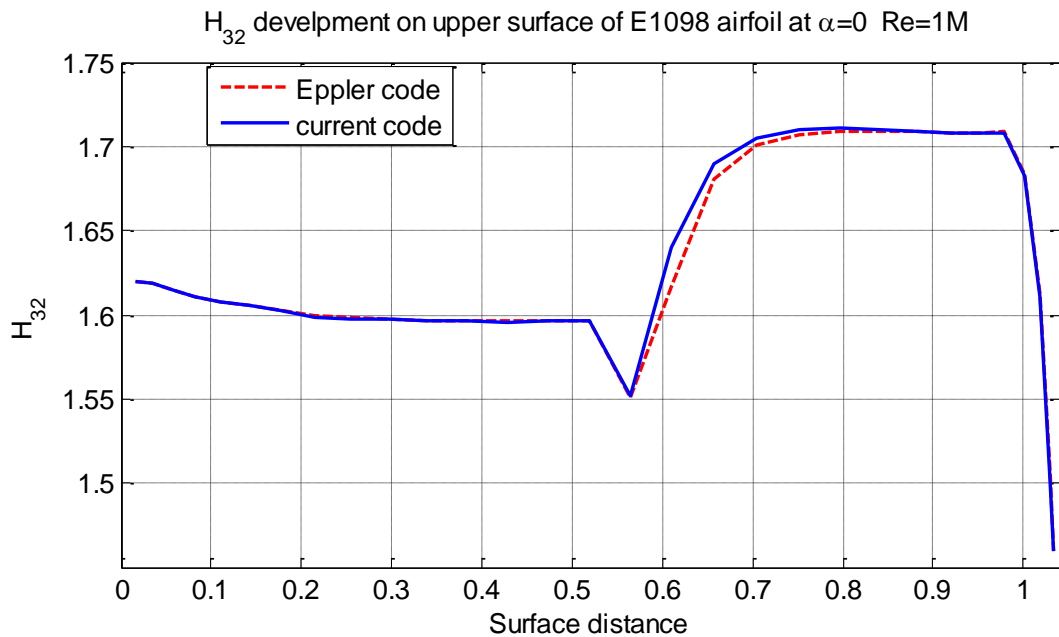


Figure 3.22 H_{32} comparisons over E1098 airfoil upper surface at Re 1E06 , $\alpha = 0$

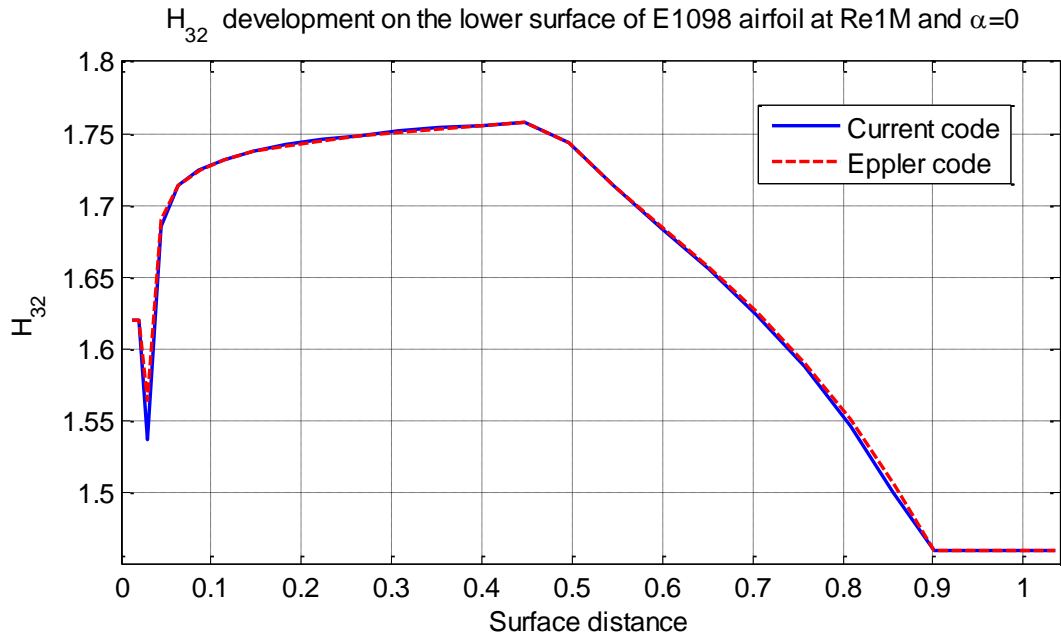


Figure 3.23 H_{32} comparisons over E1098 airfoil lower surface at Re 1E06 , $\alpha = 0$

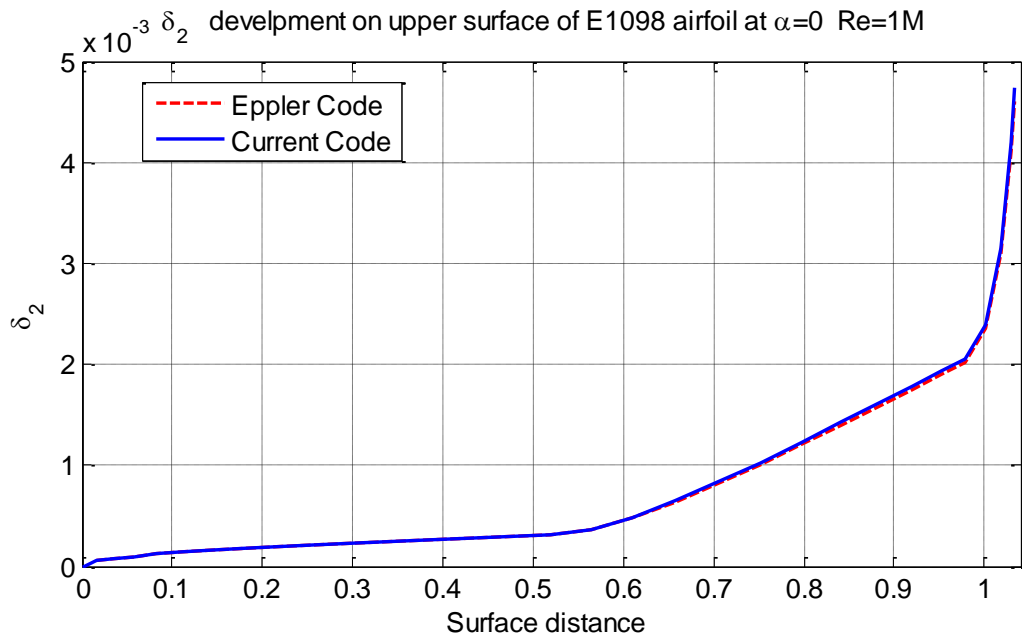


Figure 3.24 δ_2 comparisons over E1098 airfoil upper surface at Re 1E06 , $\alpha = 0$

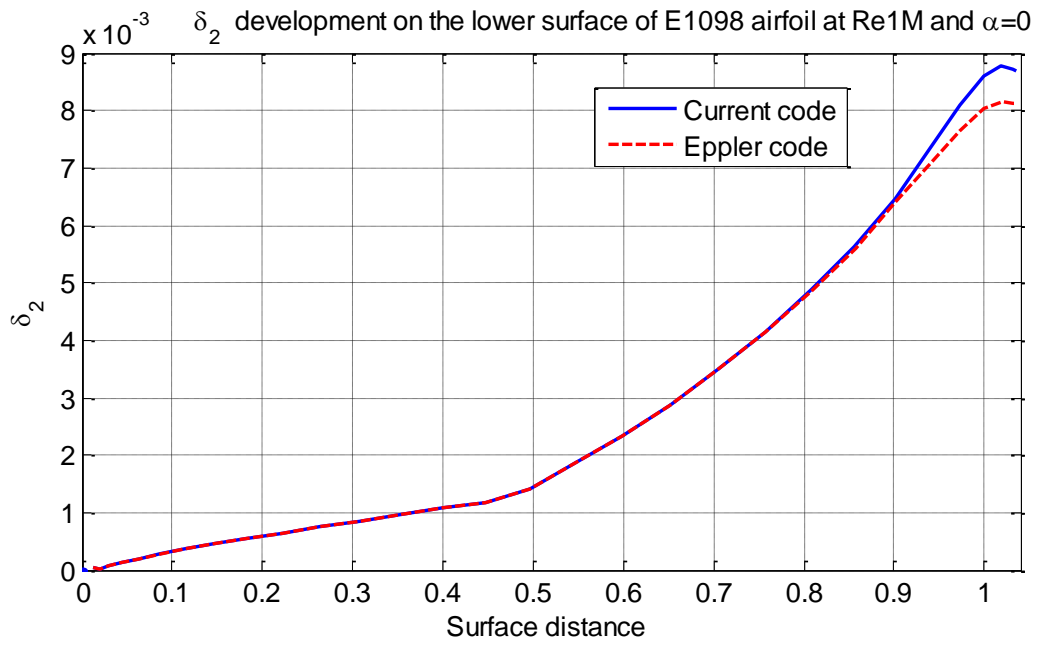


Figure 3.25 δ_2 comparisons over E1098 airfoil lower surface at $Re=1E06$, $\alpha = 0$

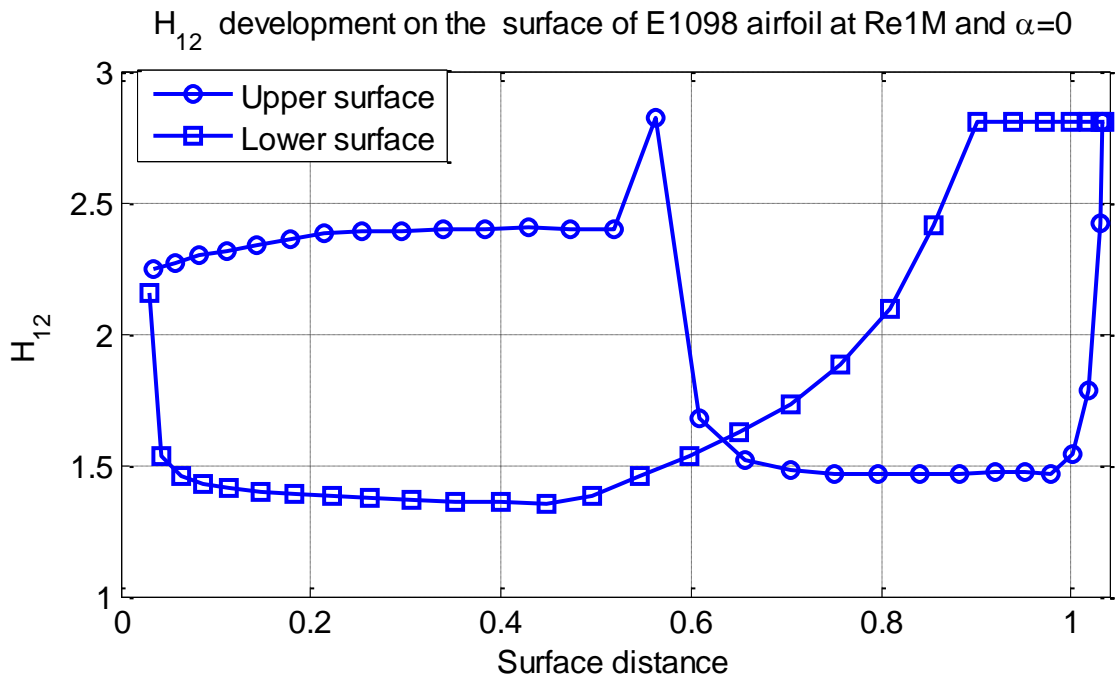


Figure 3.26 shape factor H_{12} development over E1098 airfoil surfaces as calculated

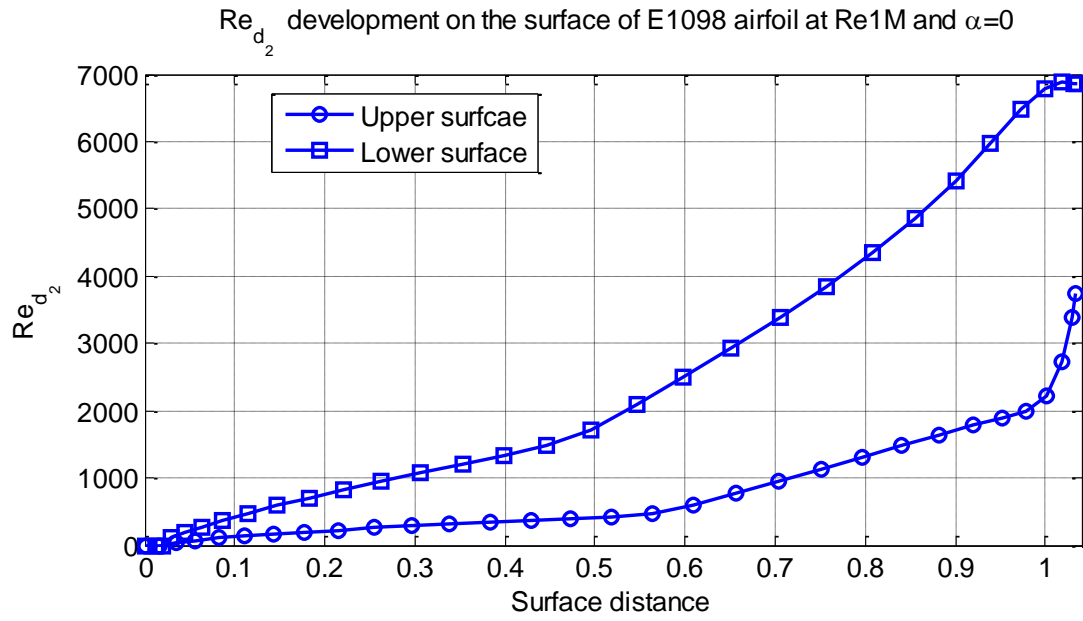


Figure 3.27 Reynolds number based on δ_2 over the airfoil surface

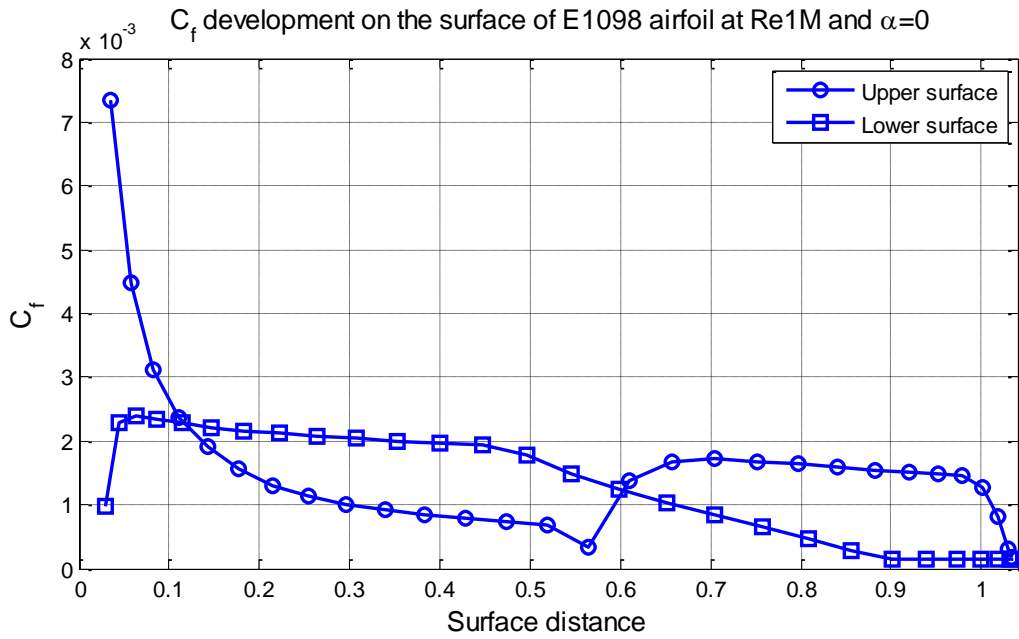


Figure 3.28 Reynolds number based on C_f over the airfoil surface

3.10.2 Comparisons with XFOIL code

It is known that Eppler code does not take the additional drag due to the separation bubble into account. Instead it creates a bubble warning . And the user should that the drag values are under estimated. Since laminar separation phenomenon is not taken care of ,yet, by the code it is interesting to see the comparison of boundary layer parameters with XFOIL code which uses different laminar and turbulent closure relations and do account for separation bubble affects. The boundary layer parameters comparisons are performed for NACA 4412 at Reynolds number of 1E06 and angle of attack of 2 degrees shown in Figure 3.29. The shape factor H_{12} is compared to XFOIL in Figure 3.30. It is interesting to see that the values are in close agreement up to the laminar separation point, after which values predicted by XFOIL code grow to approximately 4 (inside the bubble) while values from current computations predict a sharp decrease in H_{12} values. The reason being that for XFOIL predictions H_{12} increases up to the point of transition which is some distance backward of the laminar separation point while current computations assume transition just at laminar separation point. After a chord distance of 0.6 both curves agree and have similar trend and values, accept at trailing edge. This is expected since after this distance the boundary layer has reattached and is in equilibrium state thus both turbulent closure relations give similar results. The above differences in the key solution parameter H_{12} has manifested in the boundary layer momentum thickness δ_2 and the skin friction coefficient C_f as shown in Figure 3.31 and Figure 3.32 respectively. Next chapter deals with laminar separation bubble modeling.

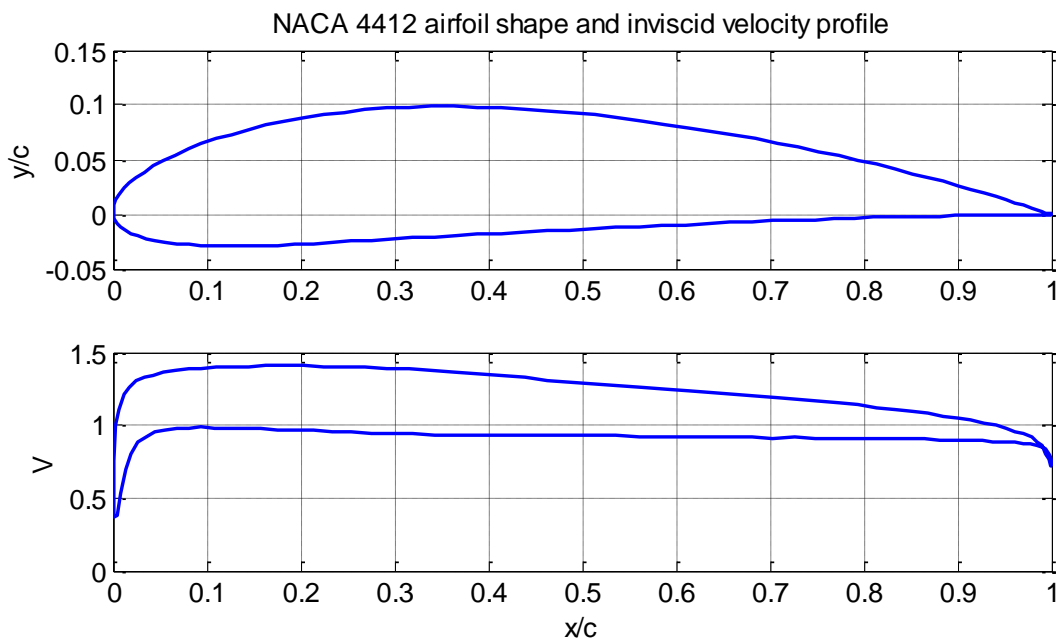


Figure 3.29 NACA 4412 airfoil shape and velocity distribution using current calculation

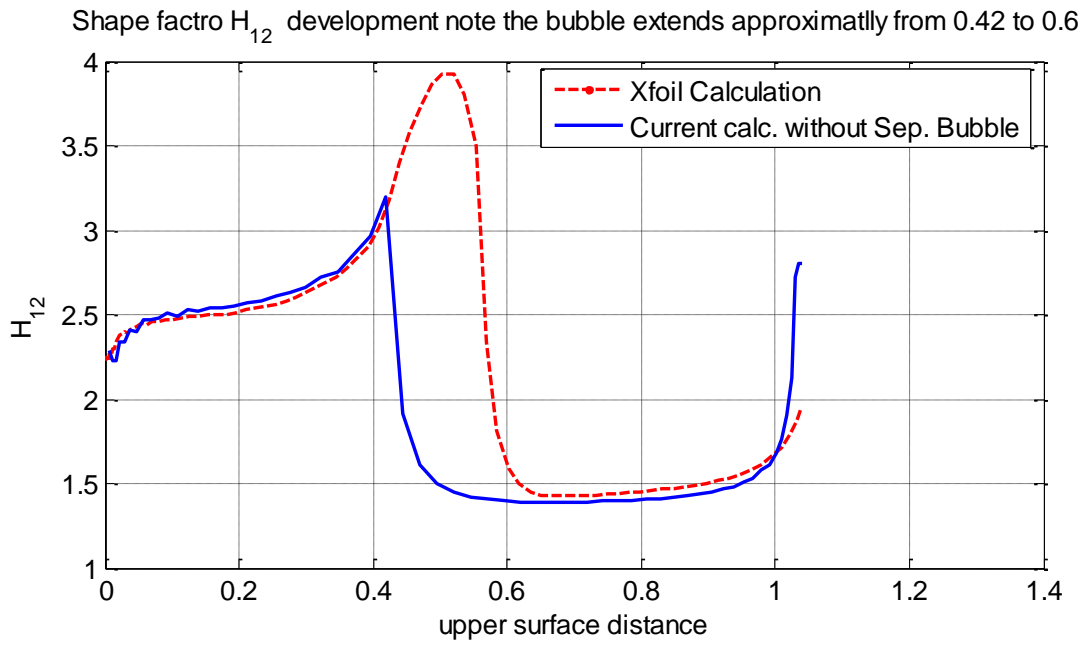


Figure 3.30 Comparisons of shape factor H_{12} ,

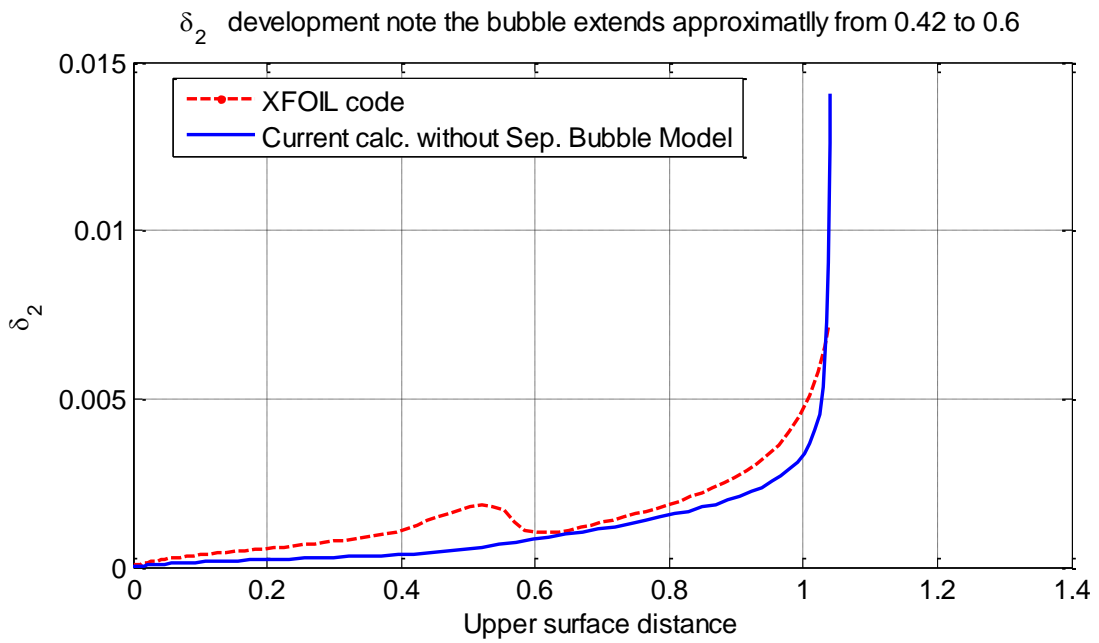


Figure 3.31 Comparisons of boundary layer thickness δ_2

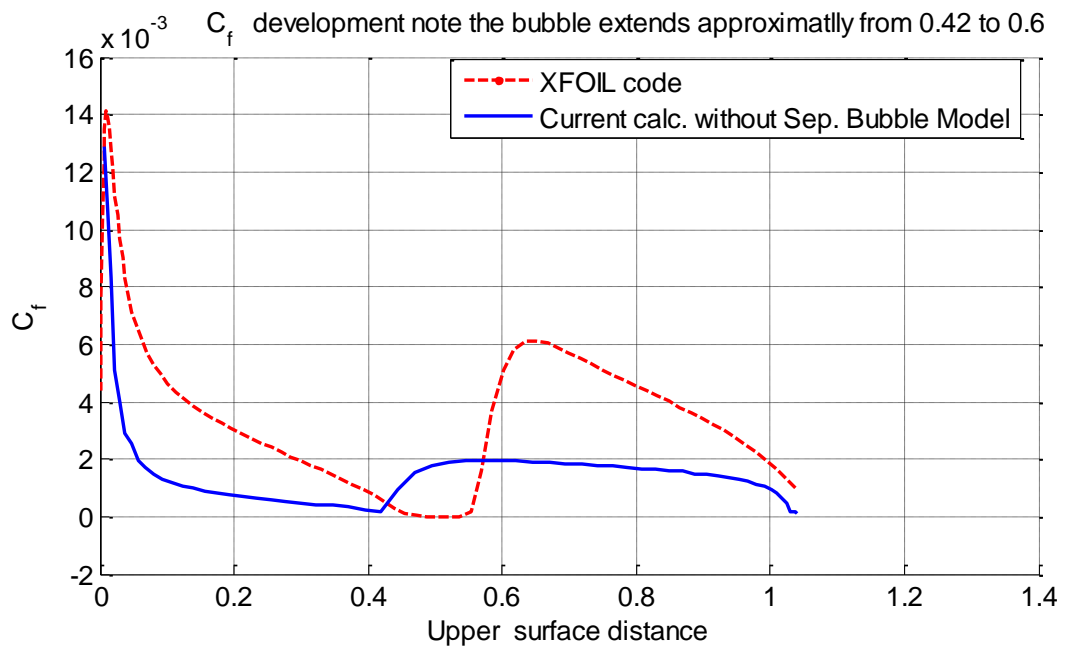


Figure 3.32 Comparisons of skin friction coefficient on upper surface C_f

CHAPTER 4

4 Laminar Separation Bubble modeling

A laminar separation bubble appears on airfoil surfaces when an attached laminar boundary layer is subjected to an adverse pressure gradient of specific magnitude that causes the flow to separate before transition occur. The separated laminar flow soon reattaches after being transformed to turbulent in a region away from the airfoil surface. This phenomenon is more important as Reynolds number is decreased, as noted by Shyy [55]. It is considered a challenge to low Reynolds number airfoil aerodynamics predictions. Laminar separation bubble is first noted by Jones (1933) [39] when he studied airfoil stall process. Since then, extensive experimental and theoretical investigations of the laminar separation bubble structures are performed. Leading edge bubble were first studied because it was believed to cause sudden airfoil stall at low speeds. Owen [41], Crabtree [46], Gaster [49][50], Horton [52][53] are among the first who contributed to laminar separation bubble research.

Mc Cullough and Gault [54] related the stall type with boundary layer features. According to their analysis, there are three types of stall that depend on boundary layer characteristics. Trailing edge stall occurs when turbulent boundary layer separation point leaves the trailing edge and moves forward. Whereas, in leading edge stall laminar boundary layer separates near leading edge without subsequent reattachment. The third type of stall is called thin airfoil stall when the separated laminar boundary layer reattaches (as turbulent boundary layer) and the turbulent reattachment point moves toward the trailing edge as the angle of attack is increased causing decreased lift which limits aircraft operations at low speeds [53].

Recently, remotely piloted vehicles (UAVs), Micro Air Vehicles (MAVs) and wind turbine applications mostly operate at Reynolds number range below 1 million, as argued by Muller [51], Figure 4.1. At this Reynolds number range laminar separation bubble may appear on airfoil near mid chord, causing a significant decrease in lift and increase in drag. Due to this reason general aviation airfoils does not perform well for these applications, and low Reynolds number effects, such as, bubble formation, its structure ,separation, transition and reattachment conditions has to be studied.

Classically laminar separation bubbles are classified as short and long bubbles, see the review by Tani [40]. Bubbles are alternatively classified depending on their effect on inviscid pressure distribution rather than on its length. Laminar separation bubbles may show local

pressure distribution change (Weak bubbles) or it may significantly alter the pressure distribution (strong bubble).

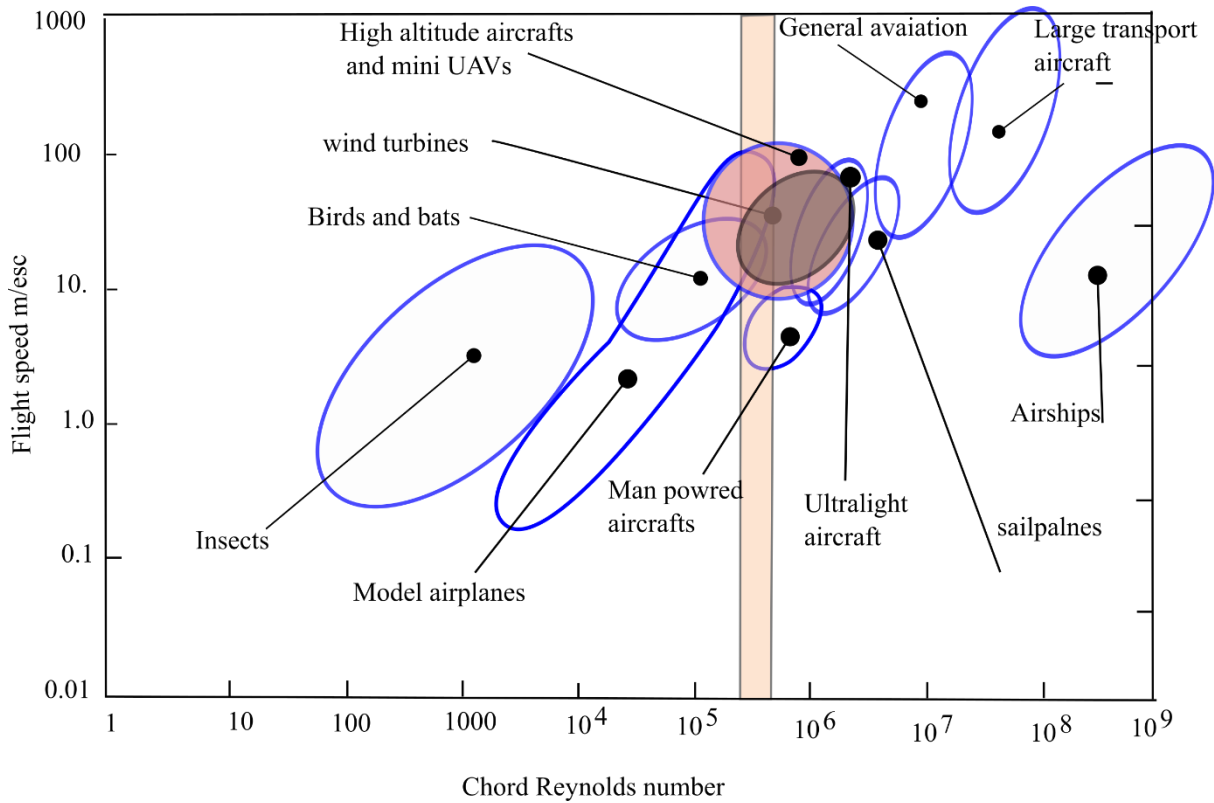


Figure 4.1 Chord Reynolds number Vs. flight speed for different natural and manmade objects

It is the estimation of increased drag and the investigation of type of airfoil stall that motivate most of recent laminar separation bubbles studies. These methods vary from issuing a warning so that the designer may suggest airfoil shape modifications to the evaluation of global bubble effects on pressure distribution.

Horton was the first who presented laminar separation bubble structure as can be seen in Figure 4.2. The flow at low Reynolds number usually starts laminar and thus is more likely to separate. Thus a mild pressure gradient will cause laminar boundary layer separation just after maximum velocity point. The separation never happens in the favorable pressure gradient part, it always happens in adverse pressure gradient region. The boundary layer moves away from the wall as a result of separation creating a region of approximately stagnant air followed by reversed flow region.

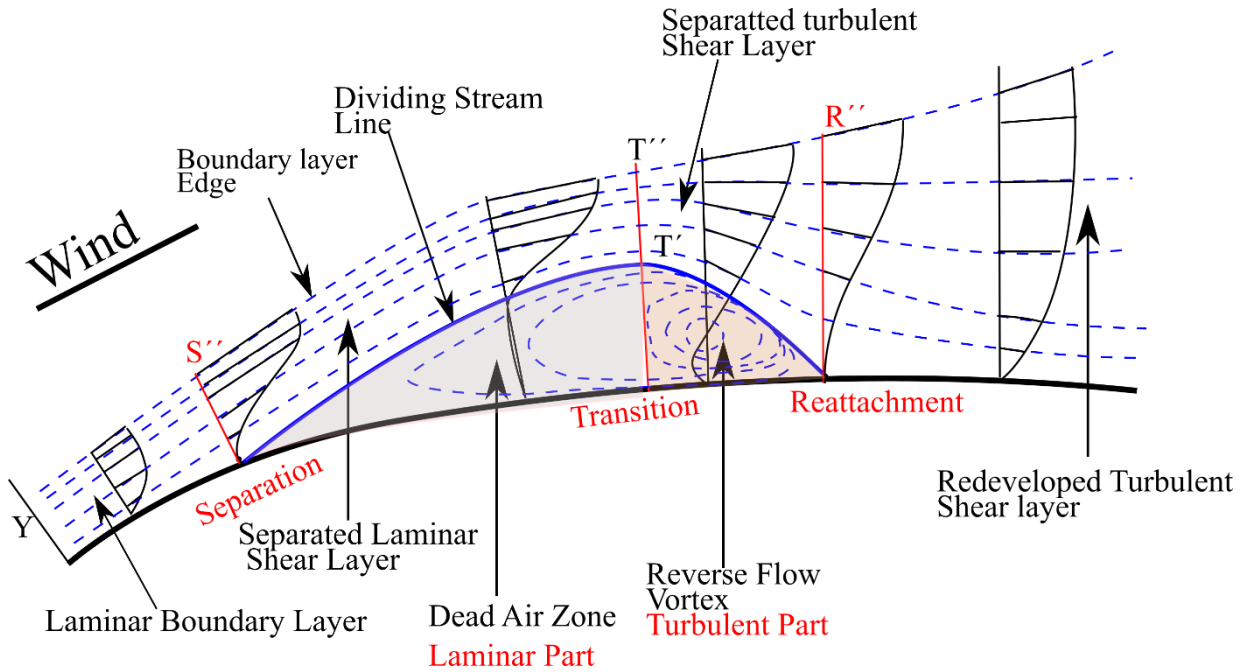


Figure 4.2 A schematic shape of short laminar separation bubble.[52]

The flow undergoes a transition to turbulent at a point above this region in the shear layer. The turbulent flow as known with higher mixing and more resistance to separation may reattach to the surface after some distance along the surface from the transition point. If the flow reattaches again a laminar separation bubble is formed, but if the turbulent flow fails to reattach to the surface the turbulent boundary layer continue separated (sometimes this it is understood as a long bubble which extends into the wake). Laminar separation bubble length decrease with an increase of angle of attack up to a point when it suddenly increases. This phenomenon is called bubble bursting and is explained as a failure of turbulent boundary layer to reattach again to the surface. Laminar separation bubble bursting causes high and sudden drop in lift and an increase in drag. A typical pressure distribution is shown in Figure 4.3.

Gaster has related this phenomenon to the boundary layer conditions at separation. He developed an empirical relation between Re_{δ_2} and Gaster parameter P given by Eqn. (4.1), which expresses the average velocity gradient over the length of the bubble. He found from experimental measurements analysis that at bursting P is a function of $Re_{\delta_{2s}}$ at separation.

$$P = \frac{\delta_{2s}^2}{\nu} \frac{U_s - U_R}{L} \tag{4.1}$$

Where U_s and U_R are the velocities at separation and reattachment points respectively. L is the bubble length defined as the surface distance from separation point to reattachment.

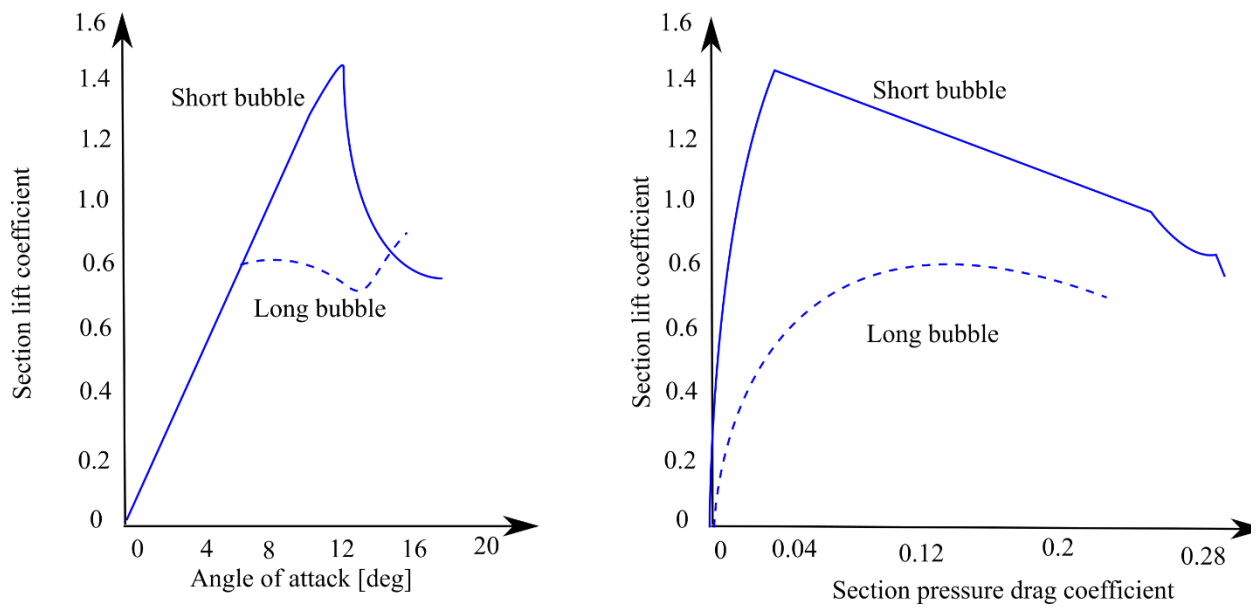


Figure 4.3 Effect of long and short bubble at high Reynolds number[51]

While, short bubble affects mostly the stall behavior of airfoil long bubble has an un-preferred effect on the entire polar.

Numerical methods are also used by many authors such as Cebeci [42], Alam & Sandham [43], Jones [44], Cadieux[45] to investigate numerically bubble formation and effects. They predicted bubble structure in two dimensional flow in order to simulate experiments. In some cases three dimensional studies are performed as flow is really three dimensional on wing sections. Alam, used Direct Numerical Simulations (DNS) to study short laminar separation bubbles [46]. Crivellini has. Studied laminar separation bubble on low Reynolds number operating airfoils using RANS modeling by means of an high-accuracy solver and experimental verification [47].

Although, numerical methods provide large quantity of detailed information about the flow, it is not used as routine methods, as it requires more effort in domain size selections and grid sensitivity analysis, in addition to the choice of turbulence models. Bubble forcing method also has an effect on obtained results. Due to these reasons it is hard to be used for optimization purposes especially if many shapes is to be analyzed. It is more suitable if a given shape is to be analyzed such that experimental measurements are more focused and specific. In the last decades successful airfoil designs for different applications were possible using inviscid-viscous interaction methods followed by experimental measurements.

Airfoil design, analysis and optimization will require the development of laminar separation bubble model that is faster than finite differences or N-S equation solvers. Dini used an

inviscid–viscous interaction model to predict effects of laminar separation on airfoil drag at low Reynolds numbers. The method is based on the hypothesis that laminar separation bubble can be modeled using local flow parameters. Boundary layer development a head of the bubble is performed to predict both separation conditions and forward disturbances information needed to predict transition. This method shows very good accuracy regarding the prediction of the modified inviscid distribution and the increase in drag in the range of Reynolds number as low as 100,000 [35]. This range represents most interesting operational range of UAV's and wind turbines, as argued by Muller's in Figure 4.1.

Drela and Giles used interactive methods that make use of integral boundary layer formulation these methods provide efficient solution procedures, with accuracy contained within boundary layer assumptions applicability. Eppler also uses this formulation to issue a warning of expected bubble effect on airfoils. Eppler's method is used successfully to design airfoils for many applications in the past for Reynolds number 500,000 and higher. For lower Reynolds numbers, however, it is difficult to use this criteria to eliminate bubble by modifying the shape of airfoil since laminar separation bubble is always present at Reynolds number lower than 500,000 [51]. Therefore, an improvement in LSB prediction will result in better estimation of aerodynamic characteristics at this range.

4.1 Reynolds number and angle of attack variation

At higher Reynolds numbers natural flow transition from laminar to turbulent inside the boundary layer happens very quickly in the favorable pressure region, where no laminar separation risk is expected. The turbulent boundary layer is more resistant to adverse pressure gradients and usually flow may separate close to the trailing edge (Turbulent separation), as seen in Figure 4.4. As the angle of attack is increased this separation point moves forward and as a result airfoil lift decreases. The resulting lift curve has smooth shape indicating smooth airfoil stall.

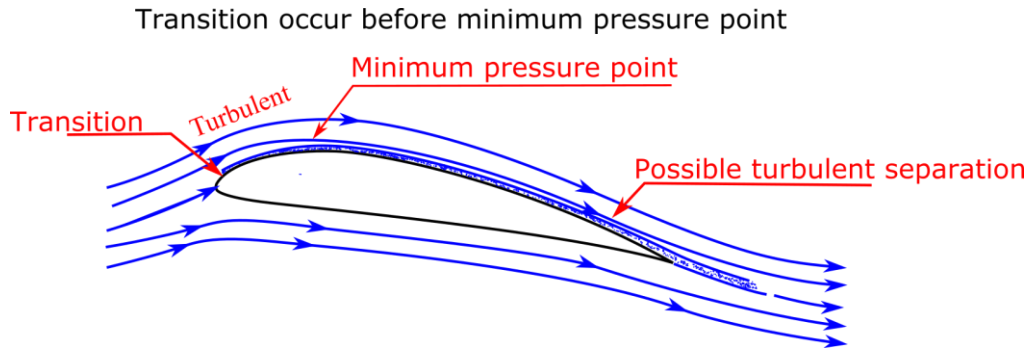


Figure 4.4 High Reynolds number flow over a large wing

At lower Reynolds numbers laminar boundary layer continue inside the region of adverse pressure gradient, without transition. At some point laminar separation may occur and the boundary layer moves away from the airfoil surface, see Figure 4.5 for which angle of attack is small and the flow transition occurs far from the wall. Turbulent reattachment occur after that and turbulent flow continue to the trailing edge. Figure 4.6, shows a case when higher angle of attack is encountered where bubble is shorter and closer to the leading edge. Figure 4.7 shows a case when the bubble bursts and airfoil stalls. Airfoil characteristics are affected by stall type and bubble length. Figure 4.3 shows effect of short and long bubble on drag polar and lift curve. While, short bubble affects mostly the stall behavior of airfoil long bubble has an un-preferred effect on the entire polar. It is thus avoided in the design process.

Laminar separation occurs before transition

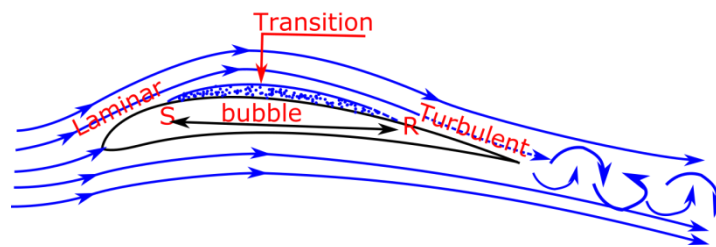


Figure 4.5 Low Reynolds number flow at low angle of attack

Laminar separation occur during adverse pressure gradient, followed by transition and subsequent reattachment resulting in additional drag.

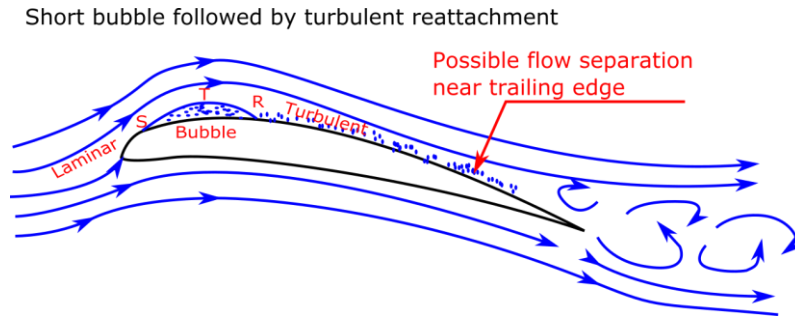


Figure 4.6 Low Reynolds number flow over airfoil at higher angle of attack, a case when higher angle of attack is encountered where bubble is shorter and closer to the leading edge

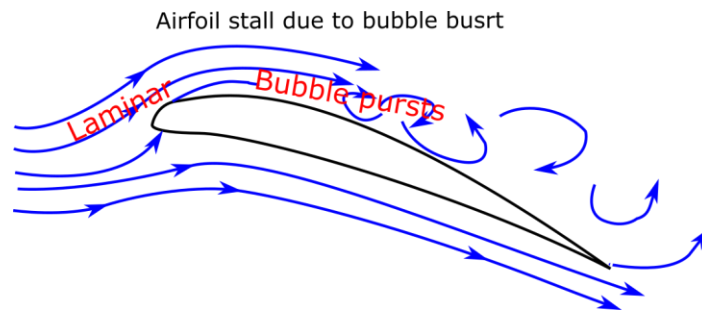


Figure 4.7 Low Reynolds number flow at stall, when the bubble bursts, airfoil stalls and airfoil characteristics are affected by stall type and bubble length.

4.2 Laminar separation bubble model

The model adopted in this work is developed by Dini [35] and [36], in which a weakly interacting laminar separation bubble in two dimensional incompressible flow over airfoils is modeled. The main aim of the model is to compute the increased airfoil drag that result from bubble formation.

A weakly interacting bubble is characterized by dominant local effect on pressure distribution. The model focus on the calculation of the shear layer through different bubble parts as illustrated in the following sections. Laminar separation bubble starts when a laminar flow separates, at a point S , causing the boundary layer to move away from the airfoil surface, see Figure 4.8. The point of laminar separation can be predicted by the solution of integral boundary layer method described in chapter (2). The shear layer grows until transition from laminar to turbulent occurs at point T . The region between points S and T is characterized by presence of velocity plateau distribution shown on Figure 4.8. The location of transition is to be calculated since it determines the bubble length and thus bubble drag. The surface distance between the point of separation and the point of transition is denoted by l_1 . After transition occurs at point T the flow becomes turbulent and the pressure recovers leading to

reattachment at point R , with length l_2 . In many cases, the pressure recovery region is observed to continue downstream of reattachment point, and the velocity distribution undershoots the inviscid velocity distribution curve and merges after some distance with inviscid curve at point M , shown on Figure 4.8.

Therefore, the bubble is divided into three regions:

- Laminar region that starts from point of laminar separation and ends at point of transition.
- Turbulent pressure recovery region, from the point of transition to reattachment.
- Undershoot region where the smooth merge of the velocity distribution with inviscid distribution happen.

The main goal is to estimate the drag contribution of the separation bubble. This goal is established through the correct calculation of the boundary layer momentum thickness δ_2 across the above three bubble regions.

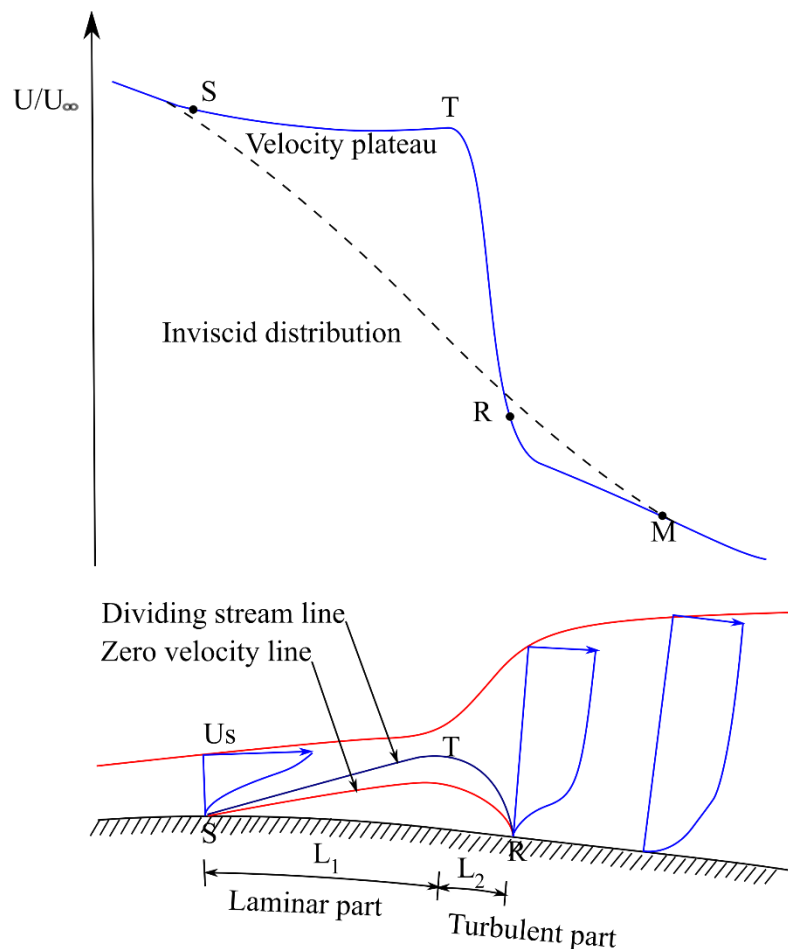


Figure 4.8 schematic of bubble and its effects on pressure distribution [dini]

4.2.1 Laminar part of the bubble [36]

The solution of integral boundary layer equations described in chapter (2) is continued until laminar separation occurs. Laminar separation is indicated when the shape parameter H_{32} decreases to the value 1.51509. Starting at this point, the laminar velocity plateau function is computed based on local boundary layer parameters U_s and δ_{2s} as follows:

The average velocity gradient over the bubble area is first estimated from the velocity distribution. It is defined as the change in velocity $\Delta\left(\frac{U}{U_\infty}\right)$ divided by the difference in chord $\Delta\left(\frac{s}{c}\right)$ between the point of laminar separation to the point of reattachment. Since, the point of reattachment is not known at the beginning of the calculation iterative procedure is used to fix this value.

Reynolds number based on momentum thickness at separation $R_{\delta_{2s}}$ is computed as

$$R_{\delta_{2s}} = R \frac{U_s}{U_\infty} \frac{\delta_{2s}}{c} \quad (4.2)$$

Gaster parameter P is computed depending on the local boundary layer parameters at the separation point U_s and δ_{2s} as

$$P = R \left(\frac{\delta_{2s}}{c}\right)^2 \frac{\Delta\left(\frac{U}{U_\infty}\right)}{\Delta\left(\frac{s}{c}\right)} \quad (4.3)$$

Where R is chord based Reynolds number, U is inviscid velocity at separation point location S, and U_∞ is free stream velocity.

The pressure recovery DU calculated using experimentally fitted data as shown in Figure 4.9. and is given by the following equation

$$DU = \begin{cases} 0.0610 + 0.3048 P + 0.5072 P^2 & - P < 3 \\ 0.0152 & - P > 0.3 \end{cases} \quad (4.4)$$

The velocity plateau function is computed starting from separation point until transition is triggered at point T, and is given by the following equation

$$\frac{U}{U_s} = 1 - DU \left\{ 1 - \exp \left[\frac{1}{DU} \frac{U'_s}{U_s} (s - s_s) \right] \right\} \quad (4.5)$$

Where U'_s is the slope of velocity profile at separation point, and subscript s indicate condition at separation. The variable S is the surface distance along the airfoil upper or lower side.

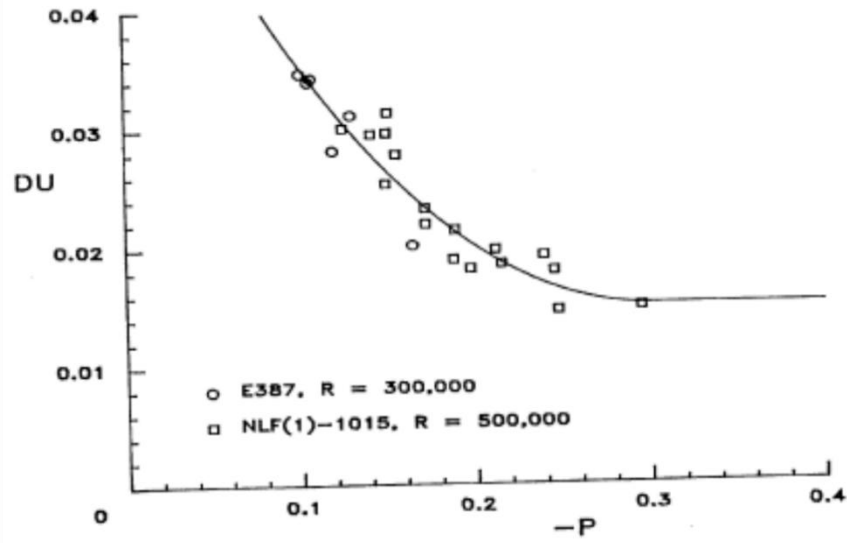


Figure 4.9 Pressure recovery in the laminar part of the bubble as function of Gaster's pressure gradient parameter

The boundary layer closure correlations adopted for the laminar part of the bubble are given by

$$H_{12} = \frac{H_{32} - 1.94068}{0.08} + \left[\left(\frac{H_{32} - 1.94068}{0.04} \right)^2 - 64.4 \right]^{\frac{1}{2}} \quad (4.6)$$

$$R_{\delta 2} \frac{c_f}{2} = \begin{cases} -0.067 + 0.01977 \frac{(7.4 - H_{12})^2}{H_{12} - 1} & H_{12} < 7.4 \\ -0.067 + 0.022 \left[1 - \frac{1.4}{H_{12} - 6} \right]^2 & H_{12} \geq 7.4 \end{cases} \quad (4.7)$$

$$R_{\delta 2} \frac{c_D}{H_{32}} = 0.207 - .003(H_{12} - 4)^2 \quad (4.8)$$

The integral boundary layer equations (Chapter 2) are solved in direct mode using these correlations, derived by the above velocity plateau function.

The separation angle γ is defined in Figure 4.10, as the tangent of the separation stream line that makes with the surface. It is calculated from the empirical relationship proposed Wortmann (1974) [56] as:

$$\tan \gamma = -\frac{64P}{R\delta_{2s}} \quad (4.9)$$

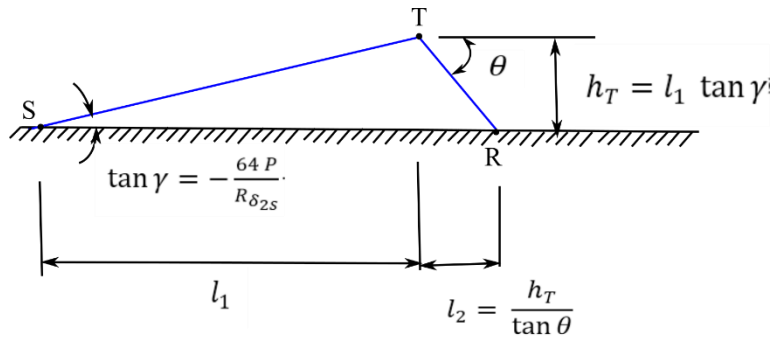


Figure 4.10 Bubble geometry and scaling parameters

4.2.2 Transition

Prediction of transition location inside the bubble has important role in determining the bubble drag. Eppler criteria is very useful in predicting transition at high Reynolds numbers for which transition occurs usually in favorable pressure gradient region. When bubble presents in the flow, however, more accurate criteria is necessary in which upstream disturbance history is taken into account and transition inside the shear layer can be predicted. The transition prediction method adopted here is e^n method.

It is a semi-empirical transition prediction approach. Using this method one can distinguish between leading edge and med-chord bubbles and also model the effect of pressure distribution variations upstream of the bubble location.

The logarithm of the ratio of disturbance amplitude at station s to its amplitude at natural stability s_0 is defined as factor $n(s)$, where s is the chord station. In this manner, transition is assumed to occur if the ratio n reaches a predefined critical value n_{cr} . This value is observed experimentally to be in the range from 9 at low turbulence wind tunnels up 14 at some flight test. It is also Reynolds number dependent. An approximate e^n method developed by Drela [1986] is used in this work. The amplification factor $n(s)$ derived by Drela is given by

$$n(s) = \int_{s_0}^s \left[\frac{dn}{dR\delta_2} (H_{12}) \right] \frac{m(H_{12}) + 1}{2} \frac{l(H_{12})}{\delta_2(s)} ds \quad (4.10)$$

Where:

$$\left[\frac{dn}{dR_{\delta_2}}(H_{12}) \right] = 0.01[\{2.4 H_{12} - 3.7 + 2.5 \tanh(1.5(H_{12} - 3.1))\}^2 + 0.25]^{\frac{1}{2}} \quad (4.11)$$

$$l(H_{12}) = \frac{6.54 H_{12} - 14.07}{H_{12}^2} \quad (4.12)$$

$$m(H_{12}) = \frac{0.058 (H_{12} - 4)^2}{(H_{12} - 1) - 0.068} \frac{1}{l} \quad (4.13)$$

and s_0 is the location at which $R_{\delta_2} = R_{\delta_{20}}$ which is defined with the following function

$$\begin{aligned} \log_{10}[R_{\delta_{20}}(H_{12})] \\ = \left[\frac{1.415}{H_{12} - 1} - 0.489 \right] \tanh \left[\frac{20}{H_{12} - 1} - 12.9 \right] + \frac{3.295}{H_{12} - 1} + 0.440 \end{aligned} \quad (4.14)$$

During the boundary layer development the value of H_{12} , R_{δ_2} are available at each point s . Thus, $R_{\delta_{20}}$ is calculated at each point s using Eq.(4.14). The chord station at which $R_{\delta_2} = R_{\delta_{20}}$ is taken as the lower integration limit s_0 in Eqn.(4.10). Therefore at this point the computation of value of the amplification factor $n(s)$ starts. Drela added this equation to the system of equations that are solved by finite difference in XFOIL code [57]. When integral boundary layer approach is adopted, like in this work, the amplification factor $n(s)$ is computed by integrating this equation with the boundary layer integral equations.

The integration continue until the value of $n(s)$ equals the predefined value $n_{critical}$, at which transition from laminar to turbulent is assumed. And the code switches to calculation of turbulent part of the bubble. In wind tunnels it was reported that $n=9$ is an accurate approximation.

The transition point corresponds to the highest point of the bubble h_T , and the surface length from the separation point to this point corresponds to the laminar part of the bubble l_1 . The bubble height at transition is given by the empirical relation

$$h_T = l_1 \tan \gamma \quad (4.15)$$

Where γ is the separation angle defined by Eq.(4.9) above.

4.2.3 Turbulent part of the bubble

The turbulent shear layer spreading angle θ is modeled as

$$\tan \theta = 0.0975 + 2.5 \times 10^{-8} R \quad (4.16)$$

When transition location l_1 is specified the turbulent length of the bubble l_2 is thus calculated by

$$l_2 = \frac{h_T}{\tan \theta} \quad (4.17)$$

Following this derivation, bubble geometry has the shape shown in Figure 4.10. The reattachment location is given by the summation of separation and l_1 and l_2 surface distances. In order to account for drag increment from the bubble the turbulent part of the bubble is solved. The solution is based on assumed shape factor H_{32} in the form given in the Figure 4.11, and formulated by the Eqns.(4.18) to (4.24):

$$\bar{H}_{32}(\bar{y}) = \sin\left(\frac{\pi}{\bar{y}}\right) \quad (4.18)$$

Where

$$\bar{H}_{32} = \frac{H_{32} - (H_{32})_R}{A_i[(H_{32})_T - (H_{32})_R]} - 1 \quad (4.19)$$

$$\bar{y} = \left(\frac{2}{3} - \bar{y}_0\right)\sigma + \bar{y}_0 \quad (4.20)$$

$$\bar{y}_0 = \frac{\pi}{3\pi - \sin^{-1}(1/A_1 - 1)} \quad (4.21)$$

$$\sigma = \begin{cases} (s - s_T)/l_2 & s \leq s_R \\ [(s - s_T)l_2 - 1]SF + 1 & s > s_R \end{cases} \quad (4.22)$$

$$SF = \sqrt{\frac{A_1}{A_2}} \quad (4.23)$$

$$A_1 = 0.5 + e^{-300(h_T/c)} \quad (4.24)$$

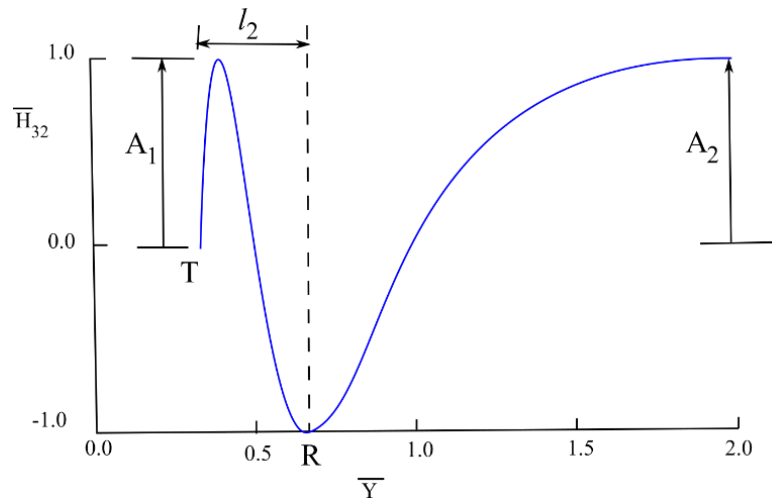


Figure 4.11 normalized shape factor turbulent recovery function

While A_1 is calculated based on bubble height at transition, the value of A_2 is obtained iteratively so that the solution merges with inviscid smoothly. The computations is repeated with different values of A_2 until the error in the slope of the obtained velocity distribution and the inviscid solution is acceptably small, at the point where the two solutions cross each other. One deg. error was found to be satisfactory.

It is known that the value of the shape factor H_{32} at separation equals 1.51509 is equivalent to $H_{12} = 4.0$. The value H_{12} rises inside the laminar part of the bubble above the value of 4.0 up to the transition point when it has the maximum value where it starts to decrease to 4.0 again at reattachment point, as discussed by Drela [58]. The behavior of H_{32} is just the opposite and normally presented in the boundary layer development chart after boundary layer calculation are performed. In fact, in laminar part of the bubble velocity is almost constant, and thus the pressure, which means that the momentum thickness δ_2 is almost constant. The variation in the shape factors in the turbulent part of the bubble reflects a jump in pressure which in turn produces additional drag, known as bubble drag. If the above mentioned maximum value of H_{12} is kept low the resulting increase in drag will be also low. This can be accomplished by proper choice of velocity distribution in the area around the bubble location. This method is known as transition ramp normally used in inverse design. This approach can be also utilized if airfoil design by shape perturbation is selected. A target pressure distribution is pre-specified and the airfoil shape is found by optimal optimization methods. If a bubble effect is

to be minimized the pressure distribution can be modified in the region ahead and over the bubble.

The solution of turbulent part of the bubble is performed by integrating the boundary layer integral equation in inverse mode, derived by the above H_{32} shape factor model. The integral boundary layer equations in inverse mode are slightly different than standard Von Karman equations stated in chapter (2). In the turbulent part of the bubble shear stress is the most important quantity and that is why it is modeled by the shear stress lag equation, which models the dissipation coefficient in the turbulent boundary layer. The accurate modeling of dissipation coefficient is necessary to get correct prediction of pressure jump in the turbulent part of the bubble.

Once the shape factor H_{32} is calculated, it is used to drive the solution of the system of equations Eqn.(4.25) to Eqn.(4.29) for the variables U , δ_2 and C_τ . Specifically, the abrupt increase in the value of δ_2 is of great concern because it will lead to the additional drag, and thus accounts for transitional bubble effect. It will be shown also in the pressure distribution which can be compared with measurement.

$$\frac{dU}{ds} = \left[\frac{c_f H_{32}}{2} - C_D + \delta_2 \frac{dH_{32}}{ds} \right] \frac{U}{\delta_2 H_{32} (H_{12} - 1)} \quad (4.25)$$

$$\frac{d\delta_2}{ds} = \left[-\frac{3c_f H_{32}}{2(H_{12} + 2)} + C_D - \delta_2 \frac{dH_{32}}{ds} \right] \frac{(H_{12} + 2)}{H_{32}(H_{12} - 1)} \quad (4.26)$$

$$\frac{\delta}{C_\tau} \frac{dC_\tau}{ds} = 4.2(C_{\tau eq}^{0.5} - C_\tau^{0.5}) \quad (4.27)$$

Where

$$C_{\tau eq} = \frac{0.015 H_{32}}{1 - U_{slip}} \left[\frac{H_{12} - 1}{H_{12}} \right]^3 \quad (4.28)$$

$$\delta = \delta_2 \left(3.15 + \frac{1.72}{H_{12} - 1} \right) + \delta_1 \quad (4.29)$$

C_D , H_{12} , and C_f is given by

$$C_D = f \cdot C_{D Drela} \quad (4.30)$$

$$f = \begin{cases} 1 + (C_{Dmax} - 1) \left(\frac{s - s_T}{l_2} \right)^2 & 0 \leq \frac{s - s_T}{l_2} \leq 1 \\ 1 + (C_{Dmax} - 1) e^{-T \left(\frac{s - s_T}{l_2} - 1 \right)} & \frac{s - s_T}{l_2} > 1 \end{cases} \quad (4.31)$$

$$r = 15 - 1000 \frac{h_T}{c} \quad (4.32)$$

$$C_{Dmax} = 1.0 + \sqrt{200 \frac{h_T}{c}} \quad (4.33)$$

$$C_{D Drela} = c_f U_{slip} + 2C_\tau (1 - U_{slip}) \quad (4.34)$$

$$U_{slip} = \frac{H_{32}}{6} \left[\frac{4}{H_{12}} - 1 \right] \quad (4.35)$$

$$H_{12} = \begin{cases} \frac{H_{120}}{1 + \left(\frac{H_{32} - H_{320}}{c_1} \right)^{\frac{1}{1.27}}} & C_f > 0 \\ H_{120} + \left(\frac{H_{32} - H_{320}}{c_2} \right)^{\frac{1}{c_3}} & C_f < 0 \end{cases} \quad (4.36)$$

Where

$$H_{320} = 1.505 + \frac{4}{R_{\delta_2}} \quad (4.37)$$

$$H_{120} = 3 + \frac{400}{R_{\delta_2}} \quad (4.38)$$

$$c_1 = 0.081 (R_{\delta_2} - 300)^{0.1} \quad (4.39)$$

$$c_2 = 0.0158 (R_{\delta_2} - 300)^{0.08} \quad (4.40)$$

$$c_3 = 1.06 + \frac{3000}{(R_{\delta_2} + 600)^{1.5}} \quad (4.41)$$

The C_f coefficient is calculated at each point by fitting a parabola between the values at transition C_{fT} , minimum, C_{fmin} and at reattachment $C_f = 0$. Where

$$C_{fmin} = -\sqrt{0.0002 \frac{h_T}{c}} \quad (4.42)$$

4.2.4 Intersection with inviscid distribution

The above procedure is valid for surface points up stream of the reattachment point. The calculation procedure continues from point of reattachment to the point where the obtained velocity U curve crosses the inviscid distribution. At crossing, the slopes are compared. If the difference in slope is greater than 1 deg another value of the factor A_2 is used to repeat the calculations. When the slop difference condition is satisfied the bubble model is terminated. The integration of the integral boundary layer equations continue using Drela turbulent closure up to the trailing edge.

If at reattachment the calculated velocity U is higher than the inviscid velocity the merge happens from above and A_2 is not iterated as argued by Dini [35].

4.2.5 Attached turbulent boundary layer

After the intersection with the inviscid profile is established, the integration of the integral boundary layer equations (4.43), (4.44), and (4.45) is continued in direct mode using the relations Eq.(4.46) to (4.56)

$$\frac{d\delta_2}{ds} = \frac{c_f}{2} - (H_{12} + 2) \frac{\delta_2}{U} \frac{dU}{ds} \quad (4.43)$$

$$\frac{d\delta_3}{ds} = c_D - 3 \frac{\delta_3}{U} \frac{dU}{ds} \quad (4.44)$$

$$\frac{\delta}{c_\tau} \frac{dc_\tau}{ds} = 4.2 (c_{\tau eq}^{0.5} - c_\tau^{0.5}) \quad (4.45)$$

$$C_{\tau eq} = \frac{0.015 H_{32}}{1 - U_{slip}} \left[\frac{H_{12} - 1}{H_{12}} \right]^3 \quad (4.46)$$

$$\delta = \delta_2 \left(3.15 + \frac{1.72}{H_{12} - 1} \right) + \delta_1 \quad (4.47)$$

The skin friction coefficient is obtained from the equation

$$C_f = \frac{0.3e^{-1.33H_{12}}}{(\log R_{\delta_2})^{1.74+0.31H_{12}}} + .00011 \left[\tanh \left(4 - \frac{H_{12}}{0.875} \right) - 1 \right] \quad (4.48)$$

$$C_D = c_f U_{slip} + 2C_\tau (1 - U_{slip}) \quad (4.49)$$

$$U_{slip} = \frac{H_{32}}{6} \left[\frac{4}{H_{12}} - 1 \right] \quad (4.50)$$

$$H_{12} = \begin{cases} \frac{H_{120}}{1 + \left(\frac{H_{32} - H_{320}}{c_1}\right)^{\frac{1}{1.27}}} & C_f > 0 \\ H_{120} + \left(\frac{H_{32} - H_{320}}{c_2}\right)^{\frac{1}{c_3}} & C_f < 0 \end{cases} \quad (4.51)$$

Where

$$H_{320} = 1.505 + \frac{4}{R_{\delta_2}} \quad (4.52)$$

$$H_{120} = 3 + \frac{400}{R_{\delta_2}} \quad (4.53)$$

$$c_1 = 0.081 (R_{\delta_2} - 300)^{0.1} \quad (4.54)$$

$$c_2 = 0.0158 (R_{\delta_2} - 300)^{0.08} \quad (4.55)$$

$$c_3 = 1.06 + \frac{3000}{(R_{\delta_2} + 600)^{1.5}} \quad (4.56)$$

The turbulent separation is triggered if the following condition is meet

$$H_{32} = 1.505 + \frac{400}{R_{\delta_2}} \quad (4.57)$$

The drag is then calculated by squire young formula as

$$C_d = \frac{\delta_{2TE}}{c} \left(\frac{U_{TE}}{U_\infty}\right)^{2.5+0.5 H_{12TE}} \quad (4.58)$$

The computation procedure is best explained through a Figure 4.12 and flow chart Figure 4.13.

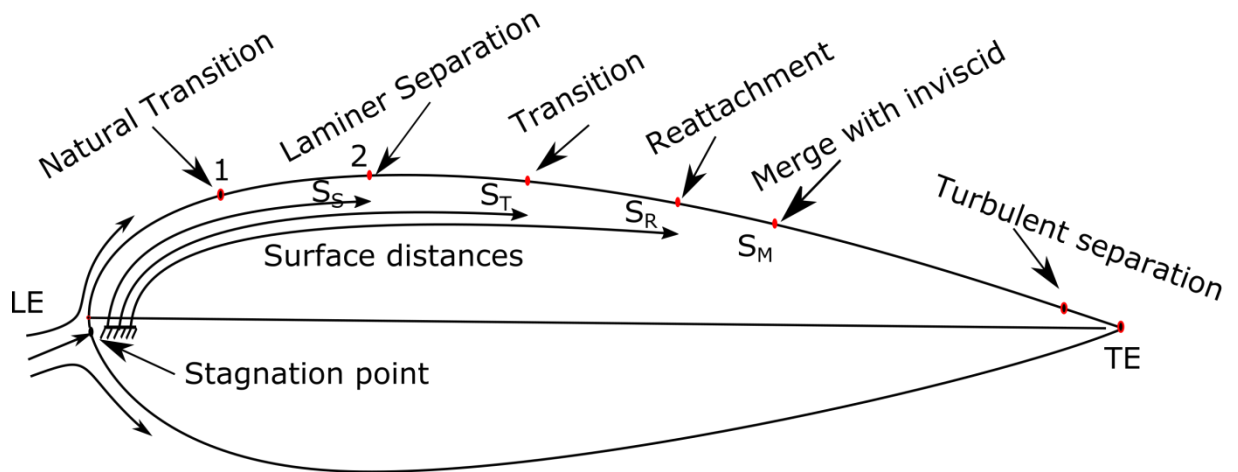


Figure 4.12 schematics of possible flow on airfoil with and without bubble

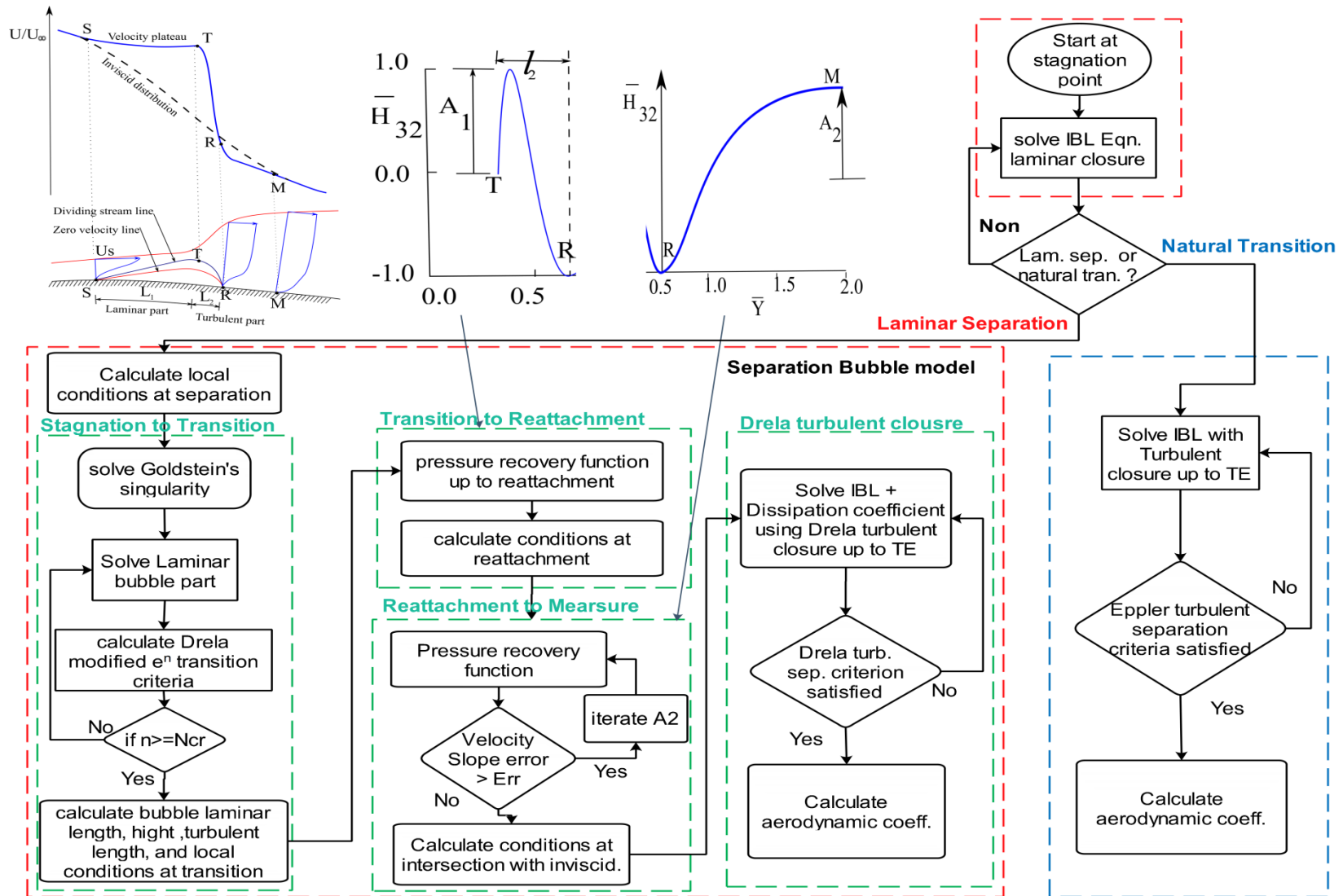


Figure 4.13 Flow chart for laminar separation bubble model

4.3 Validation of Aerodynamic calculations

Validation is performed by comparison with available experimental data from literature for incompressible flow at Reynolds number from 200,000 to 500,000 from NASA [59], and results from Illinois university [60], and [61]. Results are also verified by comparison with XFOIL code. The inviscid solution obtained from conformal mapping is utilized by momentum and energy integral equations solver. The resulting drag polar shows good agreement with experimental data. The computation cost is very small compared to other methods. The exception is when the interaction between viscous and inviscid is not weak, particularly close to maximum lift. The location of turbulent separation point is used to correct the lift and moment coefficients, which is successfully used to design large number of airfoils in the past. In fact, maximum lift coefficient is over estimated in most of the tested cases.

The validation process is performed for lift coefficient, drag coefficient, pressure distribution and boundary layer features for two airfoils at different angles of attack and Reynolds numbers.

The Eppler E387 airfoil is selected for the comparison since it is widely used in the Reynolds number range 200,000 to 500,000 and experimental data are available from different wind tunnels.

Figure 4.14 and Figure 4.15 show comparisons of calculated lift and drag coefficients compared to experimental measurement from [61] at Reynolds number of 300,000. The comparison show excellent agreement with experimental measurement both in lift and drag curves. At this Reynolds number a laminar separation bubble is formed on the airfoil upper surface during angles of attack up to approximately 7 degrees, as shown in Figure 4.16. The bubble starts at about mid chord and extends to 65% of the chord length. As the angle of attack is increased the bubble decreases in length and moves toward the airfoil leading edge. Figure 4.16 also shows a comparison of location of upper surface boundary layer features at Reynolds number 300,000 at different angles of attack. The figure shows location of laminar separation points, reattachment points and turbulent separation points. At low angles of attack current calculations, experimental measurement, and XFOIL results show similar trend for location of laminar separation and reattachment points. As the angle of attack increases above 8 degrees theoretical calculations fail to predict the short leading edge bubble shown by

experimental measurement. The turbulent separation location is very close to the trailing edge at low angles of attack, as the angle of attack is increased it moves forward in the direction of the leading edge causing smooth curvature in lift curve and increased drag. Experimental measurement show a sudden jump in location of turbulent separation location after certain angle of attack, while current calculations and XFOIL results show smooth variations up to high angle of attack.

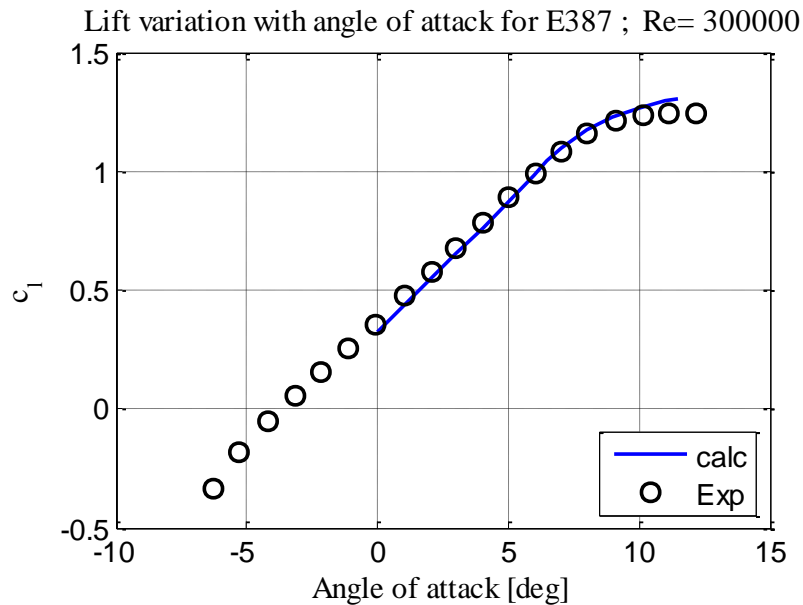


Figure 4.14 C_l versus α for for E387 airfoil at Re 300000, Exp from [61].

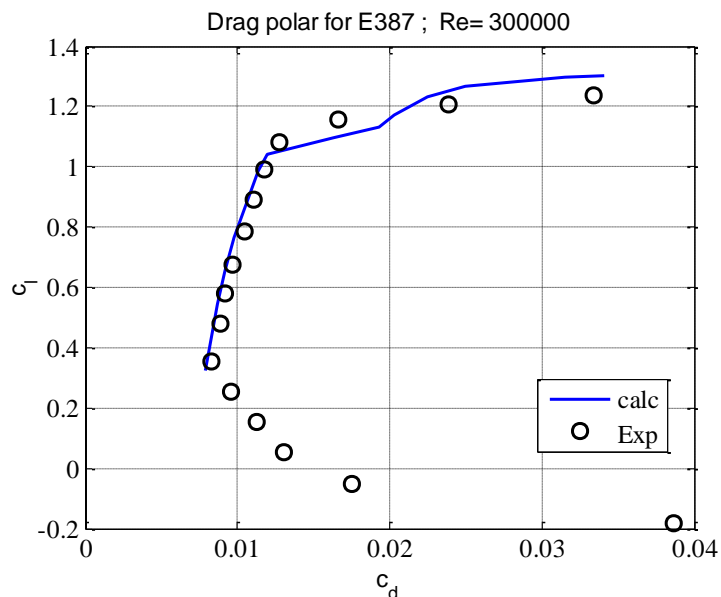


Figure 4.15 C_d versus C_l for for E387 airfoil at Re 300000, Exp from [61].

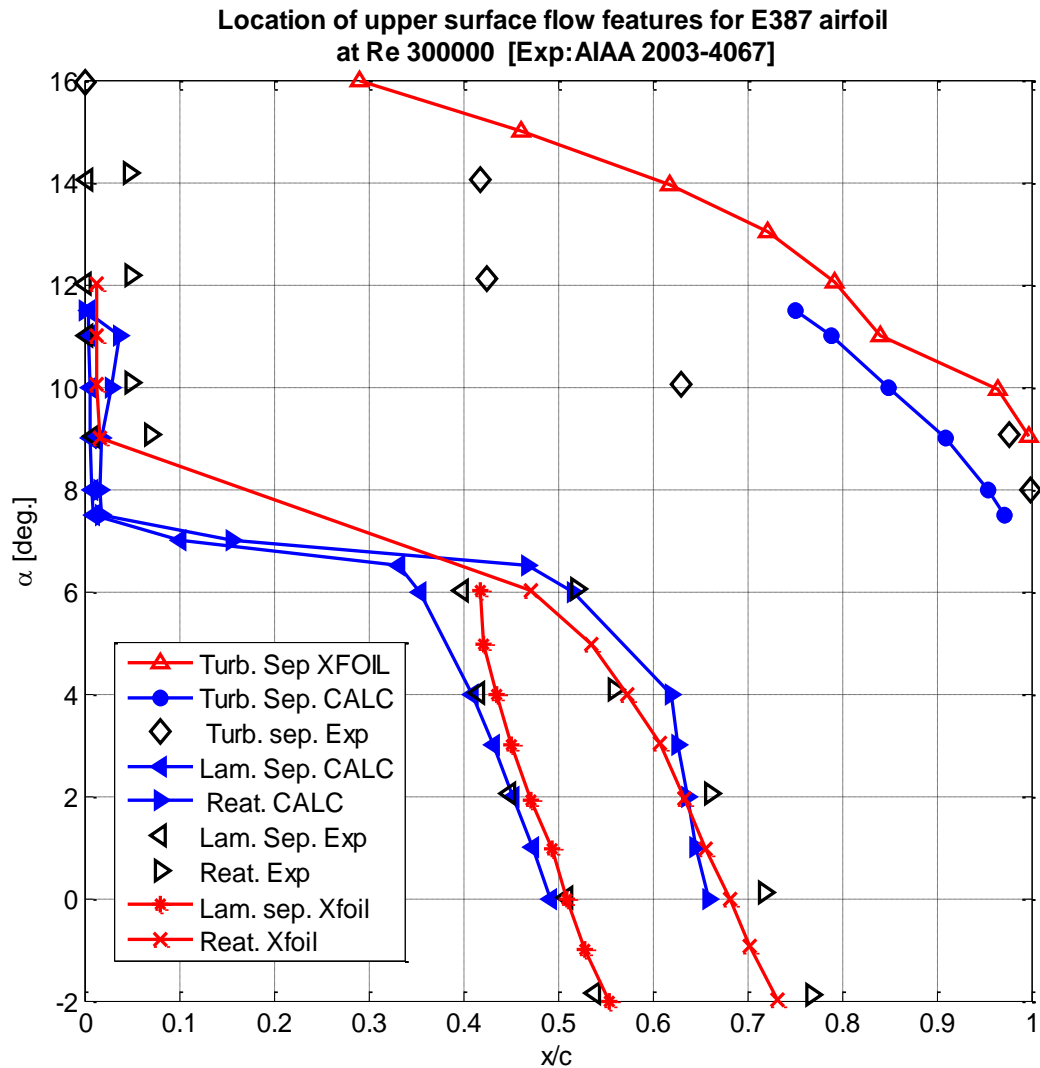


Figure 4.16 Comparisons of upper surface boundary layer features for E387 airfoil at Re 300,000

Pressure distribution

The pressure distribution calculated by the above method is compared to experimental measurement at angle of attack of 2 degrees and Reynolds number of 300,000, as shown in [59]. The laminar separation bubble calculations follow closely the experimental measurements. The bubble pressure variations is well predicted, the upper surface bubble is clearly shown, and the lower surface has nearly constant pressure over most of its length. Reference back to Figure 4.16 the pressure distribution show a large bubble that start at approximately 0.5c up to .65c. Details of upper surface boundary layer parameters are shown in Figure 4.19.

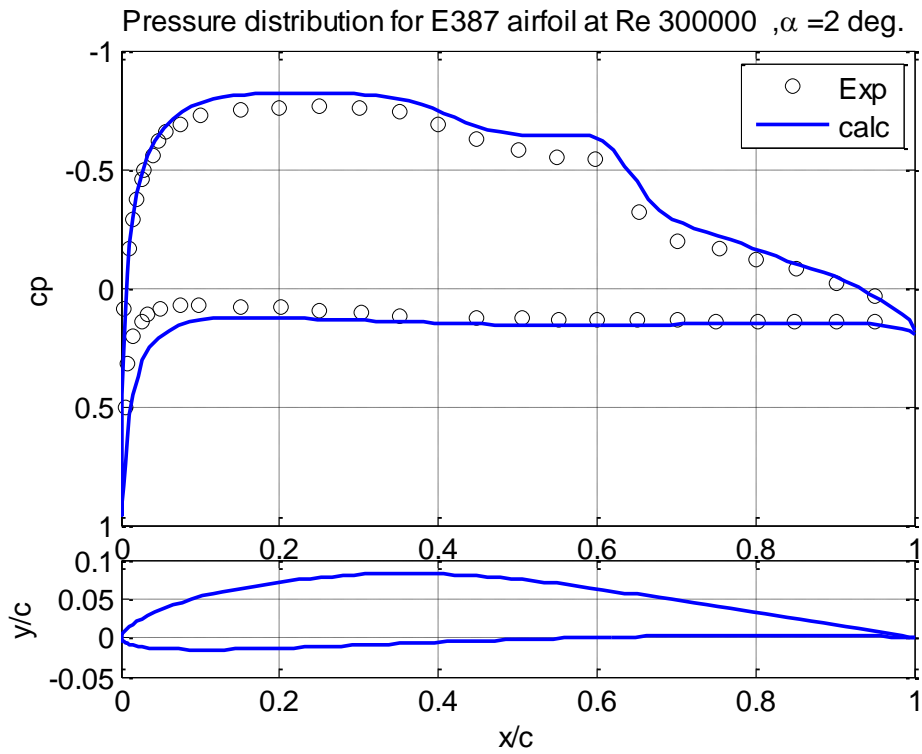


Figure 4.17 comparison of experimental and calculated pressure distribution for E387 airfoil at Re 300000 and angle of attack 2 deg.

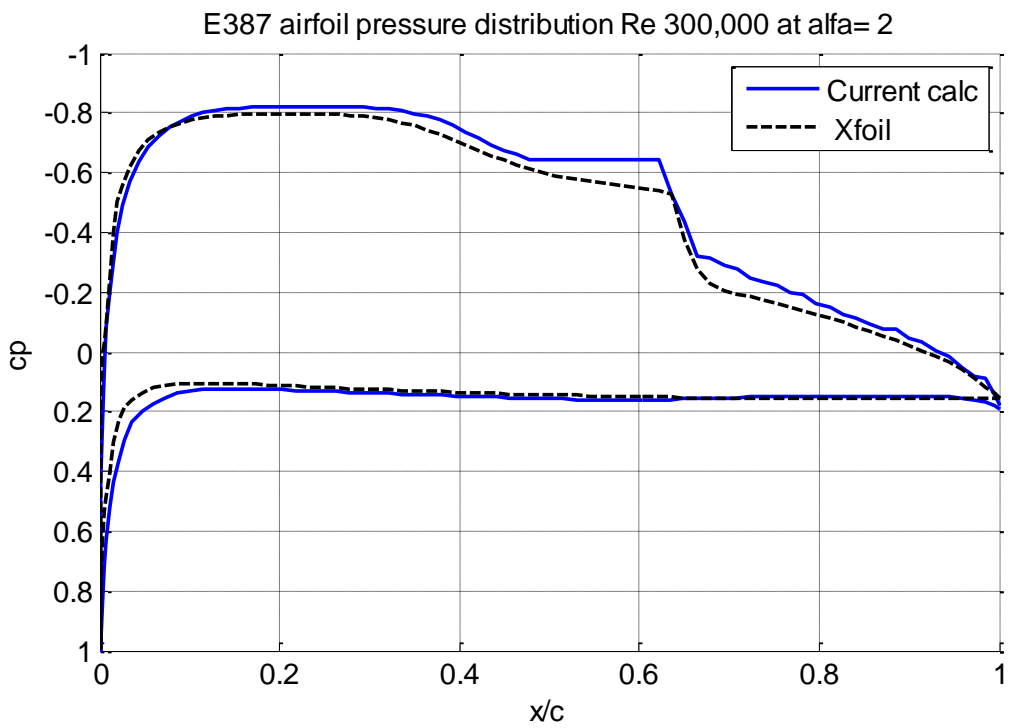


Figure 4.18 Comparison of pressure distribution with Xfoil code for E387 airfoil at Re 300000 and angle of attack 2 deg.

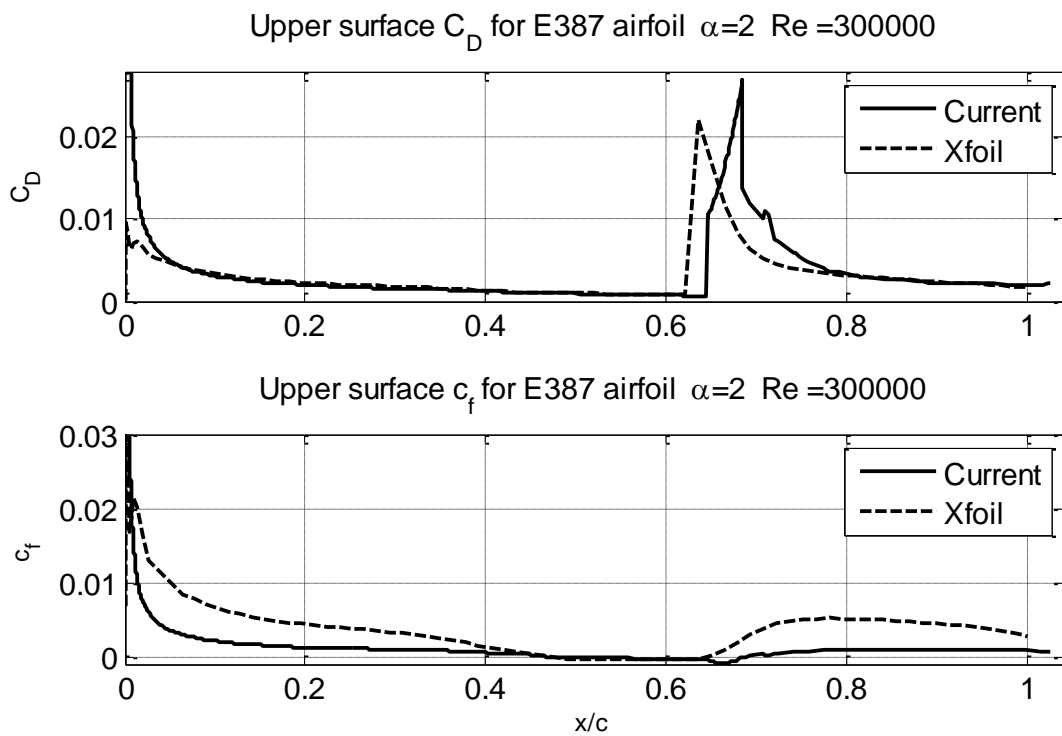
Boundary layer parameters

Figure 4.19 show upper surface boundary layer parameters as computed by the current code compared with that calculated by XFOIL. It shows laminar separation point at corresponding to $H_{32} = 1.51$ or $H_{12} = 4$. The boundary layer momentum thickness δ_2 variations show sudden increase inside turbulent part of the bubble as expected. The values of dissipation coefficient C_D and the friction coefficient c_f are also shown.

Figure 4.20 show upper surface boundary layer development as obtained for the above case. the points of laminar separation , transition and reattachment are indicated on the chart.

Comparisons with XFOIL code is also presented in Figure 4.21 and Figure 4.22 . H_{12} shape factor is XFOIL main shape factor. Comparisons show similar trend and similar maximum value. The momentum thickness δ_2 , which is the most important boundary layer parameter we looked for by this modeling to calculate drag , show good agreement with XFOIL.

Comparisons of friction coefficient C_f , dissipation coefficient C_D , velocity distribution $\frac{U}{V_\infty}$ and Reynolds number based on momentum thickness Re_{δ_2} show generally good agreement with XFOIL calculation. Lower surface boundary layer parameters are shown in Figure 4.23 to Figure 4.26, in which a laminar flow is preserved up to close vicinity to the trailing edge. Comparisons with XFOIL very close agreement. Boundary layer development chart shown on Figure 4.26 indicate a laminar separation very close to the trailing edge.



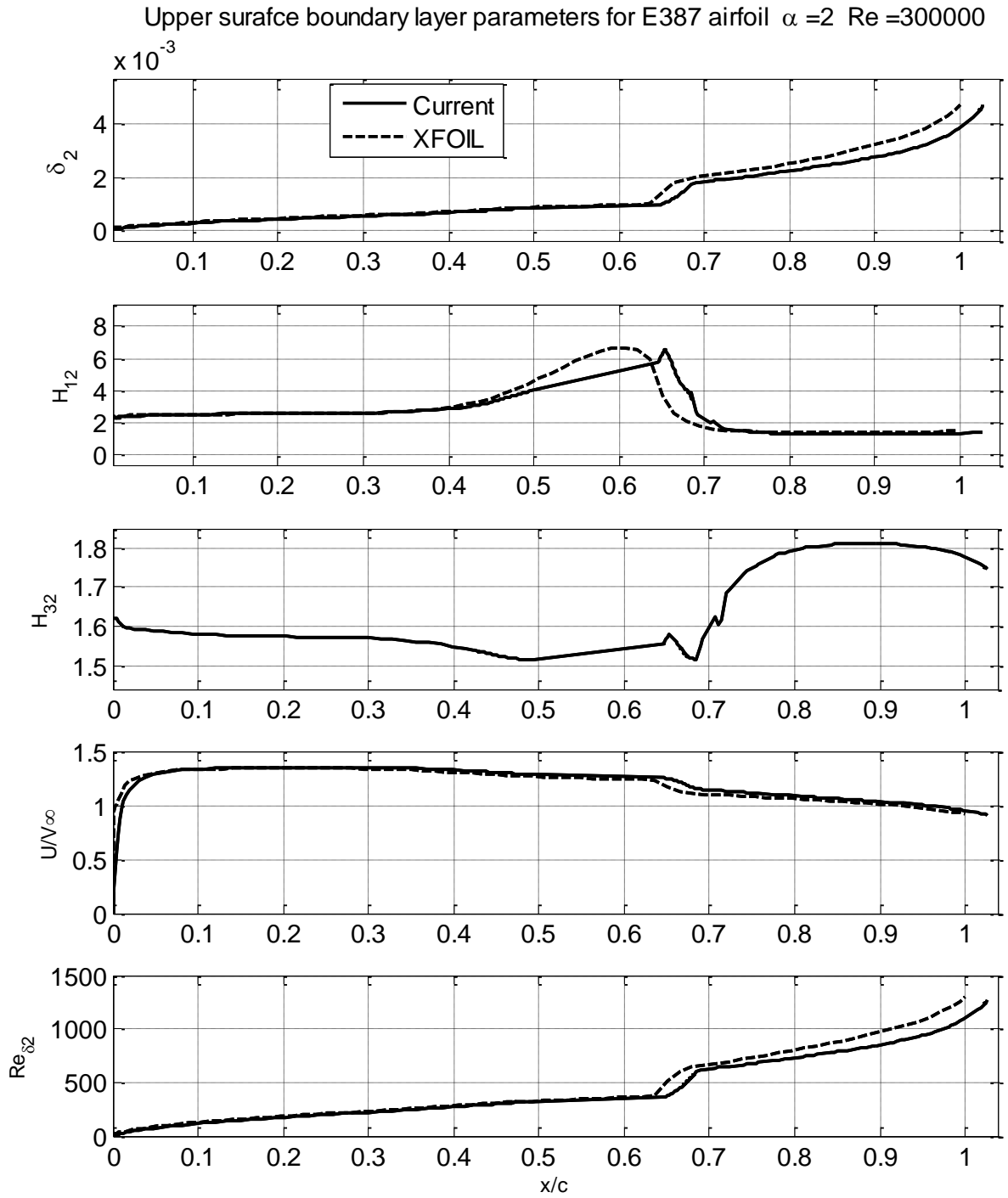


Figure 4.19 Upper surface boundary layer parameters at Re 300000 and $\alpha=2$ deg. (continued)

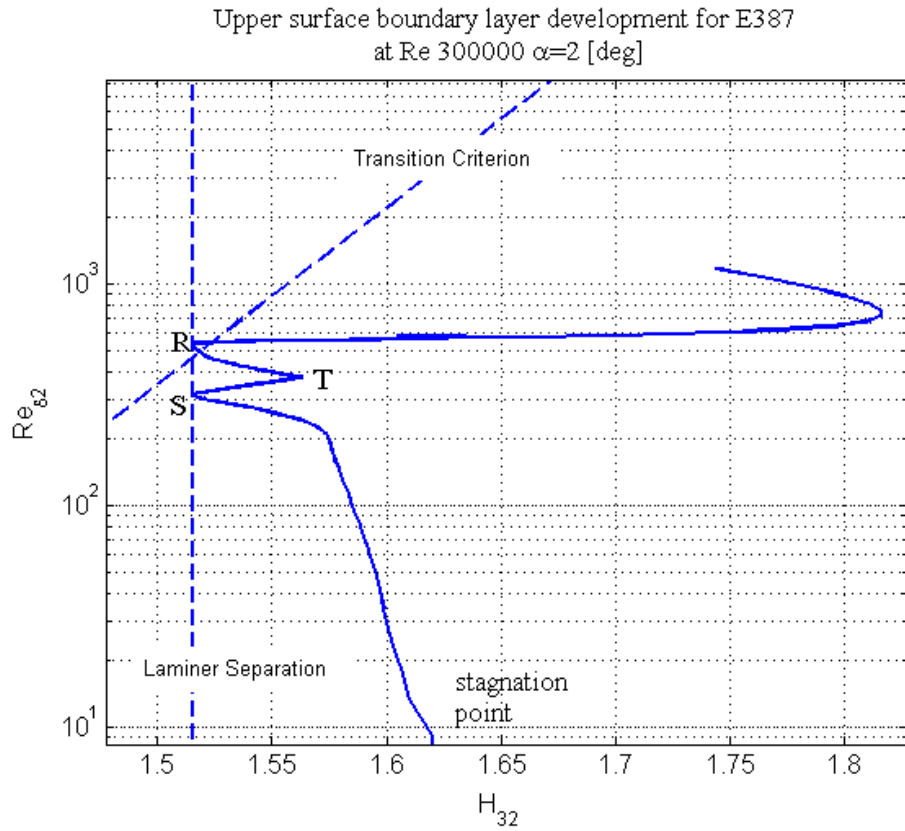


Figure 4.20 Upper surface boundary layer development chart for E387 at Re 300000 and $\alpha = 2$ deg.

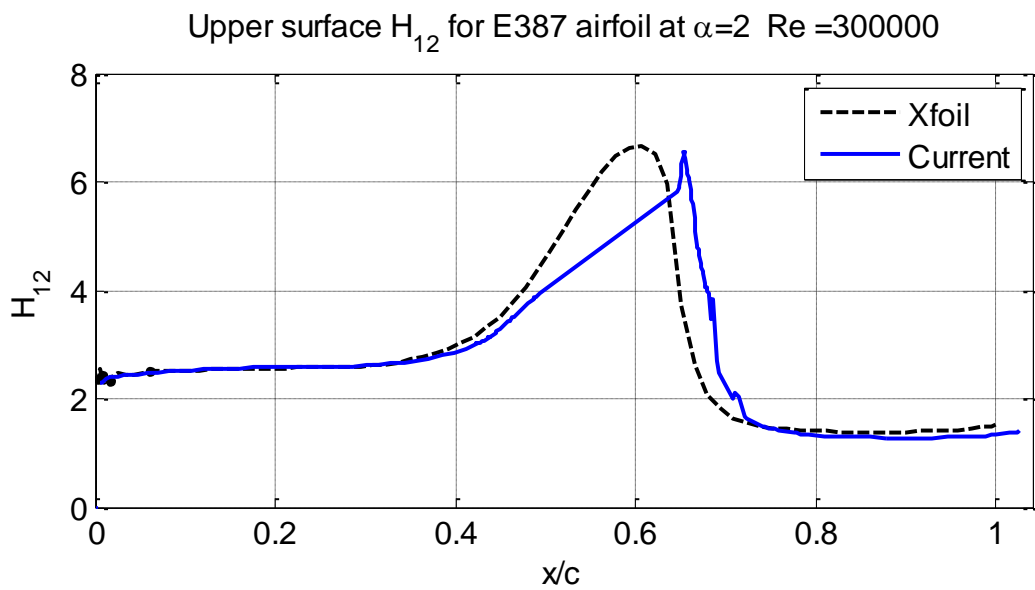


Figure 4.21 Comparison of upper surface boundary layer shape factor H_{12} for E387 at Re 300000 and $\alpha = 2$ deg.

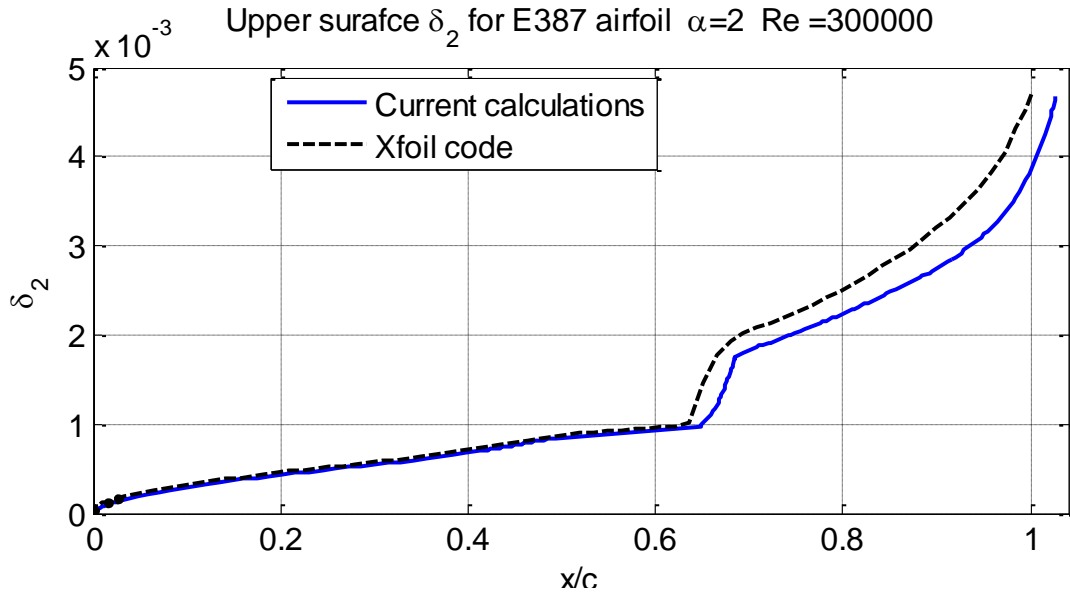


Figure 4.22 Comparison of upper surface boundary layer momentum thickness for E387 at $Re=300000$ and $\alpha=2$ deg.

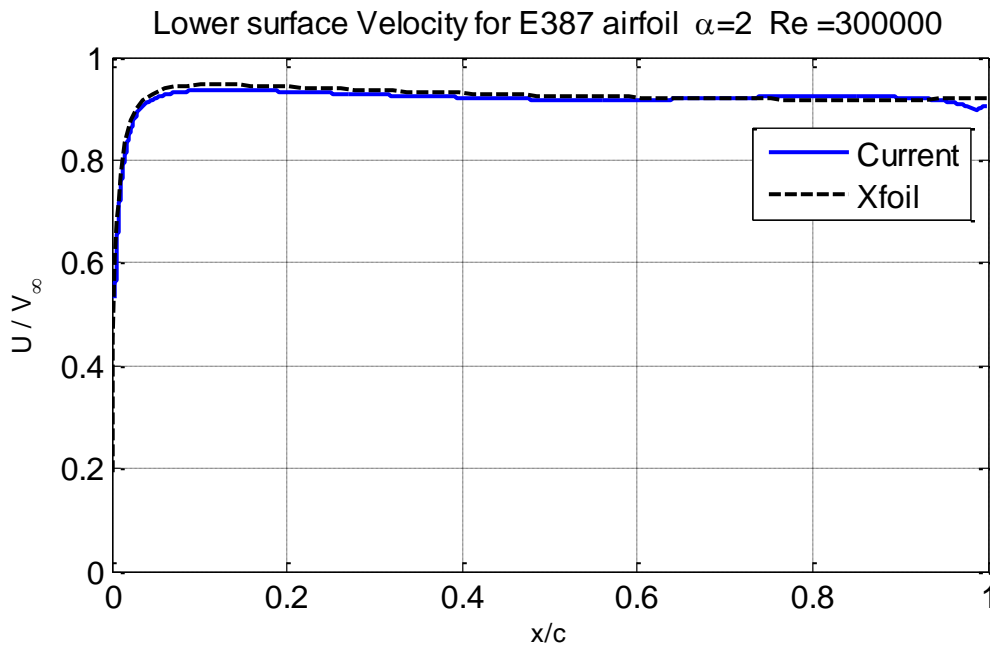


Figure 4.23 Lower surface velocity distribution for E387 at $Re=300000$ and $\alpha=2$ deg.

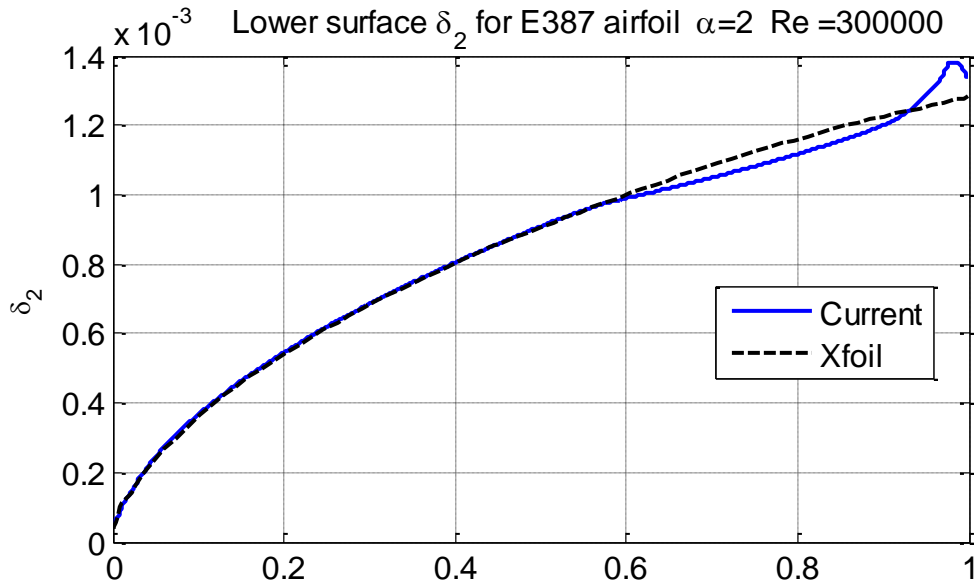
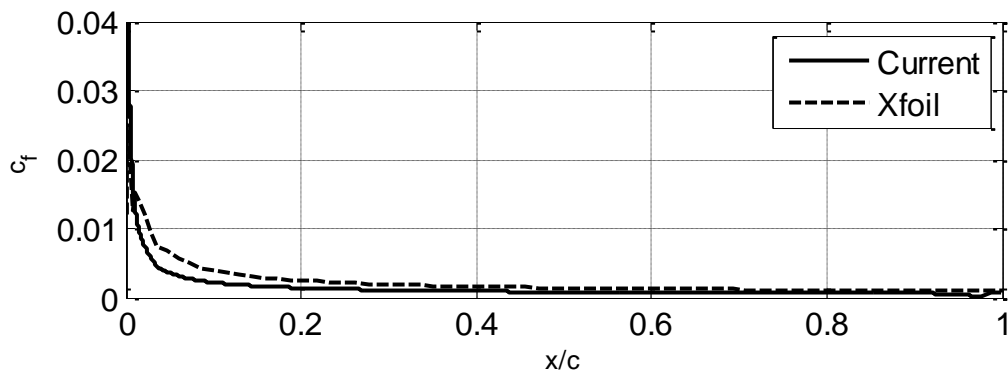
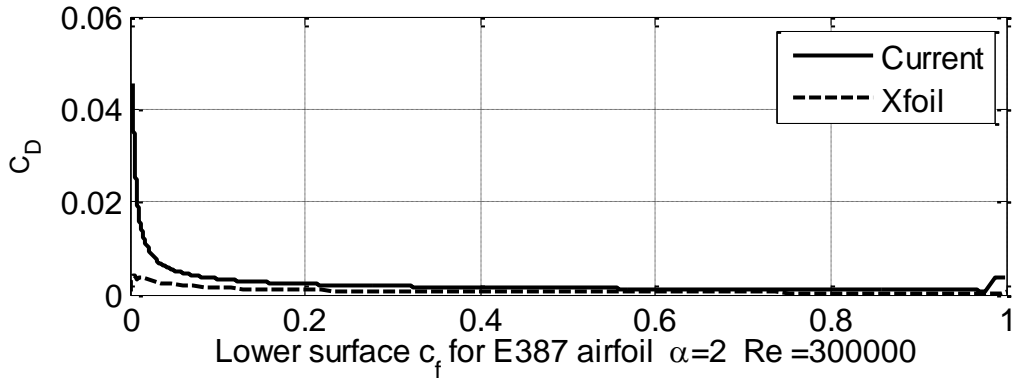


Figure 4.24 Variation of momentum thickness for the lower surface of E387 at Re 300000 and $\alpha = 2$ deg.

Lower surface boundary layer parameters for E387 airfoil $\alpha = 2$ Re =300000



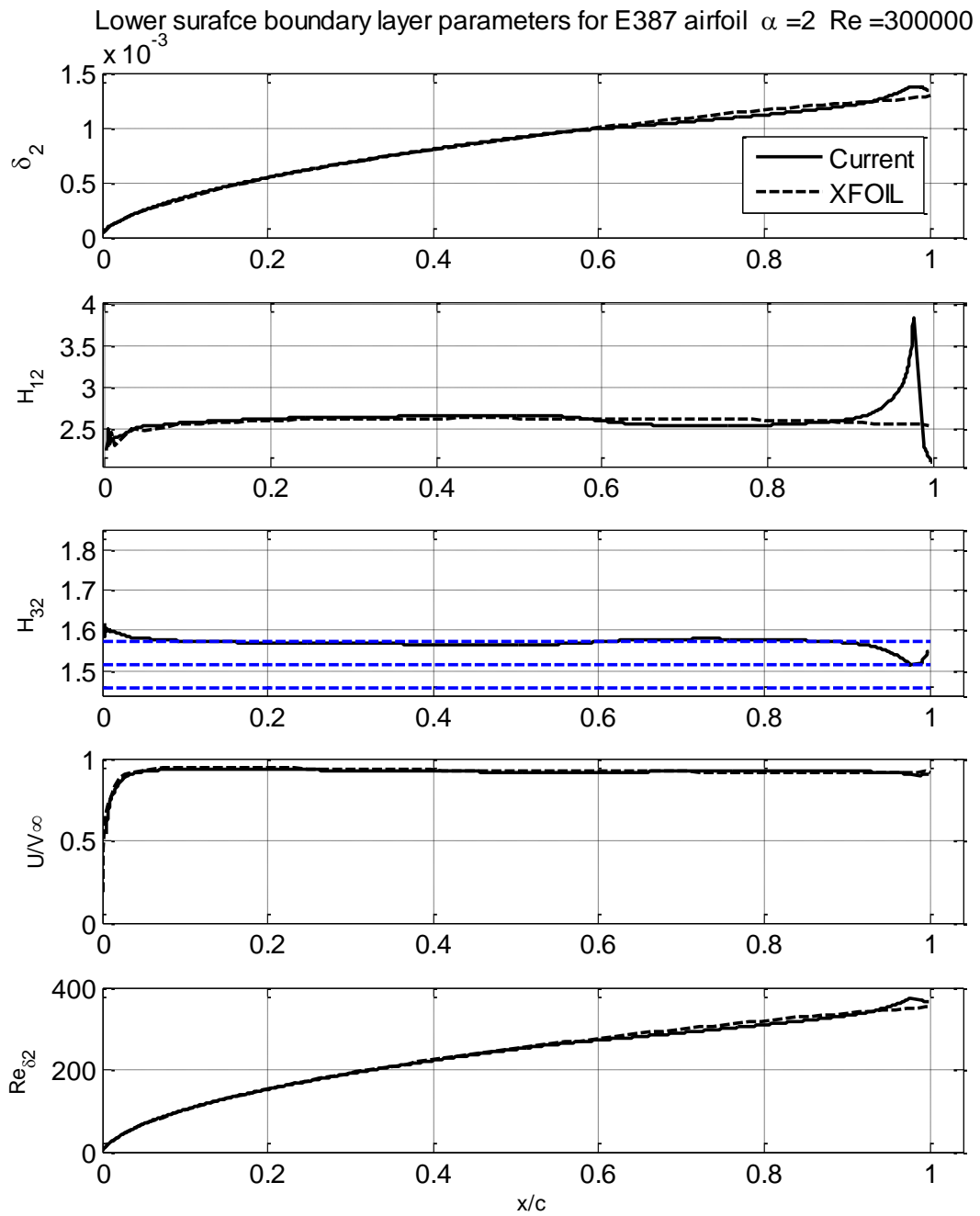


Figure 4.25 Lower surface boundary layer development parameters at Re 300000 and $\alpha=2$ deg.
(continued)

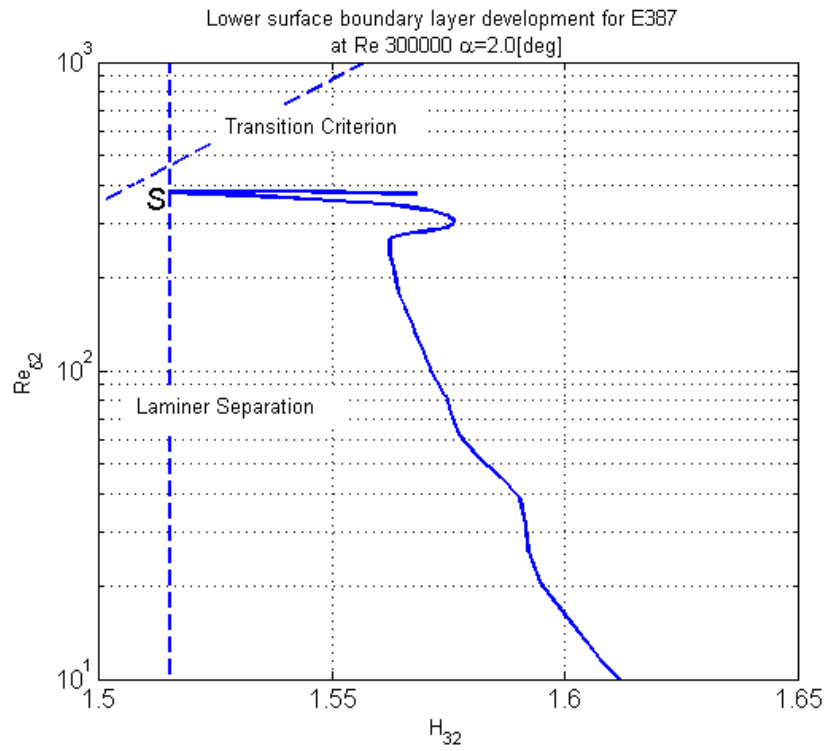


Figure 4.26 Lower surface boundary layer development chart for E387 at Re 300000 and $\alpha = 2$ deg.

4.3.1 Variation of aerodynamic coefficients with Reynolds number

Aerodynamic lift and drag coefficients of two airfoils at three Reynolds numbers are plotted in the following figures from Figure 4.27 to Figure 4.32. Comparisons show generally a good agreement with experimental data. When large separations are present, however, the current calculations over estimate both lift and drag. Maximum lift coefficient is over estimated but the angle of attack of maximum lift is computed with fair accuracy.

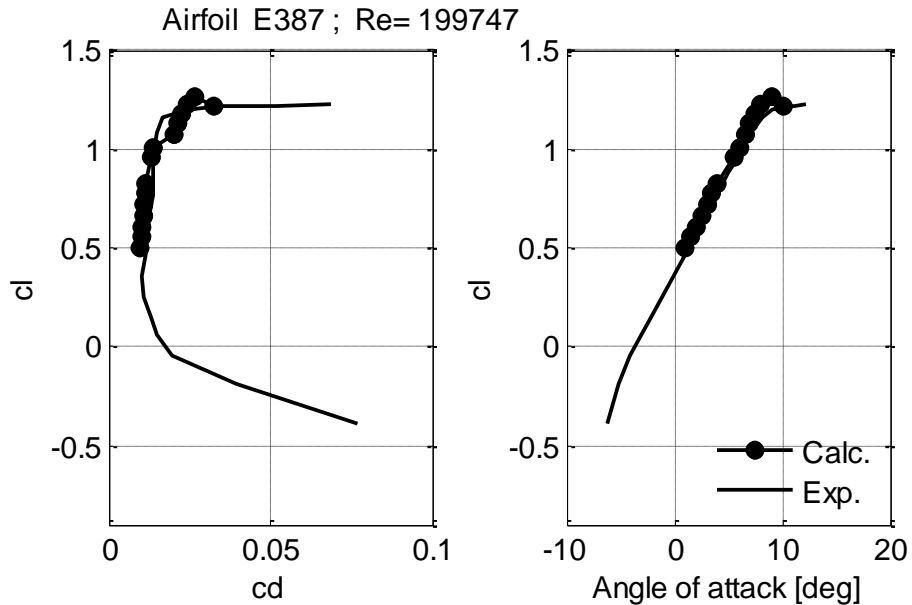


Figure 4.27 Comparisons between calculated and experimental data for E387 at Re=200,000.

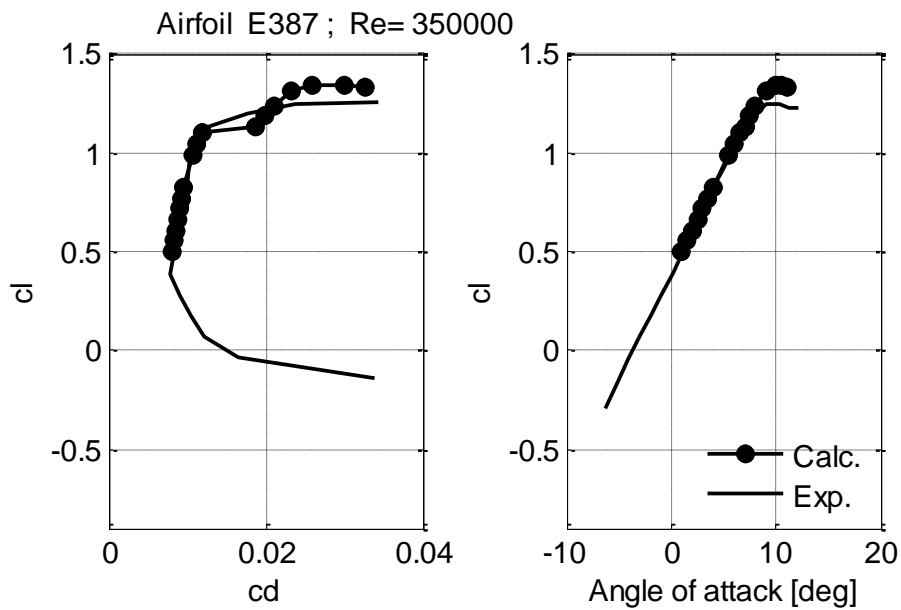


Figure 4.28 Comparisons between calculated and experimental data for E387 at Re=350,000.

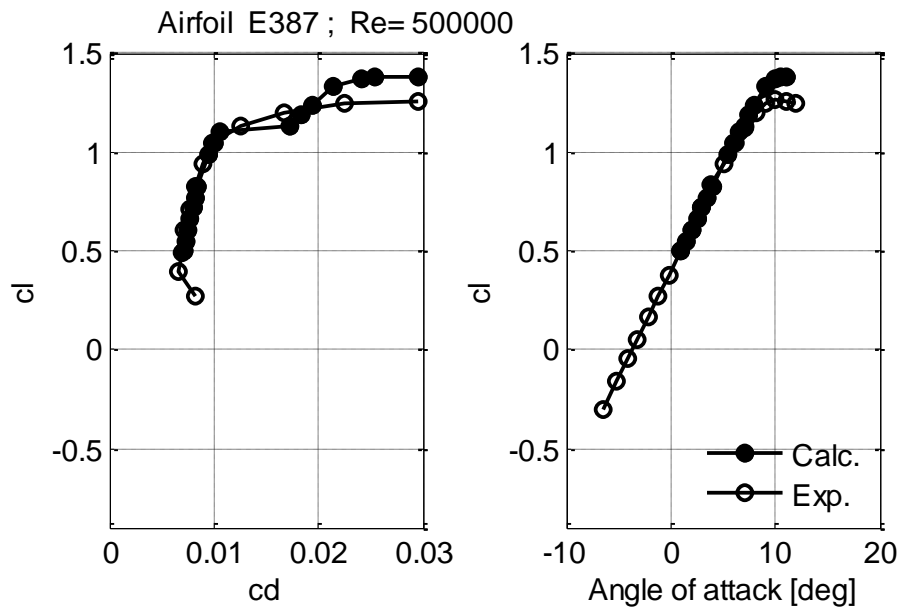


Figure 4.29 Comparisons between calculated and experimental data for E387 at Re=500,000.

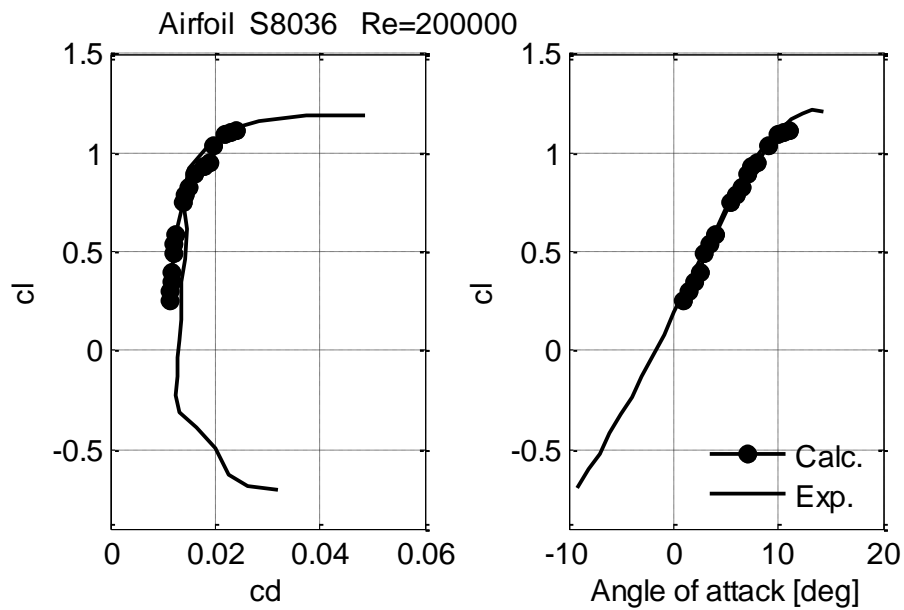


Figure 4.30 Comparisons between calculated and experimental data for S8036 at Re=200 000

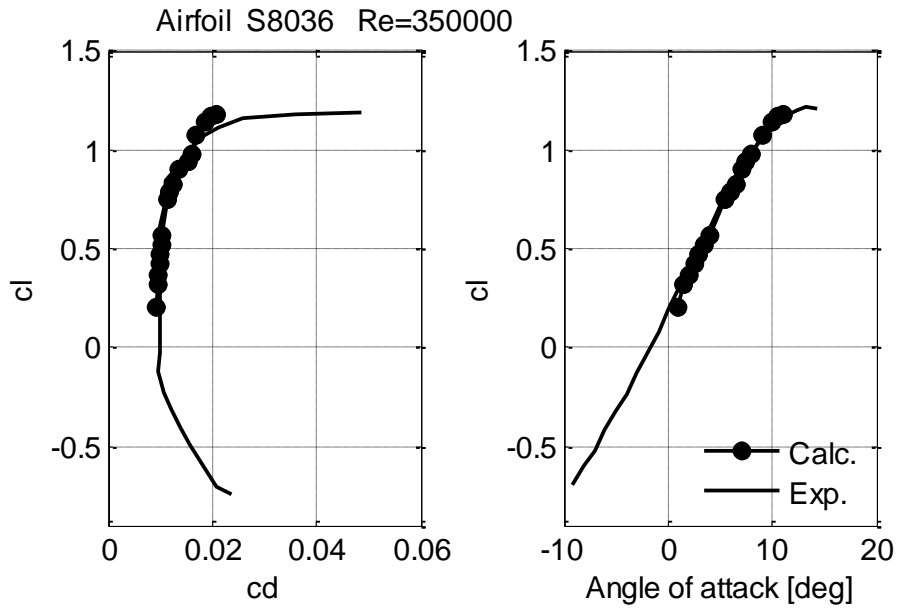


Figure 4.31 Comparisons between calculated and experimental data for S8036 at Re=350,000

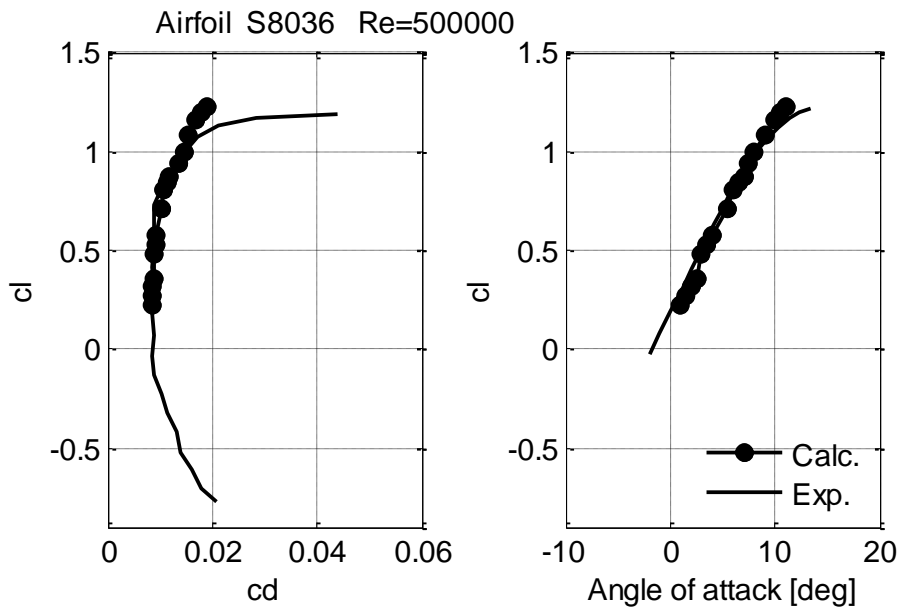


Figure 4.32 Comparisons between calculated and experimental data for S8036 at Re=500,000.

4.3.2 Variation of boundary layer features with Reynolds number

Boundary layer flow features are the positions on the airfoil surface where important changes happen in the boundary layer flow on upper or lower surfaces, such as location of laminar separation point, transition point, reattachment point and turbulent separation point. When laminar separation bubble occurs transition is assumed inside the bubble.

Current calculation results are compared with published experimental data for two selected airfoils. The first airfoil is Eppler low Reynolds number airfoil E387 which is used as benchmark for validating low Reynolds number aerodynamic computations. It is extensively tested in NASA Langley Low Turbulence Pressure Tunnel (LTPT, where drag polar, and pressure measurements at low Reynolds numbers are published [59]. Recently, E387 airfoil is tested in the University of Illinois at Urbana-Champaign (UIUC) subsonic wind tunnel [60], [61], which is intended to validate and refine airfoil low Reynolds number computation methods. The second airfoil is Selig S8036 low Reynolds number airfoil designed for soft stall characteristics. Experimental measurement data for these two airfoils at flow Reynolds numbers are 200,000, 350,000 and 500,000 are used in the validation of current computations. These measurements include drag polar and location of upper surface boundary layer flow features.

Comparisons of measured [59] and calculated pressure distributions over E387 airfoil at Reynolds number of 300,000 and at angles of attack of 4, and 6 degrees are shown in Figure 4.33 and Figure 4.34. The location of the separation bubble is clearly observed on the upper surface. Calculated pressure distribution agrees with experimental data and XFOIL results. The bubble location is calculated with acceptable accuracy for optimization computations.

The general observation is that the bubble moves upstream as angle of attack increase, with length being shorter. Figure 4.18 shows comparisons of locations of upper surface features of the two airfoils at different angles of attack and Reynolds numbers of 200,000, 350,000, and 500,000. The computed laminar separation, Reattachment, and turbulent separation locations on upper surface are compared to experimental measurements. Laminar separation and reattachment locations from XFOIL are also shown for E387 at Reynolds number 350,000.

A laminar separation bubble extends on the upper surface starting approximately at mid chord. As angle of attack increases the bubble moves toward the leading edge, and its length decreases. When the bubble length close to leading edge is very short, it could be interpreted

as a transition without bubble. Current calculations follow the general trend of both experimental measurement and XFOIL predictions. As Reynolds number increases the laminar separation bubble tend to shorten in length, which is in agreement with the general fact that laminar separation bubble is more dominant in low Reynolds number range. The results of XFOIL and current calculations seem to under estimate the reattachment point location, this is also noted [62]. For low angles of attack turbulent separation take place at or very close to the trailing edge. When angle of attack increases further turbulent separation moves forward causing high increase in drag and loss in lift.

In all cases turbulent separation point assessed by current computations and XFOIL code at high angles of attack is more aft than the measured locations. This miss-predictions has the consequence of over estimating the angle of maximum lift, and thus the value of maximum lift coefficient.

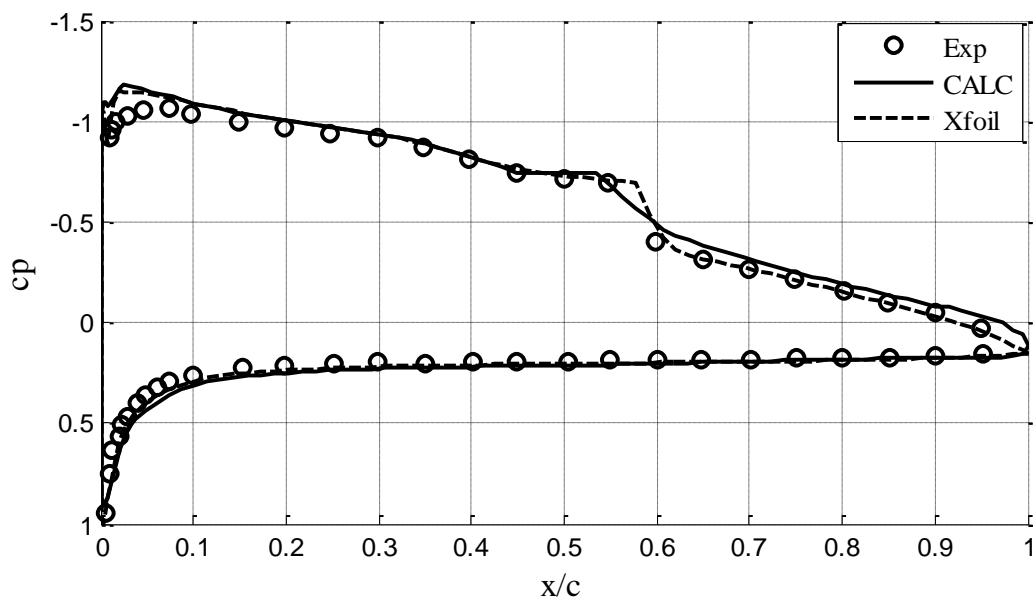


Figure 4.33 Pressure distribution for E387 at Re 300 000 and $\alpha = 4^\circ$

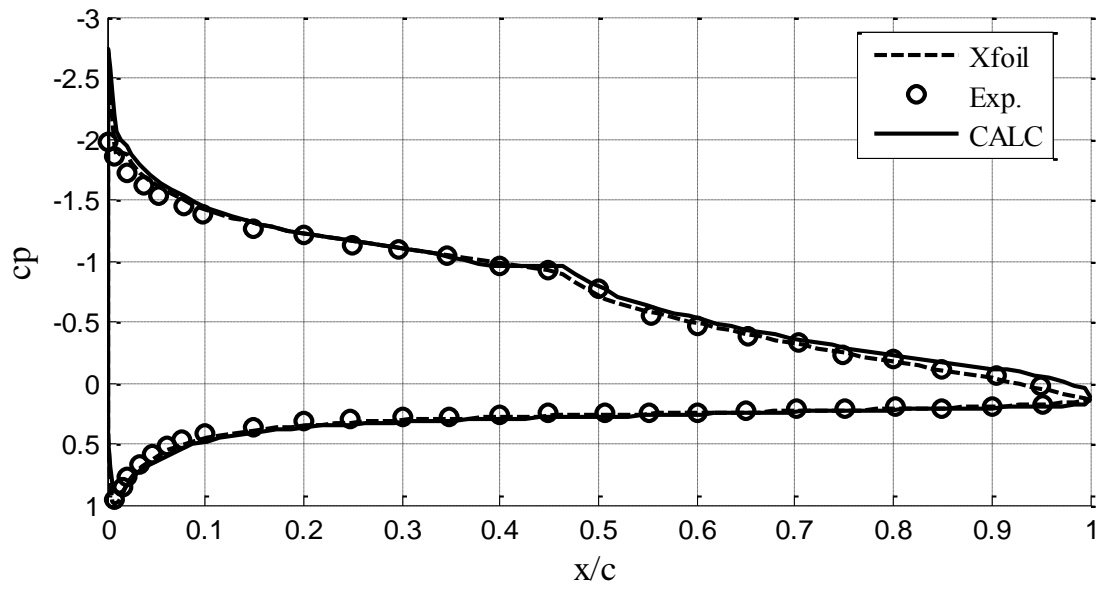


Figure 4.34 Pressure distribution for E387 at Re 300 000 and $\alpha = 6^\circ$

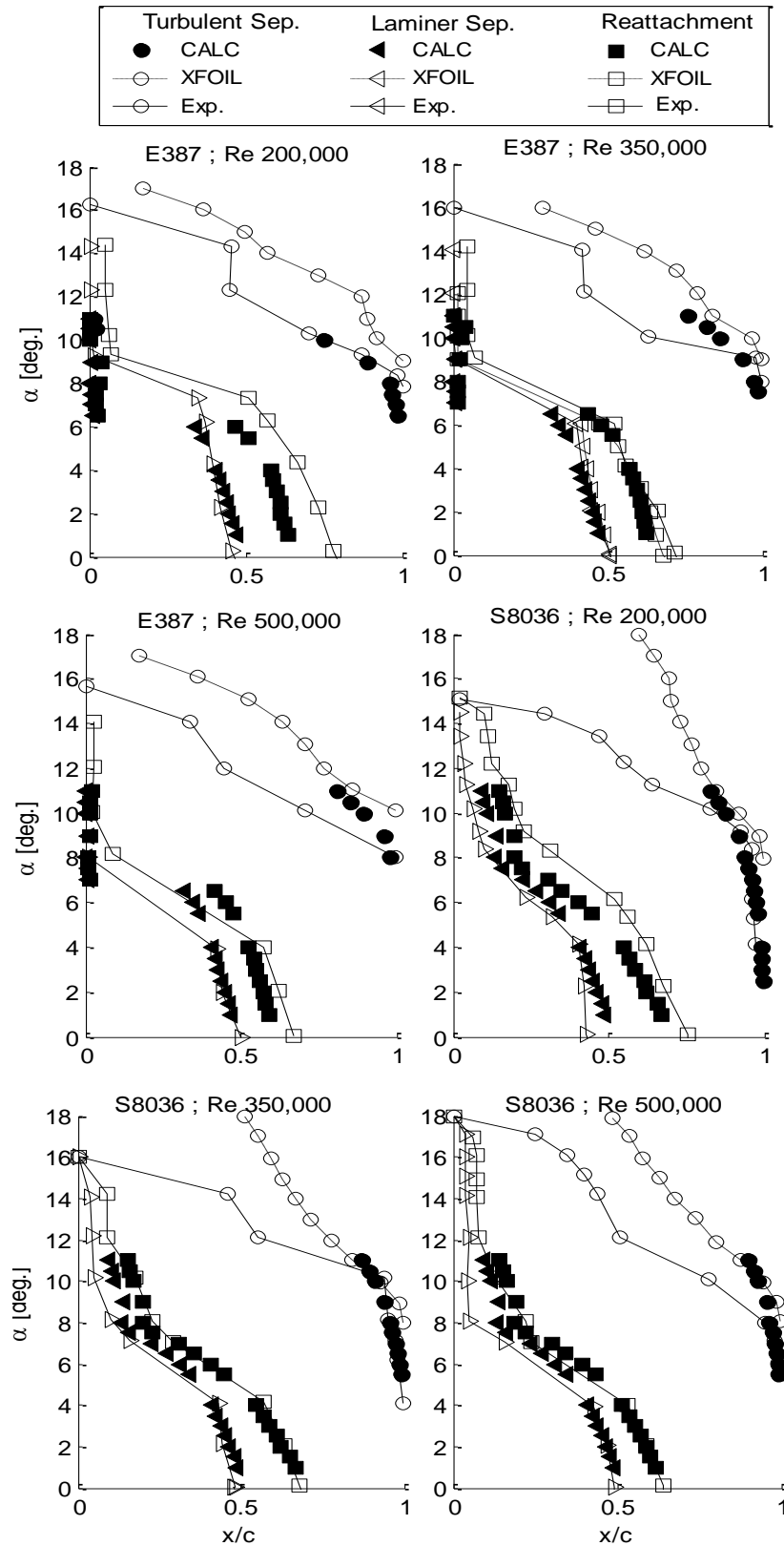


Figure 4.35 Comparisons of locations of upper surface flow features for E387 and S8036 at Re 200,000, 350,000, and 500,000. (Solid lines represent experimental data, dashed lines is XFOIL, and filled symbols are current calculations).

CHAPTER 5

5 Airfoil Parametric Representation

5.1 General Requirement

Parameterization is defined as representing aerodynamic characteristics, such as shape or pressure distribution, in terms of few numerical parameters. These parameters are called design variables. Parameterization is often applied to aerodynamic geometric characteristics of airfoils, wings or even complete configuration. When the design variables are modified the aerodynamic performance is correspondingly changed. The optimization algorithm and the designer should look for the design variables that will improve aerodynamic, structure or flight performance. This process is called optimization. The aerodynamic analysis will lead to a selection of a set of design variables that satisfies predefined requirements. Each design variable can change within specified range. Design space is defined by the ranges of all design variables. For instance, airfoils can be described using NACA representation (discussed in the next section). Four digit NACA definition uses only 3 parameters to represent airfoils. The low number of parameters allows fast design and analysis but it may not cover all possible airfoil shapes. Other airfoil parameterization methods are in use that can cover more design space and produce improved performance. Conversely, a higher number of design parameters may lead to improvement in performance, but requires higher computational cost during the optimization process. Therefore, in many cases tradeoff studies between computational cost and number of required parameters is necessary. Computational cost is often measured by number of calls to analysis code. In this work the parameterization method that will capture a global design space with reduced number of design parameters is used.

Airfoil parametric representation is considered recently by many authors for use in numerical optimization and design. One main reason is that aerodynamic analysis codes ask for many airfoil coordinate points (about 100 points or more). Using these coordinates as design variables results in non-smooth airfoils which is not aerodynamically acceptable and will also result in very long optimization time due to large number of design variables. By selecting

proper airfoil parametric representation method this problem can be solved. Klfan, [63] stated a number of factors that are considered during the choice of parametric representation methods for aerodynamic design. Selection of optimization algorithm, computational cost required to reach optimum design, and if the optimum design is contained in the design space, and whether it can be found by search algorithms.

Parametric airfoil representation methods work with parameterization of airfoil shape, which means that it represent airfoils with few parameters that control airfoil counters. NACA 4 digit airfoil representations uses 3 parameters, PARSEC method uses 11 parameters to represent upper and lower airfoil surfaces, CST method on the other hand uses a number of coefficients in polynomial series which can produce rounded leading edge and sharp trailing edge shapes. The following section describes some airfoil parametric representation methods.

5.2 NACA Airfoil Series

Airfoils shape is defined in a variety of methods. NACA has its own methods of representing groups of airfoils, such as 4 digit 5 digit or 6 digit series. Reference [65] provides details of NACA definitions. Although, these airfoils are successfully used in many applications, a need for airfoil shapes that perform better in for specific applications, such as blade design, propellers, or at low Reynolds number has derived the research toward other airfoil representation methods.

NACA airfoils grouped in series such as 4-digit, 5-digit and 6-digit series. Their coordinates were derived from either geometrical methods using analytical equations that describe the camber distribution and the thickness distribution along the chord line, see Figure 5.1, or are derived using theoretical methods like 6-digit series.

5.3 4-digit series airfoils

It is the first series of airfoils designed using this approach. They have 4 digits; the first digit is denoted by (m) specifies the maximum camber in percent of airfoil chord. The second digit represents the position of maximum camber (p) in tenths of airfoil chord. The last two digits represent the maximum airfoil thickness (t) in percent of chord. Thus NACA2412 airfoil, for example, has 2% camber located at 40% of its chord from leading edge and 12% chord thick. This representation requires specification of these 3 parameters to find out the airfoil coordinates for upper and lower airfoil surfaces. as in Figure 5.1.

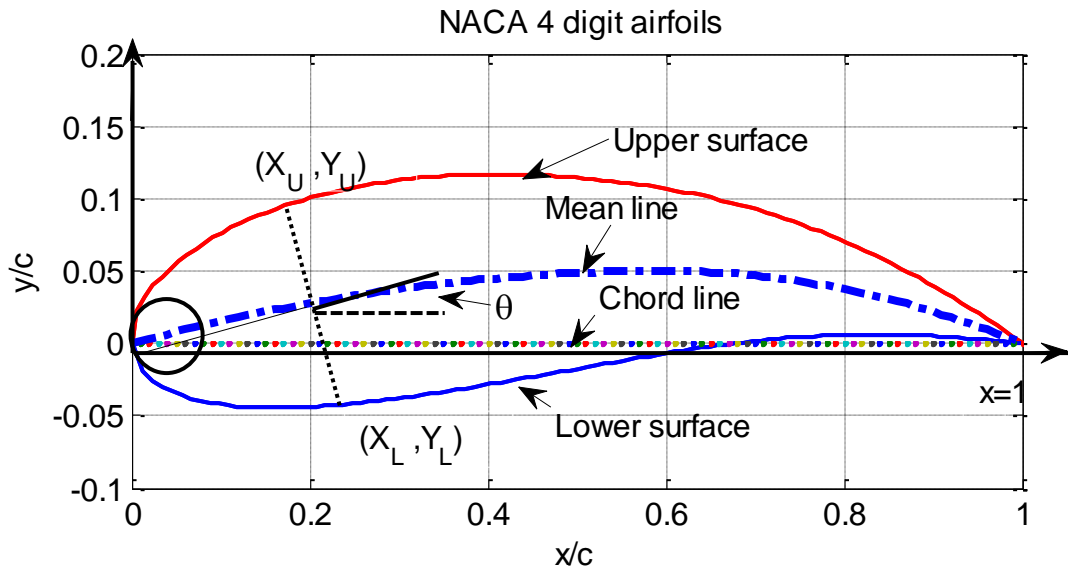


Figure 5.1 NACA Airfoil geometrical parameters

The procedure to find the airfoil coordinates is summarized by the following steps and sample calculations are shown in Figure 5.2 :

- a. Chord length is made non dimensional by dividing by chord, thus x varies from 0 at LE to 1 at TE.
- b. Using the values of p and m , it is possible to compute mean camber for each value of x using the following equations:

$$y_c = \frac{m}{p^2} (2px - x^2) \quad \text{for } x \text{ from } 0 \text{ to } p \quad (5.1)$$

$$y_c = \frac{m}{(1-p)^2} [(1-2p) + 2px - x^2] \quad \text{for } x \text{ from } p \text{ to } 1 \quad (5.2)$$

where

y_c is camber coordinates.

p - is first digit in NACA designation divided by 100.

m - is the second digit value in NACA designation divided by 10.

t - is the last two digits divided by 100.

- c. Compute the thickness distribution around the mean camber by substituting t into the following equation:

$$\pm y_t = \frac{t}{0.2} (0.2969\sqrt{x} - 0.1260x - 0.0351x^2 + 0.2843x^3 - 0.1015x^4) \quad (5.3)$$

- d. Calculate the upper (x_u, y_u) and lower (x_L, y_L) airfoil coordinates using:

$$\theta = \arctan\left(\frac{dy_c}{dx}\right)$$

$$X_u = x - y_t \sin\theta$$

$$X_L = x + y_t \sin\theta$$

$$Y_u = y_c + y_t \cos\theta$$

$$Y_L = y_c - y_t \cos\theta$$

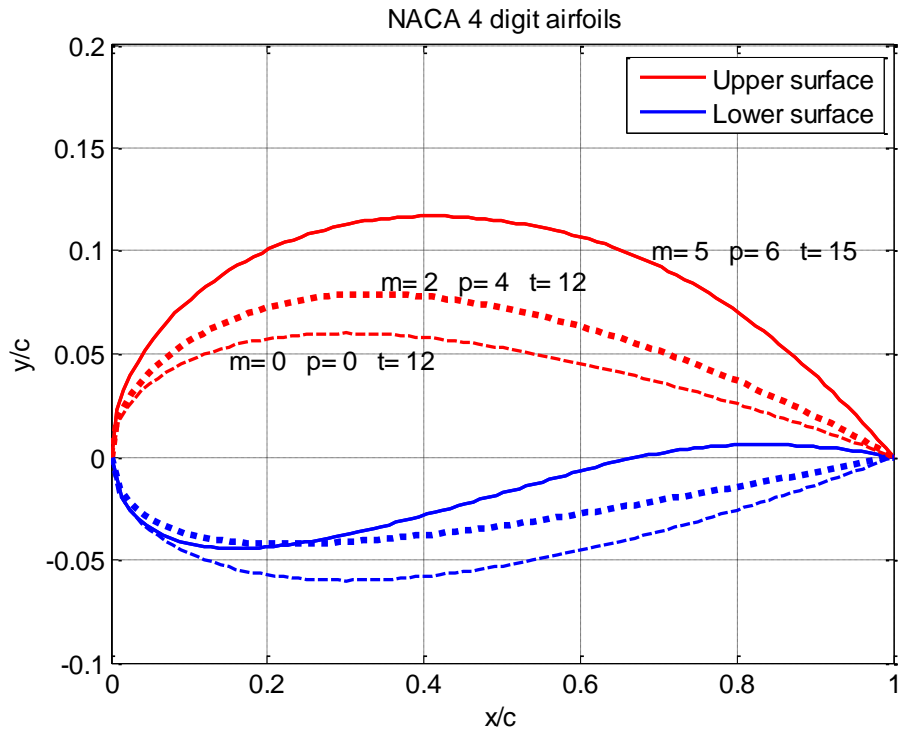


Figure 5.2 NACA 4- digit airfoil representation parameters

5.4 PARSEC Method

It is a commonly used method. This method is originally developed by Sobieczky, 1998 [66] for used in subsonic and transonic airfoils. Its main idea is expressing the airfoil surface as an unknown linear combination of appropriate mathematical function, and selecting a number of important geometric characteristics of the airfoil as the design variables, in such a way that the airfoil shape can be determined from these variables by solving a linear system of equations. Eleven airfoil geometric characteristics are used to represent airfoil as illustrated in Table (1) and Figure 5.3.

Table 5.1 Parsec method parameters

r_{LE}	Leading edge radius
X_{up}	X location of Upper crest
Y_{up}	Y location of Upper crest
Y_{xxup}	Upper surface curvature
X_{Lo}	X location of Lower crest
Y_{Lo}	Y location of Lower crest
Y_{xxLo}	Lower surface curvature
DY_{TE}	Trailing edge thickness
Y_{TE}	Trailing edge y location
α_{TE}	Trailing edge direction
β_{TE}	Trailing edge included angle

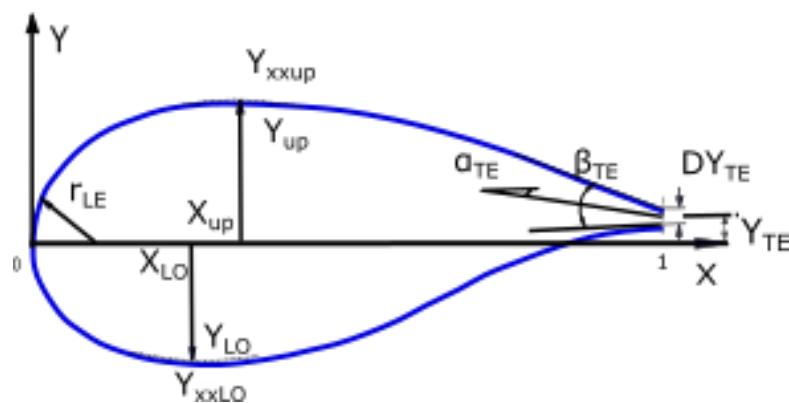


Figure 5.3 PARSEC method for airfoil parameters

The parsec equation is given by Eq.(1)

$$Y_j = \sum_{n=1}^6 a_{n,j} X_j^{n-\frac{1}{2}} \tag{5.4}$$

Where j takes a value of 1 for upper surface and 2 for the lower surface, the coefficients and are determined by using the above mentioned airfoil geometric characteristics.

The above equation can be written for the upper and lower airfoil surfaces as follows

$$Y_{up} = \sum_{n=1}^6 a_n X_{up}^{n-\frac{1}{2}} \quad (5.5)$$

$$Y_{LO} = \sum_{n=1}^6 b_n X_{LO}^{n-\frac{1}{2}} \quad (5.6)$$

A specific relations can be derived for the upper and lower surfaces as follows

$$r_{LE} = \left[\frac{1 + \left(\frac{dz}{dX}\right)^2}{\left(\frac{d^2z}{dX^2}\right)} \right] \quad (5.7)$$

1- Leading edge radius

For upper surface $\Gamma_{LEUP} = \left| \frac{(a_1)^2}{2} \right| \quad (5.8)$

For lower surface $r_{LELO} = \left| \frac{(b_1)^2}{2} \right| \quad (5.9)$

2- Trailing edge position

For lower surface $Y_{TEUP} = Y_{TE} + \frac{1}{2}DY_{TE} \quad (5.10)$

For lower surface $Y_{TELO} = Y_{TE} - \frac{1}{2}DY_{TE} \quad (5.11)$

3- Airfoil coordinates

$$Y_{up} = \sum_{n=1}^6 a_n X_{up}^{n-\frac{1}{2}} \quad (5.12)$$

$$Y_{LO} = \sum_{n=1}^6 b_n X_{LO}^{n-\frac{1}{2}} \quad (5.13)$$

4-Trailing edge slope

$$\left(\frac{dY}{dX}\right)_{TEUP} = \tan(\theta_{up}) = \tan(\alpha_{TE} + \frac{1}{2}\beta_{TE}) = \sum_{n=1}^6 \left(n - \frac{1}{2}\right) a_n X_{TE}^{n-\frac{3}{2}} \quad (5.14)$$

$$\left(\frac{dY}{dX}\right)_{TELO} = \tan(\theta_{LO}) = \tan\left(\alpha_{TE} - \frac{1}{2}\beta_{TE}\right) = \sum_{n=1}^6 \left(n - \frac{1}{2}\right) b_n X_{TE}^{n-\frac{3}{2}} \quad (5.15)$$

5- Slope at any maximum thickness

$$Y_{xup} = \left(\frac{dY}{dX}\right)_{X=Xup} = \sum_{n=1}^6 \left(n - \frac{1}{2}\right) a_n X_{UP}^{n-\frac{3}{2}} = 0 \quad (5.16)$$

$$Y_{xLO} = \left(\frac{dY}{dX}\right)_{X=XLO} = \sum_{n=1}^6 \left(n - \frac{1}{2}\right) b_n X_{LO}^{n-\frac{3}{2}} = 0 \quad (5.17)$$

6- Curvature

$$Y_{xxup} = \left(\frac{d^2Y}{dX^2}\right)_{X=Xup} = \sum_{n=1}^6 \left(n - \frac{3}{2}\right) \left(n - \frac{1}{2}\right) a_n X_{UP}^{n-\frac{5}{2}} \quad (5.18)$$

$$Y_{xxLO} = \left(\frac{d^2Y}{dX^2}\right)_{X=XLO} = \sum_{n=1}^6 \left(n - \frac{3}{2}\right) \left(n - \frac{1}{2}\right) b_n X_{LO}^{n-\frac{5}{2}} \quad (5.19)$$

These equations can be written in matrix form as for the upper and lower surfaces separately.

$$A_{up}.B_{up} = C_{up} \quad (5.20)$$

$$A_{LO}.B_{LO} = C_{LO} \quad (5.21)$$

Where the matrices are given as

$$A_{up} = \begin{bmatrix} 1 & 0 & 0 & 0 & 0 & 0 \\ X_{TE}^{\frac{1}{2}} & X_{TE}^{\frac{3}{2}} & X_{TE}^{\frac{5}{2}} & X_{TE}^{\frac{7}{2}} & X_{TE}^{\frac{9}{2}} & X_{TE}^{\frac{11}{2}} \\ X_{UP}^{\frac{1}{2}} & X_{UP}^{\frac{3}{2}} & X_{UP}^{\frac{5}{2}} & X_{UP}^{\frac{7}{2}} & X_{UP}^{\frac{9}{2}} & X_{UP}^{\frac{11}{2}} \\ \frac{1}{2}X_{TE}^{\frac{1}{2}} & \frac{3}{2}X_{TE}^{\frac{3}{2}} & \frac{5}{2}X_{TE}^{\frac{5}{2}} & \frac{7}{2}X_{TE}^{\frac{7}{2}} & \frac{9}{2}X_{TE}^{\frac{9}{2}} & \frac{11}{2}X_{TE}^{\frac{11}{2}} \\ \frac{1}{2}X_{UP}^{\frac{1}{2}} & \frac{3}{2}X_{UP}^{\frac{3}{2}} & \frac{5}{2}X_{UP}^{\frac{5}{2}} & \frac{7}{2}X_{UP}^{\frac{7}{2}} & \frac{9}{2}X_{UP}^{\frac{9}{2}} & \frac{11}{2}X_{UP}^{\frac{11}{2}} \\ -\frac{1}{4}X_{TE}^{\frac{-3}{2}} & \frac{3}{4}X_{UP}^{\frac{-1}{2}} & \frac{15}{4}X_{UP}^{\frac{1}{2}} & \frac{35}{4}X_{UP}^{\frac{3}{2}} & \frac{53}{4}X_{UP}^{\frac{5}{2}} & \frac{99}{4}X_{UP}^{\frac{7}{2}} \end{bmatrix} \quad (5.22)$$

$$A_{LO} = \begin{bmatrix} 1 & 0 & 0 & 0 & 0 & 0 \\ X_{TE}^{\frac{1}{2}} & X_{TE}^{\frac{3}{2}} & X_{TE}^{\frac{5}{2}} & X_{TE}^{\frac{7}{2}} & X_{TE}^{\frac{9}{2}} & X_{TE}^{\frac{11}{2}} \\ X_{LO}^{\frac{1}{2}} & X_{LO}^{\frac{3}{2}} & X_{LO}^{\frac{5}{2}} & X_{LO}^{\frac{7}{2}} & X_{LO}^{\frac{9}{2}} & X_{LO}^{\frac{11}{2}} \\ \frac{1}{2}X_{TE}^{\frac{1}{2}} & \frac{3}{2}X_{TE}^{\frac{1}{2}} & \frac{5}{2}X_{TE}^{\frac{3}{2}} & \frac{7}{2}X_{TE}^{\frac{5}{2}} & \frac{9}{2}X_{TE}^{\frac{7}{2}} & \frac{11}{2}X_{TE}^{\frac{9}{2}} \\ \frac{1}{2}X_{LO}^{\frac{1}{2}} & \frac{3}{2}X_{LO}^{\frac{1}{2}} & \frac{5}{2}X_{LO}^{\frac{3}{2}} & \frac{7}{2}X_{LO}^{\frac{5}{2}} & \frac{9}{2}X_{LO}^{\frac{7}{2}} & \frac{11}{2}X_{LO}^{\frac{9}{2}} \\ -\frac{1}{4}X_{TE}^{\frac{-3}{2}} & \frac{3}{4}X_{LO}^{\frac{-1}{2}} & \frac{15}{4}X_{LO}^{\frac{1}{2}} & \frac{35}{4}X_{LO}^{\frac{3}{2}} & \frac{53}{4}X_{LO}^{\frac{5}{2}} & \frac{99}{4}X_{LO}^{\frac{7}{2}} \end{bmatrix} \quad (5.23)$$

$$B_{UP} = \begin{bmatrix} a_1 \\ a_2 \\ a_3 \\ a_4 \\ a_5 \\ a_6 \end{bmatrix} \quad (5.24)$$

$$B_{LO} = \begin{bmatrix} b_1 \\ b_2 \\ b_3 \\ b_4 \\ b_5 \\ b_6 \end{bmatrix} \quad (5.25)$$

$$C_{UP} = \begin{bmatrix} \sqrt{2r_{LE}} \\ Y_{TEUP} \\ Y_{UP} \\ \tan(\theta_{UP}) \\ 0 \\ \frac{d^2Y}{dX^2}_{UP} \end{bmatrix} \quad (5.26)$$

$$C_{LO} = \begin{bmatrix} -\sqrt{2r_{LE}} \\ Y_{TELO} \\ Y_{LO} \\ \tan(\theta_{LO}) \\ 0 \\ \frac{d^2Y}{dX^2}_{LO} \end{bmatrix} \quad (5.27)$$

The unknown coefficients a_n and b_n are found by solving the above system of equations $B_{UP} = A_{UP}^{-1} C_{UP}$ and similarly $B_{LO} = A_{LO}^{-1} C_{LO}$. The obtained coefficients are feed back to the original equations and the airfoil coordinates x/c and y/c are calculated. A sample calculation is shown on Figure 5.4, with PARSEC parameters given in Table 5.2

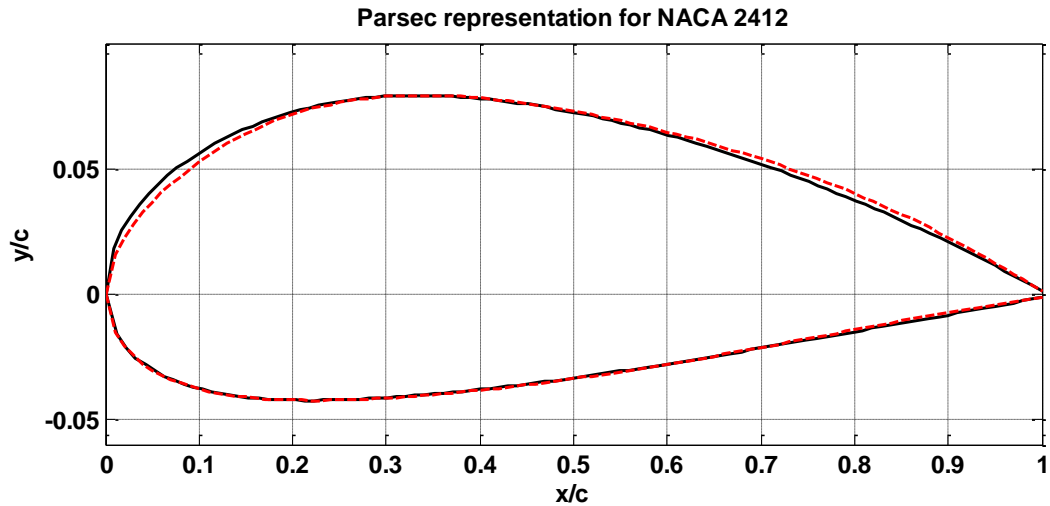


Figure 5.4 Parsec representation (dotted line) of NACA 4412 airfoil (solid line)

Table 5.2 Values of PARSEC parameters for NACA2412

parameter	Meaning	Value
r_{LE}	Leading edge radius	0.0119
X_{up}	X location of Upper crest	0.3391
Y_{up}	Y location of Upper crest	0.0792
Y_{xxup}	Upper surface curvature	-0.6222
X_{Lo}	X location of Lower crest	0.2226
Y_{Lo}	Y location of Lower crest	-0.0424
Y_{xxLo}	Lower surface curvature	0.3815
DY_{TE}	Trailing edge thickness	0.0025
Y_{TE}	Trailing edge y location	0
α_{TE}	Trailing edge direction	-5 deg
β_{TE}	Trailing edge included angle	15.9752 deg

5.5 Bezier Parameterization

Bezier curves are special curves in which they are controlled by control points [96]. They curve starts and ends at a control point but it is not necessary to pass through each intermediate control point. For n degree Bezier curve n+1 control points are required. Figure 5.5 Two Bezier curves of order 5 representing upper surface of an airfoil. A Bezier curve is defined by Eq.(5.28) for given control points P_i and Bernstein polynomials B_i^n .

$$P(t) = \sum_{i=0}^n P_i B_i^n(t) \tag{5.28}$$

Bezier curves are based on Bernstein polynomials B_j^n which is given as

$$B_i^n = \binom{n}{i} (1-t)^{n-i} t^i \tag{5.29}$$

where $i=0,1,2,3$. and $\binom{n}{i}$ is a binomial coefficient given as

$$\binom{n}{i} = \frac{n!}{i!(n-i)!} \tag{5.30}$$

If $n=3$ Bezier curve is to be written the following Bernstein polynomial of $n+1=4$ terms is constructed as

$$B_0^3 = (1-t)^3 \tag{5.31}$$

$$B_1^3 = 3t(1-t)^2 \tag{5.32}$$

$$B_2^3 = 3t^2(1-t) \tag{5.33}$$

$$B_3^3 = t^3 \tag{5.34}$$

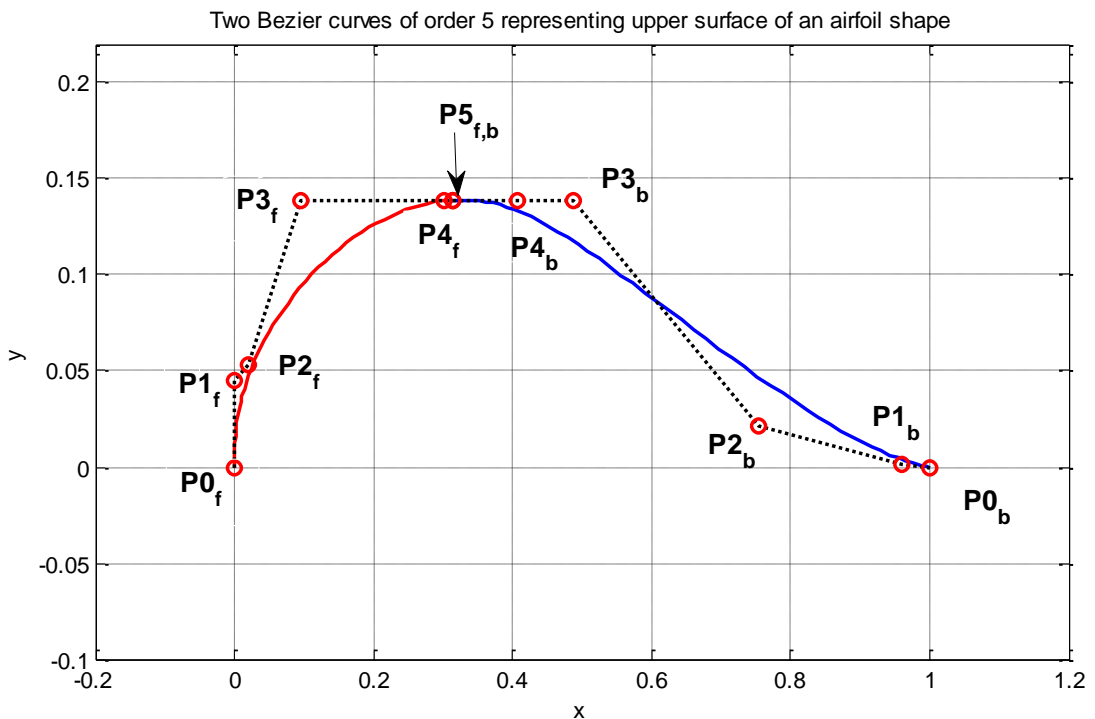


Figure 5.5 Two Bezier curves of order 5 representing upper surface of an airfoil

Figure 5.5 shows two Bezier curve of order 5 which requires 6 control points. First curve (red) represents forward part of airfoil upper surface and second curve (blue) represents backward part of upper surface. Red circles are control points denoted by subscript b and f for forward and backward part respectively. Bezier curves has useful properties that makes it suitable for airfoil shape representation, these properties are

- a) A single Bezier curve is continuous, their derivatives can be calculated analytically because it is a polynomial. The curve is also bounded by straight lines connecting it's control points.
- b) Curves start and end with control point which makes the curve contained between the control points.
- c) Initial curve slope can be controlled by location of next point , for example 2nd control point located at same x distance from 1st point will generate a curve having 90 degrees, as shown in Figure for forward part, note that the curve does not pass through the second point .
- d) Airfoil maximum thickness can be controlled by specifying coordinates of the last points in each part, (P_5) which is also common for both part.
- e) First and second order continuity at maximum thickness is assured by giving same y coordinate for points P_3 and P_4 of forward and backward parts.
- f) Finally, the trailing edge location and angle are controlled by backward part 1st and second points.

Thus, in order to represent airfoil upper surface with 5 degree Bezier curve some constraints should be applied. Table 5.3 shows these constraints for upper surface, a similar constraints is applied to the lower surface.

Table 5.3 Five point Bezier curves constraints

Point /Coordinates		Constraints for Forward part	Constraints for Backward part
1	x	Fixed at axis origin x=0	Fixed at x=1
	y	Fixed at axis origin y=0	Fixed at y=0 or specific value.
2	x	Fixed at x=0	Floats between the two neighboring points
	y	Floats between the two neighboring points	Floats between given max. and min. to give logical TE angles.
2	x	Floats between the two neighboring points	Floats between the two neighboring points
	y	Floats between the two neighboring points	Floats between the two neighboring points
3	x	Floats between the two neighboring points	Floats between the two neighboring points
	y	Fixed to y = maximum thickness	Fixed to y = maximum thickness
4	x	Floats between the two neighboring points	Floats between the two neighboring points
	y	Fixed to y = maximum thickness	Fixed to y = maximum thickness
5	x	Fixed to the position of maximum thickness	Fixed to the position of maximum thickness
	y	Fixed to y = maximum thickness	Fixed to y = maximum thickness

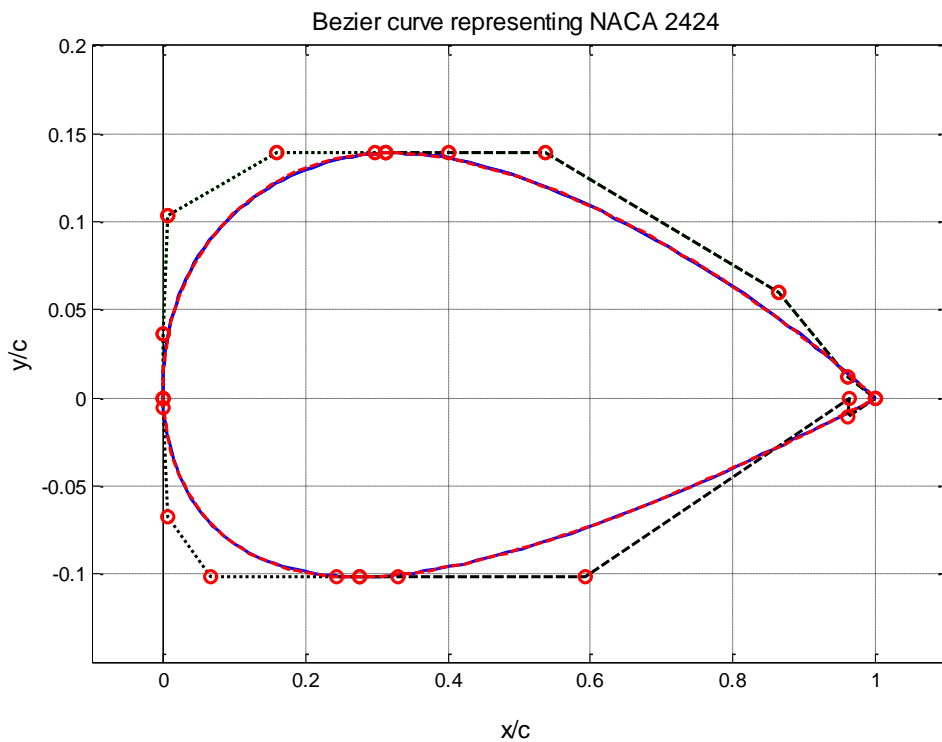


Figure 5.6 NACA 2424 airfoil represented by Bezier curve using the above method

Figure 5.6 NACA 2424 represented by 4 Bezier curve, and NACA representation , They are very close and hardly be distinguishable . (Red) circles represent control points. dotted lines is enclosing shape. Bezier curve parameters are shown on Table 5.4, with 11 parameters for each curve.

Table 5.4 Bezier curve parameters used to generate NACA 2424

point	0	1	2	3	4	5	6	7	8	9	10
PU	0.0364	.0071	0.1035	0.1594	0.2978	0.4007	0.5363	0.8638	0.0597	0.96	0.0117
PL	-0.0052	0.0069	-0.0672	0.0669	0.2445	0.3290	0.5929	0.9638	-0.0005	0.960	-0.0111

5.6 CST Method

This method is developed by Brenda Kulfan in Boeing Commercial Airplanes, as illustrated in [97], and [98], and its characteristics has been thoroughly studied in many works as in [99]. In CST method an airfoil geometry is expressed by the mathematical expression of Eq.(5.35)

$$\xi(\psi) = \sqrt{\psi} (1 - \psi) \sum_{i=1}^N A_i \psi^i + \psi \xi_T \quad (5.35)$$

Where $\psi = \frac{x}{c}$, $\xi = \frac{y}{c}$ and $\xi_T = \frac{\Delta \xi_{TE}}{c}$

In this expression airfoil nose shape is governed by the term $\sqrt{\psi}$, while the term $(1 - \psi)$ controls the trailing edge angle and the last term $\psi \xi_T$ represents the trailing edge thickness. The term $\sum_{i=1}^N A_i \psi^i$ shapes the rest of the airfoil surface. The equation can be rearranged to give the so called class function and denoted by $S(\psi)$ given by Eq.(5.36).

$$S(\psi) = \frac{\xi(\psi) - \psi \xi_T}{\sqrt{\psi} (1 - \psi)} \quad \text{with} \quad S(0) = \sqrt{2 r_{LE} / c} \quad \text{and} \quad S(1) = \tan \beta + \frac{\Delta Z_{TE}}{c} \quad (5.36)$$

The shape function can be formulated by using Bernstein polynomial in which first term represent leading edge radius and last term represent trailing edge angle and thickness. The rest of the terms can not affect neither leading edge radius nor trailing edge properties, and thus called shaping terms.

If Bernstein polynomial of order n is used then the shape function takes the form

$$S_i(\psi) = K_i \psi^i (1 - \psi)^{n-i} \quad \text{with} \quad K_i = \binom{n}{i} = \frac{n!}{i!(n-i)!} \quad (5.37)$$

Using this shape function the airfoil upper and lower surfaces can be expressed as

$$\begin{aligned}\xi_{up} &= \sqrt{\psi} (1 - \psi) \sum_{i=1}^N A_{up} S_i(\psi) + \psi \Delta\xi_{up} \\ \xi_{LO} &= \sqrt{\psi} (1 - \psi) \sum_{i=1}^N A_{LO} S_i(\psi) + \psi \Delta\xi_{LO}\end{aligned}\tag{5.38}$$

Where $\Delta\xi_{up} = \frac{Y_{uTE}}{c}$ and $\Delta\xi_{LO} = \frac{Y_{LTE}}{c}$ are upper and lower trailing edge thicknesses respectively.

The coefficients A_{up} and A_{LO} can be found for different airfoil shapes. This formulation methodology is suitable for systematic design optimization approach. Figure 5.7 shows construction of airfoil upper surface using various Bernstein polynomials shape function $S_i(\psi)$, along with corresponding airfoil terms (by using only one term with $i = 1, 2, \dots$ or N in the ξ_{up} and ξ_{LO} equations (5.38)).

The terms of the shape function always sum up to 1. The sum of airfoil terms results in airfoil surface coordinates. It is worth to note that the coefficients A_{up} and A_{LO} are set to 1 in the shown example, which means that they are not used. When these coefficients are assigned to some value they will scale up or down the corresponding term, and thus different airfoil shape is formed with any perturbed coefficient.

Figure 5.7 through Figure 5.10 show airfoil upper surface constructed with different degree of polynomials. The values of the polynomials coefficients will differ with n and will change with the scaling coefficients A 's.

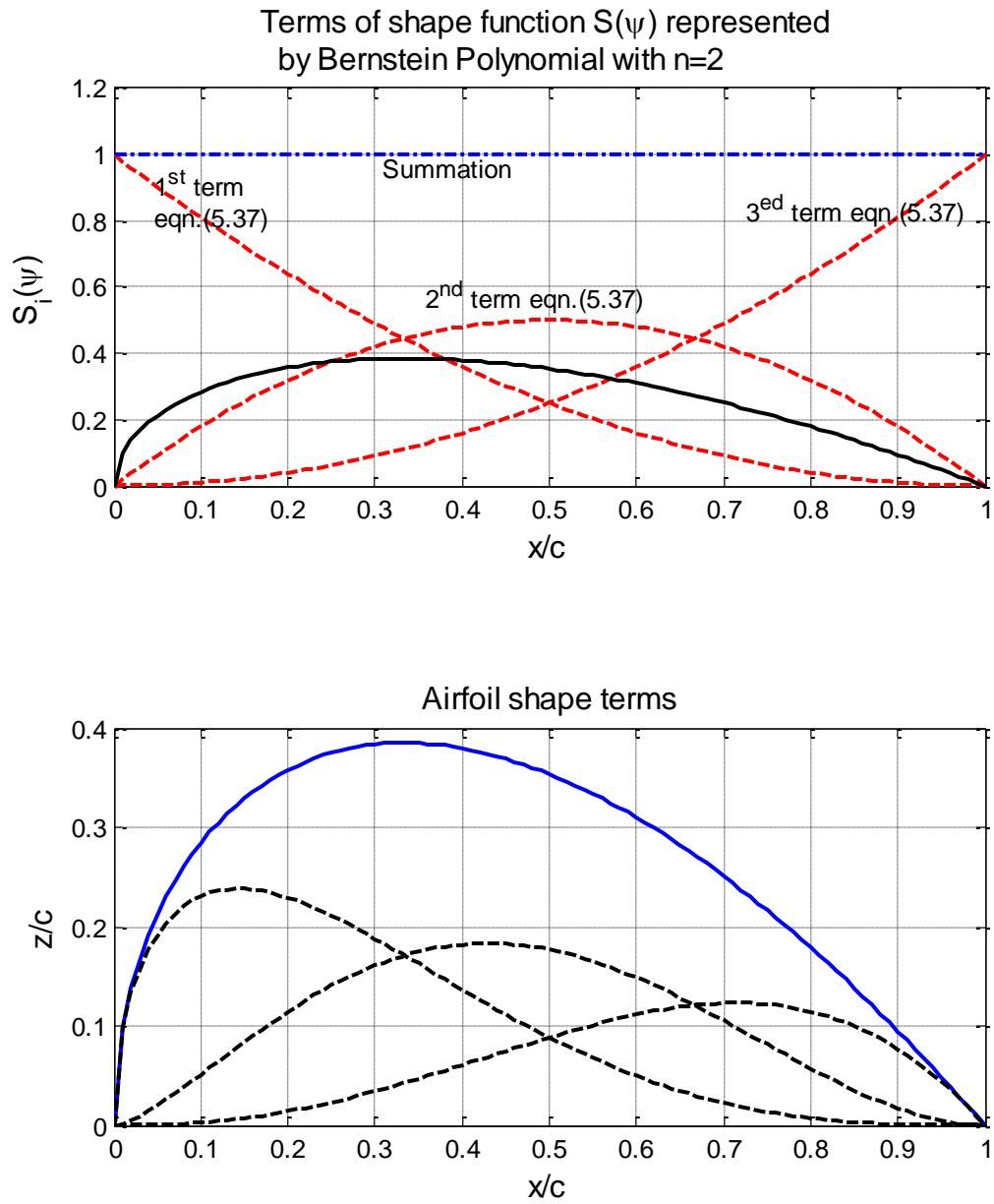


Figure 5.7 CST representation of airfoil upper surface using 3 terms ($n=2$). Upper part: Shows 3 terms of Bernstein polynomial of equation (5.37) (dotted curve), and its summation is equal to 1 . Lower part: Shows airfoil upper surface shape (solid) and terms of equations (5.38) (dotted), The summation of these three curves at each point results in a point on airfoil surface.

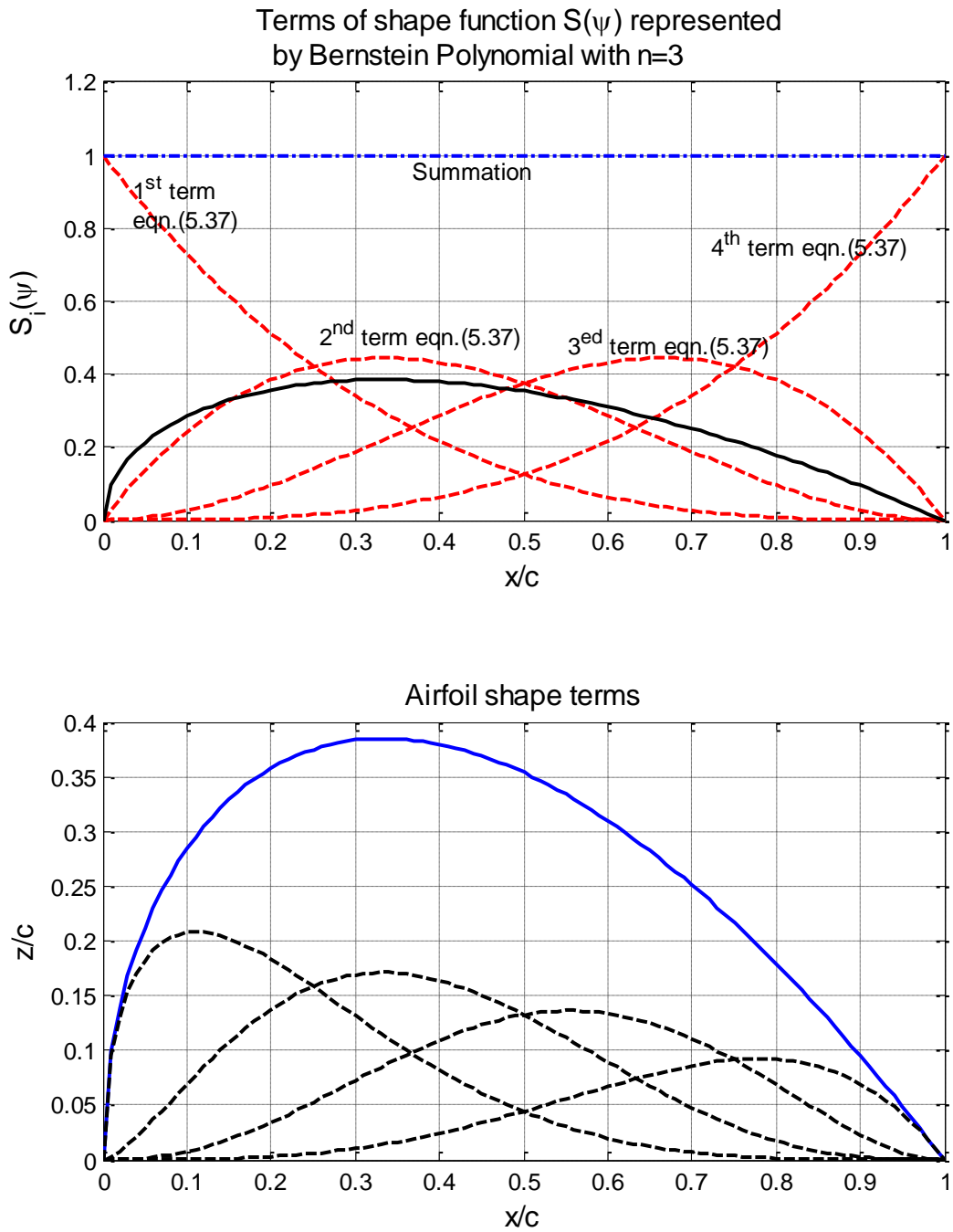


Figure 5.8 CST representation of airfoil upper surface using 4 terms ($n=3$). Upper part: Shows 4 terms of Bernstein polynomial of equation (5.37) (dotted curve), and its summation is equal to 1 . Lower part: Shows airfoil upper surface shape (solid) and terms of equations (5.38) (dotted), The summation of these four curves at each point results in a point on airfoil surface.

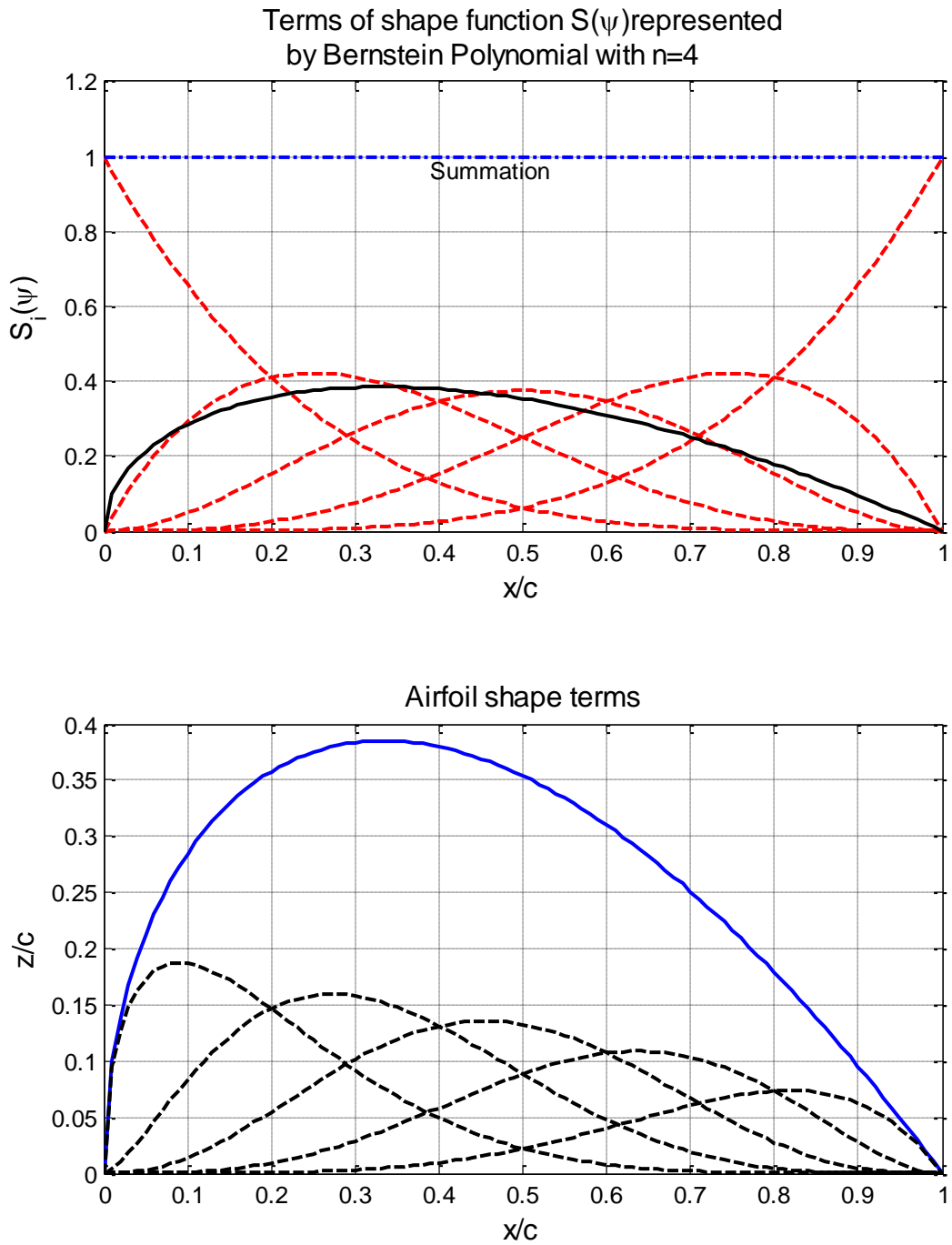


Figure 5.9 CST representation of airfoil upper surface using 5 terms ($n=4$)

Upper part: Shows 5 terms of Bernstein polynomial (dotted) equation (5.37), and the summation of these terms equal 1 is one.

Lower part: Shows airfoil upper surface shape (solid) and the five terms of equations (5.38) (dotted).

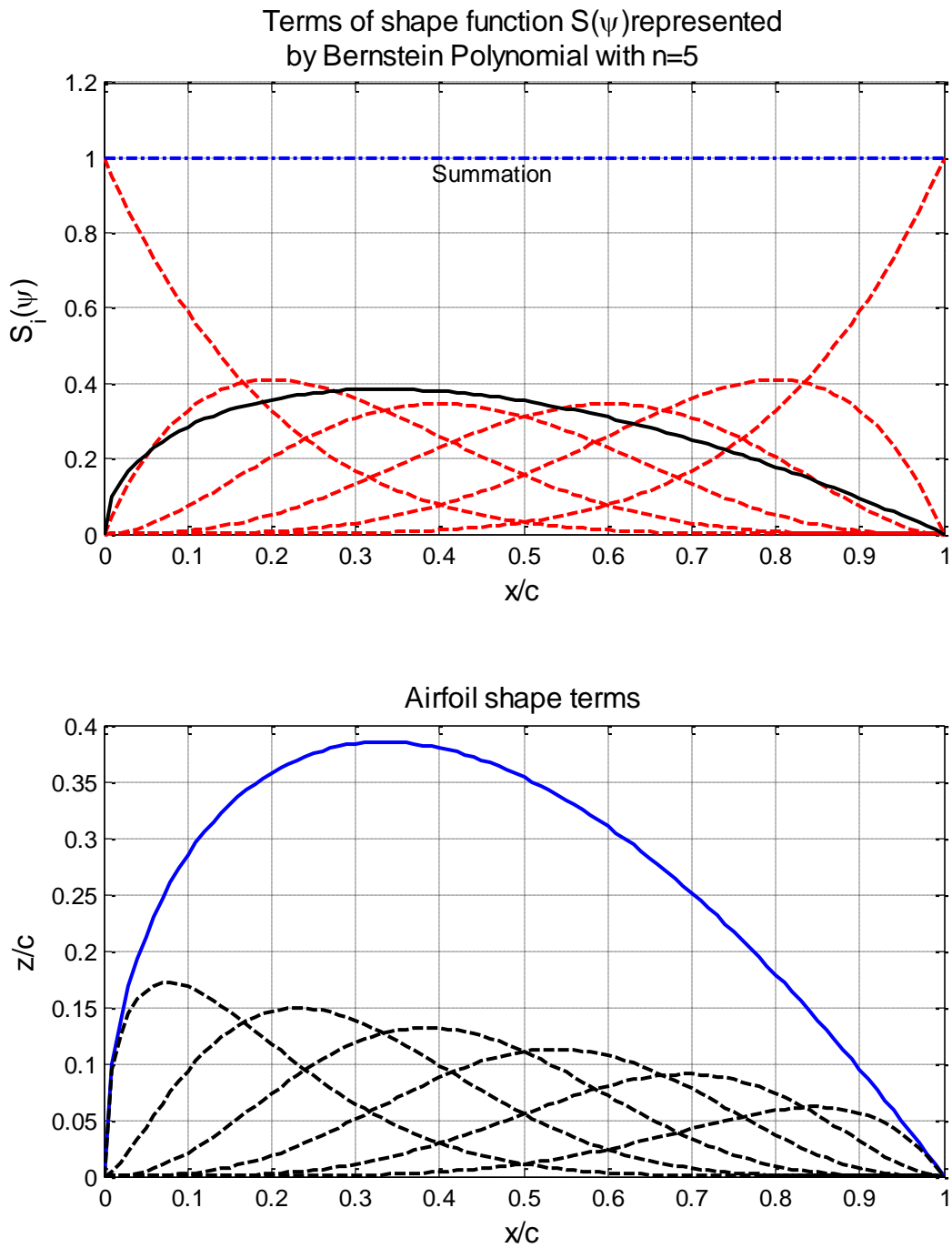


Figure 5.10 Construction of an airfoil upper surface shape using $n=5$

Upper part: Shows 5 terms of Bernstein polynomial (dotted) equation (5.37), and the summation is one.

Lower part: Shows airfoil upper surface shape (solid) and the six terms of equations (5.38) (dotted)

It is shown in [63] that a relatively low order Bernstein polynomial, (such as $n=6$ to $n=9$), matches the airfoils geometries, slopes and second derivatives. It is also shown that pressure distributions and aerodynamic forces are also matched. The results also indicated that lower order Bernstein Polynomials, corresponding to fewer design variables, (perhaps $n=4$ to $n=6$), should be adequate for developing optimum designs.

5.7 Matching of NACA 4412 Airfoil shape

An example of CST method is shown in Figure 5.11 in which NACA 2412 is represented by 2 coefficients for upper and other 2 coefficients for lower surfaces. The difference in airfoil coordinates is shown in the lower part of the same figure. The maximum difference is about $2.1E-3$ which is fairly satisfactory for optimization purposes given that it will be computationally inexpensive. With 4 coefficients CST fits NACA2412 with high accuracy Figure 5.13 maximum differences in order of 10^{-4} . Figure 5.12.and Figure 5.14 show the fitness value versus the number of generations. About 50 generations are required to reach the best close to the best accuracy for 2 coefficients as compared to about 200 for the 4 coefficients case. The mean value is improved faster as a property of genetic search algorithms. The value of best generation is shown in the lower part of each figure, where the upper surface coefficients are positive while the lower are negative.

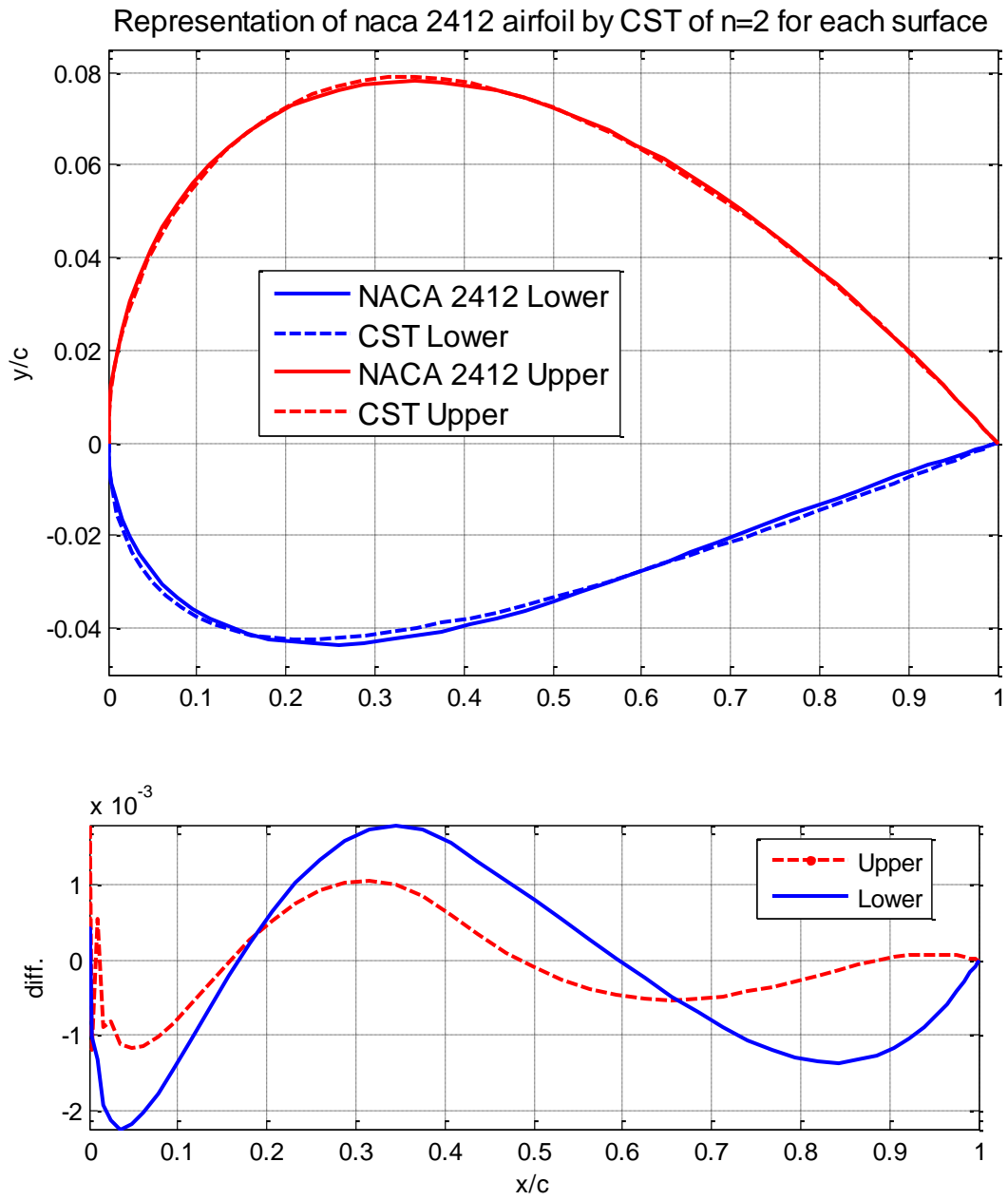


Figure 5.11 NACA 2412 represented with two coefficients for each surface and difference y in coordinates. $A_{up} = [0.1995 \ 0.2103]$ and $A_{LO} = [-0.1350 \ -0.0584]$

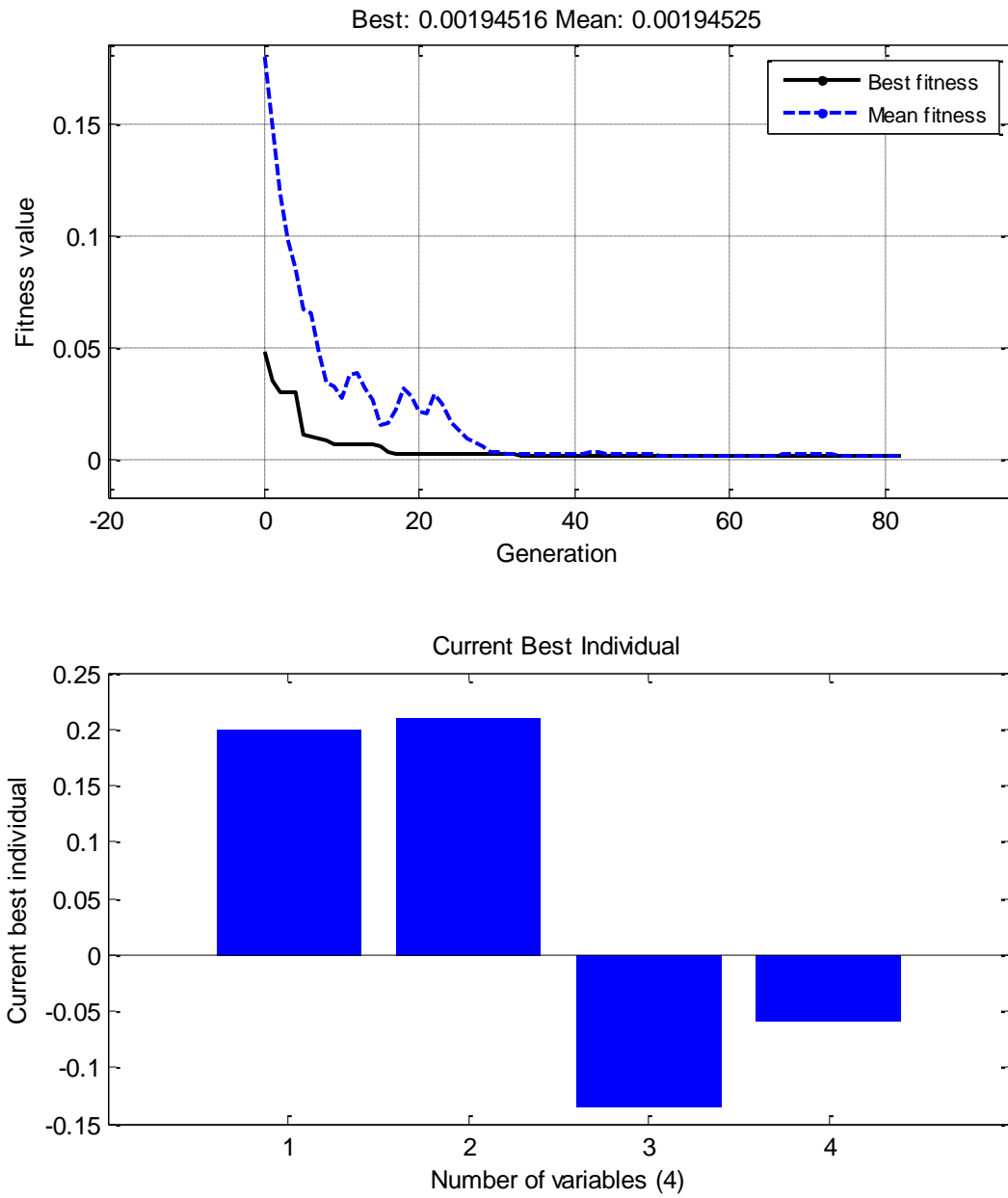


Figure 5.12 Convergence history and coefficients with best values when two CST coefficients for each surface are used.

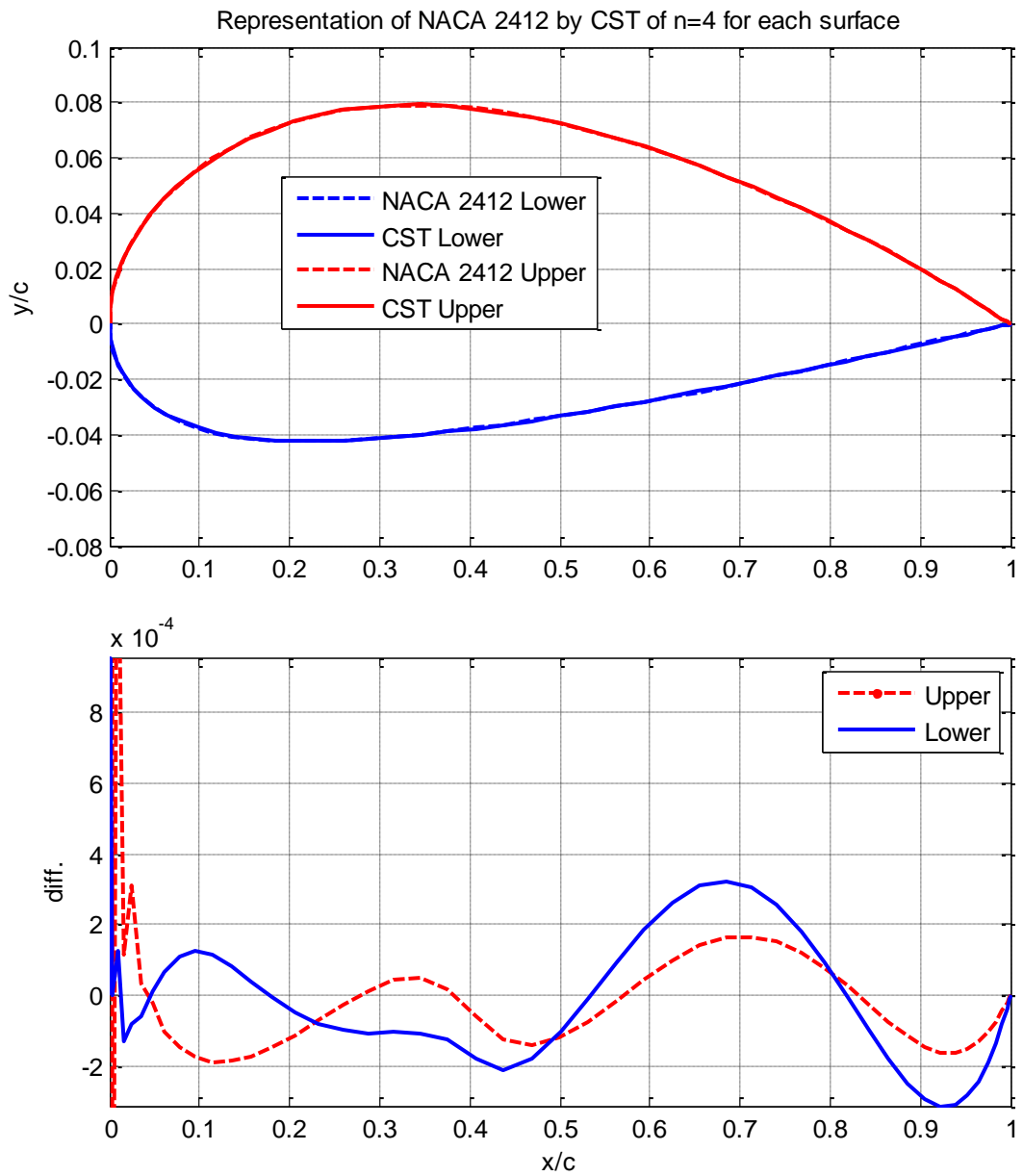


Figure 5.13 NACA 2412 represented with four coefficients for each surface and difference in y coordinates. $A_{up} = [0.1899 \ 0.2254 \ 0.1847 \ 0.2193]$ and $A_{LO} = [-0.1518 \ -0.0788 \ -0.0990 \ -0.0677]$.

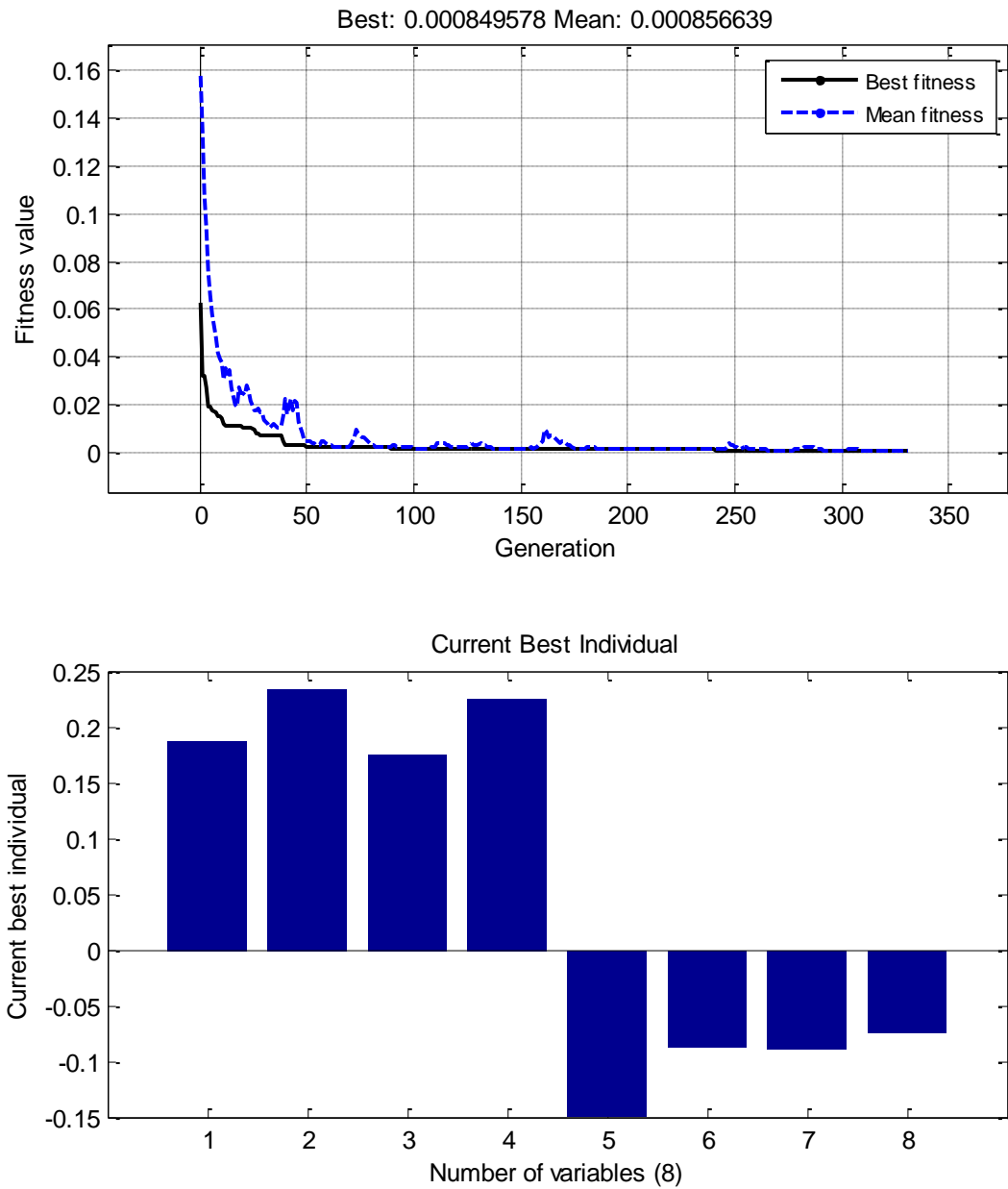


Figure 5.14 Convergence history and coefficients with best values when four CST coefficients for each surface.

5.8 Matching of Target Pressure Distribution

In order to check the capability of CST method to match a given pressure distribution, a study is performed in which a pressure distribution around known NACA 2412 is calculated at angle of attack of 2 degrees and Reynolds number of 300,000. This pressure distribution is used as input to the optimization code as target pressure distribution C_{p_t} . Genetic Search Algorithms GA optimization is used to find the CST aerodynamic shape that produces this pressure distribution.

The optimization procedure should converge to the same starting airfoil, or to a shape which is very close to it. The objective function for this case is based on finding the difference between calculated pressure distribution and target pressure distribution. The difference is calculated as the mean of difference squared between two functions as given by Eqn.(5.39).

$$diff = \frac{\sum_{i=1}^N (C_P^T - C_P^K)^2}{N} \quad (5.39)$$

Where C_P^T is target pressure distribution at each airfoil surface point from $i = 1$ to N and C_P^K is the pressure distribution calculated at k^{th} iteration step.

This error measure is used as objective function during the optimization process. It should rapidly diminish as the optimization method converges to the target pressure distribution shape. It is worth to note that the number of iterations needed to converge depends on the starting point. Figure 5.15 shows NACA 2412 airfoil and, Figure 5.16 shows target pressure distribution. Two CST and four CST coefficients are discussed in the following sections.

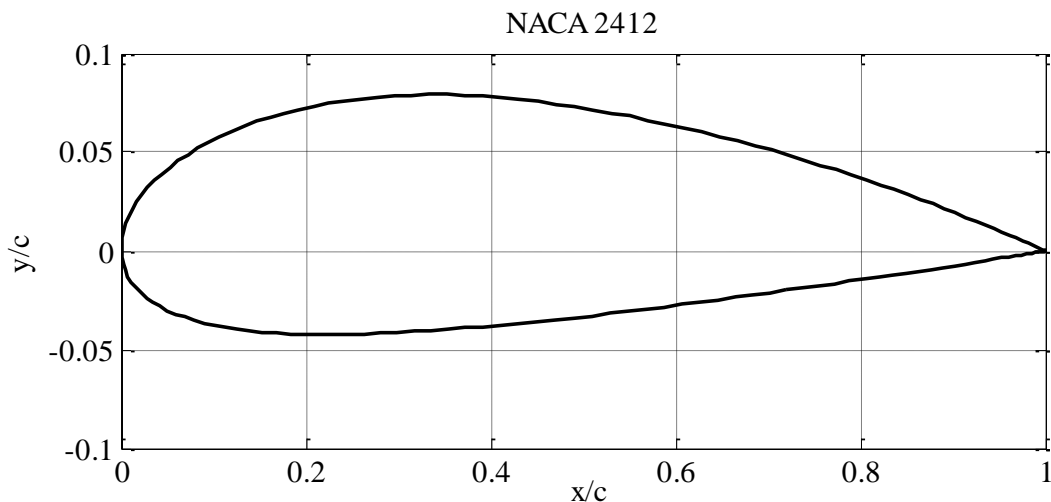


Figure 5.15 NACA 2412 used as test airfoil

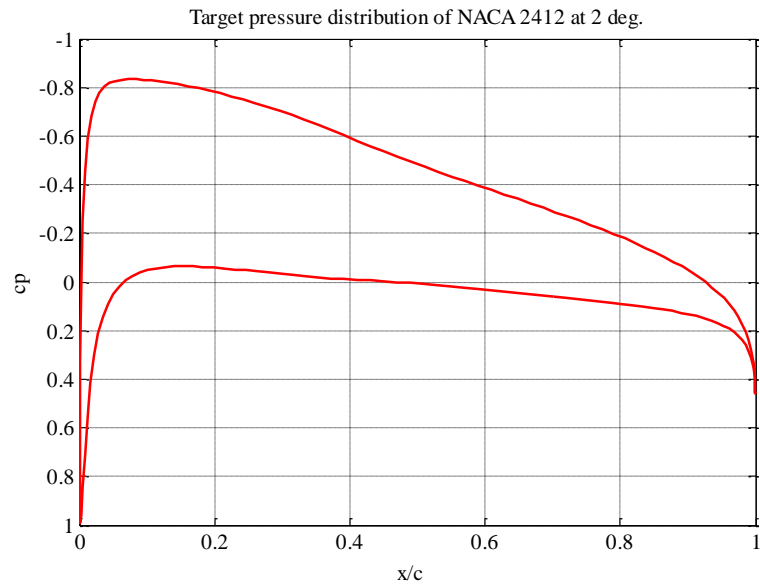


Figure 5.16 Target pressure distribution

5.8.1 CST with n=2 parameters

The accuracy of CST method can be checked for different number of parameters. N=2 uses two coefficients for each airfoil side, and thus 4 optimization parameters are used by genetic search algorithm. Results of optimization are shown in Figure 5.18 and Figure 5.19.

For this case, the CST takes about 35 generations to converge to the target pressure distribution with a value of fitness function of 3.4×10^{-4} . The parameters for n=2 are $A_{up} = 0.1995 \quad 0.2107$ and $A_{Lo} = -0.1351 \quad -0.0585$. The pressure distribution is matched exactly from engineering point of view. As can be seen in Figure 5.19, and the found airfoil shape is very close to the target NACA2412 airfoil, as seen in Figure 5.17.

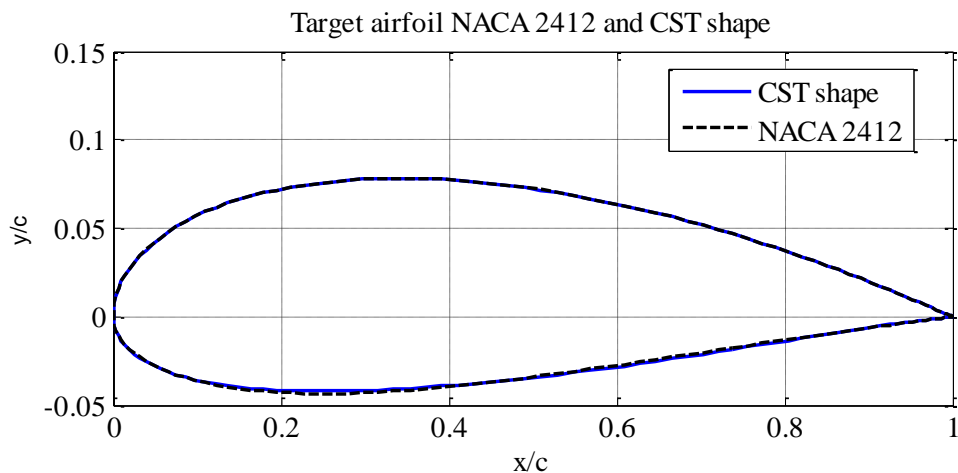


Figure 5.17 NACA 2412 airfoil and obtained CST shape when number of CST parameters N=2

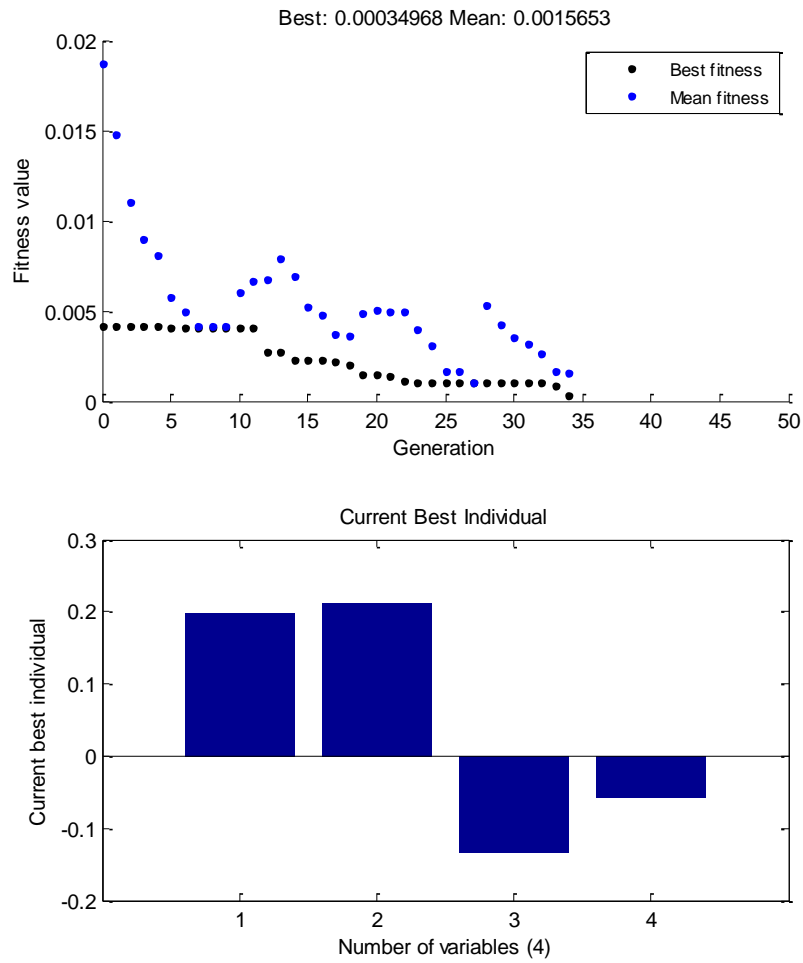


Figure 5.18 Fitness value versus number of generations for target pressure distribution at $\alpha=2$ degrees and number of CST coefficients $N=2$.

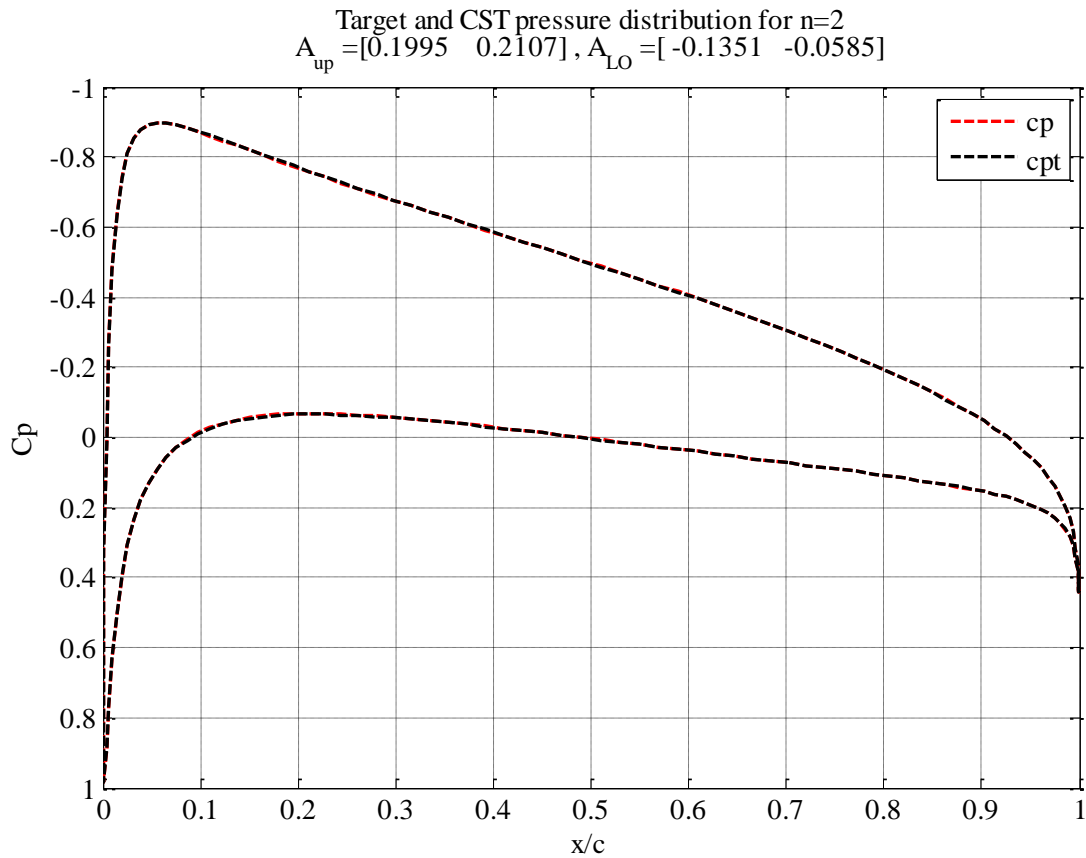


Figure 5.19 Comparison of target and CST pressure distributions when number of CST parameters N=2

5.8.2 CST with n=4 parameters

In this case total number of parameters is 8, the optimization algorithm will require more computations to converge at the target shape.

By comparing Figure 5.18 and Figure 5.21, the number of representation parameters is increased from n=2 to n=4, which results in increase number of GA generations from 35 to 50 generations to reach the same fitness function. The CST parameters for n=4 are

$$A_{UP} = 0.1991 \quad 0.2047 \quad 0.2039 \quad 0.2126$$

$$A_{LO} = -0.1400 \quad -0.0891 \quad -0.1064 \quad -0.0509$$

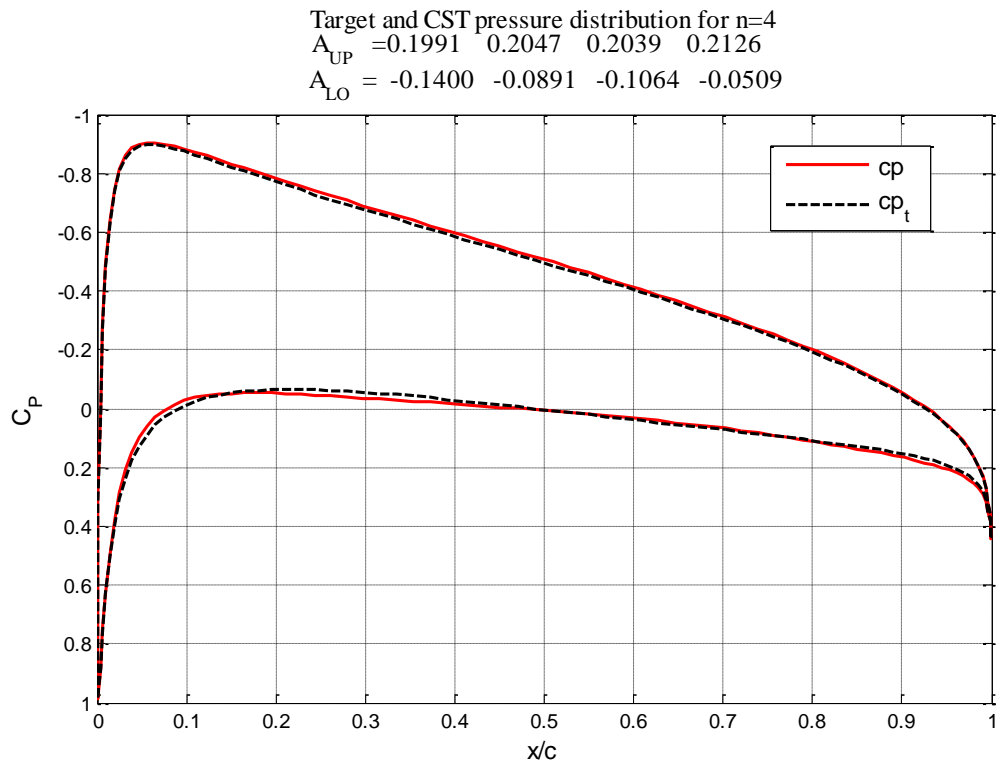


Figure 5.20 Comparison of target and CST pressure distributions when number of CST parameters
 $N=4$

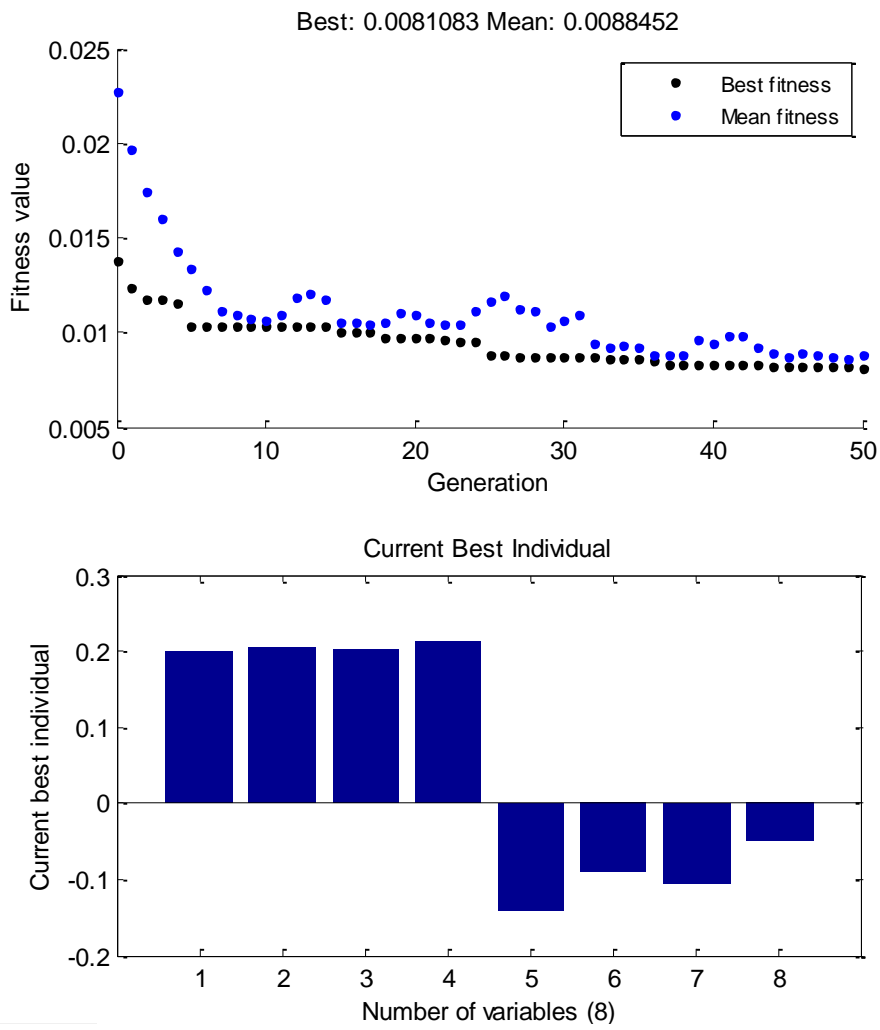


Figure 5.21 Fitness value versus number of generations for target pressure distribution at $\alpha=2$ degrees and number of CST coefficients $N=4$

CHAPTER 6

6 Aerodynamic design and shape Optimization

Aerodynamic design is historically classified into two classes of problems. These classification are the direct and inverse airfoil design problems. Direct airfoil design problem means finding performance parameters for given airfoil at given flow conditions, while the inverse design problem deals with finding airfoil shape that has pre-specified performance (most often velocity or pressure distributions), this is illustrated in Figure 6.1.

Optimization can be applied to both forms of the design problems. If the problem is set as direct optimization, the airfoil shape is changed until the required fitness function is satisfied. For the inverse optimization problem the airfoil target performance is pre-specified and the optimization methods searches for the corresponding airfoil shape. Although, an initial design point (shape) is required, the design should converge to the optimum shape regardless of the initial shape. This is usually checked by repeating the optimization process with different initial shapes.

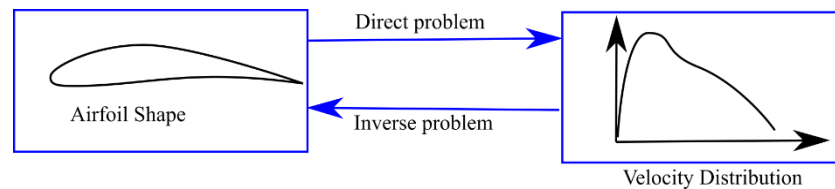


Figure 6.1 Inverse and direct aerodynamic problems

The other important issue is multipoint design. One essential design requirement in airfoil design process is to check airfoil performance at off design conditions. For instance, design requirement can be formulated to maximize lift or minimize drag, or to maximize lift to drag ratio, or to optimize airfoil thickness, or pitching moment. These requirements can be placed at one angle of attack or flight condition (design condition or point). The other flight conditions are checked later after the design is obtained, this approach is called single design point. Multipoint design is possible with more complex objective functions and demanding computational cost. Michael S. Selig [67] and [68], has presented a multipoint inverse airfoil design for incompressible potential flow which was basically based on Eppler work [27].

6.1 Inverse design approach

In this design approach a target pressure (or velocity) distribution and an initial airfoil shape are usually specified for given flow Reynolds number and angle of attack. The pressure distribution of the initial airfoil is then computed and compared to the target pressure distribution. The airfoil shape is manipulated by the inverse design method in order to overlap its pressure distribution with target pressure distribution. For instance, if the pressure distribution of a known airfoil shape is specified as target pressure distribution, the inverse design method should converge to the target airfoil shape. This constitutes an advantage because the required performance (pressure distribution) is already specified, which makes inverse design a powerful design method.

The choice of pressure distribution as target performance characteristics was derived from the fact that favorable pressure distributions will delay transition from laminar to turbulent flow [28] as noted by Schlichting [69] and adopted by Liebeck in his works [70] - [72] and used by Wortmann [73] to design glider airfoil series. Miley [74] had theoretically investigated the influence of lowered Reynolds numbers on airfoil designs based on the requirement to achieve transition upstream of a major adverse pressure gradient. Maughmer and Somers [75], and others as has used similar design philosophy to design laminar flow airfoils with aft pressure recoveries for a wide range of application. Startford [77] and [78] has adopted the idea that keeping the flow on the edge of separation can result in airfoil shapes that have prolonged laminar flow, with minimal energy lose.

Hence, inverse design approach possesses the advantage that the required performance (in terms of velocity or pressure distributions) is already specified. This advantage puts a difficult task to the designer who should formulate the design requirements in terms of target pressure distribution. Inverse design methods are formulated to calculate airfoil shapes for given pressure distribution, but not to optimize the problem. Target pressure optimization will do the job of finding the optimum airfoil shape. The difference between the target pressure distribution and the calculated pressure distribution for i^{th} iteration is used to correct the airfoil shape toward the target pressure distribution. This correction, often, results in non-smooth airfoil shape therefore smoothing procedures are applied to the resulting shape. Connecting airfoil shape with pressure distribution and smoothing form a major drawback for this type of inverse formulation method.

Eppler [27] establishes conformal mapping method to find out the airfoil shape for given target velocity distribution at known segments over a unit circle, which is mapped to the airfoil. His method forms the bases of many successful airfoil designs for different applications [67][68][80].

6.2 Direct design approach

Direct design is the approach used when the airfoil shape is given and the performance characteristics (velocity distribution or drag polar) is calculated at known flow conditions. It is referred to as direct analysis problem. Because the airfoil is given it is always specified as realistic airfoil shape. A new airfoil is generated depending on optimization fitness function which requires more aerodynamic function calls than inverse approach that searches around the required performance shape. Therefore direct methods cover wider search space and come with variety of airfoil shapes, and it is up to the designer to put additional constraints such as, lift or drag or moment coefficients or some geometric constraints for example, the maximum thickness or nose radius or trailing edge angle. A comparison between direct and inverse design approaches is illustrated in the following table

Table 6.1 comparison between direct and inverse design approaches

Characteristic	Direct approach	Inverse approach
Required performance	No direct control on airfoil performance.	The designer specifies the required performance.
Problem formulation	Problem is solved in direct manner	Inverse formulation is needed.
Airfoil shape	Always results in realistic airfoil shapes.	Additional conditions are required, since non-realistic shape may appear.
Computer computations	Requires relatively large number of aerodynamic code calls to arrive at required performance.	Generally, smaller number of aerodynamic code calls.
Designer experience	More suitable with low experience design engineers.	Higher experience is required to identify target pressure distribution, or other performance specifications.
Search space	Depends on parameterization method	Depends on inverse formulation and airfoil smoothing as well as parameterization method.

6.3 Numerical Optimization

Nowadays, variety of optimization tools are accessible to the designer which are suitable for use to wide range of applications. They utilize a different search techniques, gradient based optimization, and genetic search algorithms are most popular techniques. These techniques are used for one point optimization in which an airfoil is designed for one operating point and other operating conditions are analyzed after the optimum shape is found. Multipoint optimization, on the other hand, can also be implemented. It demands more computational cost, especially if the number of design parameters is high. Multipoint design approach can be combined with inverse airfoil design formulation to minimize computational cost. Inverse design can be efficiently achieved through direct aerodynamic calculations. Firstly, the target airfoil performance is specified, and secondly, the airfoil shape is perturbed to match the target performance. Airfoil shape perturbation is accomplished through airfoil parameterization with a set of design parameters. These design parameters are used by the optimization method to generate new airfoil shapes toward the optimum solution.

The general flow chart for most of optimization methods starts with given vector of design parameters, Figure 6.2. Each combination of these design parameters produces certain aerodynamic shape or geometry. This is done inside one parameterization function as per user selection. NACA, PARSEC, CST, and Bezier curves are available as an option in this function. Each method can cover wide design space. The resulting geometric shape is analyzed by the aerodynamic function and the aerodynamic characteristics are computed. A fitness function is evaluated as a measure of performance. The main job of optimization method is to efficiently manipulate the combination of design parameters to search for improved performance in terms of better fitness value.

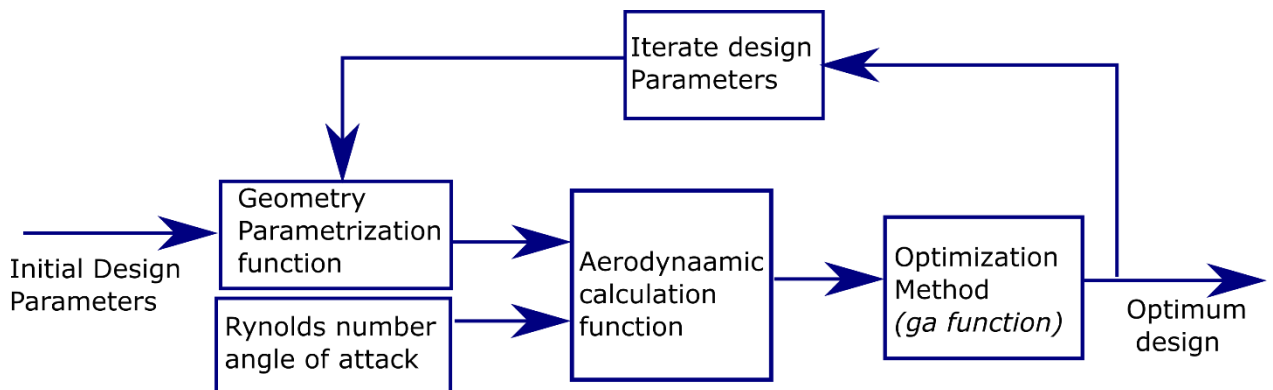


Figure 6.2 Flowchart illustrating design search and optimization process

For the optimization process to be built, the following topics are discussed:

- Choice of airfoil shape parameterization method.
- Selection of aerodynamic solver.
- Selection of the optimization method.
- Choice of constraints.
- Formulation of objective function.

The first two topics are covered in details in separate chapters. CST parameterization method will be used in the optimization. The aerodynamic model described in the previous chapters will be used for aerodynamic analysis. In the following sections some insight on the last three topics will be given. The attention will be toward aerodynamic and performance of airfoil design.

6.3.1 Formulation of the mathematical problem

For given vector of design variables, $X_j, j = 1: N$, where N is the number of design variables, the optimization finds the values of the vector X subjected to constrains of various types. Mathematically it is formulated as minimization of some function $f(x)$ as:

$$\text{minimize } f(X) \tag{6.1}$$

$$g(X) \leq 0 \tag{6.2}$$

$$h(X) = 0 \tag{6.3}$$

$$X_i^L \leq X_i \leq X_i^U \quad i = 1:N \tag{6.4}$$

The equation Eq.(6.4) represent the bounds of search space. The middle equations Eq.(6.2) and Eq.(6.3) are the inequality and equality constraints functions, respectively. These constraints can be of geometric type and some are of aerodynamic type. For example, airfoil thickness, leading edge radius, and trailing edge angle are geometric variables and can be constrained. Airfoil drag, moment, lift coefficients, and pressure distributions are used as aerodynamic constraints.

6.3.2 Genetic Search algorithms

In this project Genetic Algorithm (GA) method is selected which is included inside MATLAB *ga function* [81], or SCILAB *optim_ga* functions [104] It calls the aerodynamic function. The aerodynamic code explained in the previous chapters is written in form of aerodynamic function; whose arguments are airfoil coordinates, angle of attack, and Reynolds number.

Genetic search algorithms GAs is a widely used class of evolutionary algorithms. It can work without the need to calculate gradients (which is a drawback of gradient based optimization methods). This method uses random search that allows a global search capability over local search methods inside the design space. The name comes from the attempt to replicate life evolution. The design parameters vector, or variables, represents one aerodynamic shape i.e. one airfoil candidate. This airfoil candidate is a member of one population. GA is used in many airfoil direct and inverse design studies as [101][102], and [103].

The method starts with initial population. The objective function of the initial population is evaluated, as the first step. This is called the first generation, which is subjected to two natural selection techniques called fitness and crossover. The design with higher fitness will survive and will contribute more to the next generation of airfoil shapes. Designs having higher fitness are paired up, so that offspring (children) are constructed from them by the crossover process. By this rules the method is forced to use the best designs and their combinations exploring search space. The less fitness designs die, although, mutation process is used where few individuals are randomly changed to produce new ones. This insures the search space is covered by the method.

The *ga* optimization function asks for a set of inputs to perform the calculation. The main inputs are listed in Table 6.2, other parameters are not changed and used as in their defaults. The function returns a vector of optimum design variables together with their fitness values. Table 6.2 illustrates the input arguments to a standard *ga* function.

Table 6.2 Description of input arguments for *ga* function

Input	description
Objective function	The function that calls airfoil parameterization, performs aerodynamic calculations and returns the fitness value of each airfoil in the generation.
Number of design variables	Number of parameters required to represent airfoil shape.
Upper Bound	Upper limit for each design variable.
Lower Bound	Lower limit for each design variable.
Initial population	Values of design variables for an initial design (airfoil shape)
Fitness limit	The value used to stop search algorithm, set by the user.

6.3.3 Choice of constraints

The choice of parameterization method plays an important role in the ease of applying geometric constraints. For instance, In PARSEC method the geometric parameters like maximum thickness and position of maximum thickness are directly constrained without the need for additional formulation. For Bezier curves method there is a connection between the control point position and geometric variables, but it needs additional formulation. On the other hand, CST method requires computation of the geometric variables from airfoil coordinates. The following table lists some aerodynamic and geometric constraints commonly used:

Table 6.3 Common aerodynamic and geometric constraints

Constraints	Type	Source of constrain
Maximum and minimum thickness and its location	Geometric	Structure, fuel tank packaging, ease of manufacturing.
Leading edge radius.	Geometric	Stall characteristics.
Trailing edge angle and thickness	Geometric	Manufacturing
c_{m_0}	Aerodynamic	Tail volume, control surfaces.
c_{l_0}	Aerodynamic	Performance requirements
$c_{l \max}$	Aerodynamic	Take off, stall capability.
c_l/c_d	Aerodynamic	Performance requirements

In the airfoil design problem, the vector of design variables $X_j, j = 1: N$ can be set as target aerodynamic performance (ex. drag coefficients) at one angle of attack, or a range of angles of attack. If the pressure coefficient is the target aerodynamic performance then this function is the functional difference between calculated and target distributions.

6.3.4 Formulation of objective function

Objective function for airfoil design may vary from one application to another. Optimization algorithm manipulates airfoil shape parameters in systematic manner to satisfy the objective function. For instance, maximizing range can be formulated in terms of maximizing lift to drag ratio at specified range of angles of attack α and Reynolds numbers as given by Eq. (6.5). The negative singe is used to allow using minimization. A weighting coefficients w_i where $i = 1,2,3 \dots n$, and n is the number of angles of attack are used in the formulation. These

coefficients can have values from 0 to 1, and are chosen in such a way to allow shaping of the objective function inside the operating range of angle of attack according to the design requirements.. Higher values of the weighting factor w_i indicate more important components and lower values indicate less important components.

$$-\sum w_i \frac{c_l}{c_d}(\alpha_i) = \text{minimum} \quad (6.5)$$

The objective function for minimum drag can be formulated as follows:

$$-\sum w_i \cdot c_d(\alpha_i) = \text{minimum} \quad (6.6)$$

Optimizing airfoils for specific pressure distribution can be achieved by similar objective function formulations as given by Eq.(6.7)

$$-\sum w_i \cdot (C_{P_i}^s - C_{P_i}^c)^2 = \text{minimum} \quad (6.7)$$

The superscripts s and c stand for specified and computed pressure coefficients respectively, and the factor w_i allows different weights being given to each component at i^{th} point. This equation means that functional difference between specified and computed pressure coefficient is minimum. The functional difference is given as the sum of the square of the difference between the specified and the computed pressure coefficient at each point i , which is always positive. This formulation permits the user to put more weight to specific location of airfoil surfaces, such as front part where pressure variation are most, or near separation bubble location.

6.3.5 Single objective versus multi objective optimization

Maximizing airfoil lift, for example, has many benefits for all aircraft performance resulting in shorter takeoff and landing distances, reduces aircraft noise, and lowers stall. It is, therefore, the dream of designing airfoil with maximum lift and low drag remains a topic of considerable interest. High airfoil lift or low airfoil drag alone are not the only desirable feature during airfoil design. Aerodynamic characteristics like lift-to-drag ratio, endurance parameter, thickness, pitching moment, stall characteristics, and roughness sensitivity are always considered during airfoil design and optimization. Therefore multi objective optimization is widely anticipated in airfoil design studies. The other reason for multi-

objective optimization is that, it is difficult to control one airfoil aerodynamic characteristics without affecting the other performance characteristics.

A great deal of existing research reveals that instead of using airfoils from ready catalogues of existing airfoils, many aircraft and turbo machinery designers have utilized special airfoils which are more adequate to their functional requirements. For instance, for low Reynolds number vehicles, the preferred requirements are listed as follows:

- 1) High lift coefficient $c_l \geq 1$.
- 2) High lift-to-drag ratio c_l/c_d .
- 3) High endurance factor $c_l^{3/2}/c_d$.
- 4) High maximum lift coefficient $c_{l_{max}}$.
- 5) Smooth stall characteristics. (Turbulent separation point jump)
- 6) Limited pitching moment coefficient C_m .
- 7) Large relative thickness t/c .
- 8) Wide range of low drag angles of attack.

Due to the mentioned multipoint requirement discussion, objective function can be formulated by combining these performance characteristics. One example is illustrated by Eq. (6.8) in which the lift to drag ratio together with endurance factor can be maximized for given range of flight conditions. Where the factor w_i , and w_j are selected weighting coefficients given to each component at i^{th} point.

$$- \sum \left(w_i \frac{c_l}{c_d} + w_j \frac{c_l^{3/2}}{c_d} \right) = \text{minimum} \quad (6.8)$$

6.4 Direct Aerodynamic optimization by shape perturbation

Numerical optimization can be used to design airfoil shapes using direct aerodynamic calculations for given specific objective function. This approach is equivalent to classical inverse design problem. But it has the advantage that the aerodynamic calculations are performed in direct manner, and no need for inverse formulation. The numerical optimization procedure like one given in Figure 6.3 will search for the optimum shape. Designers with lower experience can specify the initial shape from similar or like designs. The choice of initial shape shouldn't, in principle, affect the resulting optimum airfoil, but it will affect the computational cost.

The flowchart of Figure 6.3 illustrates the method. In this method the new airfoil shape is calculated based on GA population which is then parameterized to realistic airfoil shape. The airfoil parameterization method can be selected by the designer, detailed explanation of airfoil parameterization methods are given in separate chapter. It is important to mention that for high number of parameters (design variables) wider search space can be covered and new shapes can result. This is not without cost, the computational time and number of iteration required will increase dramatically with increased number of design variables. This is one drawback of direct optimization approach.

Direct design method avoids the difficulty of using the differences in pressure distributions to drive the new airfoil shape. This difficulty, common to inverse methods, comes from unsmooth shapes, and the need to extra formulations to relate the required shape perturbation to the differences in pressure distribution. Furthermore, working with limited number of parameters in airfoil parameterization will reduce the number of design variables (about 11) compared to using pressure differences at each airfoil coordinate point, which is usually more than 50 points.

The aerodynamic computations, which is the heart of the direct design procedure can be performed by various aerodynamic codes having different levels of accuracy. These codes use theories ranging from inviscid potential flow theory to CFD methods. The accuracy of the whole optimization process is off course highly dependent on the accuracy of the aerodynamic calculation code.

The designers usually verify the convergence of the optimization process by repeating the calculations with different initial airfoil shape and make sure that the procedure converges to the same or very close shapes.

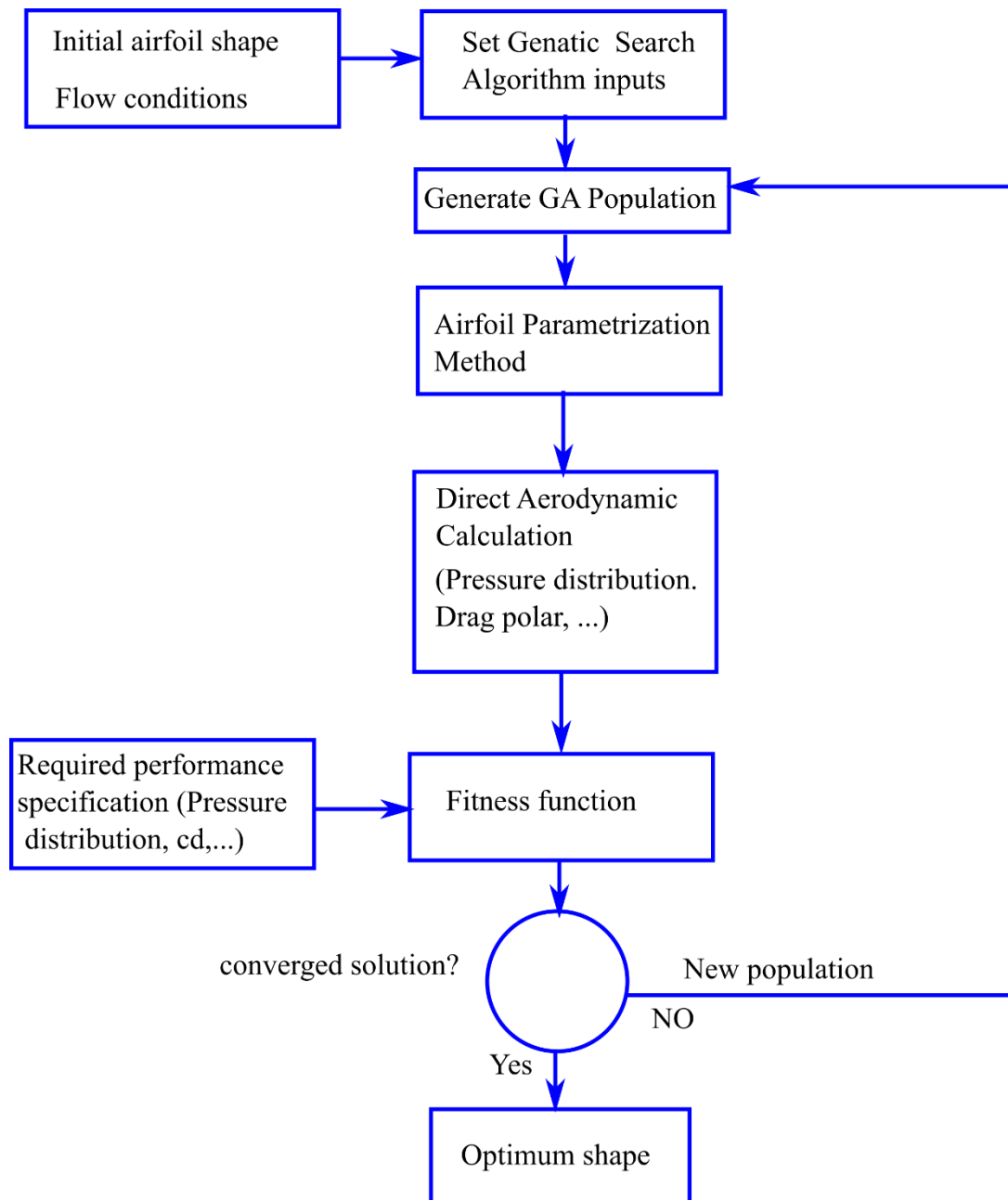


Figure 6.3 Flowchart illustrating Direct Aerodynamic Optimization by shape perturbation

CHAPTER 7

7 Airfoil Optimization Case Studies

This chapter deals with using the code developed in the previous chapters together with genetic optimization (GA) to search for optimized airfoils with different objectives and constraints. It is aimed at showing the flexibility of systematically changing airfoil geometry to get required airfoil performance characteristics, and the ability to formulate various objective functions and constraints that best suit the problem under hand. In this study, for objective function formulation weighted sum approach is adopted with penalty terms added to enforce constraints.

Optimization has been in use as a design method to find solutions to various aerodynamic problems. It is used in transonic range of flight since 1970th by authors like Hicks and Murman [82] and Hicks and Vanderplaats [83]. The optimization process has been limited to few design variables due large number of computations needed for finite differences and limited computer capabilities. In the 1990th computer speed and memory have been improved and numerical optimization methods appeared, such as gradient methods, and genetic search algorithms and others. One illustrative work on application of airfoil design at low speeds based on NACA airfoil representation is given in [95], in which the procedure of airfoil optimization is demonstrated using inviscid flow solver.

Airfoil optimization in low Reynolds number regime where laminar flow covers large portion of airfoil surfaces, depends primarily on the prediction of transition. Transition devices and trips are usually used to fix transition at single point. But, from aerodynamic point of view, since transition point varies with speed and angle of attack it is more efficient to design by laminar separation bubble control approach. Furthermore, such devices may not be practical when the wing surface is made of delicate materials such as foam, which are used in many UAV designs. It is obvious that laminar separation bubble control approach requires an aerodynamic code that can predict separation bubble effects on pressure distribution, and computes the variation of aerodynamic performance due to perturbations in airfoil geometry.

The code developed in this work is validated for Reynolds numbers of 2×10^5 , 3×10^5 and 5×10^5 [84]. The results of validation show comparable results with experimental

measurement for Eppler low Reynolds number airfoil E387 and for S8036 low Reynolds number airfoil designed for soft stall characteristics. Although this code results deviate from experimental measurement as separation point moves forward (which depends also on airfoil shape and angle of attack), it is possible to use with high degree of confidence. That is because it is based on solid aerodynamic theory and being widely used computation methods. This reason makes this code results follow the trend of similar aerodynamic codes in this class, such as XFOIL for which aerodynamic features are calculated with same order of magnitude as was shown in the comparisons of boundary layer features [84].

Airfoil design is mostly driven by minimization of drag. It is possible to design airfoils at low Reynolds number based on laminar separation bubble (LSB) control instead of eliminating the LSB totally by forcing early transition since the later will increase the turbulent friction drag. Therefore, in low Reynolds number airfoils the primary concern is to control bubble losses rather than minimizing skin friction drag [11]. It is worth to note, that at low Reynolds number, laminar separation bubble (LSB) has a major contribution in airfoil drag. LSB also moves and changes in length with changes in angle of attack. When angle of attack increases LSB moves in the forward direction with decrease in length, and at much higher angles a forward sudden jump in turbulent separation point occurs, causing much higher drag and decrease in lift. As angle of attack is decreased the separation bubble becomes longer, which may, not reattach resulting in a higher separation drag.

Historically, The inverse design approach utilizes the so called a transition ramp, in which the pressure distribution of the forward portion of upper airfoil surface (suction side) is shaped in such away to allow long weak pressure gradient with extended attached laminar flow. This pushes the laminar separation point backward and forms a (LSB) as a mechanism for turbulent transition. Therefore most of instability changes will occur at the back of the ramp and inside the bubble which limits turbulent transition point to jump close to the leading edge causing sudden stall. In inverse design, the transition ramp shape (length, slope and arc shape) are varied, to control bubble movement and improve airfoil performance. In general total drag with transition ramp can be larger but airfoil stall characteristics and off design performance are improved.

There are few airfoil geometry parameters that have an effect on performance, such as leading edge radius, thickness, trailing edge angle, position of maximum thickness. These airfoil

geometric parameters are used by NACA and utilized by PARSEC airfoil parameterization method. Bezier curves and CST parameterization methods, on the other hand, utilize control points and polynomial coefficients which are not directly related to airfoil geometric parameters.

Therefore, similar to transition ramp approach, airfoil upper surface geometry can be modified by these last two methods to achieve low drag bubble characteristics. The effect of upper surface shape on pressure distribution and drag polar is studied in [11]. Figure 7.1 shows effect of perturbing an airfoil surface on drag polar at Reynolds number of 2.5×10^5 . Pushing airfoil surface around the maximum thickness down has the effect to generate a faster pressure rise and a decrease in drag but also a decrease in maximum lift. Modification of airfoil surface in the opposite direction causes more drag associated with getting higher values of maximum lift coefficient, as seen.

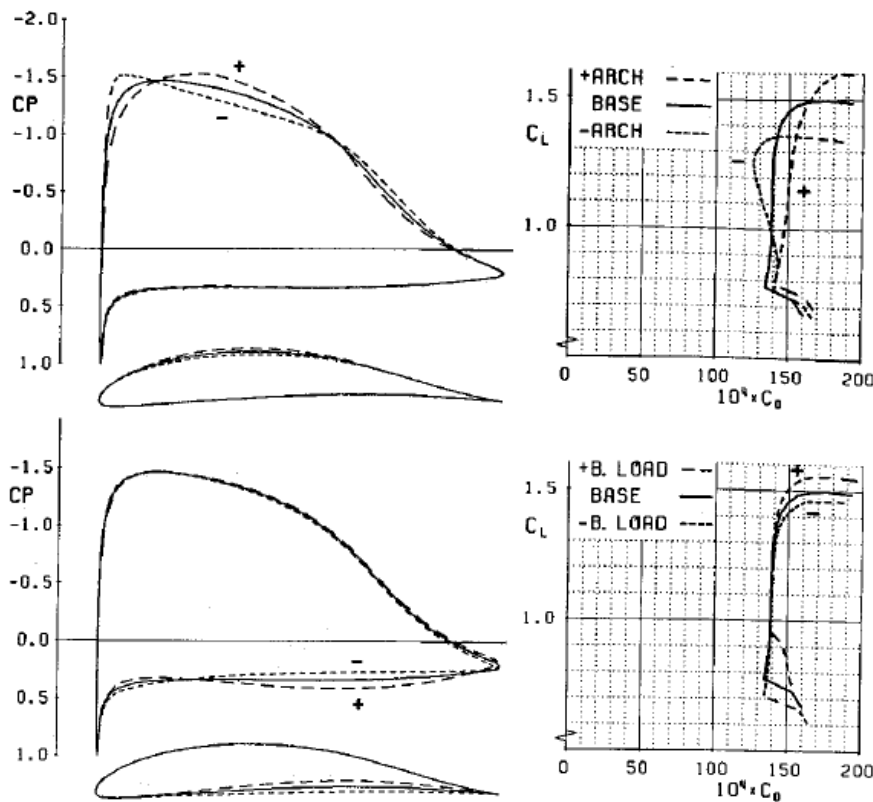


Figure 7.1 Relations between pressure distribution shape, and drag polar, and airfoil shape [11]

The airfoil lower surface shape affects both pitching moment coefficient and maximum lift coefficient. Moving lower surface up (inside the airfoil) increases pitching moment

coefficient and maximum lift coefficient, and show variation in drag at extreme sides of the polar. While moving it down (outside) has the opposite effect.

The systematic modification of airfoil geometry is an efficient airfoil design approach when done with optimization techniques. In which upper surface shape is controlled through the choice of parameterization method coefficients that will cover variety of shapes. The LSB model will calculate the drag associated with each shape and finally, the optimization technique will drive the optimization process to the minimum drag shape.

7.1 Problem formulation

In this chapter a number of airfoil design methods are examined with systematic airfoil geometric modification approach. The first method is design to meet given target pressure distribution. The second design method is based on specifying design point which could be Single Point (SP), for one angle of attack or a multi point (MP) a set of angles of attack. The objective that has to be satisfied can vary from single objective (SO) to multi objective (MO). Therefore, in the rest of this chapter the following design concepts are demonstrated:

1. **Design to meet specific pressure distribution. (section 7.5).**
2. **Design for Single Point Single Objective (SPSO) (section 7.6).**
3. **Design for Single Point Mingle Objective (SPMO) (section 7.7).**
4. **Design for Multi Point Single Objective (MPSO) (section 7.8).**
5. **Design for Multi Point Single Objective (MPMO) (section 7.9).**
6. **Design at different Reynolds numbers. (section 7.10).**

An example of single objective is unconstrained drag minimization. If in addition to drag minimization the designer wants to maximize or minimize specific aerodynamic coefficient (lift or moment coefficient, for example) a multi-objective problem is formulated. Weighting coefficients are assigned by the designer to each term in the formulation. Other coefficients are also used to set approximate order of magnitude to each objective. Additional terms are added to the objective for each constraints violation.

In all of these cases geometric constraints (bounds), CST airfoil parameterization method and initial airfoil (E387 airfoil) are kept the same. This allows the effect of objective function formulation, angle of attack and Reynolds number to be analyzed for different formulations. The code developed in the previous chapters is used throughout the analysis at Reynolds number $R_e = 3 \times 10^5$ and the critical value of disturbance amplification $N_{cr} = 12$.

7.2 Geometric constraints:

Geometric constraints are placed to search around the starting airfoil. The geometric constraints are shown in Figure 7.2. The airfoil upper surface can take any smooth shape between the upper limit (dotted dashed line) and the lower limit (dashed line) beneath it. The lower surface will be constrained in similar manner between its upper and lower limit lines shown in the lower side. It is clear that lower surface is allowed to have some points above the real axis causing aft loaded airfoils. It is worth to note that y axis is exaggerated in all airfoil shapes to show the small differences.

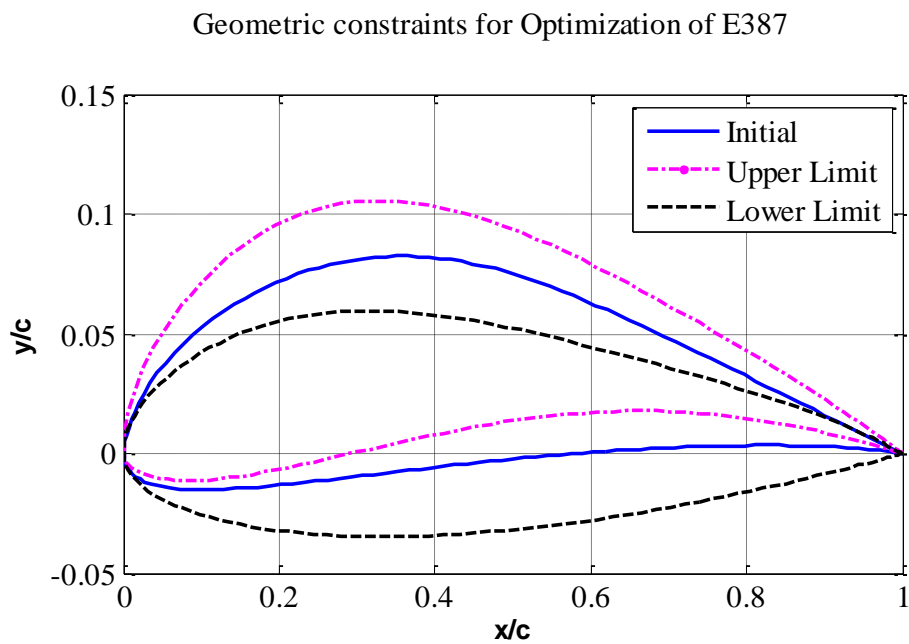


Figure 7.2 SPSO geometric constraints

7.3 Airfoil Parameterization

Airfoil parameterization with CST method is used with 4 coefficients to each surface. The following table shows the upper and lower surfaces as well as the initial airfoil.

Table 7.1 Parameters for CST method

	Upper surface				Lower surface			
UB	0.22	0.35	0.2	0.25	-0.06	0.01	0.08	0.1
LB	0.133	0.2	0.09	0.18	-0.09	-0.09	-0.09	-0.09
Initial	0.1349	0.3291	0.1062	0.2218	-0.0758	-0.0001	0.004	0.03

7.4 Formulation of the objective function

The objective function in this project is formulated based on weighed sum approach. A constraints enforcement function is necessary to grantee the operation at the desired aerodynamics requirements. In this approach, the two functions are combined into single merit equation using user specified constants.

The objective functions \bar{f} can be written in verity of forms, as explained in pervious chapter. The aerodynamics constraints function g can be formulated to specify the required aerodynamic coefficients range. For example, in lift constrained drag minimization problem the objective function is given by $\bar{f} = c_d$ and the aerodynamic constraints equation g is given by $g = c_{ld} - c_l$. Where c_{ld} is the desired lift coefficient and c_l is the calculated lift coefficient for the given airfoil parameterization vector x , flow angle of attack α and Reynolds number.

When these two functions are combined a weighing coefficients are introduced, as w_{cd} and w_{cl} in the following formulation

$$\bar{f} = w_{cd} c_d - K_{cl} w_{cl} (c_{ld} - c_l) \quad 7.1)$$

7.4.1 Equality and Inequality Constrained Optimization and Penalty Function

In practice a penalty term is added to the objective function when a constraint is violated. The goal of penalty function is to change a constrained optimization problem to unconstrained optimization one.

The penalty function for inequality constraints can be formulated as in the following equation where K is a positive integer representing how strong the penalty will be applied.

$$\varphi(x) = \begin{cases} 0 & \text{for all } x < 0 \\ K x^3 & \text{for all } x \geq 0 \end{cases} \quad 7.2)$$

The function will look as in Figure 7.3. When the penalty term is applied to the objective function it is casted in the form $\varphi(x_0 - x)$ for the constraint $x \geq x_0$ such that the optimization is forced to choose values of x greater than x_0 , because the objective function will be smaller for any $x \geq x_0$. The shape of the added term is shown in Figure 7.4, which illustrates how penalty function is used to strongly enforce two different constraints $x \geq 1$ and $x \geq 3$. It is clear that the objective function will be smaller for values of $x \geq 1$ and $x \geq 3$ when penalty terms are added.

$$f = \bar{f} + \varphi(x_0 - x) \quad 7.3)$$

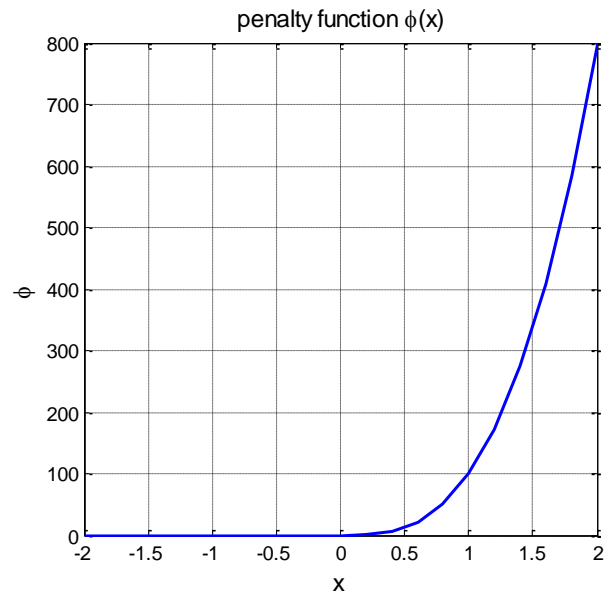


Figure 7.3 penalty function $\phi(x)$

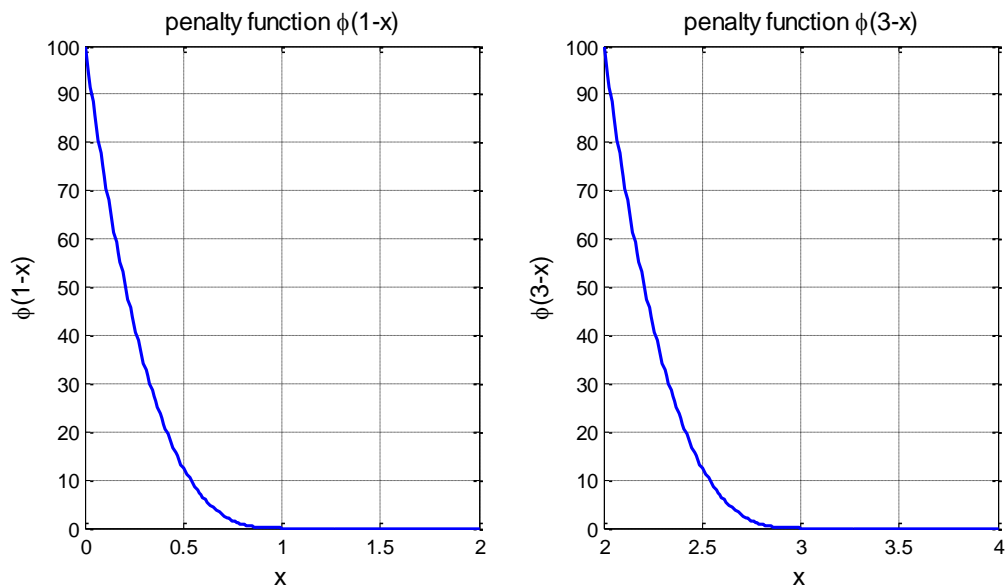


Figure 7.4 A penalty function $\phi(x_0 - x)$ added to the objective function if $x < 1$ and 3 respectively

The minimization of the function $f(x)$ can be generalized as follows, if x is the design variables, subjected to equality and inequality as in the following two equations

$$\begin{aligned}
 g_i(x) &\leq 0 \quad \text{and} \quad i = 1, 2, \dots, m \\
 h_i(x) &= 0 \quad \text{and} \quad i = 1, 2, \dots, n
 \end{aligned}
 \tag{7.4}$$

And if the penalty function ϕ is given by Eq. 7.2 then the objective function is written in the following form

$$f(x) = \bar{f}(x) + \sum_{i=1}^m \phi(k_i^{inq}, g_i(x)) + \sum_{j=1}^n \left(\phi(k_j^{eq}, h_j(x)) + \phi(k_j^{eq}, -h_j(x)) \right) \quad 7.5)$$

The first term $\bar{f}(x)$ is the aerodynamic objective. The second term is the inequality constraint and the last term represents the equality constraint. The constants k_i^{inq} and k_j^{eq} a user specified constants for inequality and equality constraints respectively. The choice of those constants is problem specific, and the user should tune the constants for his optimization [90], and [91].

In our formulation another factor $K_{cl} > 1$ is multiplied by each constrained term; if the constraint is violated. When multipoint optimization is studied this function is applied to each point separately and the sum is minimized.

7.5 Design for given pressure distribution (Inverse design)

The design cases presented in this section aims at illustrating the efficiency and accuracy of the inverse design method by using systematic airfoil shape modification enforced by optimization algorithm. A predefined pressure distribution is given and an airfoil shape that matches this pressure distribution is found. The flight conditions for the design point are Reynolds number and angle of attack. The predefined pressure distribution is called target pressure distribution and the corresponding airfoil shape is called target airfoil. This procedure is known as inverse design.

In order to check the efficiency of this procedure a known airfoil shape and pressure distribution is used. The initial airfoil is further parameterized by CST method and the obtained parameters are utilized in the optimization as design variables. The optimization procedure changes these parameters until the best functional difference in pressure distributions is obtained.

As an illustration, CST method parameterization is performed to find the parameters for two sample airfoils. A separate code is written to match a given airfoil coordinates by given number of parameters, as explained in chapter 5. The first airfoil is NACA0012 at Reynolds number of 0.3×10^6 and angle of attack of $\alpha = 4^\circ$. The second is Liebeck high lift airfoil at Reynolds number of 0.5×10^6 and angle of attack of $\alpha = 5^\circ$.

7.5.1 NACA 0012

In this case study NACA 0012 airfoil geometry is first parameterized using CST as shown in Figure 7.5 . The parameterization coefficients are shown in Table 7.2.

Table 7.2 The CST parameters for NACA 0012 airfoil

point	Upper surface	Lower surface
1	0.17072	-0.17072
2	0.16066	-0.16066
3	0.15542	-0.15542
4	0.14038	-0.14038
5	0.16382	-0.16382
6	0.11797	-0.11797
7	0.15965	-0.15965

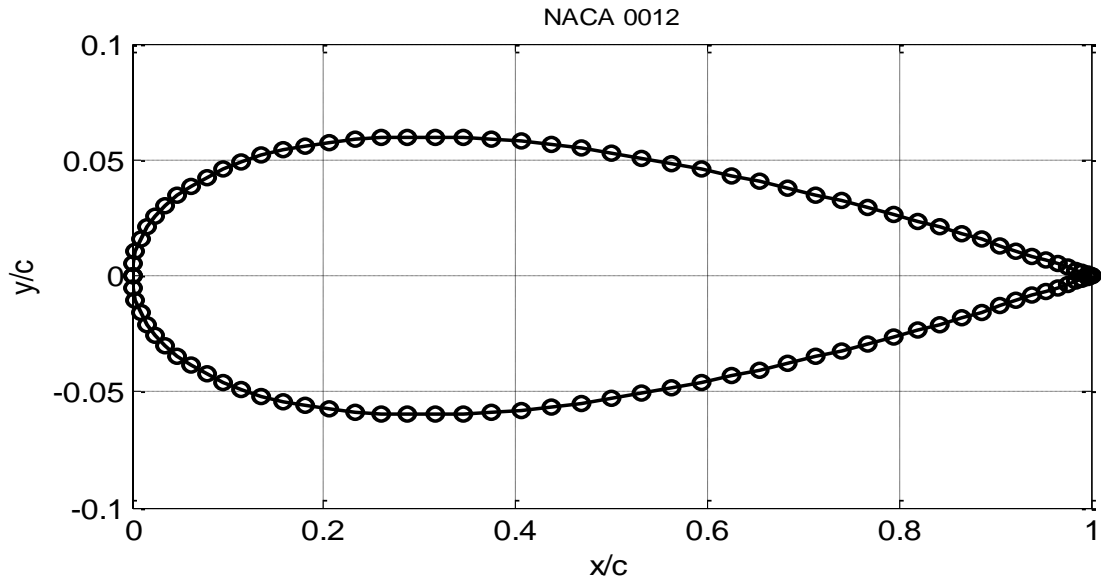


Figure 7.5 NACA 0012 geometry

The second step the pressure distribution at Reynolds number of 3×10^5 and angle of attack of $\alpha = 4^\circ$ is used as target pressure distribution as shown in Figure 7.6.

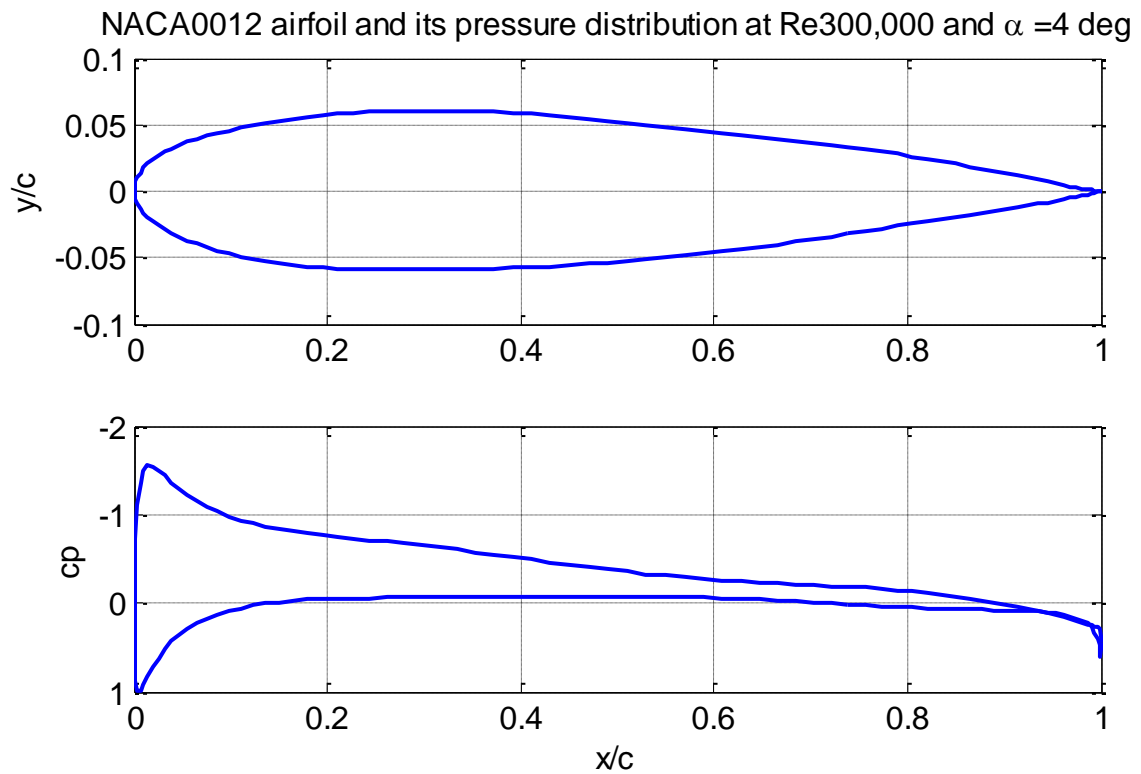


Figure 7.6 Target airfoil shape and target pressure distribution at Reynolds number of 3×10^5 and at angle of attack of 4 degrees

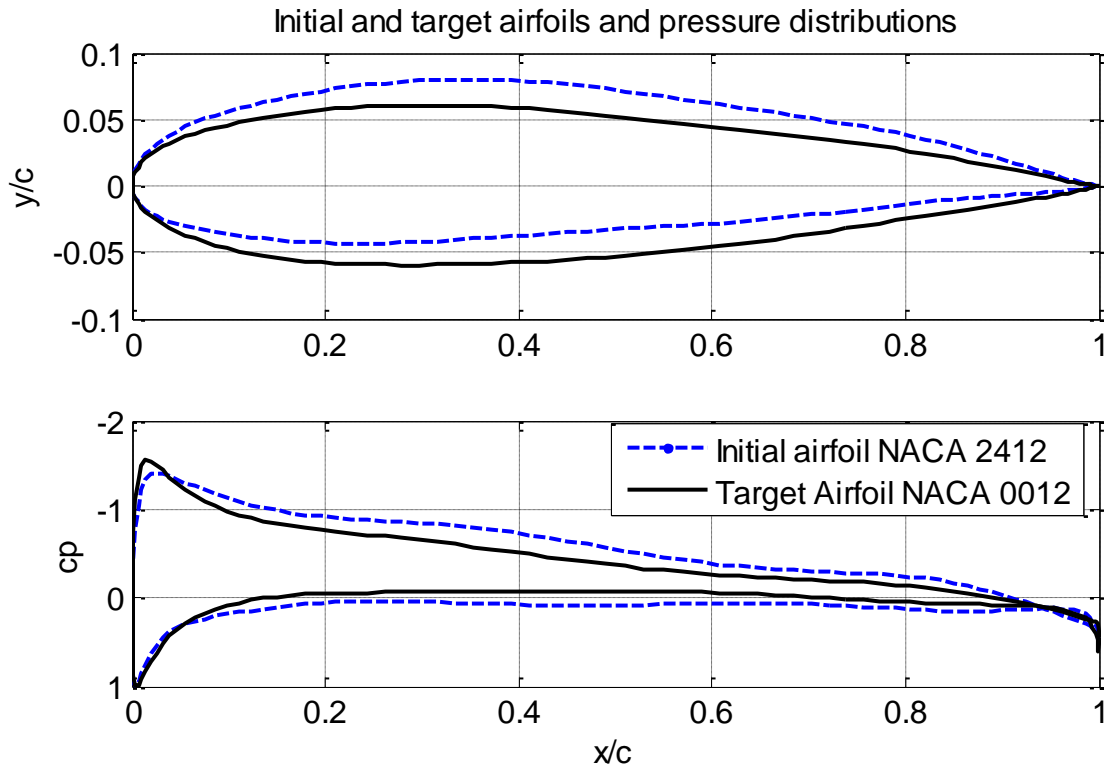


Figure 7.7 Initial and target airfoils and corresponding pressure distributions

The optimization process is started from NACA2412 airfoil as shown in Figure 7.7. The optimization process uses 7 parameters for each surface. The objective function calculates the functional differences between target and current pressure distributions as per Eq.(5.39). The difference is calculated as the mean of difference squared between two functions as given by

$$diff = \sqrt{\frac{\sum_{k=1}^N (C_p^T - C_p^K)^2}{N}} \quad (7.6)$$

Where, C_p^T is the target pressure distribution at each airfoil surface point from $i = 1$ to N , and C_p^K is the pressure distribution calculated at k^{th} iteration step.

This error measure is used as objective function during the optimization process. It should rapidly diminish as the optimization method converges to the target pressure distribution shape. The results of optimization after 5 generations are shown in Figure 7.8, where in the upper part, the airfoil geometry is compared to target airfoil and the error difference in

y coordinate is compared. In the lower part the target and current pressure distributions are compared and the local difference are shown. The differences are drawn as function of surface distance from lower surface trailing edge to upper surface leading edge in clock wise direction. It can be seen that the maximum difference in y airfoil coordinates is lower than 2×10^{-3} . The pressure distribution show close agreement with the target with maximum difference of 0.02. Figure 7.9 show the same after 15 generations. The difference in airfoil shapes is about 11×10^{-4} close to the lower surface leading edge. The difference in pressure distribution is much improved with maximum difference of 0.015.

The convergence history is shown in Figure 7.10. The optimization process is rapidly converging to the target pressure distribution and at the same time the airfoil is closer to the target airfoil.

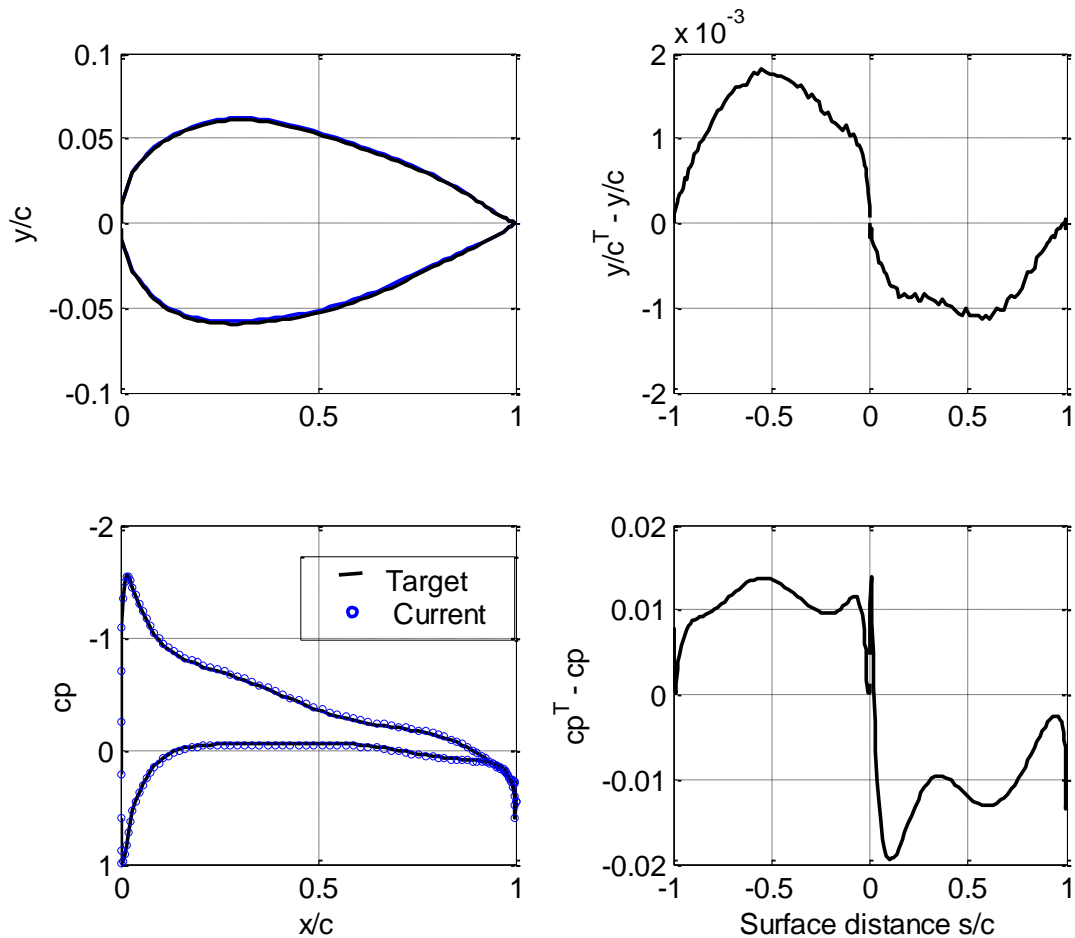


Figure 7.8 Airfoil shape and pressure distribution after 5 generations

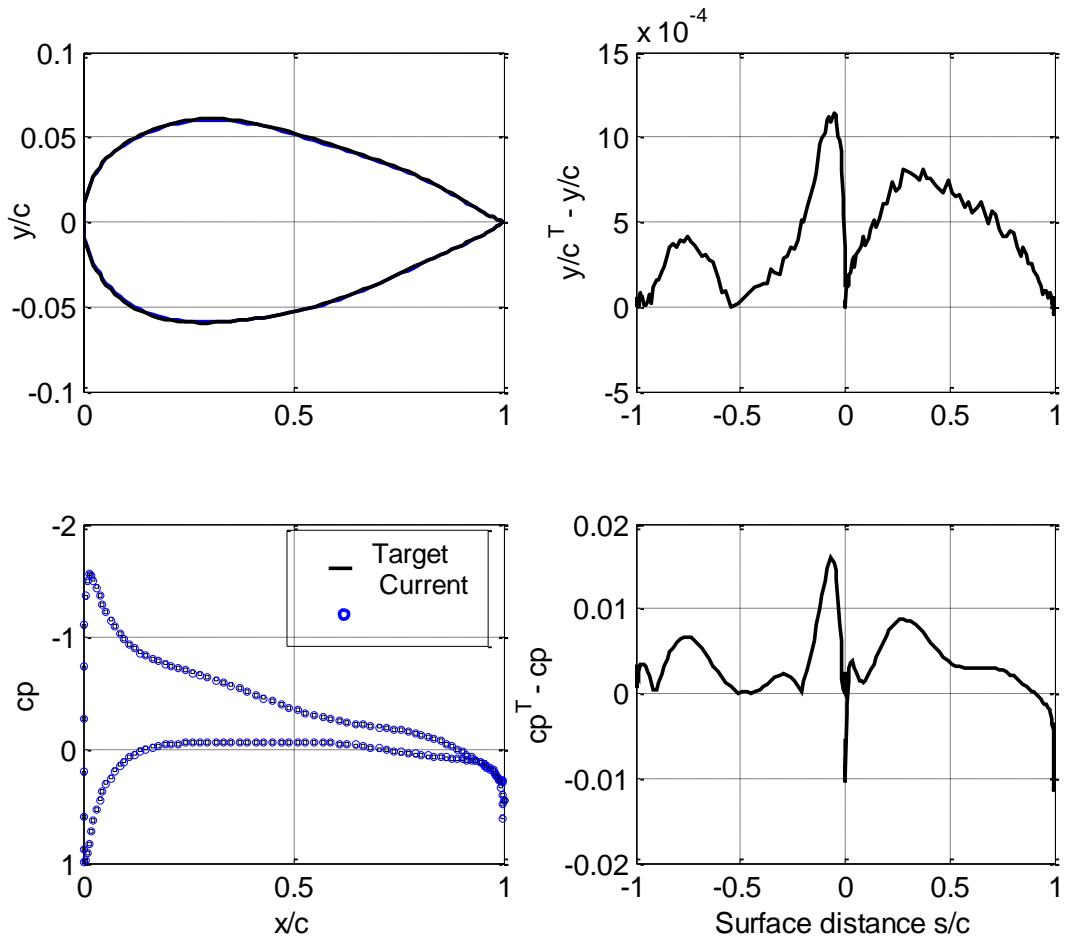


Figure 7.9 Airfoil shape and pressure distribution after 15 generations

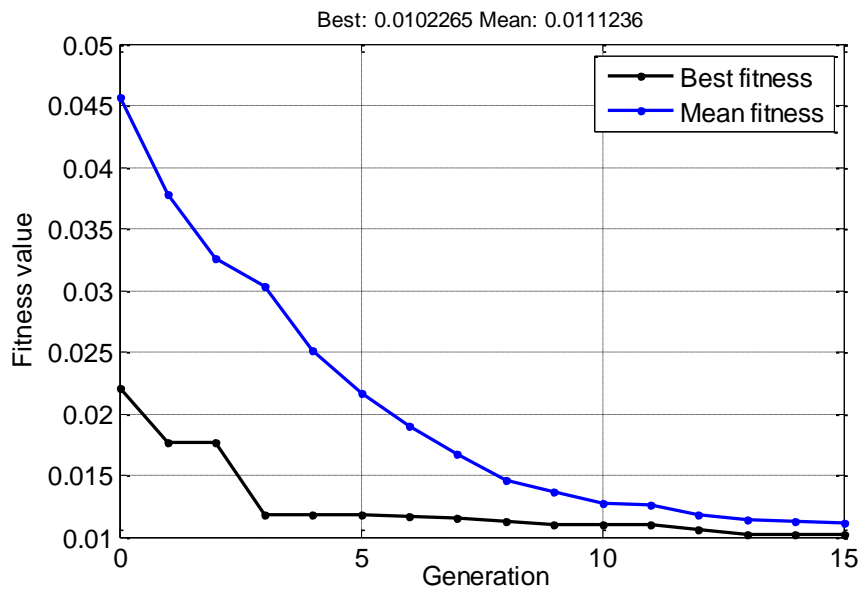


Figure 7.10 Convergence history for case of NACA 0012 airfoil

7.5.2 LIEBECK LNV109A high lift airfoil

Liebeck utilizes the inverse design method for development of a class of airfoils with high lift [92]. He uses the Stratford pressure distribution [93] to recover the pressure without separation. The Liebeck LNV109A airfoil is selected as illustrative example as shown below in Table 7.3 and Figure 7.11.

Table 7.3 CST parameters used to represent LNV109A Liebeck airfoil

point	Upper surface	Lower surface
1	0.25479	-0.26097
2	0.37004	0.1911
3	0.37664	-0.22163
4	0.24632	0.18688
5	0.093813	-0.0019703
6	0.17872	-0.007597
7	0.015989	0.040923

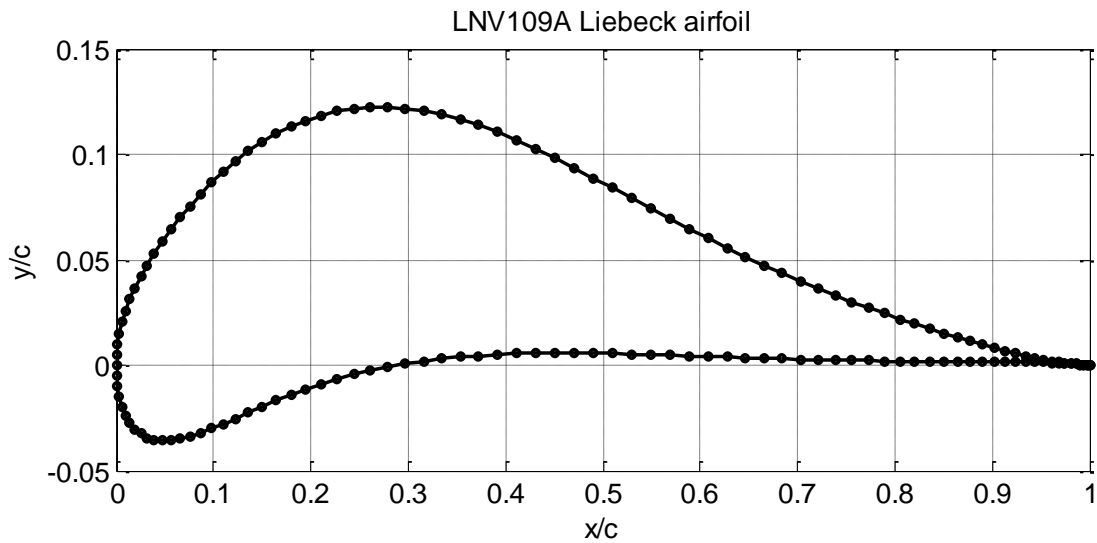


Figure 7.11 Liebeck LNV109A airfoil geometry

The flight condition selected for this case are Reynolds number of 5×10^5 and $\alpha = 5^\circ$. the target pressure distribution is shown in Figure 7.12. The optimization process started from NACA2412 as shown in Figure 7.13.

Optimization results are shown in Figure 7.14 and Figure 7.15 from which it is clear that the airfoil shape is constructed with very good accuracy and also the pressure distribution

differences are very low at the last generation. The convergence history shows that the inverse design approach examined here successfully constructed the target airfoil with very high accuracy. One advantage of this method is its simplicity in which only target pressure distribution is required, and no need for smoothing, in contradictory to other methods that use local pressure differences to modify the local normal to the airfoil surface.

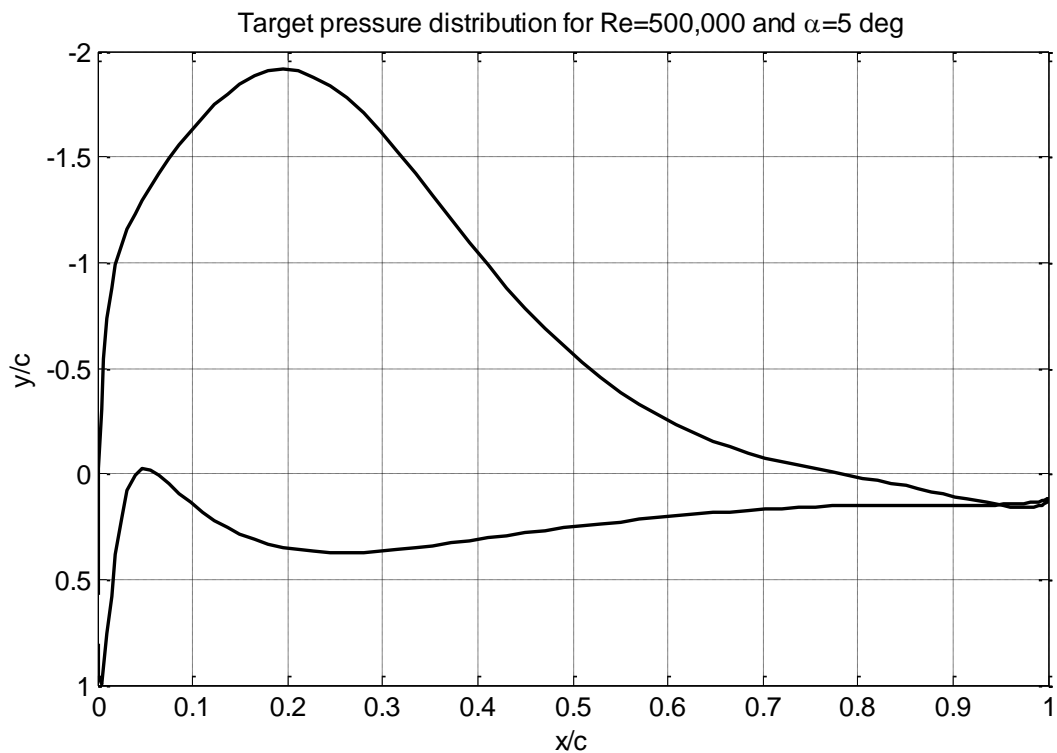


Figure 7.12 Target pressure distribution for Liebeck airfoil LNV109A at Reynolds number of 0.5×10^6 and $\alpha = 5^\circ$

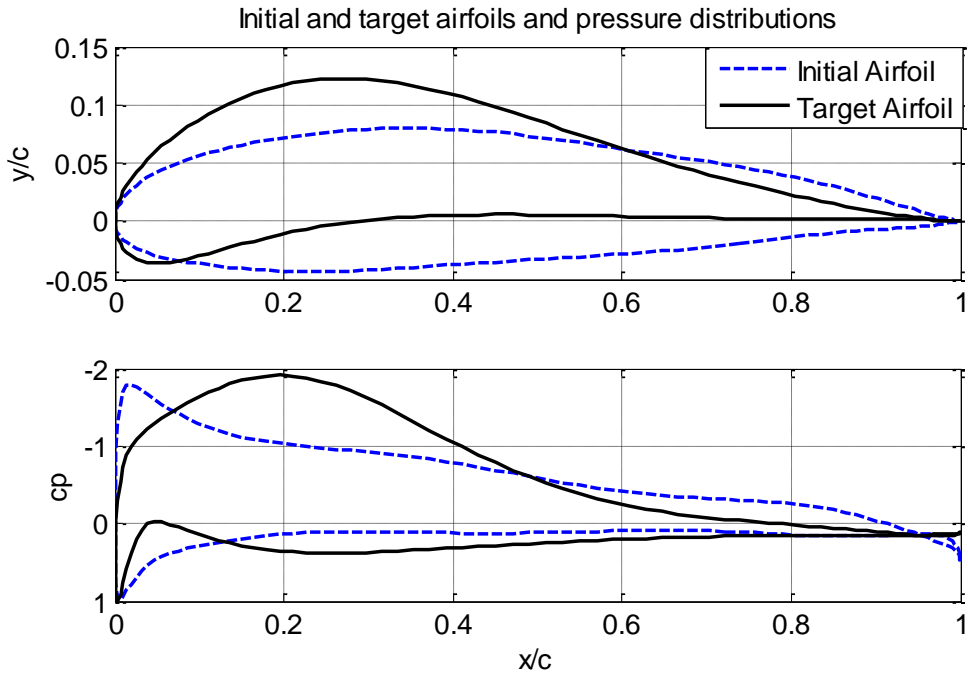


Figure 7.13 Target airfoil (LNV109A) and initial airfoil (NACA 2412) and pressure distributions at Reynolds number of 0.5×10^6 and $\alpha = 5^\circ$.

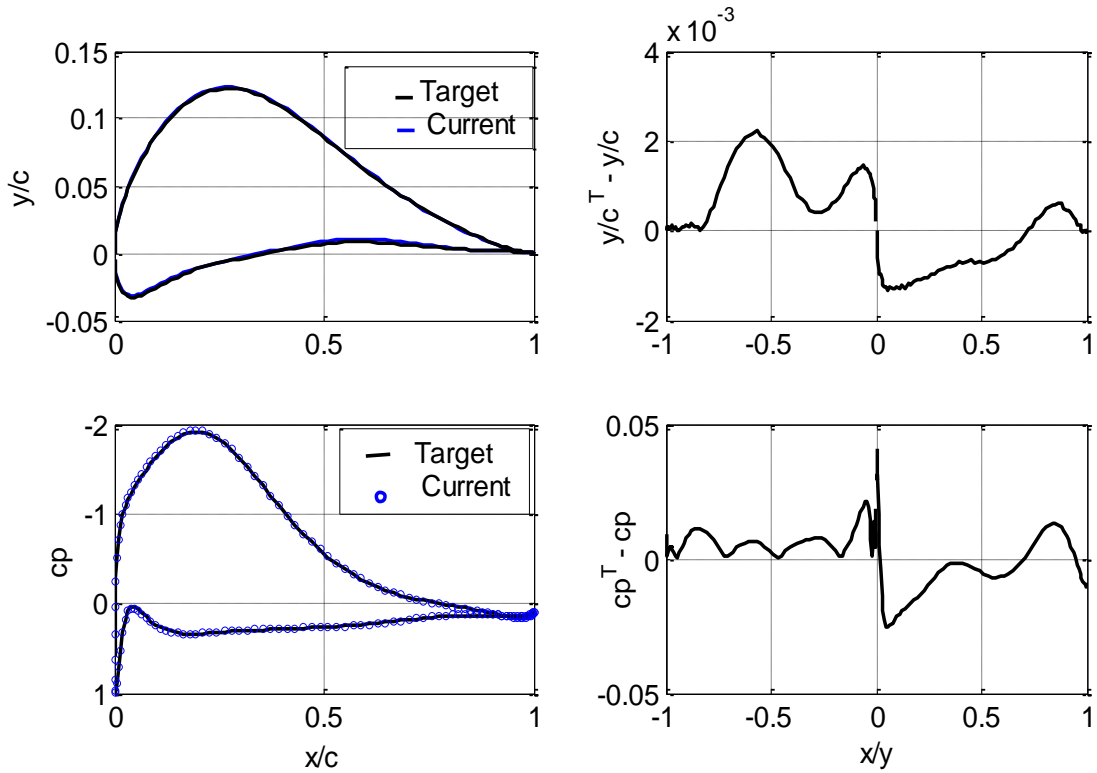


Figure 7.14 Airfoil shape and pressure distribution after 15 generations

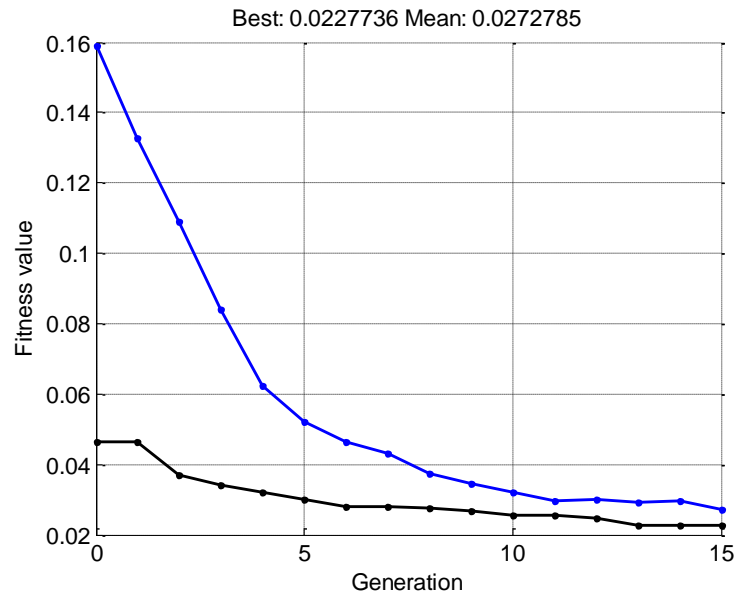


Figure 7.15 Convergence history for Liebeck LNV109A airfoil

7.6 Single point single objective

The objective of minimizing drag is examined. The optimization starts with Eppler E387 low Reynolds number airfoil. A single point in terms of angle of attack is targeted for drag minimization. The data for the starting airfoil are used as reference throughout the analysis of the results.

The objective function is formulated as follows:

$$f = c_d \tag{7.7}$$

7.6.1 Aerodynamic constraints

In this case no aerodynamic constraints are applied to the optimization problem. Only the objective function which searches for minimum drag coefficient at the design point is formulated.

7.6.2 Optimization Results

Genetic search optimization started with the initial airfoil parameters constrained by upper and lower bounds shown in Table 7.1 arrives at final shape after 15 generations with 480 function evaluations, as shown in Figure 7.16 which results from Genetic search process. Figure 7.16 consist of four subplots. Subplot (a) shows the best airfoil shape fitness and the

mean fitness value for each generation. It is good to note that, the fitness value means airfoil drag in this case, and individual refers to airfoil shape. Subplot (b) shows the best and the worst fitness together with mean value, it is evident that the genetic search algorithms has reached close to the best fitness just after 10 generations, after which there were no much changes in the best fitness value. The values of the best individual (airfoil shape) is shown in subplot (c) the first four numbers represent upper surface and the last four numbers represent lower surface. Subplot (d) shows the fitness (drag coefficient) of each individual (airfoil). It is clear that the fitness most individuals in this generation is very close to the best except few with have higher fitness values.

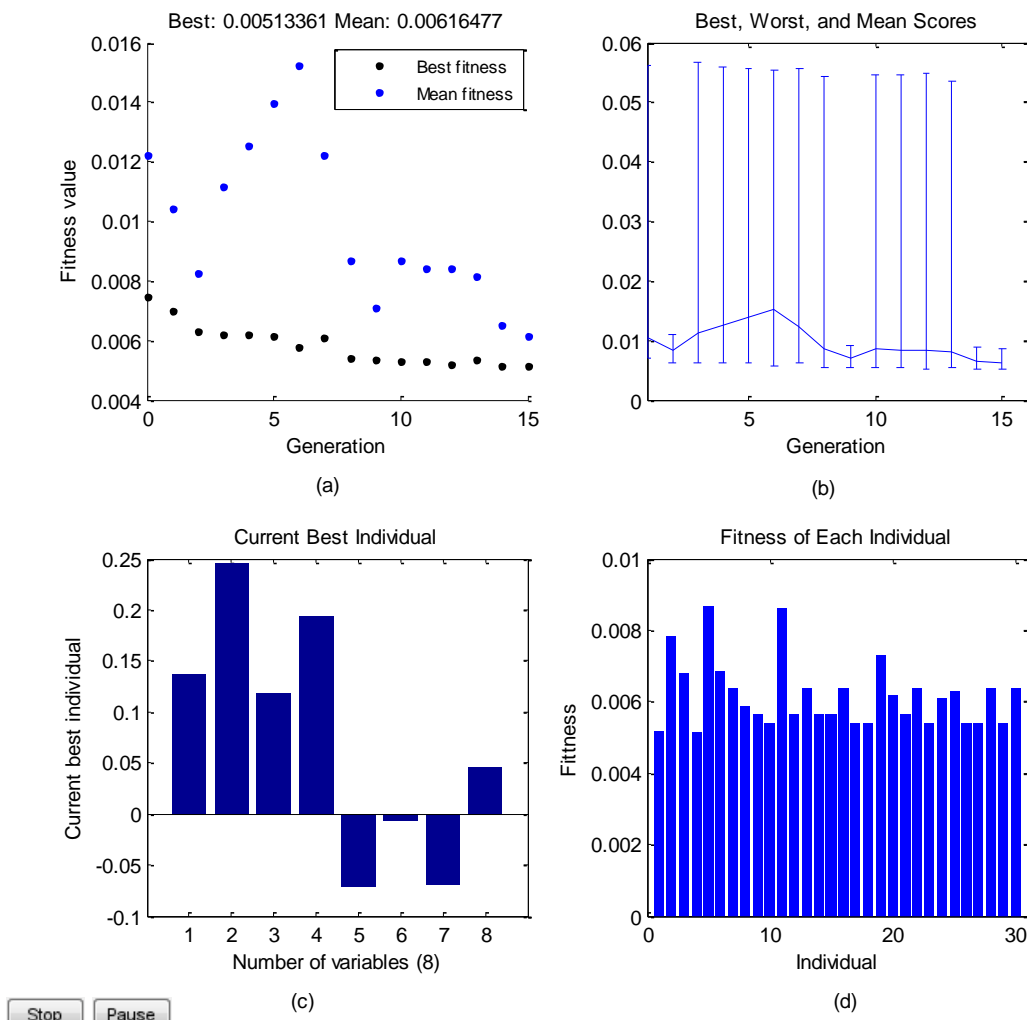


Figure 7.16 Results of genetic search method, (a) best airfoil fitness and mean for each generation. (b) Best, worst and mean scores in each generation. (c) The parameters of the best airfoil shape at last generation. (d) The fitness of each airfoil shape in the current generation.

The best airfoil CST parameters are shown in Table 7.4. The comparison in geometry between initial and optimized at single point for drag is shown in Figure 7.17.

Table 7.4 Initial and best airfoil CST method parameterizations

	Upper surface				Lower surface			
Initial	0.1349	0.3291	0.1062	0.2218	-0.0758	-0.0001	0.004	0.03
Best	0.136189	0.246385	0.1184	0.19312	-0.07124	-0.006552	-0.07006	0.046167

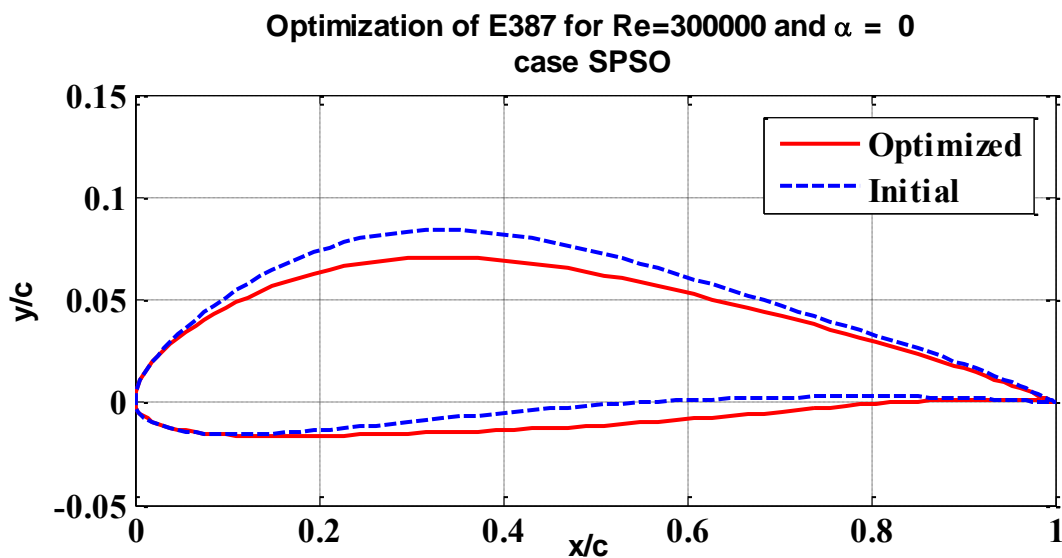


Figure 7.17 Comparison in airfoil shape

7.6.3 Airfoil shape and pressure distributions

The optimization process finds airfoil shape that is in general close to initial shape. The upper and lower surfaces being lower than that of the initial airfoil, making upper and lower surface pressure distributions more close as seen in Figure 7.18 . This will result in decreased drag but lift will also decrease at this angle of attack. The moment coefficient will also decrease since airfoil shape has less bottom loading. This is expected since there is no aerodynamic constraints applied to the optimization process. The laminar separation bubble extends around the med chord, the reattachment point is about 0.65 chord is shown on the figure. The laminar separation points on both airfoils are close but the optimized airfoil has less velocity drop which is proportional to bubble drag. The length of this bubble is approximately equal, as seen from the length of velocity plateau and reattachment phases of

the laminar separation bubble shape. This can explain the lower drag associated with the optimized airfoil. Bubble length and position are most important factors in low Reynolds number drag reduction, as reported by many authors [11]. This means that part of drag reduction is achieved by proper laminar separation bubble location as a result of airfoil shape manipulations.

Aft of reattachment the pressure distribution shows wavy like curve, this is not related to the airfoil shape, nor to the airfoil parameterization method. It is caused by the turbulent Drela closure formulation incorporated in the laminar separation bubble model after turbulent reattachment occurs.

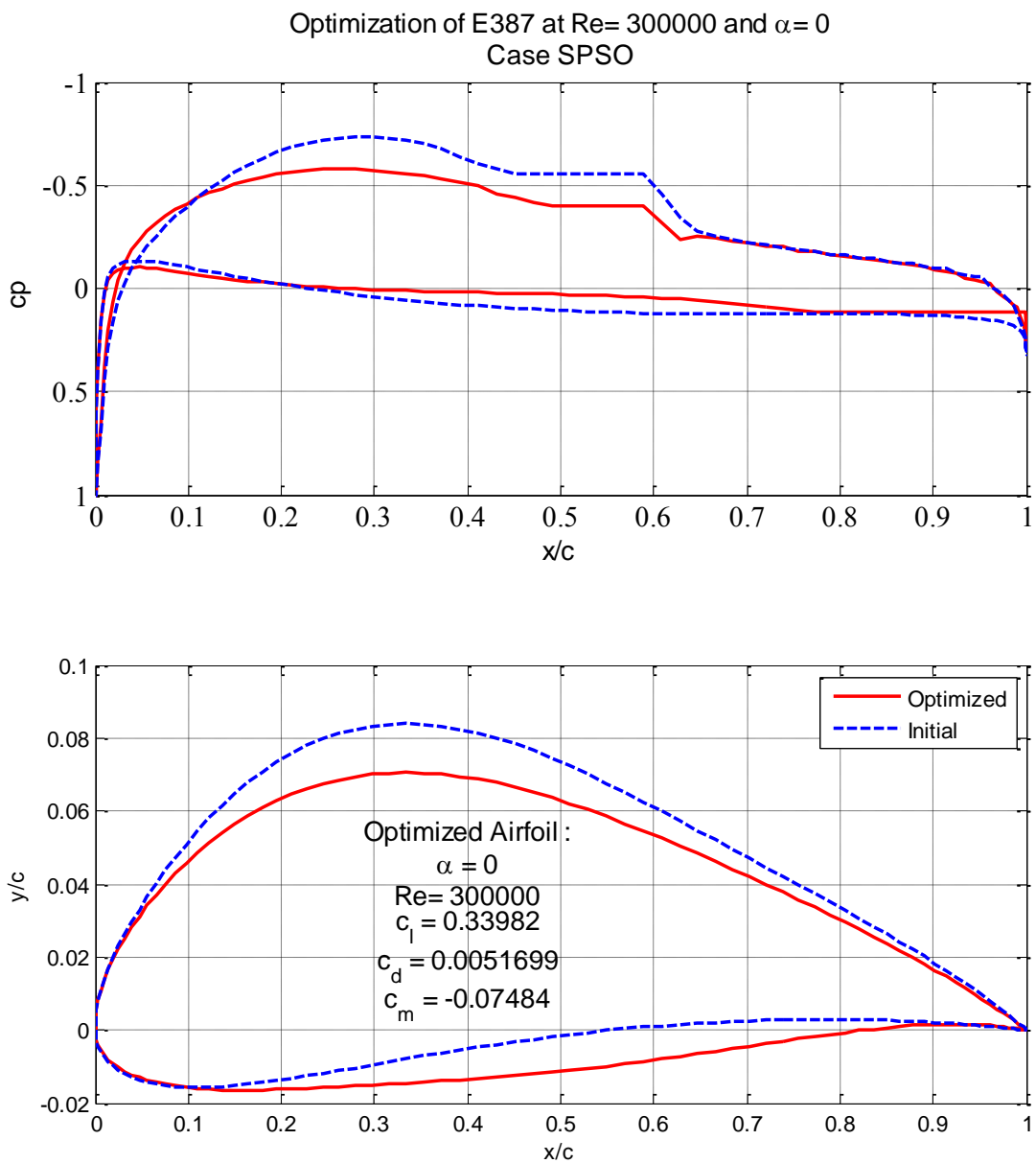


Figure 7.18 Airfoil shape and pressure distribution for SPSO at $Re 3 \times 10^5$ and at $\alpha = 0$

7.6.4 Aerodynamic coefficients

The aerodynamic performance of the optimized airfoil at zero angle of attack is plotted against that of the E387 airfoil as illustrated in Figure 7.19. The drag polar curves are shown in subplot (b). It consists of lift drag curve and lift curve versus angle of attack. The experimental data for Eppler 387 airfoil is also plotted for comparison. At zero angle of attack at which this airfoil is optimized has less drag coefficient than the initial airfoil. The percentage decrease in drag at this point is more than 40%. The values of drag of optimized airfoil does not show improvement in the drag polar at high angles of attack, away from the design point. This is expected result in when optimization is performed at single point. The lift curve shown in subplot (b) has consistently lower lift for all angles of attack. It could be attributed to the airfoil shape modifications in the upper surface, and partly to the shorter laminar separation bubble that results in less area under the pressure distribution curve. This affects also moment coefficient which is decreased for all angles of attack as shown in subplot (d).

Lift to drag ratio as function of angle of attack is illustrated in subplot (e). The lift to drag ratio for the optimized airfoil at design point is considerably improved from about 40 to 65 with more than 60%. This shows that the optimization method can be very efficient tool in finding more suitable airfoils for specific application. In spite of this capability, the optimization with shape modification approach can be examined with more complex requirements (constraints), such as designing at range of angles of attack, design with maximum aerodynamic pitching moment or minimum lift. These cases will be illustrated in the following sections.

Optimization of E387 at $Re= 300000$ and $\alpha=0$
Case SPSO

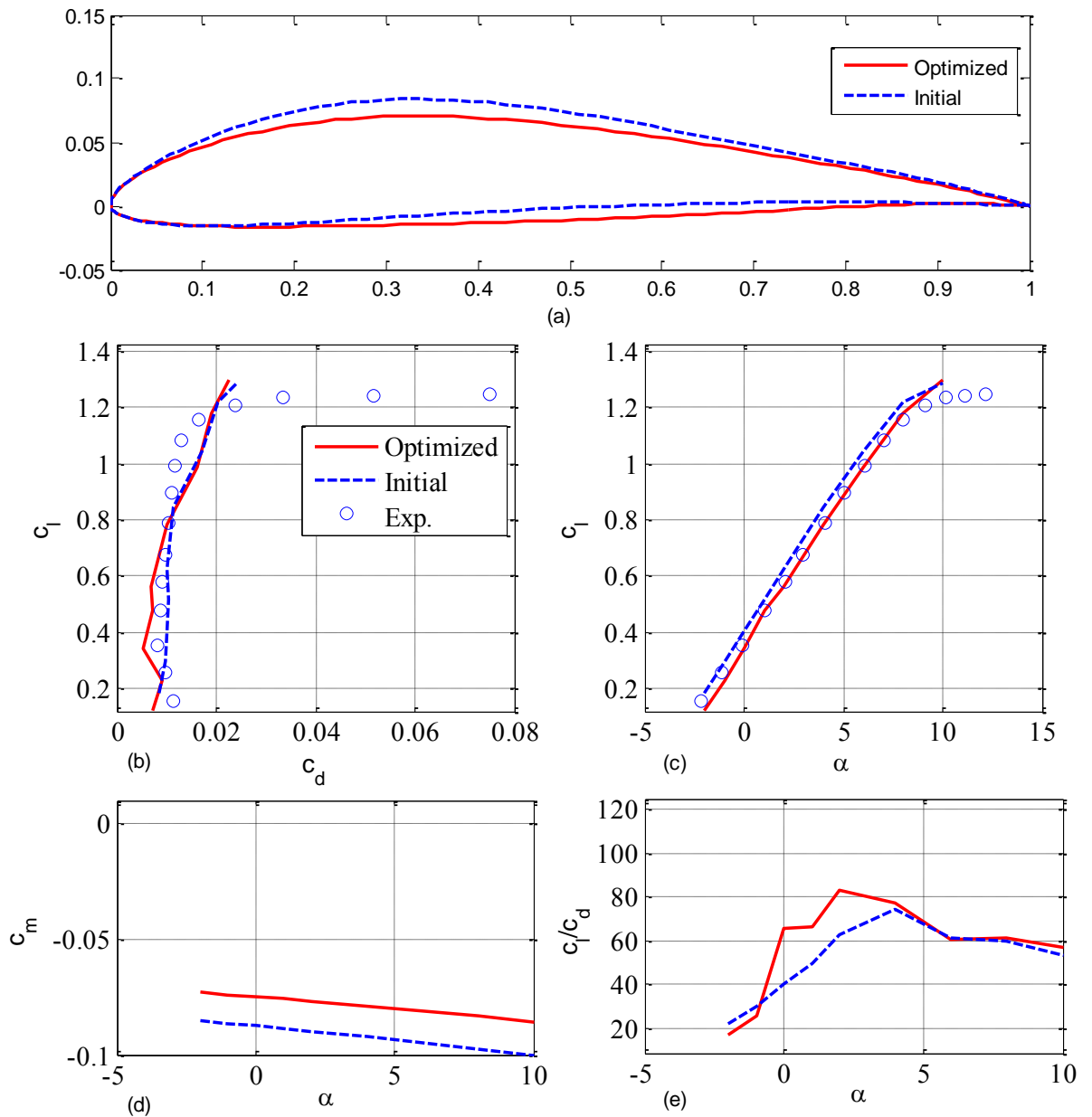


Figure 7.19 Drag polar plot of the initial and optimized airfoil at single angle of attack of zero degree

7.7 Single point multi objective

Since, aerodynamic requirements are conflicting in the sense that improving one coefficient will worsen other coefficient. For example increasing lift will result in increased drag and pitching moment. It is necessary, therefore, to put additional objectives. The most common

type of is lift constrained drag minimization for which the aerodynamic objective function to minimize drag at fixed lift is given by a weighted sum of lift and drag terms as

$$f = w_{cd} c_d + K_{cl} w_{cl} (c_{ld} - c_l) \quad 7.8)$$

Where, $w_{cd} = 1$ and $w_{cl} = 0.1$. These two terms should have same order of magnitude.

The penalty function is formulated in the code by specifying a factor $K_{cl} = 10$ whenever the absolute value of the difference in lift is greater than .05

$$K_{cl} = \begin{cases} 10 & \text{if } abs(c_{ld} - c_l) > .05 \\ 1 & \text{otherwise} \end{cases} \quad 7.9)$$

The value of the desired lift coefficient is chosen as 0.387 which is the value of lift coefficient for initial airfoil at zero angle of attack. It is required thus to keep same lift coefficient and find minimum value of drag coefficient.

The objective function can be casted in other alternative forms such as that suggested by Nemec [85] and [86]. This form is especially convenient when target drag and lift coefficients c_{dd} and c_{ld} are specified.

$$f = \begin{cases} w_{cd} \left(1 - \frac{c_d}{c_{dd}}\right)^2 + w_{cl} \left(1 - \frac{c_l}{c_{ld}}\right)^2 & \text{if } c_d > c_{dd} \\ w_{cl} \left(1 - \frac{c_l}{c_{ld}}\right)^2 & \text{Otherwise} \end{cases} \quad 7.10)$$

Where the desired c_{dd} and c_{ld} coefficients are specified by the designer. The weighting factors are specified by user. One example is to use 1.0 for lift weighing factor w_{cl} and .005 for drag weighting factor w_{cd} .

If a multipoint optimization problem is analyzed the objective computed for each point and the problem is formulated as

$$f_{multipoint} = \sum_{i=1}^N w_i f_i \quad 7.11)$$

Where N is the number of design points which can be the number of angles of attack or lift coefficients and w_i is a weighting coefficient specified by the user for each design point.

7.7.1 Optimization Results

The genetic optimization plot is shown in Figure 7.20. Subplot (a) show that the best shape is reached after 10 generations. Subplot (b) show the values of each CST parameter for the best airfoil. And subplot (c) shows the value of the fitness function for each airfoil in the last generation, the largest value indicate that the corresponding airfoil has violated the constraints and a penalty is added to the objective function.

The CST parameters for the best airfoil are shown in Table 7.4. The comparison in geometry between initial and optimized airfoils is shown in Figure 7.21.

Table 7.5 Initial and best airfoil CST method parameterizations

	Upper surface				Lower surface			
Initial	0.1349	0.3291	0.1062	0.2218	-0.0758	-0.0001	0.004	0.03
Best	0.14265	0.27109	0.142083	0.182703	-0.068476	-0.00689	0.00882	-0.04419

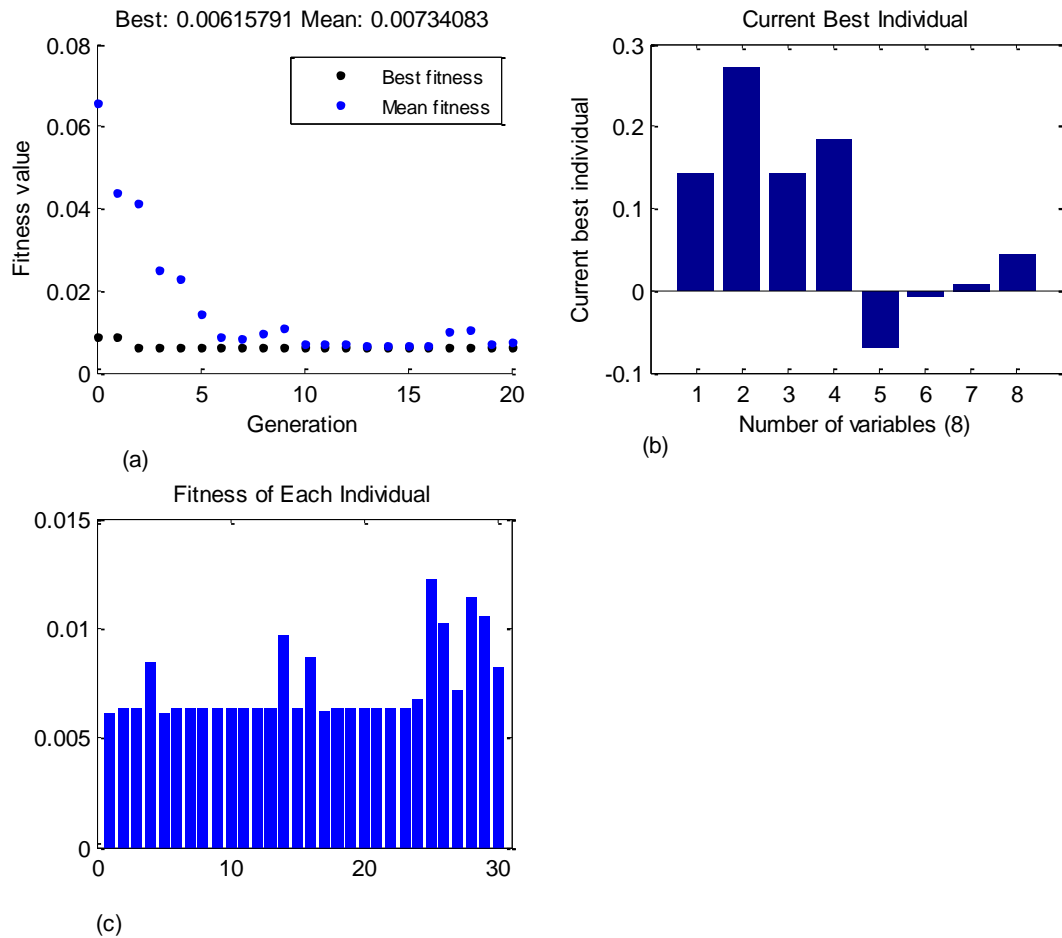


Figure 7.20 Results of genetic search method, (a) best airfoil fitness and mean for each generation. (b) The parameters of the best airfoil shape at last generation. (c) The fitness of each airfoil shape in the current generation.

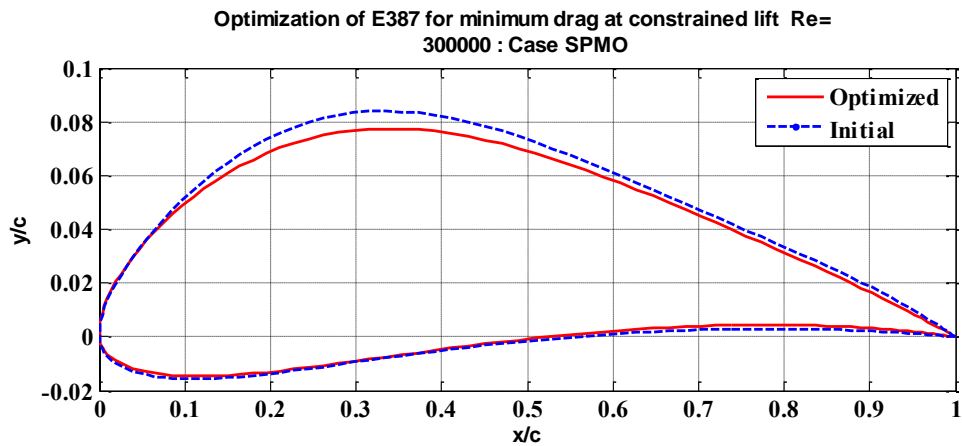


Figure 7.21 comparison of airfoil shape for SPMO

7.7.2 Airfoil shape and pressure distributions

The airfoil shape has lowered upper surface which results in less severe bubble and thus less drag the lower surface is only slightly modified, as can be seen from comparisons of pressure distribution plot shown in Figure 7.22.

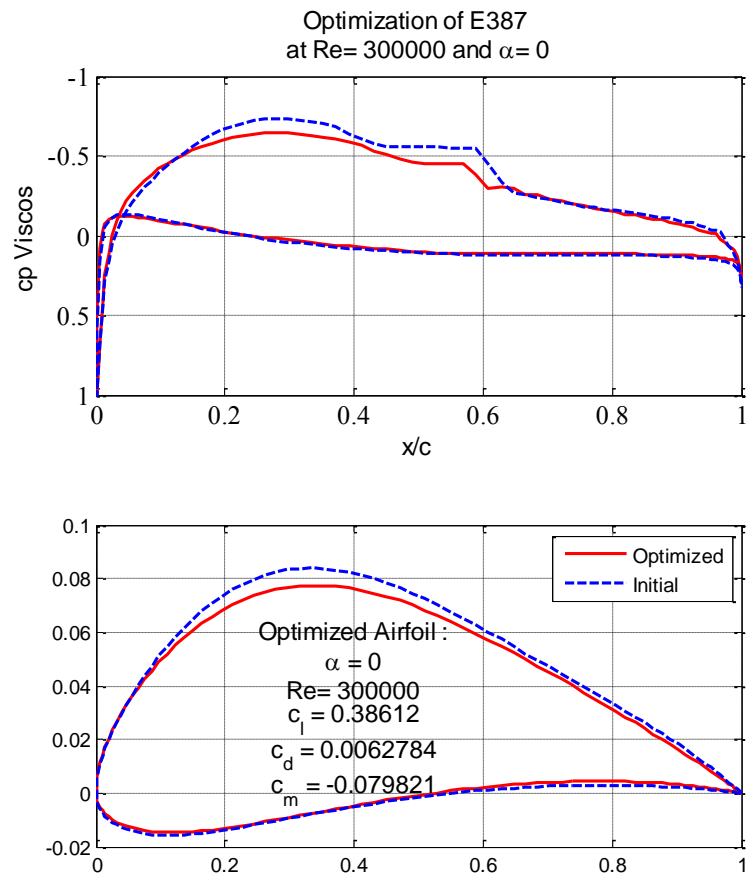


Figure 7.22 Airfoil shape and pressure distribution

7.7.3 Aerodynamic coefficients

Figure 7.23 shows comparison of aerodynamic coefficients for optimized and initial airfoil. Drag polar curve show that the lift constraint is satisfied. The drag is improved over the entire range with about 20% as compared with experimental data at the same angle of attack. The aerodynamic lift to drag ratio show considerable improvement of about 50% as compared with experimental data at the same angle of attack. The values moment coefficient for optimum airfoil is not constrained, but it shows a lower values as compared with initial airfoil.

Optimization of E387 for minimum drag at constrained lift at $Re= 300000$
Case SPMO

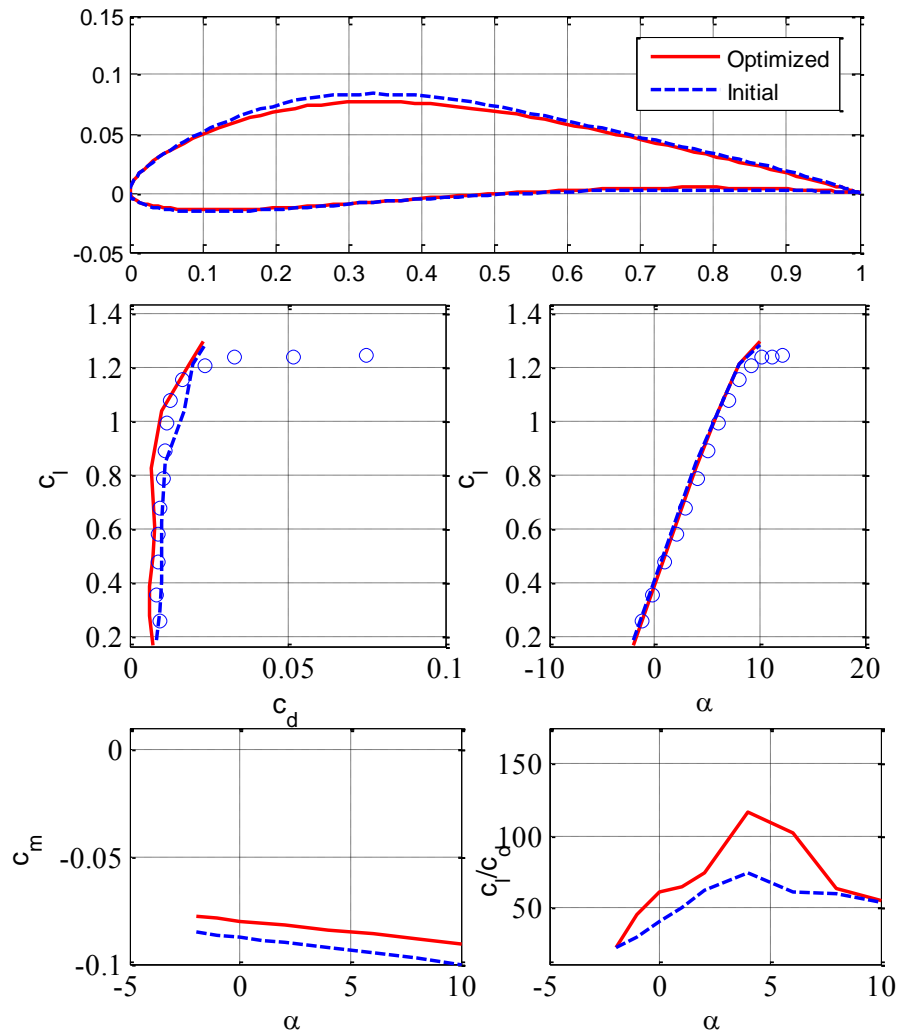


Figure 7.23 Drag polar for SPMO drag minimization at given lift for zero angle of attack.

In order to verify results a comparison with XFOIL code is performed for the optimized and initial airfoil shapes. Table 7.6 shows numerical values obtained from XFOIL code. Figure 7.24 shows comparison between optimized and initial airfoils performed by FOIL code. It shows an improvement in drag similar to the results obtain by current work code. XFOIL results are more optimistic for which the drag improvement at the design point is less than 10 %.

Table 7.6 XFOIL Results for Optimized and initial airfoils

AOA	cl		cd		cm	
	Optimized	initial	Optimized	initial	Optimized	Initial
0	0.3929	0.4114	.0076	0.00833	-.0812	-.0845
2	0.611	0.6276	0.00861	.00933	-.08	-.0831
4	0.8285	0.8439	.00979	.01057	-.0788	-.0821
6	1.0319	1.049	.01118	.01137	-.075	-.0785
8	1.1667	1.1627	.02135	.02199	-.0639	-.0639
10	1.2984	1.2813	.03329	.0358	-.0526	-.0509

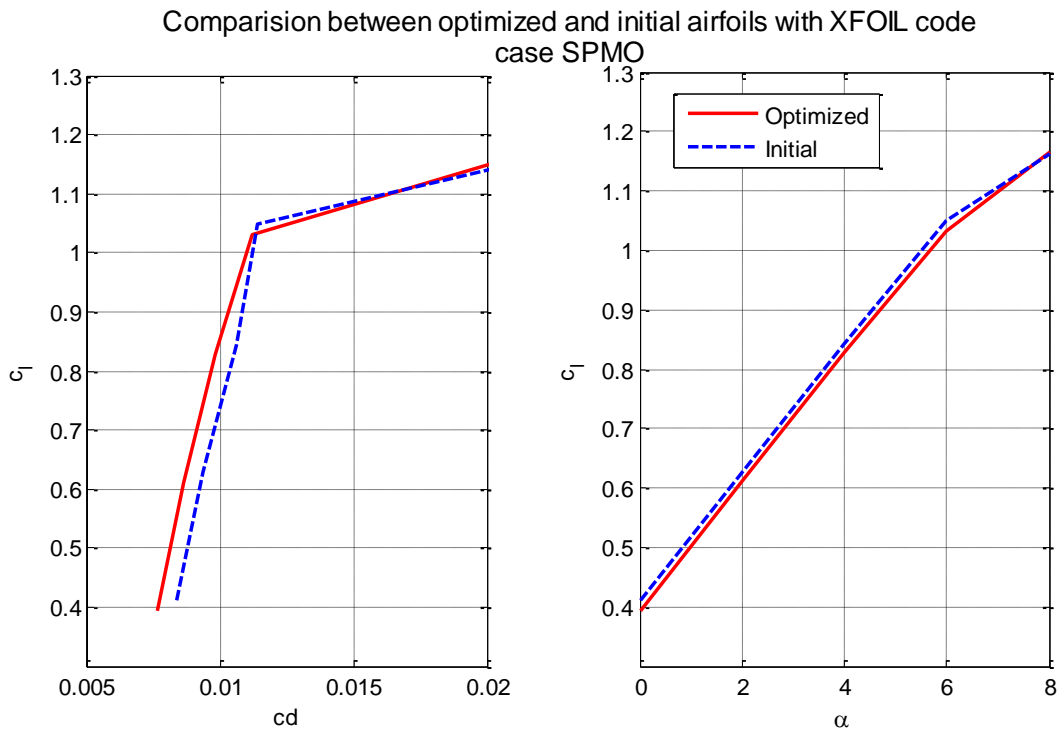


Figure 7.24 XFOIL results for optimized and initial airfoils

7.8 Multi point single objective

The single point optimization show a short coming when the optimized performance is improved just at a single point, but the performance at off design points are not improved. This short coming is eliminated by including off design points in the optimization process. This approach is demonstrated through the objective of minimizing drag at a range of angles of attack. The design points are a set of angles of attack N_α and the objective is to minimize the drag at these angles of attack. The objective function is formulated as in the following eqn.

$$f = \sum_{i=1}^{N_\alpha} w_i (c_d)_i \quad 7.12)$$

The weighting factor vector is chosen by the user to set the importance of the angle of attack range for intended application.

7.8.1 Aerodynamic constraints

In this case no aerodynamic constrains are applied to the optimization problem. The objective function is formulated to search for minimum drag over the design points range.

7.8.2 Optimization Results

Multipoint single objective optimization is started using the geometric constraints mentioned in section (7.2) for a set of angles of attack of 0, 2, 4, and 5 degrees. The optimization arrives at final shape after 20 generation with about 600 function evaluations. Figure 7.25 show the genetic optimization results. It consists of four subplots; subplot (a) shows the best airfoil shape fitness and the mean fitness value for each generation. From this subplot, it is evident that the genetic search algorithms have reached close to the best fitness just after 12 generations. The values of the best individual (airfoil shape) is shown in subplot (b) the first four numbers represent upper surface and the last four numbers represent lower surface. Subplot(c) shows the fitness (drag coefficient) of each individual (airfoil) in the last generation. It is clear that the fitness of the most individuals in this generation is very close to the best fitness, as the optimization process converges to the optimum airfoil.

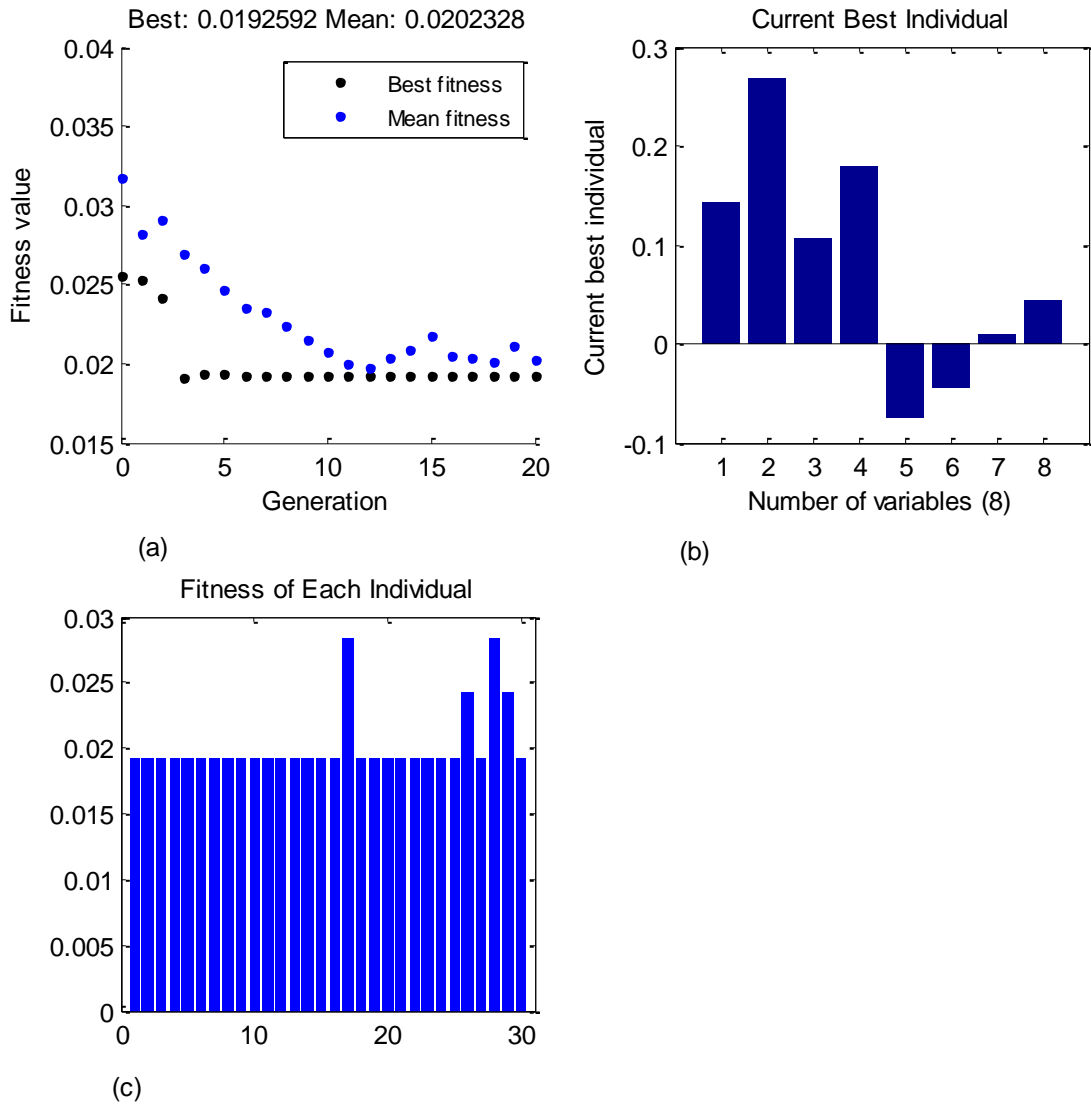


Figure 7.25 Results of genetic search method, best airfoil shape and mean for each generation (a), the best airfoil shape at the final generation (b), the fitness of each airfoil shape in the final generation (c).

7.8.3 Airfoil shape and pressure distributions

The best airfoil shape is shown in Figure 7.26. From this figure, it can be seen that the forward portion of the upper surface is pushed down and the backward portion is slightly above the initial airfoil upper surface. The apparent reason is to avoid separation bubble drag, which is clear from comparison of airfoil shapes, and the pressure distributions shown in Figure 7.26. There is a connection between the direction of pressure distribution curve

movement with respect to initial pressure distribution and airfoil shape. When the airfoil upper surface is moved down from the initial, the corresponding pressure distribution is moved also down from the initial pressure distribution and vice versa. The lower surface show opposite trend, when the airfoil shape is moved down the corresponding lower surface pressure distributions tend to move up. This is called bottom loading. Higher bottom loading will increase pitching moment and will result of higher maximum lift.

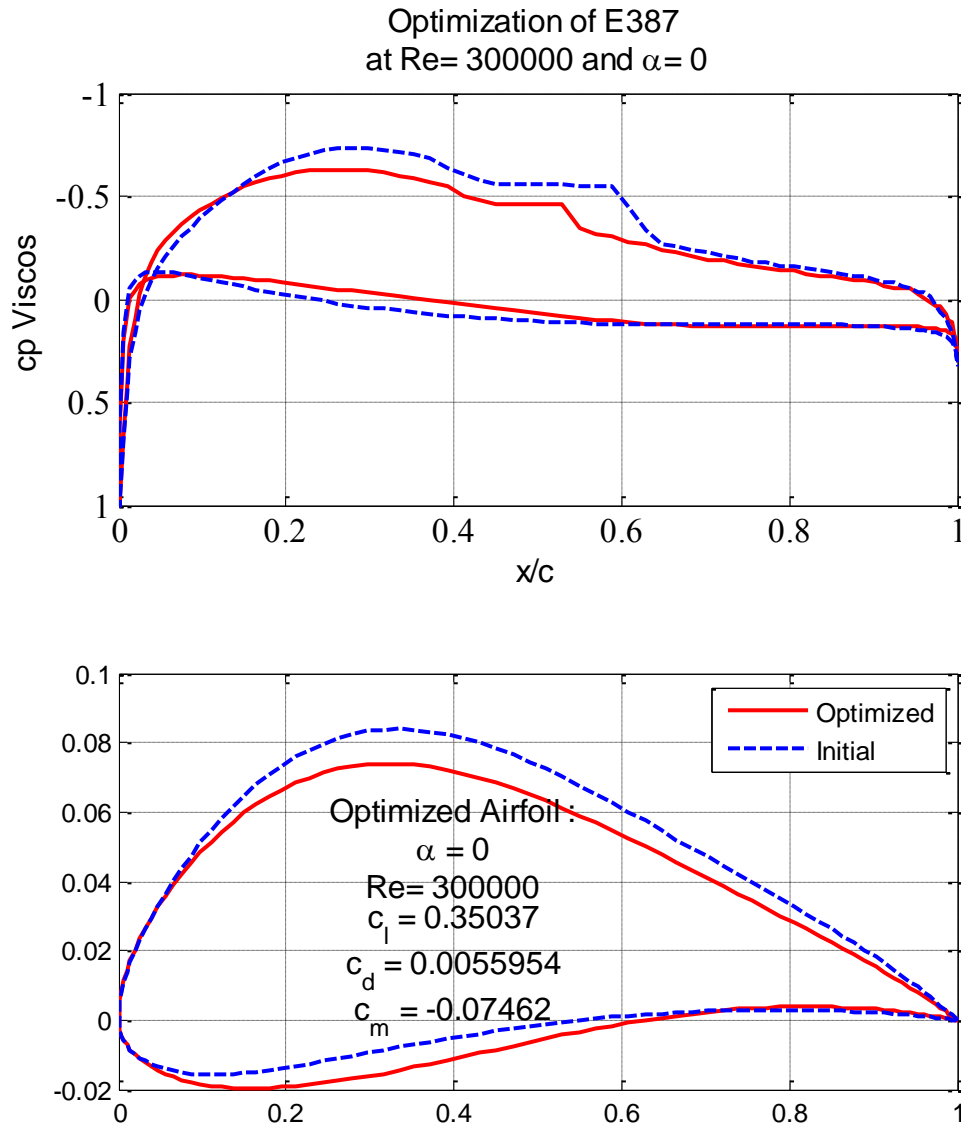


Figure 7.26 Optimized airfoil for MPSO for minimum drag at range of angles of attack

7.8.4 Lift and drag polar

Aerodynamic characteristics for the best airfoil are shown in Figure 7.27 . The drag polar shows a considerable improvement in drag coefficient over the whole range of design angles of attack (0, 2, 4 and 5) with about 25% compared to experimental data. The lift coefficient is slightly decreased as a result of upper surface shaping and bottom loading. From the figure, the lift to drag ratio shows similar improvement within the operating range.

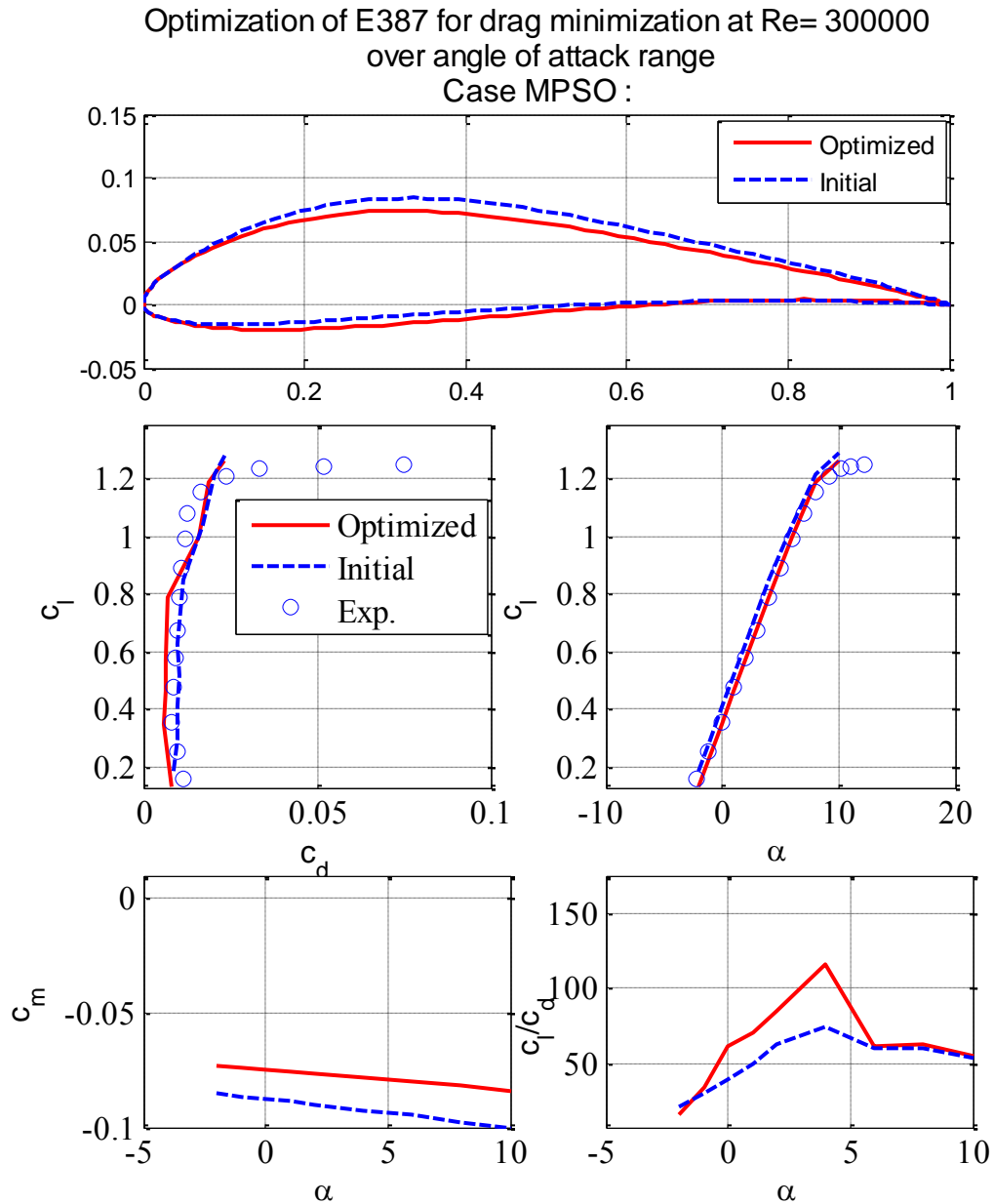


Figure 7.27 Aerodynamic performance showing comparison with experimental lift and drag coefficients for initial airfoil.

7.9 Multi point Multi Objective

Airfoil design requirements has growing combinations even for one application. For instance, the requirement of low drag at a range of angles of attack and at the same time achieving high maximum lift at low pitching moment. These requirements can be formulated by means of multipoint multi objective design (MPMO).

The convenience of MPMO problem formulation constitutes a major advance of direct design by shape perturbation approach. That is because the formulation is performed in terms of the required performance parameters directly and not through pressure distribution or transition curve as in the case of classical inverse design. The optimization method will select the shape which will satisfy these multiple objectives.

It is useful to know that low drag requirement at low Reynolds number is mostly concerned with extent of laminar flow over upper and lower surfaces (before transition), while higher maximum lift requirement is related to transition point movement as angle of attack is increased [94].

In this section multipoint multi objective airfoil design by geometry perturbation technique is examined using drag minimization at given lift coefficients.

7.9.1 Drag minimization at a range of operating lift coefficients

It is possible to minimize drag and have strong control on lift coefficient through specifying lift coefficient required for each operating point. In this example the lift coefficient is specified as that of the low Reynolds number Eppler 387 airfoil and are given in the following table

Table 7.7 Design lift coefficient at four operating points

Angle of attack [deg.]	0	2	4
Design lift coefficient	0.4055	0.626	0.8463
Weighting factor	1.0	1.0	1.0

7.9.2 Objective function formulation

It is required to minimize drag at these operating points as compared to the initial airfoil and satisfying a given lift requirement. Therefore, the objective function is formulated in two terms given by Eq. 7.13.

$$f = \sum_{i=1}^{N_{\alpha}} w_{cdi}(c_d)_i + \sum_{i=1}^{N_{\alpha}} w_{cli}(K_{cl})_i \cdot [(c_l)_i - (c_{ld})_i] \quad 7.13$$

The coefficients w_{cd} and w_{cl} are the weighting coefficients for lift and drag coefficients respectively at each operating point i . These coefficients are used to get same order of magnitude of each term in the objective function, therefore the values are set to $w_{cd} = 1$ and $w_{cl} = 0.1$ for all operating points. The coefficient K_{cl} is a coefficient calculated by the penalty function that is used to exclude airfoils with unsatisfactory lift coefficients. The penalty function coefficient K_{cl} is set to 1 if the absolute difference between the design and the calculated lift coefficient is less than 0.05 and set to 10 otherwise. The airfoils with $K_{cl} = 10$ will result in higher value of objective function and thus will be rejected by optimization method.

7.9.3 Optimization Results

Multi point Multi objective optimization is started from Eppler 387 airfoil with geometric constraints described above. The population size is chosen after performing many trails. A population size of 30 shows a good compromise between computation time and airfoil shapes studied. Figure 7.28 shows three subplots representing the convergence of genetic algorithm method. The fitness values versus number of generations show that the best airfoil shape is obtained after 11 generations, with mean being improved after each generation. The values of the (8) geometric shape parameters for the best airfoil are also shown. The number of aerodynamic function calls is about 600.

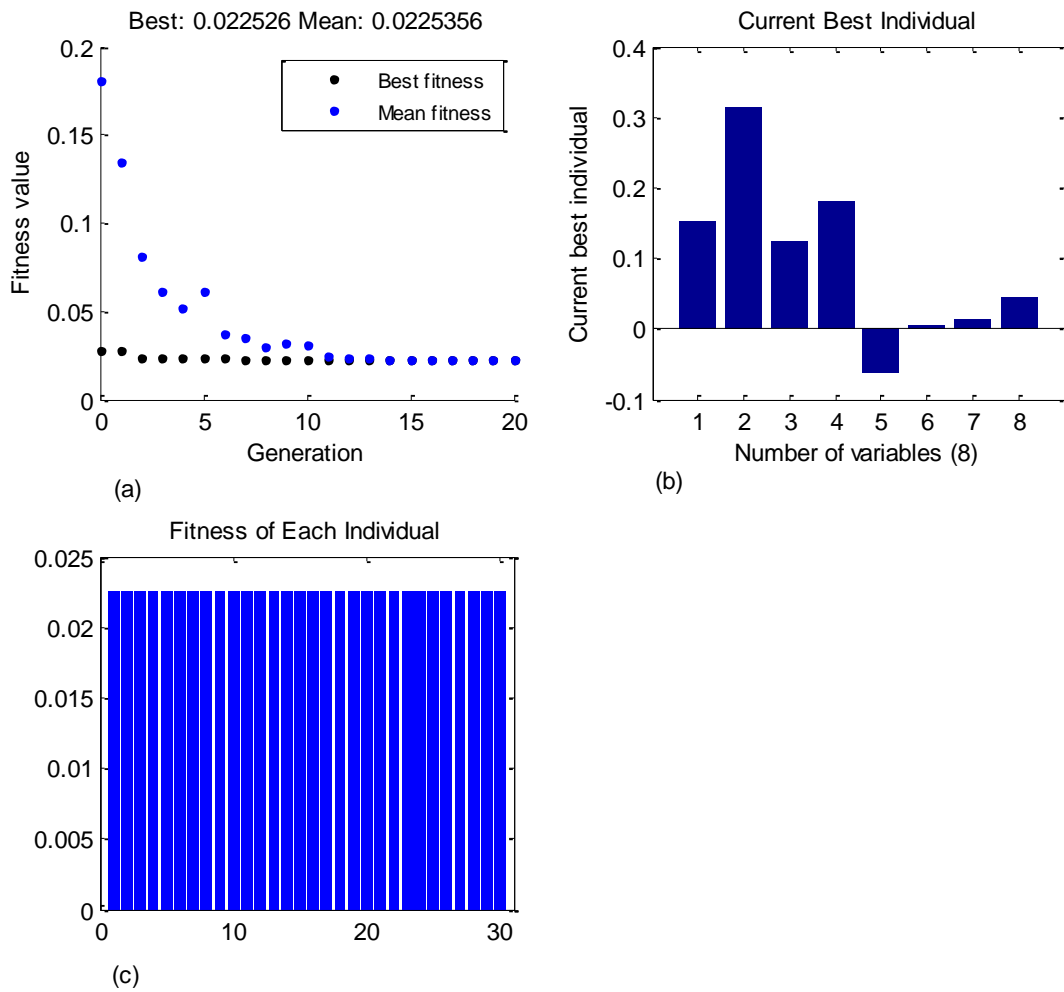


Figure 7.28 Genetic optimization results.

7.9.4 Airfoil shape and pressure distributions

The airfoil shape shown in Figure 7.29, where the forward part of the upper surface is shifted up and the backward part is shifted down. The lower surface has less bottom loading. Figure 7.30 and Figure 7.31 show pressure distributions at $\alpha = 0$ and 4° . It can be seen that the bubble effect is smaller.

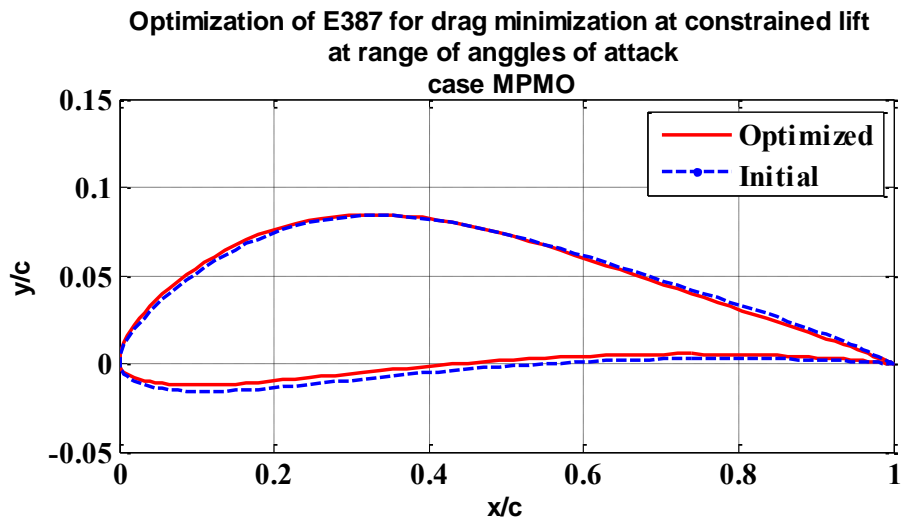


Figure 7.29 Airfoil shape

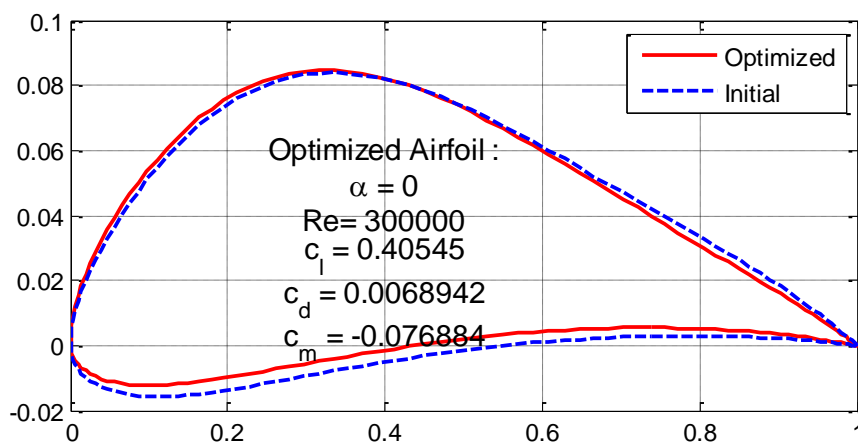
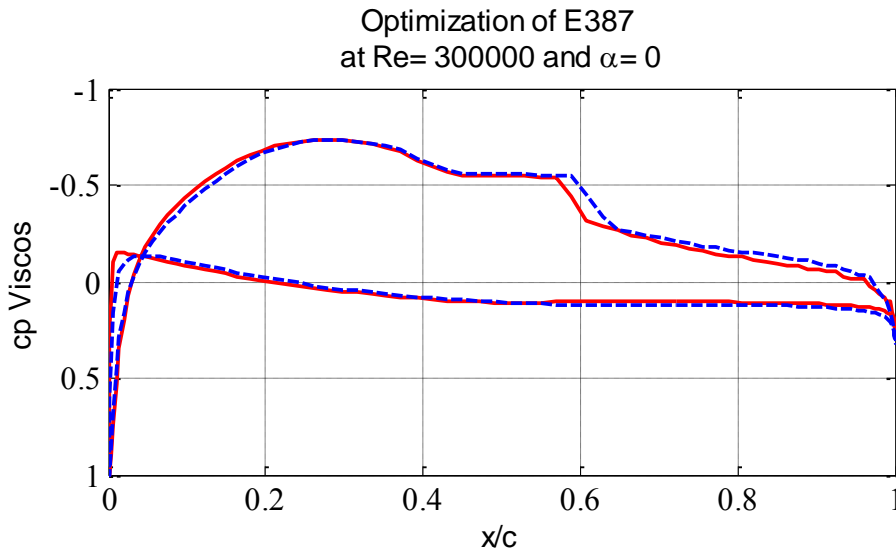


Figure 7.30 Best airfoil shape for Multipoint Multi objective optimization

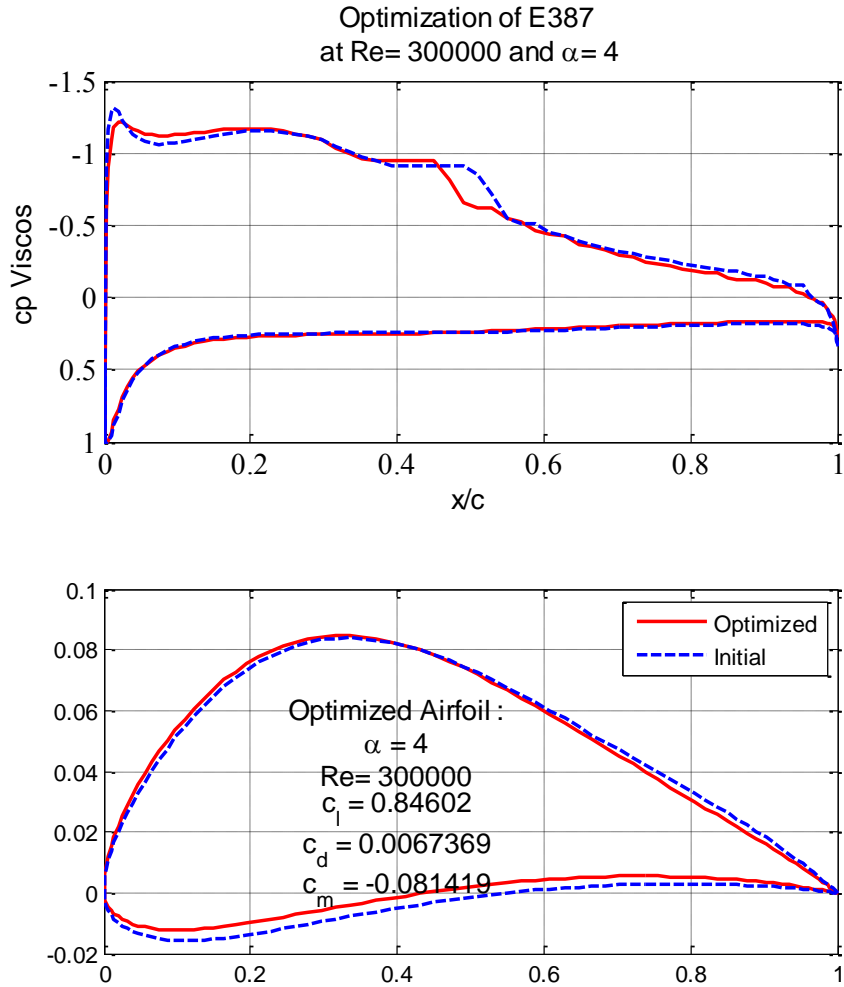


Figure 7.31 Comparison of pressure distributions for initial and optimized airfoils at $\alpha = 4 \text{ deg}$ $Re = 300,000$ for MPMO

7.9.5 Lift and drag polar

The objective function was formulated to minimize drag at a set of given operating lift coefficients. Figure 7.32 show a comparison between optimized and initial airfoils. It is clear from the figures that optimized airfoil has considerably less drag over the whole drag polar range. More drag improvement is seen at low angle of attack range with average value of about 27 % as compared to experimental data. Since high reduction in bubble effect is seen from pressure distribution comparisons in the above section, this drag reduction can be attributed to lower bubble drag obtained by systematically changing airfoil shapes. The lift

coefficient is kept equal to initial airfoil. The maximum lift to drag ratio within the design range is about 125 at $\alpha = 4$.

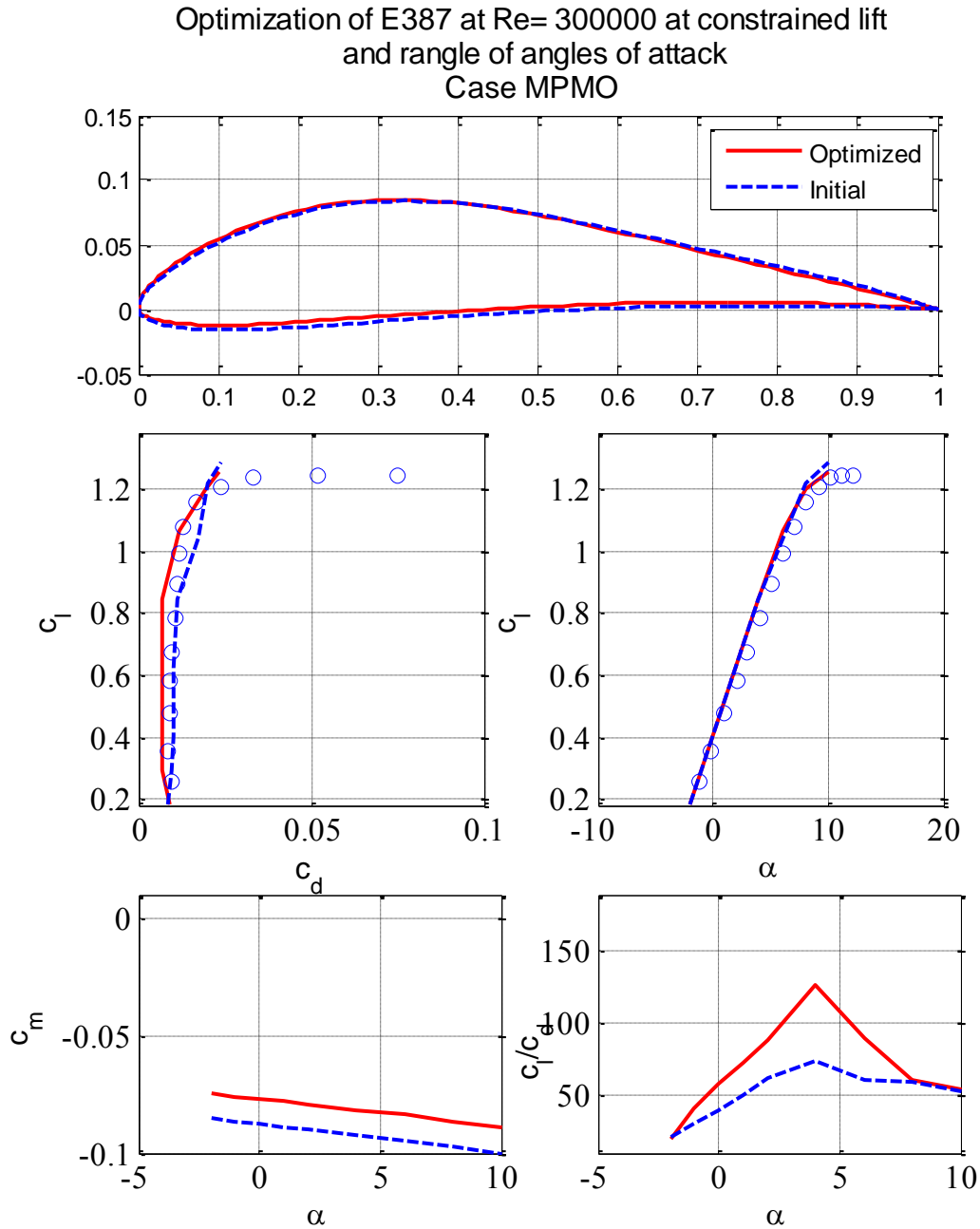


Figure 7.32 Drag polar showing an improvement in drag at design lift coefficients

7.10 Design at different Reynolds numbers

Low Reynolds number below 500,000 is considered low range. This range covers many applications like unmanned aerial vehicles, human powered aircrafts, wind turbines and propellers. Performance of airfoils at low Reynolds number was a point of continuing experimental and theoretical research. Model wind tunnel at Stuttgart university [88], Low Turbulence Tunnel at Delft [89], Langley Low-Turbulence Pressure Tunnel (LTPT) [59] and lately by Illinois university [61] have been active research facilities.

The most pronounced effect of operation at lower Reynolds number is the increase in airfoil drag as shown by experimental investigations and theoretical research [87] [59]. Therefore operation at lower Reynolds number is less aerodynamically efficient due to large decrease in L/D ratios. The main reason is the increased viscous effects at low Reynolds numbers, compared to very thin viscous layer associated with high Reynolds numbers. The lift coefficient does not increase with this increase in drag. This is illustrated in Figure 7.33 and Figure 7.34 for low Reynolds number airfoils Eppler 387 and S8064 airfoils respectively.

From these two figures it is evident that as Reynolds number decreases aerodynamic drag increases. For Reynolds numbers lower than 200,000 experimental observations show great degradation in airfoil performances due to domination of viscous effects. It is also shown that for Reynolds numbers above 50,000 and moderate angles of attack the flow always reattach after being separated due to laminar separation, as suggested by Carmichael [1] and argued by Shyy [2].

Due to this domination it is important to check the accuracy of the developed code at low Reynolds numbers as low as 200,000. Figure 7.35, Figure 7.36, and Figure 7.37 show comparison of data computed by current method and experimentally measured drag polar for Eppler 387 airfoil at Reynolds numbers 2×10^5 , 3×10^5 and 5×10^5 respectively. These results show generally good agreement in lift and drag coefficients. At higher angles of attack where separation plays a major role the computed results deviate slightly from experimental data. Drag coefficient is still calculated with acceptable accuracy at all angle of attack up to maximum lift. The maximum lift itself is hard to calculate and it is still a nightmare for most aerodynamic prediction codes. This code over estimates maximum lift as most of theoretical and CFD codes do as argued in [7] and [8].

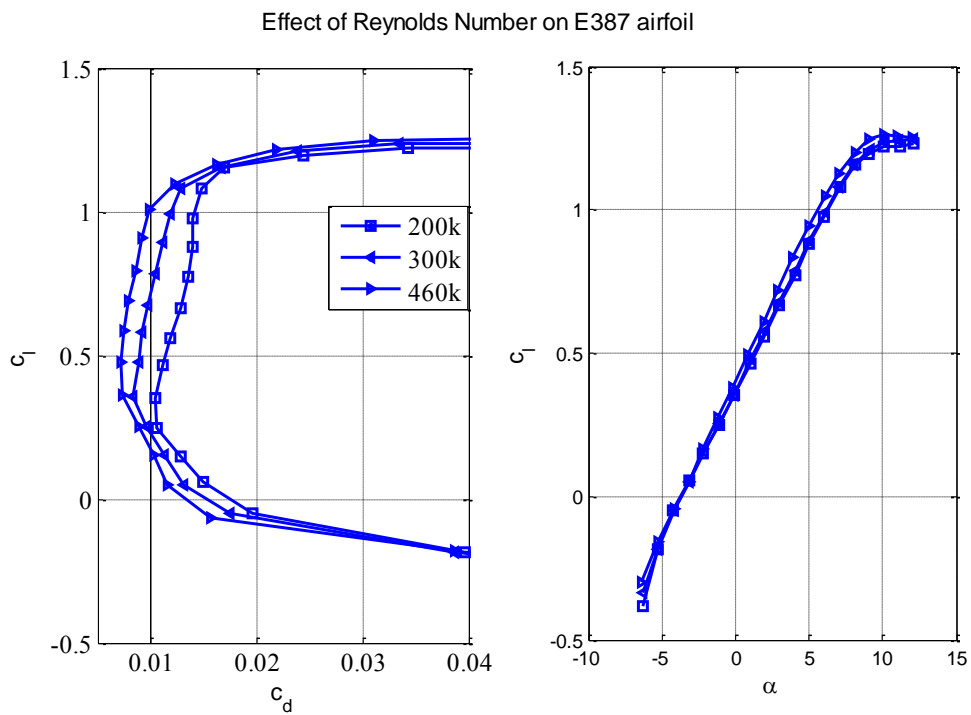


Figure 7.33 Effect of Reynolds number on E387 airfoil characteristics [61].

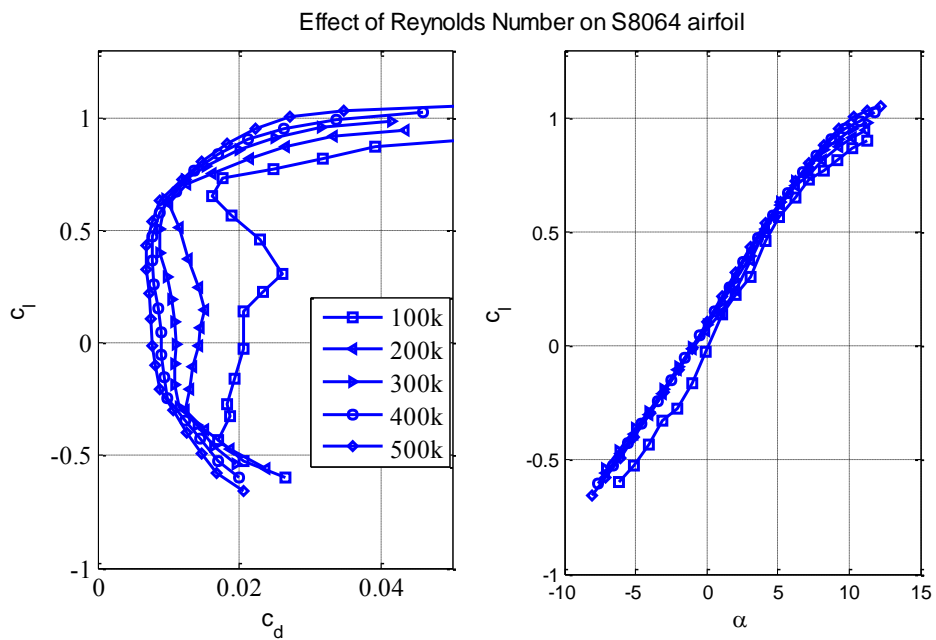


Figure 7.34 Effect of Reynolds number on S8064 airfoil aerodynamic characteristics [61].

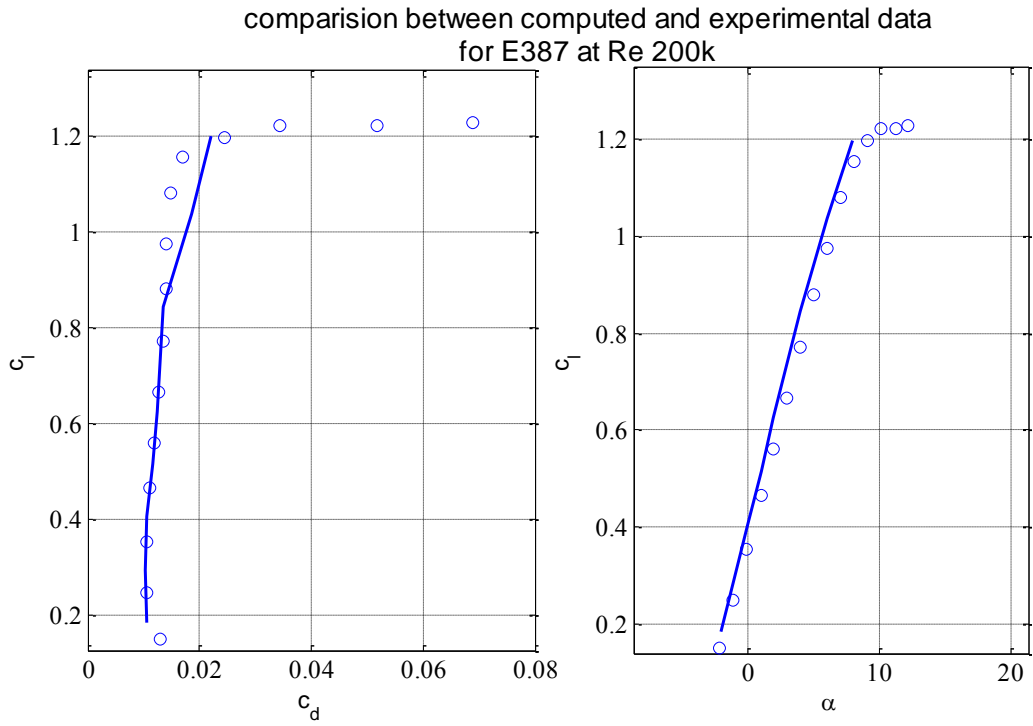


Figure 7.35 Comparison between experimental [61] and computed for E387 airfoil at 200,000

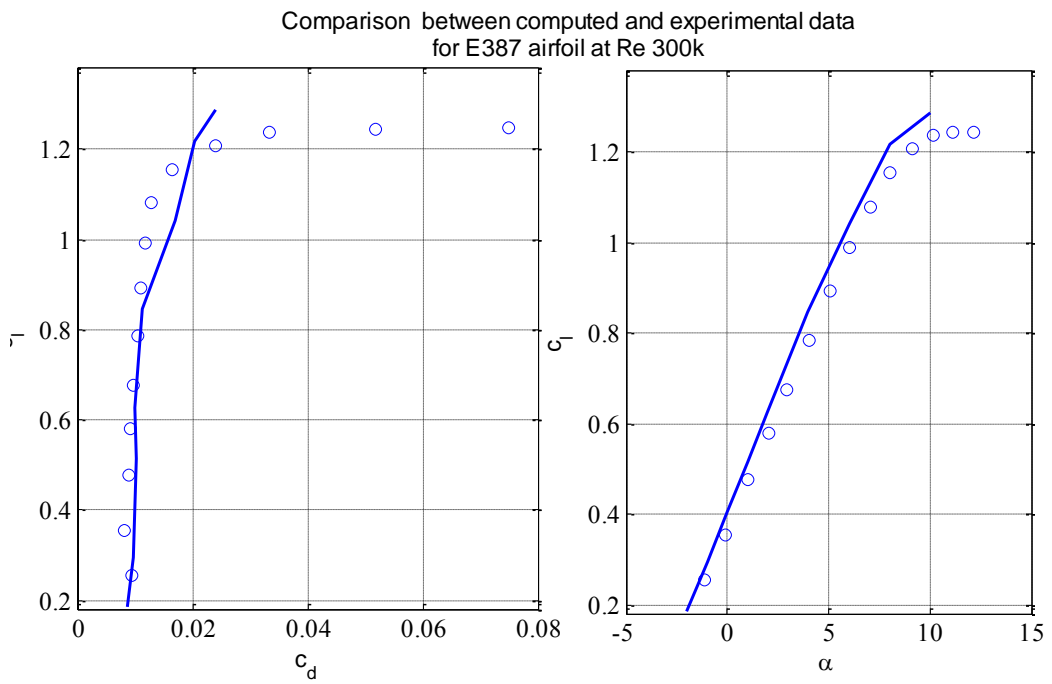


Figure 7.36 Comparison between experimental [61] and computed for E387 airfoil at 3×10^5

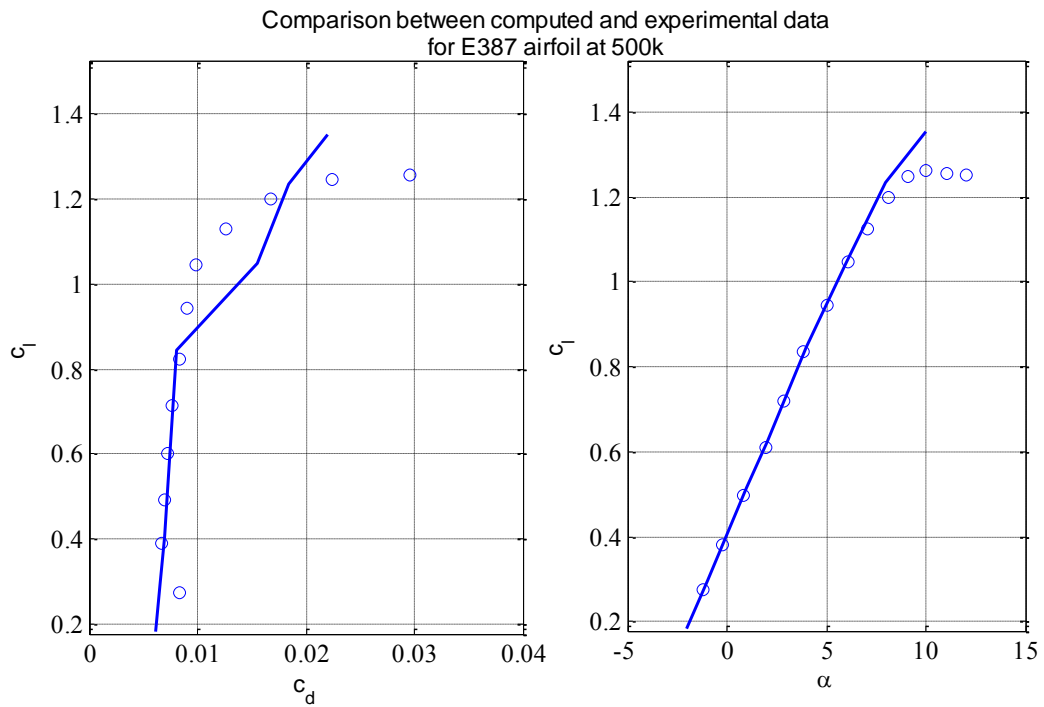


Figure 7.37 Comparison between experimental [61] and computed for E387 airfoil at 500,000

7.10.1 Optimization at different Reynolds numbers

During this exploration of the optimization process a multi point multi objective case is examined. The design point and objective functions are kept same as that used in section 7.9. These data are repeated for convenience. For the purpose of illustration same data is used for all Reynolds numbers.

Table 7.8 Design lift coefficient at three operating points

Angle of attack [deg.]	0	2	4
Design lift coefficient	0.4055	0.626	0.8463
Weighting factor	1.0	1.0	1.0

Therefore, the objective function repeated from section 6.

$$f = \sum_{i=1}^{N_{\alpha}} w_{cdi}(c_d)_i + \sum_{i=1}^{N_{\alpha}} w_{cli}(K_{cl})_i \cdot [(c_l)_i - (c_{ld})_i] \tag{7.14}$$

The coefficients w_{cd} and w_{cl} are the weighting coefficients for lift and drag coefficients respectively at each operating point i .

The objective is to minimize drag at the given lift coefficients with equal weights given to each operating point. Results of optimization for Reynolds numbers 2×10^5 , 3×10^5 and 5×10^5 are shown in Figure 7.39, Figure 7.40, and Figure 7.41, respectively. Experimental data for the initial airfoil are also shown for comparison. It is clear that design lift coefficient is achieved in all cases with drag being minimized for all operation points. The objective function formulation was convenient for this design example. Comparison of obtained airfoil shapes is shown in Figure 7.38. The airfoils optimized at low Reynolds numbers have the highest thickness and that at high Reynolds number results in less thickness. This is attributed to the high desired lift coefficient imposed on airfoils at low Reynolds numbers in this example. For Reynolds number of 500,000 this lift was achieved with thinner airfoil, but for the airfoil optimized at Reynolds number of 200,000 a thicker airfoil is required for the same lift.

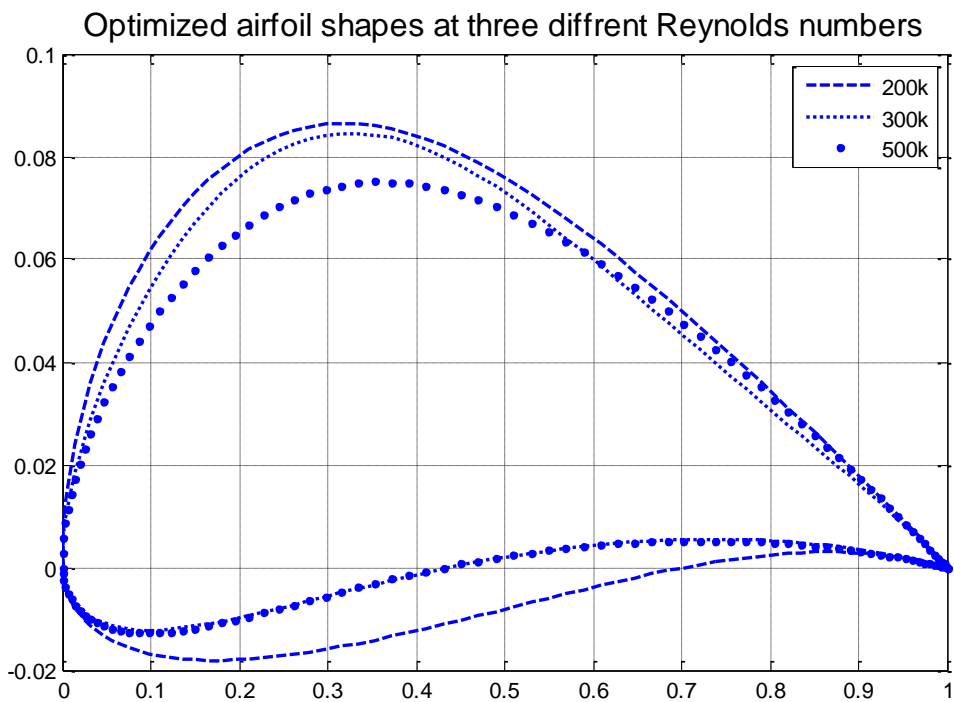


Figure 7.38 Comparison between optimized airfoil shapes at different Reynolds numbers

Optimization of E387 at $Re= 200000$ and a range of angles of attack
Case MPMO 01

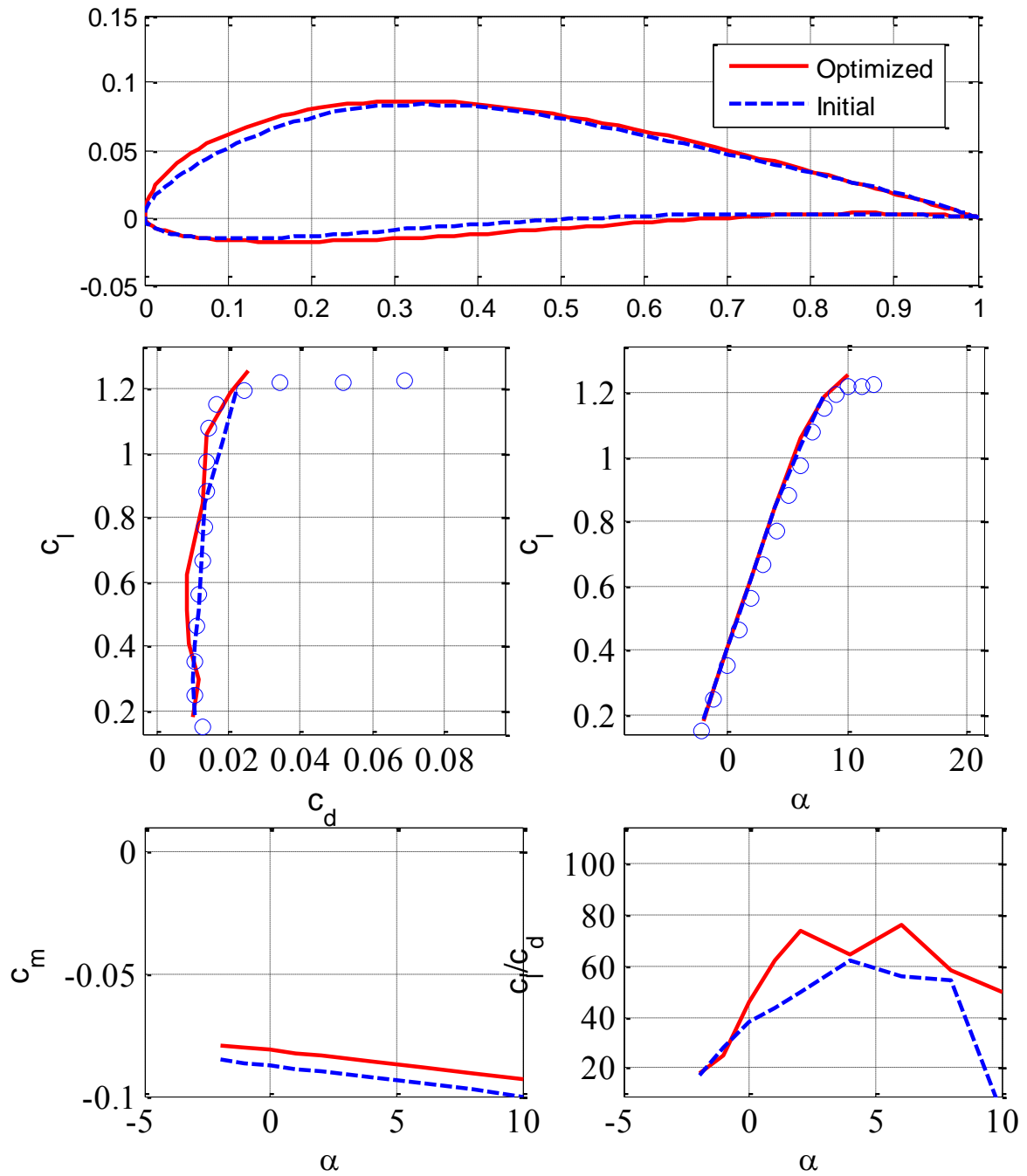


Figure 7.39 Minimization of drag coefficient at Reynolds numbers 2×10^5 . Open circles are experimental data for initial airfoil [61]

Optimization of E387 at $Re= 300000$ at constrained lift and range of angles of attack
Case MPMO

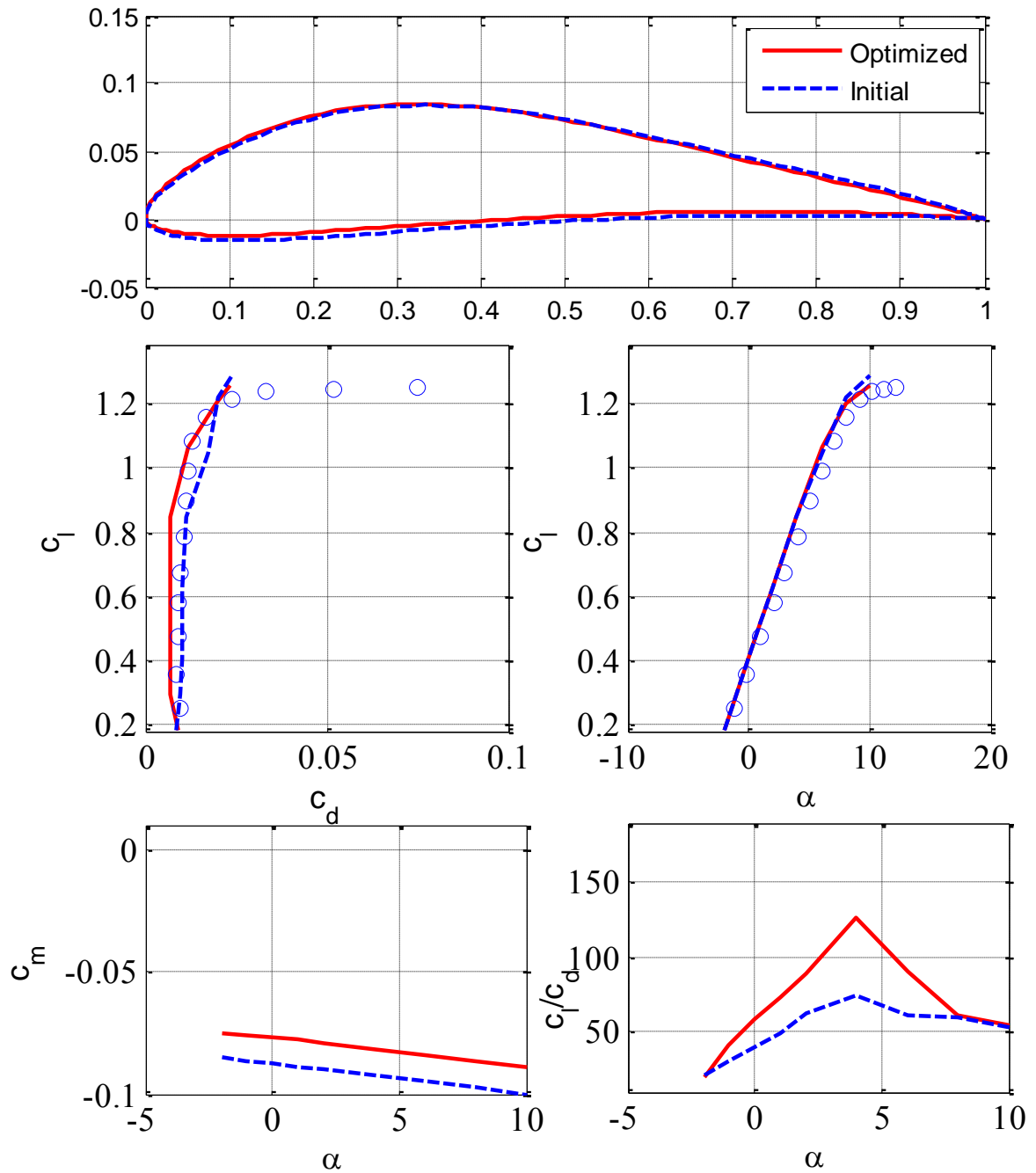


Figure 7.40 Minimization of drag coefficient at Reynolds numbers 3×10^5 . Open circles are experimental data for initial airfoil [61]

Optimization of E387
 at $Re=500000$
 Case MPMO MPMO₀1

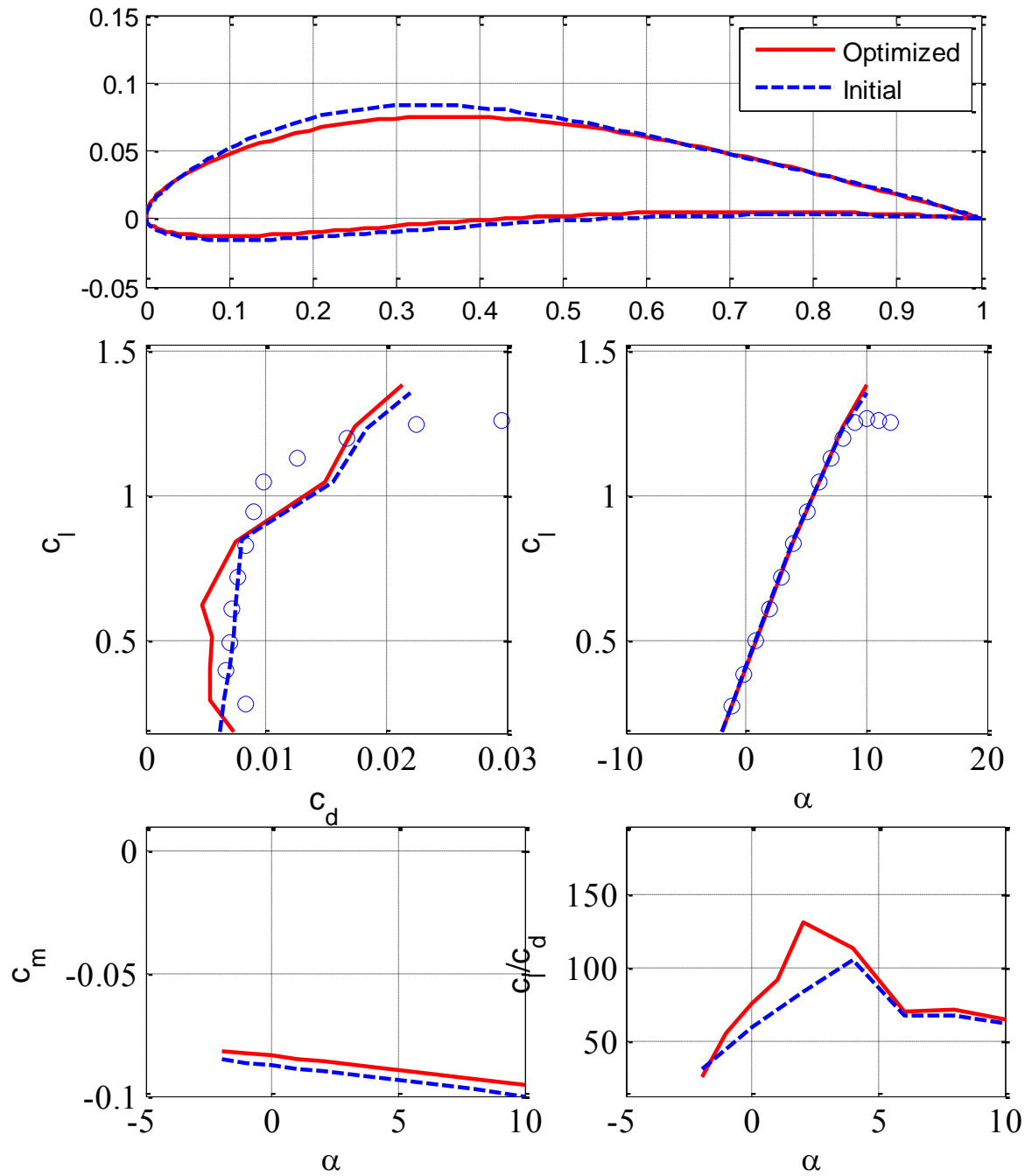


Figure 7.41 Minimization of drag coefficient at Reynolds numbers 5×10^5 . Open circles are experimental data for initial airfoil [61]

CHAPTER 8

8 Conclusion

In this thesis, the aerodynamic analysis and design of airfoils flying at low Reynolds numbers is studied. **Firstly**, aerodynamic inviscid and viscous solutions are performed and the formation of the laminar separation bubble on the airfoil surfaces has been modeled and validated by comparisons with available experimental measurements for two airfoils, namely E387 and S8036 in important range of Reynolds numbers (from 2×10^5 to 5×10^5). The developed method is implemented in a Matlab code.

Secondly, Aerodynamic parameterization methods applied to airfoils, such as NACA, PARSEC, Bezier curves, and CST methods are reviewed and computer codes are written for each method. **Thirdly**, another code is written for various airfoil objective functions and constraints formulations. **Finally**, the developed codes are called by a genetic search function to explore various case studies of airfoil aerodynamic optimizations by systematic shape perturbations.

8.1 Aerodynamic analysis

The adopted aerodynamic calculation is as follows, conformal mapping method is used to solve potential flow equations. Karman-Trefftz conformal mapping calculation procedure starts with mapping a given airfoil shape into a true circle in three subsequent transformations, then multiplication of derivatives of these transformations with velocity distribution around a circle. The value of the circulation is fixed by applying Kutta condition at trailing edge image of the true circle. The resulting inviscid velocity distribution at a specified angle of attack is used to derive the boundary layer solution.

The boundary layer integral equations solution enables the assessment of lift viscous corrections, total drag, and laminar separation bubble location. The calculation procedure is repeated by adding boundary layer momentum thickness to the airfoil sides, until the change in airfoil shape is negligibly small. This requires only few iterations, making this approach very efficient for airfoil design by systematic airfoil shape perturbation.

Two transition criteria are implemented. When natural transition happens first on the airfoil surface Eppler modified transition criterion is applied to predict point of natural transition.

This criterion is used in the past to design airfoils for various applications. However, when laminar separation occurs before natural transition, it is assumed that, transition occur inside the bubble and the conditions at transition is calculated using Drela e^n transition criterion which constitutes an important part of laminar separation bubble effort. A critical value of the disturbance amplification factor $N_{cr} = 12$, which is used to predict transition, is found to be satisfactory.

When a laminar separation bubble is encountered during boundary layer development procedure a function is used to accumulate the increment in boundary layer momentum thickness δ_2 during each phase in the bubble structure. The boundary layer momentum thickness at the trailing edge is used to calculate total drag using Squire-Young formula. Main boundary layer features are also calculated. These features are locations on airfoil surface where laminar separation, transition, reattachment, and finally turbulent separations occur. The results of the code are validated using comparison with experimental measurements from literature for E387 and S8036 airfoils and shown to be close to both experimental and XFOIL predictions at moderate angles of attack. The following points can be concluded:

- In linear range of angles of attack, where airfoil optimization is expected, both lift and drag are computed with reasonable accuracy.
- Curves of boundary layer flow features on upper surface and drag polar show satisfactory agreement with measurement and XFOIL code.
- Separation bubble location can be also assessed in consistence with measurements as seen from pressure distribution comparisons.
- Very weak laminar separation bubble is not captured by this procedure; however this weak bubble often causes small drag penalties and can be neglected.
- When angle of attack is high, and when turbulent separation occurs on the upper surface, maximum lift coefficient is overestimated.
- Bubble length predicted by current computation is shorter than that obtained from experimental measurements, this may lead to underestimation of bubble effect or to estimate transition without bubble in cases when laminar separation bubble experimentally exists on airfoil surface.
- Turbulent separation point locations obtained from current computations are located between experimental and XFOIL results.

- Although computed lift and drag coefficients deviate from measured data at higher angles of attack, the predicted aerodynamic data allows the use of current procedure in design and optimization of airfoils for variety of applications without human intervention utilizing systematic shape perturbation approach.

8.2 Airfoil parameterization

Four known airfoil parameterization methods are reviewed. CST method with 2 and 4 coefficients is examined to fit two objectives. The first objective is representation of NACA 2412 airfoil geometry. In case of 2 coefficients the maximum difference in airfoil coordinates is about $2.1E-3$ which is fairly satisfactory for optimization purposes. With 4 coefficients CST fits NACA2412 with one order of magnitude higher accuracy and the maximum difference is in order of 10^{-4} . About 50 generations are required for 2 coefficients as compared to about 200 for the 4 coefficients case.

The second objective is the matching of pressure distribution. For 2 coefficients, the CST takes about 35 generations to converge to the target pressure distribution with a value of fitness function of 3.4×10^{-4} . When the number of coefficients is increased from 2 to 4, the number of GA generations required to reach similar accuracy is increased from 35 to 50 generations.

8.3 Objective function and constraints

Airfoil design and optimization is indeed a constrained multi objective problem. Therefore, objective function formulation includes geometric and aerodynamic types of constraints. In this work geometric constraints are implemented using the GA function upper and lower bound constraints. Aerodynamic constraints, however, are written as part of the objective function. A weighed sum approach is used to formulate different objectives and constraints. A penalty function method is also implemented to enforce constraints.

The following computer code functions are written that implement several objective functions and constraints formulations:

- Inverse design for given pressure distribution.
- Single and multi operating points and objectives combinations SPSO, SPMO, MPSO, and MPMO.
- Drag coefficient minimization with constraints applied to lift coefficient.

- Moment coefficient minimization with constraints applied to drag and lift coefficients.
- Equality and inequality penalty functions to enforce various constraints.

8.4 Airfoil design and optimization

In the second part of the project, the developed code is used as a tool to design and optimize airfoil performance. Airfoil optimization using genetic search optimization function (GA) is successfully used to demonstrate representative case studies using systematic airfoil shape modifications, Table 8.1 illustrates summary of studied cases.

Table 8.1 Summary of the cases studies in this work

Case	Re	α [deg]	Airfoil	Objective function and constraint
Inverse deign	0.3×10^6	4	NACA0012	Matching of pressure distribution. Eq.(7.6)
Inverse deign	0.5×10^6	5	Liebeck LNV109A	Matching of pressure distribution. Eq.(7.6)
Direct -SPSO	0.3×10^6	0	Eppler 387	Unconstrained Drag coefficient minimization. Eq.7.7
Direct -SPMO	0.3×10^6	0	Eppler 387	Drag minimization, with constrained $c_l = 0.387$. Penalty function. Eq. 7.8
Direct -MPSO	0.3×10^6	0, 2, 4, 5	Eppler 387	Unconstrained drag coefficient minimization with weighting coefficients. Eq.7.12
Direct-MPMO	0.3×10^6	0, 2, 4	Eppler 387	Lift coefficient constrained [0.4055 0.626 0.8463], drag coefficient minimization with weighting coefficients [1.0 1.0 1.0], and penalty function for each α . Eq.7.13
Direct MPMO at three Reynolds numbers	0.2×10^6 0.3×10^6 0.5×10^6	0, 2, 4	Eppler 387	Lift coefficient constrained [0.4055 0.626 0.8463], drag coefficient minimization with weighting coefficients [1.0 1.0 1.0], with penalty function for each α . Eq.7.13

While the aerodynamic calculations are performed in direct way, the objective function is formulated in two ways:

Firstly, the inverse airfoil method is examined through the specification of target pressure distribution for two airfoils. It is concluded that when the target pressure distribution is specified the objective function is formulated as functional difference between target and computed pressures distributions. It is found that when the computed pressure distribution comes close to the target pressure distribution, the airfoil shape is indeed close to the target airfoil. The optimization function converges very quickly to the optimum shape, typically in 5 generations, and it takes about 15 generations to converge to the target airfoil within acceptable error tolerances. The maximum difference in airfoil shapes is about 11×10^{-4} close to the lower surface leading edge. The maximum difference in pressure distribution is 0.015.

Secondly, direct airfoil optimization is applied to optimize airfoils with several objective functions and constraints formulations, as summarized in Table 8.1. Various combinations of objective functions and constraints are tested. The weighted sum approach is successfully utilized in this study where weighing coefficients are introduced to each term of the objective function. In case of multi point other weighing terms are also assigned to each operating point. Penalty terms are added to the objective function to insure constraints satisfaction.

The following points can be concluded:

- Airfoil optimization studies at low Reynolds numbers are successfully accomplished using the proposed code and methodology.
- Airfoil shape design is efficiently achieved by systematic shape modification and direct aerodynamic calculations by specifying pressure distribution.
- SPSO case: Unconstrained single point drag minimization at $Re\ 3 \times 10^5$ and at $\alpha = 0$ results in locally improved aerodynamic performance.
- SPMO case: Lift constrained drag minimization for which the aerodynamic objective function is formulated to minimize drag coefficient at fixed lift coefficient show that the lift coefficient has been successfully constrained resulting in less pitching moment change.

- MPSO case: Single point optimization show lower performance at off design points. In this case, the SPSO is repeated with additional operating points. It shows a smoother drag variation than the SPSO case over a wider range of angles of attack.
- MPMO case: The problem is formulated to minimize drag at a set of given operating lift coefficients. The result of optimization show improved performance over a wider range of angles of attack.
- The formulation of the objective function was quite satisfactory to this type of design problem. This formulation is very powerful when one aerodynamic coefficient is to be improved, such as drag in this case. It allows user chose of some unconstrained aerodynamics coefficients.
- This type of objective function formulation can be generalized to include as many terms as required, provided that these terms should have same order of magnitude.
- Efficient airfoil design procedure is developed that is fast and directly used for routine analysis and design of airfoils.

8.5 Future work

Although the obtained results of this thesis are satisfactory in general, there are issues where improvements are possible

1- To improve boundary layer code to predict better maximum lift coefficient c_{lmax} :

This is in fact a nightmare for aerodynamic calculations because maximum lift is associated usually with high angles of attack where severe separations occur leading to failure of classical boundary layer theory assumptions. Therefore, is particularly evident for lower Reynolds numbers where boundary layers are relatively thicker than higher Reynolds numbers where thinner boundary layers appear. The same is true for CFD numerical methods where turbulent models are used, but with less extent due to more complex mathematical models.

2- Improving airfoil closure when boundary layer iterations are performed:

The conformal mapping method used in this work is based on a closed trailing edge airfoil shape. (Trailing edge points have same coordinates). When adding boundary layer to the airfoil shape these two points will move away from each other by a distance equals to the sum of boundary layer momentum thicknesses from upper and lower sides at trailing edge points, forming an open shape. This problem is solved by extending airfoil to the point of intersection between upper and lower trailing edge points. This shows good lift and drag results as long as the extension is few percents of airfoil chord.

3- Developing a multi objective optimization function to optimize airfoils for a range of Reynolds numbers:

The same method of objective function formulation may be used to develop an objective function to optimize airfoils for a Reynolds number range.

4- The optimization method may be extended to 3D wings

9 References

- [1] Carmichael, B. H. "Low Reynolds number airfoil survey, volume 1." (1981).
- [2] Shyy, Wei, Yongsheng Lian, Jian Tang, Dragos Viieru, and Hao Liu. Aerodynamics of low Reynolds number flyers. Vol. 22. Cambridge University Press, 2007.
- [3] Lissaman, P. B. S. "Low-Reynolds-number airfoils." *Annual Review of Fluid Mechanics* 15, no. 1 (1983): 223-239.
- [4] Gad-el-Hak, Mohamed. "Control of low-speed airfoil aerodynamics." *AIAA journal* 28, no. 9 (1990): 1537-1552.
- [5] Tani, Itiro. "Low-speed flows involving bubble separations." *Progress in Aerospace Sciences* 5 (1964): 70-103.
- [6] Gopalarathnam, Ashok, and Michael S. Selig. "Low-speed natural-laminar-flow airfoils: Case study in inverse airfoil design." *Journal of aircraft* 38, no. 1 (2001): 57-63.
- [7] Maughmer, Mark D., and James G. Coder. Comparisons of theoretical methods for predicting airfoil aerodynamic characteristics. AIRFOILS INC PORT MATILDA PA, 2010.
- [8] Morgado, J., R. Vizinho, M. A. R. Silvestre, and J. C. Páscoa. "XFOIL vs CFD performance predictions for high lift low Reynolds number airfoils." *Aerospace Science and Technology* 52 (2016): 207-214.
- [9] Eppler, Richard: Airfoil Program System, User's Guide; Institut A fuer Mechanik, Universitaet Stuttgart (1988).
- [10] Drela, Mark, and Harold Youngren. "XFOIL 6.94 user guide." (2001).
- [11] Drela, Mark. "Low-Reynolds-number airfoil design for the MIT Daedalus prototype-A case study." *Journal of Aircraft* 25, no. 8 (1988): 724-732.
- [12] Leifsson, Leifur, and Slawomir Koziel. *Simulation-Driven Aerodynamic Design using Variable-Fidelity Models*. Imperial College Press, 2015.
- [13] ABBOTT, I. H. (1959). *Theory of Wing Sections, Including a Summary of Airfoil Data*. New York: DOVER PUBLICATIONS, INC
- [14] Karman, T. V. Aerodynamics, selected topics in the light of their historical development. R.S., B. (1940). On the Use of Conformal Mapping in Shaping Wing. *The Americal Mathematical Monthly*, vol 47, 362- 373.
- [15] Houghton, Edward Lewis, and Peter William Carpenter. *Aerodynamics for engineering students*. Butterworth-Heinemann, 2003.

- [16] THEODORSEN, T. a. (1933). General Potential Theory of Arbitrary wing section. NACA report No 452 .
- [17] THEODORSEN, T. (1931). Theory of Wing Sections of Arbitrary Shape. NACA No. 441
- [18] McBain, G. D. Theory of Lift: Introductory Computational Aerodynamics in MATLAB/Octave. Vol. 66. John Wiley & Sons, 2012.
- [19] Zlatko P., Slobodan S., Oscillating airfoil in incompressible inviscid fluid flow, Vazduhoplovstvo 93, Beograd, 1993. Jugoslovensko vazduhoplovno društvo.
- [20] Cooley, James W., and John W. Tukey, An algorithm for the machine calculation of complex Fourier series., Mathematics of computation 19, no. 90 (1965): 297-301.
- [21] James RM. A new look at two-dimensional incompressible airfoil theory. Rept. 1971 May;1600(10918):01.
- [22] Ives DC. A modern look at conformal mapping including multiply connected regions. AIAA Journal. 1976 Aug;14(8):1006-11.
- [23] Halsey ND. Potential flow analysis of multiple bodies using conformal mapping (Doctoral dissertation, California State University).
- [24] Halsey ND. Potential flow analysis of multielement airfoils using conformal mapping. AIAA Journal. 1979 Dec;17(12):1281-8.
- [25] Schlichting, Herrmann, and Klaus Gersten. Boundary-layer theory. Springer Science & Business Media, 2003.
- [26] de Almeida, JP Moitinho, P. Díez, and C. Tiago. Airfoil optimization with transition curve as objective function, Adaptive Modeling and Simulation 2013: 79.
- [27] Eppler, Richard. Airfoil design and data. Springer Science & Business Media, 1990.
- [28] Eppler, Richard, and Dan M. Somers. "A computer program for the design and analysis of low-speed airfoils." (1980).
- [29] Eppler, Richard. "Practical calculation of laminar and turbulent bled-off boundary layers." (1978).
- [30] Eppler, Richard; and Somers, Dan M.: Supplement to: A Computer Program for the Design and Analysis of Low-Speed Airfoils. NASA Technical Memorandum 81862, December 1980.
- [31] Drela, Mark, and Michael B. Giles. "Viscous-inviscid analysis of transonic and low Reynolds number airfoils." AIAA journal 25, no. 10 (1987): 1347-1355.
- [32] Anderson, J. "Fundamentals of Aerodynamics (Series in Aeronautical and Aerospace

- Engineering)." (2010).
- [33] Squire, H. B.; and Young, A. D.: The Calculation of the Profile Drag of Aerofoils. R. & M. NO. 1838, British A.R.C., 1938.
- [34] Tani, Itiro. "Low-speed flows involving bubble separations." *Progress in Aerospace Sciences* 5 (1964): 70-103.
- [35] Dini, Paolo, and Mark D. Maughmer. "Locally interactive laminar separation bubble mode." *Journal of aircraft* 31, no. 4 (1994): 802-810.
- [36] Dini, Paolo, and Mark D. Maughmer. "A computationally efficient modeling of laminar separation bubbles." In *Low Reynolds Number Aerodynamics*, pp. 174-188. Springer Berlin Heidelberg, 1989.
- [37] Gaster, Michael. *The structure and behavior of laminar separation bubbles*. HM Stationery Office, 1969.
- [38] Lutz, Thorsten, and Siegfried Wagner. "Numerical Shape Optimization of Subsonic Airfoil Sections." In *Proc. ECCOMAS*, pp. 11-14. 2000.
- [39] Jones, B. Melvill. *An experimental study of the stalling of wings*. Aeronautical Research Committee Reports and Memoranda 1588 (1933).
- [40] Tani, Itiro. "Low-speed flows involving bubble separations." *Progress in Aerospace Sciences* 5 (1964): 70-103.
- [41] Owen, P. R., and L. Klanfer. *On the laminar boundary layer separation from the leading edge of a thin aerofoil*. Defense Technical Information Center, 1953.
- [42] Cebeci T. Numerical instabilities in the calculation of laminar separation bubbles and their implications. *AIAA journal*. 1989 May;27(5):656-8.
- [43] Alam M, Sandham ND. Simulation of laminar separation bubble instabilities. In *Direct and Large-Eddy Simulation II 1997* (pp. 125-136). Springer Netherlands.
- [44] Jones LE, Sandberg RD, Sandham ND. Direct numerical simulations of forced and unforced separation bubbles on an airfoil at incidence. *Journal of Fluid Mechanics*. 2008 May 10;602:175-207.
- [45] Cadieux F, Domaradzki JA, Sayadi T, Bose T, Duchaine F. DNS and LES of separated flows at moderate Reynolds numbers. *Proceedings of the 2012 Summer Program, Center for Turbulence Research, NASA Ames/Stanford University, Stanford, CA, June. 2012:77-86.*
- [46] Alam M, Sandham ND. Direct numerical simulation of (short) laminar separation bubbles

- with turbulent reattachment. *Journal of Fluid Mechanics*. 2000 Jan 25;403:223-50.
- [47] Crivellini A, D'Alessandro V, Di Benedetto D, Montelpare S, Ricci R. Study of laminar separation bubble on low Reynolds number operating airfoils: RANS modeling by means of a high-accuracy solver and experimental verification. In *Journal of Physics: Conference Series 2014* (Vol. 501, No. 1, p. 012024). IOP Publishing.
- [48] Crabtree, L. F. The formation of regions of separated flow on wing surfaces. HM Stationery Office, 1959.
- [49] Gaster, M. On the stability of parallel flows and the behavior of separation bubbles. Diss. Queen Mary, University of London, 1963.
- [50] Gaster, Michael. The structure and behavior of laminar separation bubbles. HM Stationery Office, 1969.
- [51] Mueller, Thomas J. Low Reynolds number vehicles. No. AGARD-AG-288. ADVISORY GROUP FOR AEROSPACE RESEARCH AND DEVELOPMENT NEUILLY-SUR-SEINE (FRANCE), 1985.
- [52] Horton, Harry Philip. Laminar separation bubbles in two and three dimensional incompressible flow. Diss. 1968.
- [53] Horton, H. P. A semi-empirical theory for the growth and bursting of laminar separation bubbles. HM Stationery Office, 1969.
- [54] McCullough, George B., and Donald E. Gault. "Boundary-layer and stalling characteristics of the NACA 64A006 airfoil section." (1949).
- [55] Shyy, W., Lian, Y., Jian, T., Viieru, D., Liu, H.,., *Aerodynamics of low Reynolds number flyers*. Cambridge University Press, 2008.
- [56] WORTMANN, FX. The wedge angle of laminar separation bubbles. 1974. 13 (1974).
- [57] Drela, Mark. "XFOIL: An analysis and design system for low Reynolds number airfoils." *Low Reynolds number aerodynamics*. Springer Berlin Heidelberg, 1989. 1-12.
- [58] Drela, Mark. *Flight Vehicle Aerodynamics*. MIT Press, 2014.
- [59] McGhee, R. J.; Walker, B. S.; Millard, B. F. Experimental Results for the Eppler 387 Airfoil at Low Reynolds Numbers in the Langley Low-Turbulence Pressure Tunnel. NASA TM 4062, Oct. 1988."
- [60] Selig, M. S. Surface oil flow measurements on several airfoils at low Reynolds numbers. AIAA paper 2003-4067.
- [61] Williamson, G. A.; et al. Summary of Low-Speed Airfoil Data., University of Illinois

- Low Speed Airfoil Tests (2012).
- [62] Selig, M. S. Systematic airfoil design studies at low Reynolds numbers. *Progress in Astronautics and Aeronautics* 195 (2001): pp 143-167.
- [63] Kulfan, Brenda M., and John E. Bussoletti. "Fundamental parametric geometry representations for aircraft component shapes." 11th AIAA/ISSMO multidisciplinary analysis and optimization conference. Vol. 6948. sn, 2006.
- [64] Ken Joy, Geometric modeling lectures, Computer Science Department, Institute for Data Analysis and Visualization, University of California Davis
- [65] Abbott, Ira Herbert, and Albert Edward Von Doenhoff. *Theory of wing sections, including a summary of airfoil data.* Courier Corporation, 1959.
- [66] Sobieczky, Helmut. "Parametric airfoils and wings." *Recent Development of Aerodynamic Design Methodologies.* Vieweg Teubner Verlag, 1999. 71-87.
- [67] Selig MS, Maughmer MD. Multipoint inverse airfoil design method based on conformal mapping. *AIAA journal.* 1992 May;30(5):1162-70.
- [68] Selig MS, Maughmer MD. Generalized multipoint inverse airfoil design. *AIAA journal.* 1992 Nov;30(11):2618-25.
- [69] Schlichting, Hermann. *Boundary-layer theory.* (1968).
- [70] Liebeck RH, Ormsbee AI. Optimization of airfoils for maximum lift. *Journal of Aircraft.* 1970 Sep;7(5):409-16.
- [71] Liebeck RH. Design of subsonic airfoils for high lift. *Journal of aircraft.* 1978 Sep;15(9):547-61.
- [72] Liebeck RH. Low Reynolds number airfoil design at the Douglas Aircraft Company. *Aerodynamics at low Reynolds numbers Re greater than 10 to the 4 th and less than 10 to the 6 th.* 1986:7.
- [73] Wortmann, F.X., 1974. *The Quest for High-Lift.* American Institute of Aeronautics and Astronautics.
- [74] Miley SJ. On the design of airfoils for low Reynolds numbers. AIAA, MIT, and SSA, *International Symposium on the Technology and Science of Low Speed and Motorless Flight, 2 nd,* Cambridge, Mass, Army-supported research 1974 (Vol. 11, No. 13).
- [75] Maughmer MD, Somers DM. Design and experimental results for a high-altitude, long-endurance airfoil. *Journal of Aircraft.* 1989 Feb;26(2):148-53.
- [76] Somers DM, Maughmer MD. Design and Experimental Results for the S414 Airfoil.

- AIRFOILS INC PORT MATILDA PA; 2010 Aug.
- [77] Stratford BS. The prediction of separation of the turbulent boundary layer. *Journal of fluid mechanics*. 1959;5(01):1-6.
- [78] Stratford BS. An experimental flow with zero skin friction throughout its region of pressure rise. *Journal of Fluid Mechanics*. 1959;5(01):17-35.
- [79] Barrett, Thomas Robin. Aerodynamic design optimization using flow feature parameterization. PhD diss., University of Southampton, 2007.
- [80] Lane, Kevin A., and David D. Marshall. "Inverse airfoil design utilizing CST parameterization." In 48th AIAA Aerospace Sciences Meeting Including the New Horizons Forum and Aerospace Exposition, pp. 1228-1242. 2010.
- [81] Mathworks web site, <http://www.mathworks.com/discovery/genetic-algorithm.html>, 2016.
- [82] Hicks, Raymond Morton, Earl M. Murman, and Garret N. Vanderplaats. "An assessment of airfoil design by numerical optimization." (1974).
- [83] Hicks, Raymond M., and Garret N. Vanderplaats. Application of numerical optimization to the design of supercritical airfoils without drag-creep. No. 770440. SAE Technical Paper, 1977.
- [84] Mostafa Abobaker, Zlatko Petrovic, Vasko Fotev, Nouredine Toumi: Aerodynamic characteristics of low Reynolds number airfoils, *Technical Gazette*, 2017.
- [85] Nemec, Marian, and Michael J. Aftosmis. "Aerodynamic shape optimization using a cartesian adjoint method and cad geometry." *AIAA Paper 3456* (2006): 2006.
- [86] Nemec, Marian, David W. Zingg, and Thomas H. Pulliam. "Multipoint and multi-objective aerodynamic shape optimization." *AIAA journal* 42, no. 6 (2004): 1057-1065.
- [87] Lissaman, P. B. S. "Low-Reynolds-number airfoils." *Annual Review of Fluid Mechanics* 15, no. 1 (1983): 223-239.
- [88] Althaus, Dieter. "Profilpolaren für den Modellflug: Windkanalmessungen an Profilen im Kritischen Reynoldszahlbereich." Necker-Verlag, Villingen-Schwenningen, Germany (1980).
- [89] Volkers, D. F. Preliminary results of wind tunnel measurements on some airfoil sections at Reynolds numbers between 0.6×10^5 and 5.0×10^5 . Delft Univ. of Techn., 1977.
- [90] Smith, Alice E., and David W. Coit. "Penalty functions." *Handbook on Evolutionary Computation*, pages C 5 (1997): 1-6.

- [91] Bryan, Kurt, and Yosi Shibberu. "Penalty functions and constrained optimization." Dept. of Mathematics, Rose-Hulman Institute of Technology. [http:// www. rosehulman. edu/~ bryan/lottamath/penalty. pdf](http://www.rosehulman.edu/~bryan/lottamath/penalty.pdf) (2005).
- [92] Liebeck, Robert H. "A class of airfoils designed for high lift in incompressible flow." *Journal of Aircraft* 10, no. 10 (1973): 610-617.
- [93] Stratford, B. S. "The prediction of separation of the turbulent boundary layer." *Journal of fluid mechanics* 5, no. 01 (1959): 1-16.
- [94] Selig M. Low Reynolds number airfoil design lecture notes. VKI Lecture Series, November. 2003 Nov:24-8.
- [95] Hicks, Raymond Morton, and Garret N. Vanderplaats. "Application of numerical optimization to the design of low speed airfoils." (1975).
- [96] Joy KI. On-line geometric modeling notes. Computer Science Department, University of California, Davis. [http://graphics. cs. ucdavis. edu/CAGDNotes](http://graphics.cs.ucdavis.edu/CAGDNotes). 1996.
- [97] Kulfan B, Bussolletti J. "Fundamental" Parametric Geometry Representations for Aircraft Component Shapes. In 11th AIAA/ISSMO multidisciplinary analysis and optimization conference 2006 Sep 6 (p. 6948).
- [98] Kulfan BM. Universal parametric geometry representation method. *Journal of Aircraft*. 2008 Jan;45(1):142-58.
- [99] Ceze M, Hayashi M, Volpe E. A study of the CST parameterization characteristics. In 27th AIAA Applied Aerodynamics Conference 2009 Jun 22 (p. 3767).
- [100] K. Weighardt. *Über einen Energiesatz zur Berechnung laminarer Grenzschichten*, *Ing.-Arch.*, 16, pp. 231, 1948
- [101] Gardner B, Selig M. Airfoil design using a genetic algorithm and an inverse method. In 41st Aerospace Sciences Meeting and Exhibit 2003 Jan (p. 43).
- [102] Vicini A, Quagliarella D. Inverse and direct airfoil design using a multiobjective genetic algorithm. *AIAA journal*. 1997 Sep;35(9):1499-505.
- [103] Obayashi S, Takanashi S. Genetic algorithm for aerodynamic inverse optimization problems. In *Genetic Algorithms in Engineering Systems: Innovations and Applications*, 1995. GALEZIA. First International Conference on (Conf. Publ. No. 414) 1995 Sep 12 (pp. 7-12). IET.
- [104] Genetic search algorithms function, Scilab, 2017
http://gd.tuwien.ac.at/comp/scilab/manual_scilab-5.1.1_en_US/optim_ga.html

Прилог 1.

10 Изјава о ауторству

Потписани Mostafa H. S. Abobaker

број индекса D3 / 2013

Изјављујем

да је докторска дисертација под насловом

LOW REYNOLDS NUMBER AIRFOILS

АЕРОПРОФИЛИ ЗА МАЛЕ РЕЈНОЛДСОВЕ БРОЈЕВЕ

- резултат сопственог истраживачког рада,
- да предложена дисертација у целини ни у деловима није била предложена за добијање било које дипломе према студијским програмима других високошколских установа,
- да су резултати коректно наведени и
- да нисам кршио/ла ауторска права и користио интелектуалну својину других лица.

Потпис докторанда

У Београду, November 2017

Прилог 2.

**11 Изјава о истоветности штампане и електронске
верзије докторског рада**

Име и презиме аутора : Mostafa H. S. Abobaker
Број индекса D3/2013
Студијски програм Aerodynamics
Наслов рада АЕРОПРОФИЛИ ЗА МАЛЕ РЕЈНОЛДСОВЕ БРОЈЕВЕ
Ментор др Златко Петровић, ред. проф. Машинског факултета

Потписани _____

Изјављујем да је штампана верзија мог докторског рада истоветна електронској верзији коју сам предао за објављивање на порталу **Дигиталног репозиторијума Универзитета у Београду**.

Дозвољавам да се објаве моји лични подаци везани за добијање академског звања доктора наука, као што су име и презиме, година и место рођења и датум одбране рада. Ови лични подаци могу се објавити на мрежним страницама дигиталне библиотеке, у електронском каталогу и у публикацијама Универзитета у Београду.

Потпис докторанда

У Београду, 16.,Новембар, 2017.

Прилог 3.

12 Изјава о коришћењу

Овлашћујем Универзитетску библиотеку „Светозар Марковић“ да у Дигитални репозиторијум Универзитета у Београду унесе моју докторску дисертацију под насловом:

LOW REYNOLDS NUMBER AIRFOILS
АЕРОПРОФИЛИ ЗА МАЛЕ РЕЈНОЛДСОВЕ БРОЈЕВЕ

која је моје ауторско дело.

Дисертацију са свим прилозима предао/ла сам у електронском формату погодном за трајно архивирање.

Моју докторску дисертацију похрањену у Дигитални репозиторијум Универзитета у Београду могу да користе сви који поштују одредбе садржане у одабраном типу лиценце Креативне заједнице (Creative Commons) за коју сам се одлучио.

1. Ауторство
2. Ауторство - некомерцијално
3. Ауторство – некомерцијално – без прераде
4. Ауторство – некомерцијално – делити под истим условима
5. Ауторство – без прераде
6. Ауторство – делити под истим условима

(Молимо да заокружите само једну од шест понуђених лиценци, кратак опис лиценци дат је на полеђини листа).

Потпис докторанда

У Београду, November 2017

1. Ауторство - Дозвољаваате умножавање, дистрибуцију и јавно саопштавање дела, и прераде, ако се наведе име аутора на начин одређен од стране аутора или даваоца лиценце, чак и у комерцијалне сврхе. Ово је најслободнија од свих лиценци.
2. Ауторство – некомерцијално. Дозвољаваате умножавање, дистрибуцију и јавно саопштавање дела, и прераде, ако се наведе име аутора на начин одређен од стране аутора или даваоца лиценце. Ова лиценца не дозвољава комерцијалну употребу дела.
3. Ауторство - некомерцијално – без прераде. Дозвољаваате умножавање, дистрибуцију и јавно саопштавање дела, без промена, преобликовања или употребе дела у свом делу, ако се наведе име аутора на начин одређен од стране аутора или даваоца лиценце. Ова лиценца не дозвољава комерцијалну употребу дела. У односу на све остале лиценце, овом лиценцом се ограничава највећи обим права коришћења дела.
4. Ауторство - некомерцијално – делити под истим условима. Дозвољаваате умножавање, дистрибуцију и јавно саопштавање дела, и прераде, ако се наведе име аутора на начин одређен од стране аутора или даваоца лиценце и ако се прерада дистрибуира под истом или сличном лиценцом. Ова лиценца не дозвољава комерцијалну употребу дела и прерада.
5. Ауторство – без прераде. Дозвољаваате умножавање, дистрибуцију и јавно саопштавање дела, без промена, преобликовања или употребе дела у свом делу, ако се наведе име аутора на начин одређен од стране аутора или даваоца лиценце. Ова лиценца дозвољава комерцијалну употребу дела.
6. Ауторство - делити под истим условима. Дозвољаваате умножавање, дистрибуцију и јавно саопштавање дела, и прераде, ако се наведе име аутора на начин одређен од стране аутора или даваоца лиценце и ако се прерада дистрибуира под истом или сличном лиценцом. Ова лиценца дозвољава комерцијалну употребу дела и прерада. Слична је софтверским лиценцама, односно лиценцама отвореног кода.